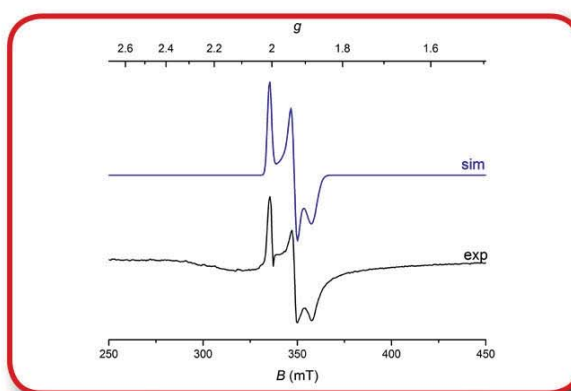
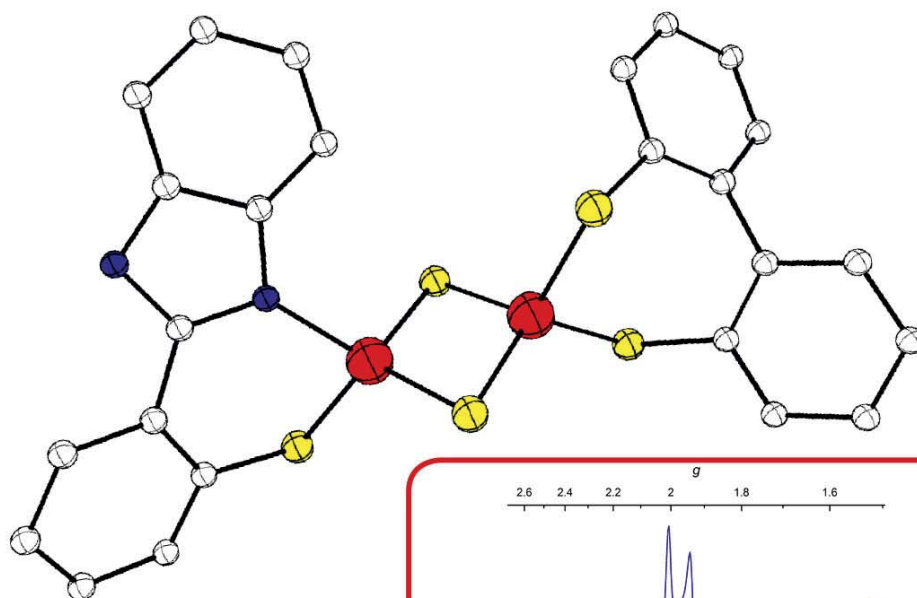


Marie Bergner

# Biomimetic Function of Iron Sulfur Clusters with Alternative Ligands: Model Studies Using Synthetic Analogues



Cuvillier Verlag Göttingen  
Internationaler wissenschaftlicher Fachverlag



Biomimetic Function of Iron Sulfur Clusters with Alternative Ligands:  
Model Studies Using Synthetic Analogues





# **Biomimetic Function of Iron Sulfur Clusters with Alternative Ligands: Model Studies Using Synthetic Analogues**



## **Dissertation**

Zur Erlangung des mathematisch-naturwissenschaftlichen Doktorgrades  
Doctor rerum naturalium (Dr. rer. nat.)  
im Promotionsprogramm BioMetals  
der Georg August University School of Science (GAUSS)

vorgelegt von  
Marie Bergner, M. Sc.  
aus Gera

Göttingen  
2017



### **Bibliografische Information der Deutschen Nationalbibliothek**

Die Deutsche Nationalbibliothek verzeichnet diese Publikation in der Deutschen Nationalbibliografie; detaillierte bibliografische Daten sind im Internet über <http://dnb.d-nb.de> abrufbar.

1. Aufl. - Göttingen: Cuvillier, 2017

Zugl.: Göttingen, Univ., Diss., 2017

Parts of this thesis have previously been published in:

M. Bergner, L. Roy, S. Dechert, S. Ye, F. Neese, F. Meyer, “*Ligand Rearrangement at Fe/S Cofactors: Slow Isomerization of a Biomimetic [2Fe-2S] Cluster*“, *Angew. Chem. Int. Ed.* **2017**, *56*, 4882-4886.

M. Bergner, S. Dechert, S. Demeshko, C. Kupper, J. M. Mayer, F. Meyer, “*Model of the MitoNEET [2Fe-2S] Cluster Shows Proton Coupled Electron Transfer*“, *J. Am. Chem. Soc.* **2017**, *139*, 701-707.

Figures are reproduced with permission from M. Bergner, S. Dechert, S. Demeshko, C. Kupper, J. M. Mayer, F. Meyer, “*Model of the MitoNEET [2Fe-2S] Cluster Shows Proton Coupled Electron Transfer*“, *J. Am. Chem. Soc.* **2017**, *139*, 701-707. Copyright 2017 American Chemical Society, and from M. Bergner, L. Roy, S. Dechert, S. Ye, F. Neese, F. Meyer, “*Ligand Rearrangement at Fe/S Cofactors: Slow Isomerization of a Biomimetic [2Fe-2S] Cluster*“, *Angew. Chem. Int. Ed.* **2017**, *56*, 4882-4886. Copyright 2017 Wiley-VCH.

© CUVILLIER VERLAG, Göttingen 2017

Nonnenstieg 8, 37075 Göttingen

Telefon: 0551-54724-0

Telefax: 0551-54724-21

[www.cuvillier.de](http://www.cuvillier.de)

Alle Rechte vorbehalten. Ohne ausdrückliche Genehmigung des Verlages ist es nicht gestattet, das Buch oder Teile daraus auf fotomechanischem Weg (Fotokopie, Mikrokopie) zu vervielfältigen.

1. Auflage, 2017

Gedruckt auf umweltfreundlichem, säurefreiem Papier aus nachhaltiger Forstwirtschaft.

ISBN 978-3-7369-9672-4

eISBN 978-3-7369-8672-5



### Betreuungsausschuss

Prof. Dr. Franc Meyer, Institut für Anorganische Chemie, Georg-August-Universität Göttingen

Prof. Dr. Kai Tittmann, Zentrum für Molekulare Biowissenschaften, Georg-August-Universität Göttingen (bis 06/2017)

Prof. Dr. Sven Schneider, Institut für Anorganische Chemie, Georg-August-Universität Göttingen (ab 06/2017)

### Mitglieder der Prüfungskommission

Referent:

Prof. Dr. Franc Meyer, Institut für Anorganische Chemie, Georg-August-Universität Göttingen

Koreferent:

Prof. Dr. Sven Schneider, Institut für Anorganische Chemie, Georg-August-Universität Göttingen

Weitere Mitglieder der Prüfungskommission:

Prof. Dr. Inke Siewert, Institut für Anorganische Chemie, Georg-August-Universität Göttingen

Prof. Dr. Manuel Alcarazo, Institut für Organische und Biomolekulare Chemie, Georg-August-Universität Göttingen

Jun. Prof. Dr. Selvan Demir, Institut für Anorganische Chemie, Georg-August-Universität Göttingen

Dr. Franziska Thomas, Institut für Organische und Biomolekulare Chemie, Georg-August-Universität Göttingen

Tag der mündlichen Prüfung: 3. 8. 2017





---

## Table of Contents

<u>1 Introduction</u> .....	1
1.1 Iron Sulfur Clusters in Nature.....	1
1.2 Iron Sulfur Cluster Biogenesis.....	2
1.3 Marcus Theory and Proton Coupled Electron Transfer.....	3
1.4 Alternative Ligands in Iron Sulfur Clusters.....	6
1.5 Iron Sulfur Clusters in Radical SAM Enzymes.....	8
1.6 Synthesis and Reactivity of Biomimetic Iron Sulfur Complexes.....	12
1.7 EPR Spectroscopy in Iron Sulfur Clusters.....	19
1.8 Mößbauer Spectroscopy in Iron Sulfur Clusters.....	21
<u>2 Thesis Outline</u> .....	25
<u>3 Characterization of a Biomimetic [2Fe–2S] Cluster in its Diferric, Mixed Valent and Protonated State</u> .....	27
3.1 Introduction.....	27
3.2 Synthesis and Structural Characterization of Diferric Cluster $4(\text{NEt}_4)_2$ .....	27
3.3 Spectroscopic Characterization of Diferric Cluster $4^{2-}$ .....	28
3.3.1 Spectroscopy in Solid State.....	28
3.3.2 Spectroscopy in Solution.....	30
3.4 Mixed Valent Cluster $4^{3-}$ .....	32
3.4.1 Characterization and Spectroscopy in the Solid State.....	32
3.4.2 Spectroscopy in Solution.....	35
3.5 Protonation of the Diferric and Mixed Valent Cluster.....	38
3.5.1 Protonation of the Diferric Cluster.....	38
3.5.2 Protonation of the Mixed Valent Cluster.....	42
3.6 Conclusion.....	44
<u>4 Slow Isomerization in a Synthetic [2Fe–2S] Cluster</u> .....	45
4.1 Introduction.....	45
4.2 Isomerization in MeCN- $d_3$ .....	46
4.3 Isomerization in DMF.....	52
4.4 Density Functional Theory (DFT) Calculations.....	55
4.5 Effect of Protonation and Cluster Redox State.....	57



---

4.6 Ligand Exchange Between Different Homoleptic [2Fe–2S] Clusters.....	58
4.7 Conclusion .....	59
<b>5 A Structural Model System for the [2Fe–2S] Cluster in MitoNEET Proteins .....</b>	<b>61</b>
5.1 Introduction.....	61
5.2 Synthesis and Crystallographic Characterization in the Solid State.....	61
5.3. Spectroscopy in the Solid State and in Solution .....	62
5.3.1 Spectroscopy in the Solid State.....	62
5.3.2 Spectroscopy in Solution .....	64
5.4 Mixed Valent Cluster $26^{3-}$ : Spectroscopy in Solid State and in Solution.....	67
5.5 Protonation of Diferric and Mixed Valent Clusters.....	70
5.5.1 Protonation of Diferric Cluster $26^{2-}$ .....	70
5.5.2 Protonation of Mixed Valent Cluster $26^{3-}$ .....	73
5.6 Conclusion .....	75
<b>6 Temperature Dependent Electrochemistry in a Series of [2Fe–2S] Clusters .....</b>	<b>77</b>
6.1 Introduction.....	77
6.2 Determination of Reaction Entropy of Electrochemical One Electron Reduction .....	79
6.3 Determination of Reaction Gibbs Free Energy and Enthalpy of One Electron Reduction .....	85
6.4 Conclusion .....	86
<b>7 Proton Coupled Electron Transfer in Biomimetic Iron Sulfur Clusters .....</b>	<b>89</b>
7.1 Introduction.....	89
7.2 Thermodynamic Square Scheme of Homoleptic Model $4^{2-}$ .....	90
7.3 PCET Reactivity in Homoleptic Model $4H^{2-}$ .....	91
7.4 Thermodynamic Square Scheme of MitoNEET model $26^{2-}$ .....	93
7.5 Kinetics of PCET in MitoNEET Model $26^{2-}$ .....	94
7.6 Comparison of Stepwise and Concerted Pathways.....	97
7.7 Conclusion .....	98
<b>8 Weak Binding Interactions Between Alkali Metal Cations and Synthetic [2Fe–2S] Clusters</b> <b>.....</b>	<b>99</b>
8.1 Introduction.....	99
8.2 Binding of Alkali Metal Cations to Homoleptic Cluster $4^{2-}$ .....	100
8.2.1 Determination of Binding Stoichiometry with $Li^+$ .....	100



8.2.2 Determination of Bonding Constants with Li <sup>+</sup> .....	102
8.2.3 Effect of Li <sup>+</sup> Binding on Electrochemical Properties of <b>4</b> <sup>2-</sup> .....	106
8.2.4 Binding of Na <sup>+</sup> to Homoleptic Cluster <b>4</b> <sup>2-</sup> .....	106
8.3 Binding Alkali Metal Ions to Heteroleptic Cluster <b>26</b> <sup>2-</sup> .....	108
8.4 Coordinating Alkali Metal Cations with Homoleptic Cluster <b>12a</b> <sup>2-</sup> .....	110
8.5 Conclusion .....	114
<b>9 Biomimetic [2Fe–2S] Clusters in Radical Reactions.....</b>	<b>115</b>
10.1 Introduction.....	115
10.2 Reactions Using Silicates as Radical Starters .....	118
10.2.1 Cluster <b>12a</b> <sup>2-</sup> and Radicals Generated from Silicates .....	118
10.2.2 Cluster <b>4</b> <sup>2-</sup> and Benzyl Radicals Generated from Silicates.....	121
10.3 Reactivity of <b>12a</b> (NEt <sub>4</sub> ) <sub>2</sub> Toward Organic Radicals Generated from DMPA .....	123
10.3.1 Spectroscopy in Solution .....	123
10.3.2 Spectroscopy in the Solid State.....	125
10.3.3 Mass Spectrometric Analysis.....	126
10.4 Reactivity of <b>4</b> <sup>2-</sup> Toward Organic Radicals Generated from DMPA.....	129
10.4.1 Spectroscopy in Solution .....	129
10.4.2 Spectroscopy in Solid State .....	131
10.4.3 Analysis of Final Reaction Products.....	132
10.5 Reactivity of a Neutral [2Fe–2S] Cluster Toward Organic Radicals Generated from DMPA .....	136
10.6 Conclusion .....	138
<b>10 Conclusion and Perspectives.....</b>	<b>141</b>
<b>11 Experimental Section.....</b>	<b>147</b>
11.1 General Considerations .....	147
11.2 Syntheses of Ligands and Clusters .....	148
11.3 Details of Cation Binding Titrations and Job Plot Experiments.....	153
11.4 Electrochemical Measurements .....	154
11.5 Double Mixing Stopped Flow Experiments .....	155
11.6 EPR Measurements.....	155
11.7 Mößbauer Measurements.....	156
11.8 X-Ray Crystallography .....	156



## 1 Introduction

---

<u>Structures of Ligands and Clusters .....</u>	<u>167</u>
<u>List of Abbreviations .....</u>	<u>169</u>
<u>References.....</u>	<u>173</u>
<u>Curriculum Vitae .....</u>	<u>183</u>
<u>Acknowledgment.....</u>	<u>185</u>

# 1 Introduction

## 1.1 Iron Sulfur Clusters in Nature

Iron sulfur clusters are ubiquitous cofactors, which exist in a variety of forms and serve a multitude of functions including electron transport, redox reactions and sensing.<sup>[1,2]</sup> They are thought to be among the oldest cofactors and are certainly among the most versatile ones.<sup>[2-5]</sup> They may even have been involved in the early evolution of life, which is supposed to have developed on the surface of iron sulfur structures.<sup>[6]</sup> They were first discovered by Beinert and Holm in 1960 using EPR spectroscopy, and since then a multitude of iron sulfur clusters have been discovered in all three kingdoms of life.<sup>[7]</sup> The most widespread forms include [2Fe-2S] clusters and [4Fe-4S] clusters but mononuclear species (rubredoxines) as well as [3Fe-4S] clusters and larger clusters exist as well, including the [8Fe-7S] P-Cluster and FeMoco found in nitrogenase (Figure 1.1).<sup>[1,8-11]</sup> Due to antiferromagnetic coupling between the two tetrahedrally coordinated iron centers, [2Fe-2S] clusters are typically found in an  $S = 0$  ground state in their diferric form.<sup>[12,13]</sup> In [4Fe-4S] cluster, two pairs of ferromagnetically  $\text{Fe}^{\text{III}}\text{Fe}^{\text{II}}$  subunits are antiferromagnetically coupled, resulting in a total  $S = 0$  ground state for the  $\text{Fe}^{\text{III}}_2\text{Fe}^{\text{II}}_2$  form.<sup>[1,12,14,15]</sup>

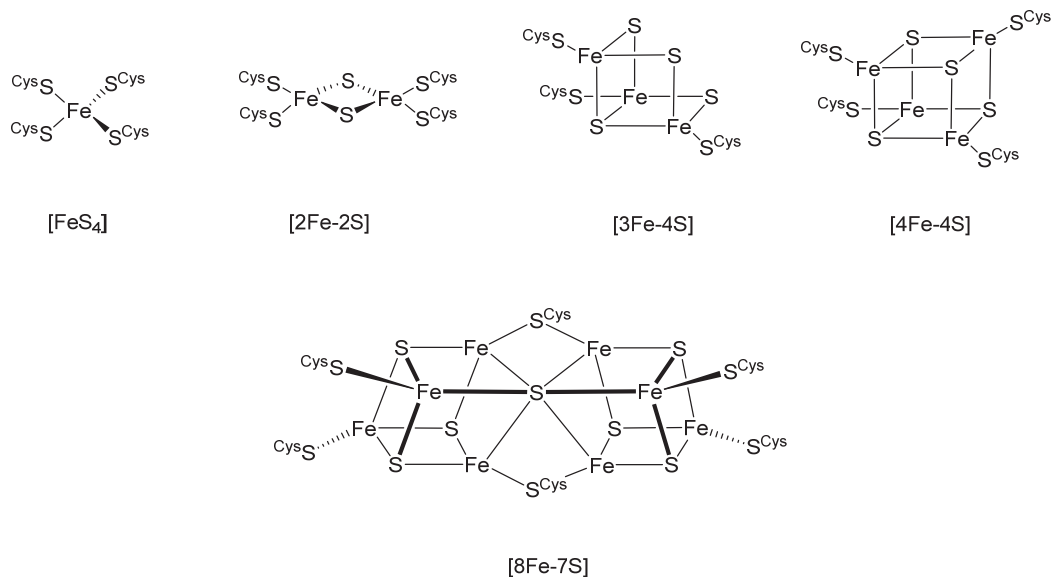


**Figure 1.1:** Different structural motifs found for biologically relevant iron sulfur clusters.

Due to the relatively easy accessibility of both the ferrous and ferric oxidation state, iron sulfur clusters are often involved in electron transfer processes, in which their redox potential spans a range from  $-600$  mV to  $+400$  mV, depending on cluster size, ligands, and the

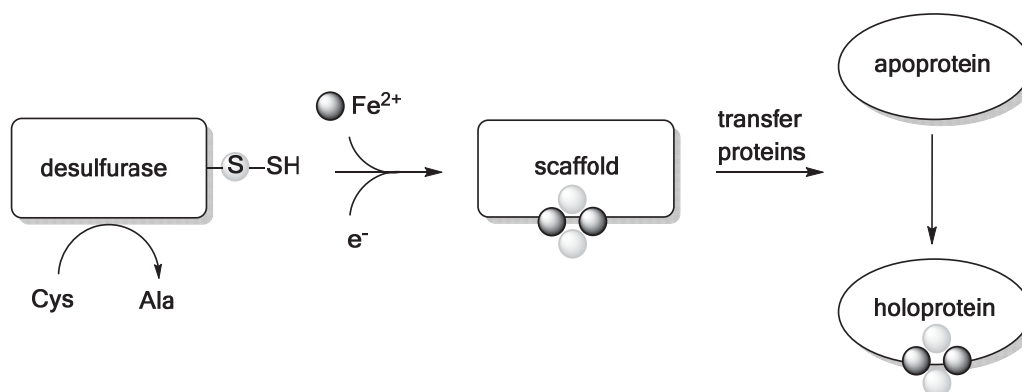


environment in the respective protein. The highest potentials are found in HiPIPs (high potential iron sulfur proteins) [4Fe–4S] clusters, which utilize the [4Fe–4S]<sup>2+/3+</sup> couple rather than the [4Fe–4S]<sup>1+/2+</sup> couple, and in [2Fe–2S] Rieske clusters, which feature two terminal histidine ligands instead of the commonly found cysteine ligands.<sup>[16–19]</sup> Iron sulfur cofactors have also been found in a number of different roles, highlighting their versatility: They are essential in catalytic transformations such as the transformation of citrate into isocitrate carried out by aconitase in the citrate cycle.<sup>[20]</sup> In this process, a non-protein coordinated iron ion of a [4Fe–4S] cluster offers a free coordination site and acts as a Lewis acid in the activation of water. Iron sulfur clusters have also been found to act as sensors for small molecules such as dioxygen or nitric oxide or for cellular conditions such as iron content or oxidative stress.<sup>[21–24]</sup> Roles of iron sulfur proteins in DNA replication and repair and thiolation of RNA have also been reported in recent years.<sup>[25–28]</sup> Additionally, iron sulfur cofactors play important roles in mediating proton coupled electron transfer (PCET) reactions, which will be explored in more detail in chapter 1.4.<sup>[29]</sup> A special role of iron sulfur cofactors as initiators and substrates of radical reactions has been described for radical SAM enzymes, which will be the focus of chapter 1.5.<sup>[30]</sup>

## 1.2 Iron Sulfur Cluster Biogenesis

Since iron sulfur clusters play important roles in a variety of biological processes, iron sulfur cluster biogenesis is an essential process in all three kingdoms of life. Defects in this process are associated with various diseases including Friedreich ataxia and IscU myopathy.<sup>[31–34]</sup> Although iron sulfur clusters can be reconstituted *in vitro* by addition of S<sup>2-</sup> and Fe<sup>3+</sup> to the respective apoproteins,<sup>[35]</sup> iron sulfur complex formation and maturation *in vivo* follows a more complex and closely regulated mechanism.<sup>[36,37]</sup> Three distinct machineries for iron sulfur cluster biogenesis exist (NIF, ISC, SUF).<sup>[31]</sup> The ISC and SUF systems are responsible for the generation and maturation of iron sulfur clusters under normal and stress conditions, respectively<sup>[38–40]</sup> whereas the NIF system carries out the maturation of nitrogenase in azototrophic bacteria. Although they operate under different conditions, the ISC and SUF systems follow a similar mechanism (Scheme 1.1). Cysteine desulfurase has been identified as the source of the sulfides in this process, which provides the sulfide needed in Fe/S cluster assembly by generating a persulfide intermediate *via* conversion of cysteine to alanine.<sup>[41]</sup> For this process an electron donor such as a ferredoxin reductase is necessary to achieve the reduction from S<sup>0</sup> to S<sup>2-</sup>.<sup>[42]</sup> Since free iron ions are cytotoxic, they must be delivered by iron donors such as the iron binding protein frataxin (in bacterial CyaY and mitochondrial Yfh1) of the ISC system.<sup>[43–45]</sup> [2Fe–2S] clusters can then be assembled on scaffold proteins such as the bacterial IscU, which contain three conserved iron sulfur cluster binding cysteine residues.<sup>[42,46,47]</sup> The thus assembled cluster can subsequently be transferred to the respective apoproteins. The transfer proteins needed in this last step must induce dissociation of the

cluster from the scaffold protein and ensure accurate transfer to the respective position in the apoprotein.<sup>[48,49]</sup> It has been shown that the scaffold protein IscU changes its conformation to facilitate release of the formed iron sulfur cluster.<sup>[50]</sup> The formation of larger clusters such as [4Fe–4S] clusters is achieved by fusion of two [2Fe–2S] clusters and is believed to require an additional reductant.<sup>[51,52]</sup> This overall principle of iron sulfur cluster biogenesis seems to be conserved in prokaryotes and eukaryotes reaching from yeast to human cells.<sup>[53–57]</sup>



**Scheme 1.1:** Overview of different steps occurring in iron sulfur cluster biogenesis, scheme modified from literature.<sup>[31]</sup>

*In vivo* and *in vitro* studies have already provided valuable insight into the cluster transfer during iron sulfur cluster biogenesis but there is only limited understanding of this process on a molecular level. Transfer of intact [2Fe–2S] clusters from the IscU protein to the target apoprotein was shown to be ATP dependent and to proceed under second order kinetics. It was proposed that cluster transfer might occur *via* successive ligand exchange after formation of a transient donor-acceptor complex, since a conserved aspartate residue Asp39 in *azotobacter vinelandinii* IscU plays a crucial role in facilitating cluster release.<sup>[58]</sup> Initial displacement of this residue and subsequent coordination of the cysteine residue of the respective apoprotein was proposed to occur as a rate determining step in cluster transfer. Additionally, chaperone and co-chaperone complexes of the scaffold and target protein need to be present during the iron sulfur cluster transfer process.<sup>[59–61]</sup> However, detailed mechanistic studies of ligand exchange and rearrangement at the [2Fe–2S] core are needed to fully understand this essential process on a molecular level.

### 1.3 Marcus Theory and Proton Coupled Electron Transfer

In 1975 Marcus and Sutin presented a theory for treating the thermodynamics of electron transfer reactions that is still widely applied today and referred to as Marcus theory.<sup>[62,63]</sup> The free energy barrier  $\Delta G^\ddagger$  for an electron transfer can be calculated from the difference in free energy of the educt and product  $\Delta G^\circ$  and the reorganization energy  $\lambda$ :

$$\Delta G = 1/4 \lambda (1 + \Delta G^\circ/\lambda)^2$$

The rate  $k_{ET}$  of the electron transfer at a temperature  $T$  is then determined as ( $k_B = 1.38 \cdot 10^{-23} \text{ J K}^{-1}$ ,  $h = 6.626 \cdot 10^{-34} \text{ J s}$ , the pre-exponential frequency factor  $\kappa$  contains the probability of crossing from one energy surface to the other and depends of the degree of adiabaticity and the general nature of the electron transfer):

$$k_{ET} = (\kappa k_B T/h) \exp(-\Delta G/k_B T)$$

Thus, according to Marcus Theory, the rate of an electron transfer step mainly depends on the following three factors: The reorganization energy  $\lambda$  is associated with geometrical changes both at the actual redox center (inner-sphere reorganization energy,  $\lambda_{\text{inner}}$ ) as well as of the surrounding protein and solvent molecules (outer-sphere reorganization energy,  $\lambda_{\text{outer}}$ ). It has to be rather small to enable efficient electron transfer since a larger reorganization energy leads to a larger activation free energy  $\Delta G^\ddagger$ . Additionally, the slope of the two parabolas of the free energy surface of both educts and products must not be too steep, since this would lead to a large  $\Delta G^\ddagger$ . Finally, the difference in free energy  $\Delta G^\circ$  between the educt and the product determines the rate of the electron transfer.  $\Delta G^\ddagger$  decreases with increasing  $\Delta G^\circ$ . A maximum rate is reached when  $\Delta G^\circ = -\lambda$  and the reaction then proceeds activationless. Upon further increase of  $\Delta G^\circ$  (*i.e.* when  $\Delta G^\circ > \lambda$ )  $\Delta G^\ddagger$  increases as well, the electron transfer is slowed down and the so called Marcus inverted region is reached.<sup>[62]</sup>

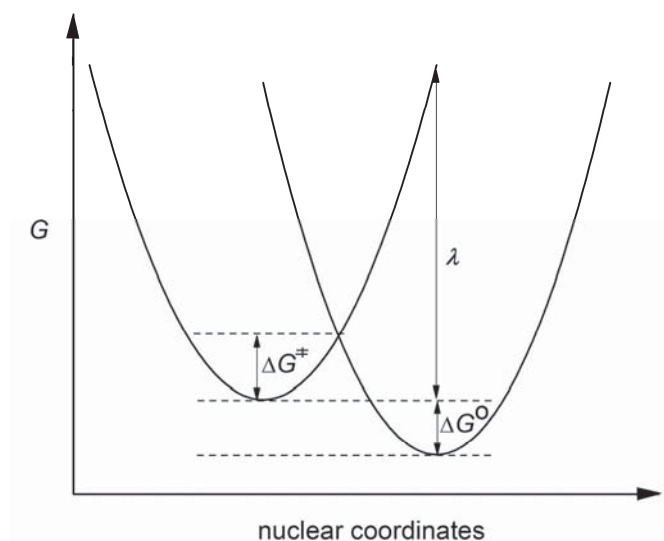
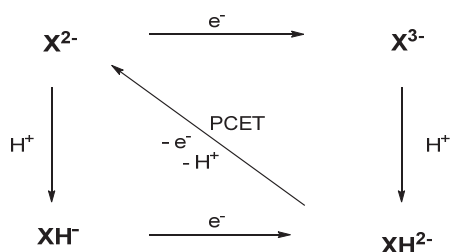


**Figure 1.2:** Parabolas of the free energy surface of the educt and product of an electron transfer reaction and relation to thermodynamic parameters.<sup>[64]</sup>

More recently, it has been shown that a Marcus Theory type description is also applicable to proton coupled electron transfer (PCET) reactions.<sup>[65–67]</sup> In the broadest sense, a PCET reaction is any reaction, in which an equal number of protons and electrons are transferred. PCET is ubiquitous in biological systems and essential in processes such as photosynthesis, in the respiratory chain, and during water oxidation.<sup>[68]</sup> It may also play a role in several processes present in solar fuel cells.<sup>[68]</sup> A concerted proton and electron transfer in metalloenzymes was first proposed by Stiefel, who described mechanistic scenarios of molybdenum enzymes in 1973.<sup>[69]</sup> A PCET process is often rationalized based on a thermodynamic square scheme (Scheme 1.2). Therein, the protonation step is described by the  $pK_a$  value, which can be determined *via* titration experiments for example. The electron transfer step is characterized by the  $E_{1/2}$  value of the corresponding redox couple, *i.e.* from the peak potentials as  $(E_{\text{red}}+E_{\text{ox}})/2$  determined *via* cyclic voltammetry (CV).



**Scheme 1.2:** Thermodynamic square scheme relating protonation, reduction and PCET in a dianionic compound  $X^{2-}$ .<sup>[64]</sup>

The overall proton and electron transfer reaction can proceed in a stepwise fashion, *i.e.* moving along the edges of the square scheme or in a concerted manner moving across the diagonal of the square scheme. If the reaction proceeds in a concerted mechanism without a discrete intermediate it is usually referred to as CPET (concerted proton and electron transfer). If the proton and electron are delivered to a single acceptor, the reaction is called HAT (hydrogen atom transfer). However, a clear distinction between CPET and HAT is not always possible.<sup>[70]</sup> A concerted mechanism is implied when the kinetic barrier of the PCET reaction, which can be derived from an Eyring plot, is smaller than the free energy differences associated with an initial PT or an initial ET step. Because of the uncertainties associated with values obtained from kinetic studies, the activation barrier should be at least several  $\text{kcal mol}^{-1}$  lower than the free energy barriers for the stepwise reactions, to draw reliable mechanistic conclusions.<sup>[70]</sup> The free energy change for the separate ET step ( $\Delta G^\circ_{\text{ET}}$ ) can be calculated according to (wherein  $F = 96485 \text{ C mol}^{-1}$ ):

$$\Delta G^\circ_{\text{ET}} = -F \cdot \Delta E^\circ = - (96.48 \text{ kJ mol}^{-1} \text{ V}^{-1}) \Delta E^\circ$$

The free energy change for the separate PT step ( $\Delta G^\circ_{\text{PT}}$ ) can be calculated according to ( $R = 8.314 \text{ J mol}^{-1} \text{ K}^{-1}$ ):

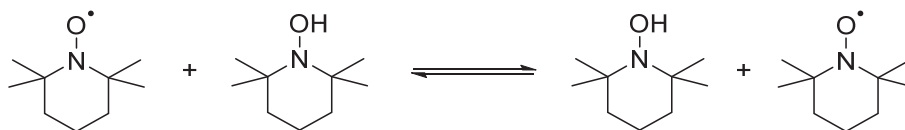
$$\Delta G^{\circ}_{\text{PT}} = -RT \ln(pK_a)$$

The bond dissociation free energy (BDFE) is directly connected to the free energy of the reaction and can be calculated as:<sup>[64]</sup>

$$\text{BDFE}_{\text{X-H}} (\text{kcal/mol}) = 1.37 pK_a + 23.06 E_{1/2} + C_{\text{G,sol}}$$

The constant  $C_{\text{G,sol}}$  describes the free energy of the formation and solvation of  $\text{H}^{\cdot}$ , and was reported as 54.9 in MeCN. The overall driving force of a PCET reaction, in which  $\text{H}^+$  and  $\text{e}^-$  are transferred from one reaction partner to the other can then be calculated from the difference of BDFEs between the two reaction partners.<sup>[64]</sup>

One typical PCET reagent for which proton and electron transfer occur in a concerted mechanism rather than in a stepwise fashion is 2,2,6,6-tetramethylpiperidinyloxy (TEMPO). The self-exchange between TEMPO and TEMPOH occurs with an Eyring barrier of  $\Delta G^{\ddagger} = 16.5 \text{ kcal mol}^{-1}$  in MeCN<sup>[71]</sup> while the free energy differences are  $\Delta G^{\circ} = 60 \text{ kcal mol}^{-1}$  both for an initial PT or an initial ET step.<sup>[64]</sup> Other well studied PCET reagents include further hydroxylamines as well as phenols, hydroquinones and catechols.<sup>[64]</sup>



**Scheme 1.3:** Self-exchange reaction between TEMPO and TEMPOH.<sup>[72]</sup>

## 1.4 Alternative Ligands in Iron Sulfur Clusters

While the majority of iron sulfur clusters are ligated by four cysteine residues of the surrounding protein, a subset of  $[2\text{Fe}-2\text{S}]$  clusters with different ligands exist has been found.<sup>[73]</sup> The most commonly observed of those alternative ligands is histidine but in most cases the role of this alternative ligand is not fully understood yet. Roles of the alternative ligands may include tuning of redox properties, mediating proton coupled electron transfer (PCET), cluster transfer or release, and sensing.<sup>[73]</sup> Some prominent examples include  $\text{Cys}_2\text{His}_2$  ligated Rieske centers,<sup>[74]</sup>  $\text{Cys}_3\text{His}$  ligated clusters as can be found in mitoNEET proteins<sup>[75]</sup> and the  $\text{Cys}_3\text{Arg}$  ligated  $[2\text{Fe}-2\text{S}]$  cluster in biotin synthase<sup>[76]</sup> (Figure 1.3).

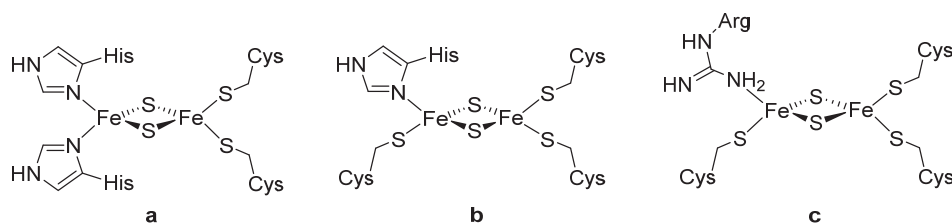


**Figure 1.3:** Coordination motifs of  $[2\text{Fe}-2\text{S}]$  clusters featuring alternative ligands *in vivo*: Rieske cofactors (a), mitoNEET proteins (b) and biotin synthase (c).

Of these examples, the Rieske center discovered in 1964 is the most thoroughly studied and its properties and function have been understood very well.<sup>[77]</sup> It features heteroleptic ligation with two histidine ligands on one of the iron centers and two cysteines on the other.<sup>[78–81]</sup> Rieske centers can be found in a multitude of electron transfer processes.<sup>[74]</sup> In respiratory and photosynthetic chains, they are responsible for the oxidation of quinole compounds in the Q-cycle, which is coupled to the generation of a proton gradient. It has been shown that the unpaired electron in the cluster's mixed valent form is located at the histidine coordinated iron site. The redox behavior of Rieske centers is strongly pH dependent, due to a coupling of the cluster's redox state to the protonation state of the histidine ligands.<sup>[78,81–86]</sup> This enables Rieske clusters to carry out PCET reactions during the conversion of hydroquinone substrates in the Q-cycle.<sup>[29]</sup>

The  $[2\text{Fe}-2\text{S}]$  cluster of mitoNEET proteins was discovered more recently in 2004 and was identified as a target for pioglitazone and thiazolidinedione drugs, which are used in the treatment of diabetes type 2.<sup>[75]</sup> Since they play a role in a number of processes related to human diseases, including proliferation of breast cancer and diabetes, the exact function of mitoNEET proteins is of special interest.<sup>[87–89]</sup> They contain a redox active and acid labile  $[2\text{Fe}-2\text{S}]$  cluster which features coordination by two cysteines on one of the iron centers and by one cysteine and one histidine on the other.<sup>[90–95]</sup> Several functions for this cluster have been proposed including redox and/or pH sensing,<sup>[96]</sup> cluster-transfer<sup>[97]</sup> and mediating redox reactions.<sup>[94]</sup> The exact function of the cluster and the role of the unique single histidine ligand have not been fully understood to date. The backside of the histidine's imidazole moiety is positioned at the surface of the protein and is thus easily exposed to changes in the environment of the protein.<sup>[93]</sup> The histidine has thus been proposed to act as a proton responsive ligand and indeed the mitoNEET  $[2\text{Fe}-2\text{S}]$  cluster shows a pH dependent redox potential.<sup>[75,98]</sup> Pulsed EPR studies have confirmed that the unpaired electron is localized on the histidine ligated iron site in the cluster's mixed valent form and reduction of the cluster was shown to be coupled to proton uptake.<sup>[99]</sup> Thus a role in PCET reactions similar to that of Rieske clusters has been proposed.<sup>[100]</sup> The redox state of the cluster is crucial in mediating the protein's reactivity. Transfer of the  $[2\text{Fe}-2\text{S}]$  cluster from mitoNEET to an acceptor protein can only occur in the diferric state while no cluster transfer has been observed in the

mixed valent form.<sup>[101]</sup> Histidine ligation was shown to be essential for this process, since no cluster transfer was observed in mutants lacking this residue.<sup>[102]</sup>

The mitoNEET [2Fe–2S] cluster is embedded in a network of hydrogen bonding residues, which are conserved throughout the protein family namely Lys55, Ser77, and Asp84 (Figure 1.4).<sup>[96]</sup> These hydrogen bonds are essential in modulating both the stability of the cluster and the functionality of the protein. They may also act as a gateway for protons during PCET reactions. Other [2Fe–2S] clusters featuring a Cys<sub>3</sub>His ligation include the bacterial transcription factor IscR which modulates the binding of DNA and glutaredoxins, which are responsible for ATF1 binding.<sup>[73]</sup>

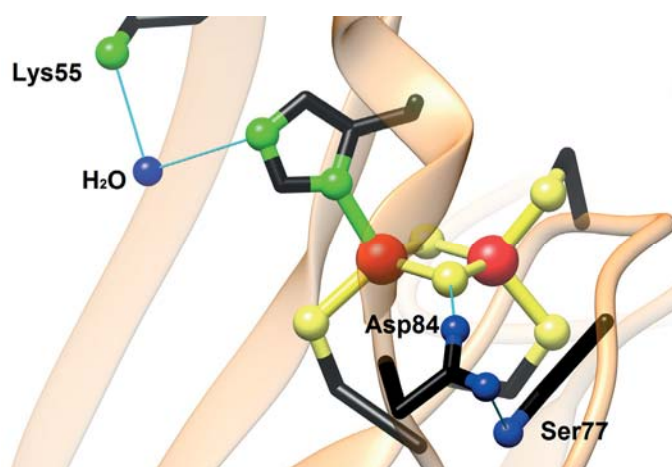
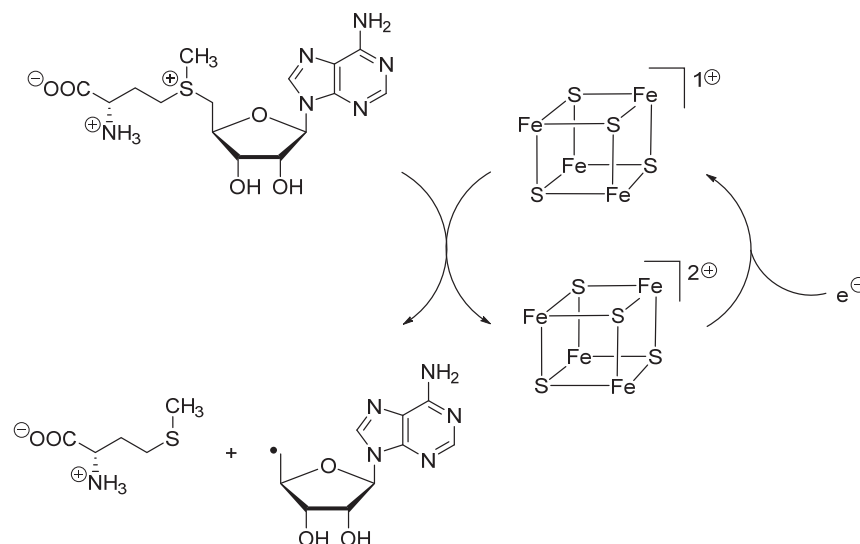


**Figure 1.4:** The [2Fe–2S] cluster of human mitoNEET protein (PDB entry 2QH7) in a network of hydrogen bonds with the conserved residues Lys55, Ser77, Asp84, and one molecule of water.<sup>[96]</sup> Color code: Fe (red), S (yellow), N (green), O (blue), C (black).

## 1.5 Iron Sulfur Clusters in Radical SAM Enzymes

All of the more than 600 enzymes in the radical SAM family mediate radical reactions by using *S*-adenosyl-*L*-methionine (SAM), which has been referred to as the “poor man’s adenosylcobalamin” because of its versatility,<sup>[103]</sup> and which can reductively be cleaved into methionine and a 5′-deoxyadenosyl (5′-doA) radical.<sup>[104–107]</sup> This radical is a potent oxidant and can abstract an H atom from the respective substrate, thus initiating substrate conversion (Scheme 1.4). All members of the radical SAM family share a [4Fe–4S] cluster coordinated by the cysteine residues of a conserved CX<sub>3</sub>CX<sub>2</sub>C motif.<sup>[106]</sup> SAM can bind to a free coordination site of this cluster in a bidentate fashion *via* its carboxylate and amino functions.<sup>[108]</sup> During turnover, the [4Fe–4S] cluster is oxidized and must be re-reduced before a second equivalent of SAM can be cleaved into methionine and 5′-doA.<sup>[109]</sup> This conserved [4Fe–4S] cluster is both crucial in delivering an electron to SAM to initiate bond

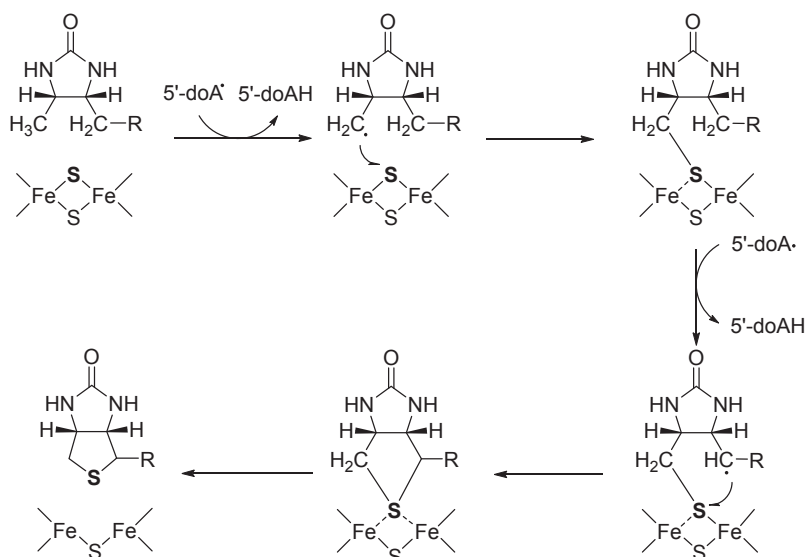
cleavage but also in positioning SAM in close proximity to the respective substrate and thus facilitating the subsequent H atom abstraction.<sup>[108]</sup> A subset of radical SAM enzymes contain so called auxiliary iron sulfur clusters. Prominent examples for this group are the two sulfur donating enzymes biotin synthase (BioB) and lipoyl synthase (LipA) as well as methylthiotransferases MiaB and RimO.<sup>[107]</sup>



**Scheme 1.4:** Radical generation from SAM mediated by a [4Fe-4S] cluster.<sup>[107]</sup>

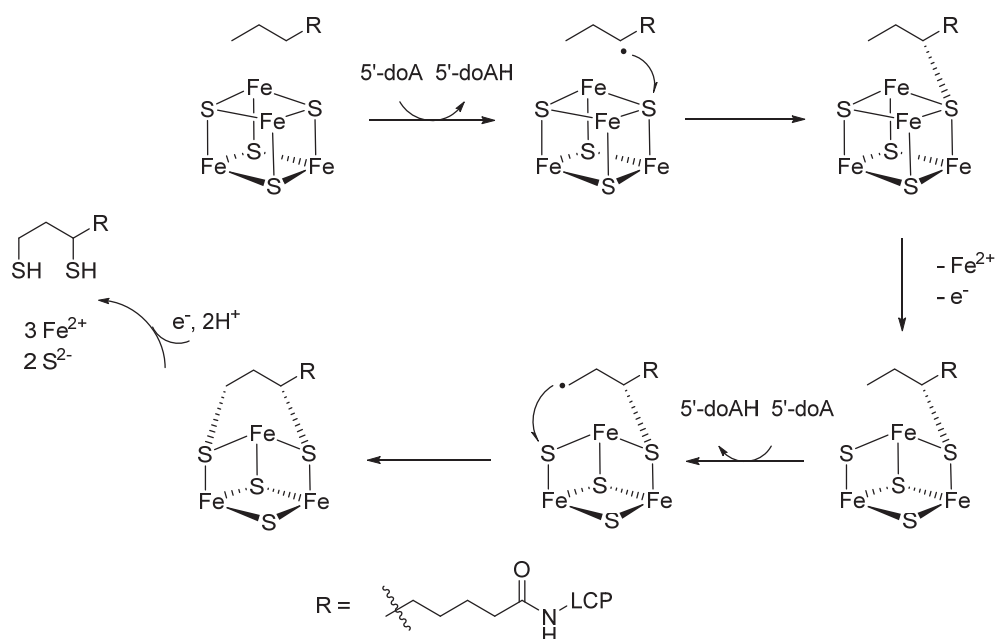
Biotin synthase (BioB) is arguably the most prominent example of a radical SAM enzyme. It catalyzes the final step of biotin biosynthesis by inserting a sulfur atom into dethiobiotin (DTB) thus closing the heterocycle of this natural product. Two equivalents of 5'-doA, *i.e.* two equivalents of SAM, are required to activate DTB in positions C6 and C9. BioB contains the conserved [4Fe-4S] cluster needed to achieve radical initiation and an auxiliary [2Fe-2S] cluster, whose role has been subject to intensive debates and is now believed to be the sulfur source of the catalyzed reaction.<sup>[110-114]</sup> The crystal structure of BioB reported in 2004 shows the substrate (DTB) placed between the [2Fe-2S] and the [4Fe-4S] cluster.<sup>[115]</sup> Reduction of the auxiliary [2Fe-2S] cluster during turnover was observed *via* EPR spectroscopy, indicating attack of an organic radical to this cluster.<sup>[116]</sup> Further evidence for a role of the [2Fe-2S] cluster as sulfur donor was provided by studies of biotin synthase reconstituted to contain a [2Fe-2Se] cluster which was shown to produce selenobiotin from dethiobiotin.<sup>[117]</sup> Based upon these findings, the following mechanism for the reaction catalyzed by BioB has been proposed (Scheme 1.5).<sup>[118]</sup> The 5'-doA radical produced from SAM abstracts an H atom from DTB resulting in the formation of a highly reactive primary radical. This radical attacks the bridging sulfide of the [2Fe-2S] cluster and forms the first C-S bond. A second 5'-doA radical then abstracts a second H atom from DTB and subsequently a second radical attack on the bridging sulfide can occur. After formation of the second C-S bond, biotin can

be released as a final product. During this process, the [2Fe–2S] cluster loses one of its bridging sulfides and must be reconstituted before a second turnover can take place.<sup>[118]</sup> BioB is thus often called a “suicide enzyme”.<sup>[30]</sup>



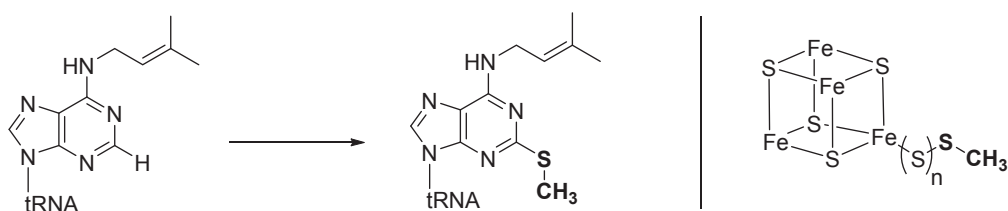
**Scheme 1.5:** Postulated mechanism for biotin biosynthesis as achieved by BioB.<sup>[118]</sup>

Similar to BioB, lipoyl synthase LipA achieves the formation of two C–S bonds on an octanoyl chain attached to a lipoyl carrier protein (LCP).<sup>[119]</sup> The crystallographic characterization reported in 2014 showed two independent [4Fe–4S] clusters.<sup>[120,121]</sup> One of them is coordinated by three cysteine residues of the conserved CX<sub>3</sub>CX<sub>2</sub>C motif and is responsible for radical generation from SAM. The second [4Fe–4S] cluster is coordinated by three cysteine ligands and one serine ligand and acts as an auxiliary cluster similar to the auxiliary [2Fe–2S] cluster in BioB. Two equivalents of SAM are needed for one turnover as two C–S bonds are formed in a stepwise mechanism (Scheme 1.6).<sup>[122]</sup> Evidence for a crosslinked enzyme-substrate intermediate was reported in 2014 relying on EPR and Mößbauer spectroscopy. It was found that the [4Fe–4S] cluster loses the serine-coordinated iron ion during the formation of this intermediate, which shows the spectroscopic characteristics of a [3Fe–4S]<sup>0</sup> cluster with an *S* = 1/2 ground state.<sup>[123]</sup> This [3Fe–4S] intermediate was also characterized crystallographically.<sup>[122,124]</sup> The auxiliary cluster is sacrificed during turnover and has to be regenerated. Thus LipA can be regarded a suicide enzyme similar to BioB.<sup>[125]</sup> Mößbauer spectroscopy revealed, that only the second [4Fe–4S] cluster which is used for radical generation remains present in the enzyme after turnover.<sup>[123]</sup>



**Scheme 1.6:** Formation of two C–S bonds on an octanoyl chain catalyzed by lipoyl synthase *via* a cross linked intermediate.<sup>[122,124]</sup>

A second type of sulfur donating radical SAM enzymes featuring auxiliary iron sulfur clusters are methylthiotransferases such as MiaB and RimO.<sup>[107,126,127]</sup> Similar to LipA, both MiaB and RimO harbor two distinct [4Fe–4S] clusters. MiaB catalyzes the methylthiolation of an adenosine nucleotide of tRNA (Scheme 1.7).<sup>[128]</sup> Similar to the reactions catalyzed by BioB and LipA, this requires the formation of a C–S bond, the H atom is abstracted from an  $sp^2$  hybridized carbon instead of from an  $sp^3$  hybridized carbon. Similar to MiaB, RimO catalyzes a methylthiolation, but in this case of an  $sp^3$  hybridized carbon of a conserved aspartate in ribosomal protein S12 in *Escherichia coli*.<sup>[129]</sup>



**Scheme 1.7:** Methylthiolation of an adenosine nucleotide of tRNA catalyzed by MiaB (left) *via* an intermediate [4Fe–4S] methyl carrier (right).

The main difference between methylthiotransferases and sulfur insertion enzymes BioB and LipA lies in their use of SAM. While BioB and LipA cleave two equivalents of SAM to generate two equivalents of 5'-doA, methylthiotransferases cleave one equivalent of SAM to generate 5'-doA but the second equivalent of SAM is used as the methyl donor.<sup>[128,130]</sup> One plausible mechanistic scenario involves the generation of a protein bound methylthio group



which is subsequently transferred to the substrate.<sup>[107]</sup> This hypothesis is supported by studies by Landgraf *et al.*, who have identified the protein bound methylthio intermediate (Scheme 1.7) and performed labeling studies showing that it is chemically competent in transferring its methylthio group to the respective substrates.<sup>[131]</sup>

### 1.6 Synthesis and Reactivity of Biomimetic Iron Sulfur Complexes

Since the discovery of their biological blueprints in the 1960s, synthetic iron sulfur clusters have largely contributed to the understanding of their structure, spectroscopic features and reactivity, and have been essential in establishing relations between structural and spectroscopic signatures.<sup>[132–134]</sup> In comparison with their biological blueprints, most synthetic iron sulfur clusters display far lower redox potentials and can only be studied in organic solvents such as MeCN.<sup>[132]</sup> They are mostly very sensitive toward the presence of oxygen and water, due to the lability of the bridging sulfides. The first synthetic [2Fe–2S] cluster **1**<sup>2-</sup> reported in 1973 features bidentate chelating thiolate ligands and was also prepared in a self-assembly reaction using FeCl<sub>3</sub>, NaSH and the deprotonated ligand *o*-xylyl- $\alpha$ - $\alpha'$ -dithiol.<sup>[135]</sup> The simple tetrachloro-coordinated cluster **2**<sup>2-</sup> is readily available from a self-assembly reaction using [FeCl<sub>4</sub>](NEt<sub>4</sub>)<sub>2</sub> and (SiMe<sub>3</sub>)<sub>2</sub>S with almost quantitative yields and has been used as a precursor in the synthesis of a number of biomimetic [2Fe–2S] clusters.<sup>[132,136,137]</sup> One example is the synthetic [2Fe–2S] cluster **3**<sup>2-</sup> reported in 2008, which is coordinated by thiolate ligands as well.<sup>[138]</sup> Through secondary bonding interactions, a five coordination of both ferric ions was achieved, which may present a model for transition states of biological conversions occurring on [2Fe–2S] clusters.

While the naturally occurring cysteine ligands have been mimicked by use of thiolate ligands in synthetic iron sulfur cluster chemistry, varying approaches for modeling the N-donor of the histidine ligands have been reported. Benzimidazole based ligands have been used by Beardwood and Gibson in the synthesis of homoleptic [2Fe–2S] clusters starting from precursor **2**<sup>2-</sup> in a simple ligand exchange reaction.<sup>[139]</sup> Among these are clusters **4**<sup>2-</sup> and **5**<sup>2-</sup> which feature mixed S/N or O/N ligation on both iron sites. The first neutral [2Fe–2S] cluster **6** was reported by Tatsumi in 2005 and features terminal monodentate amide ligands.<sup>[140]</sup> Due to its neutral charge it is soluble in a broad range of solvents and makes a multitude of reactivity studies possible. A different approach in mimicking N-donating ligands is the use of ketimate ligands such as in neutral cluster **7** reported by Holland and neutral cluster **8** reported by Driess.<sup>[141,142]</sup> In both cases the synthesis of these clusters relied on the conversion of mononuclear iron(I) species with elemental sulfur to achieve sulfide insertion as the last step of cluster synthesis. Both species have also been isolated and structurally

characterized in their mixed valent forms and an extensive delocalization was observed in **8** via Mößbauer spectroscopy. Iron(I) precursors have also been used in the synthesis of  $[2\text{Fe}-2\text{E}]$  clusters ( $\text{E} = \text{O}, \text{S}, \text{Se}$ ) by reaction with molecular oxygen, elemental sulfur or selenium.<sup>[143]</sup> These neutral diferric compounds feature bidentate N-donating capping ligands and a distorted square planar coordination of the iron centers has been observed in the  $[2\text{Fe}-2\text{O}]$  species, whereas the  $[2\text{Fe}-2\text{S}]$  and  $[2\text{Fe}-2\text{Se}]$  species show a tetrahedral coordination of the iron centers.

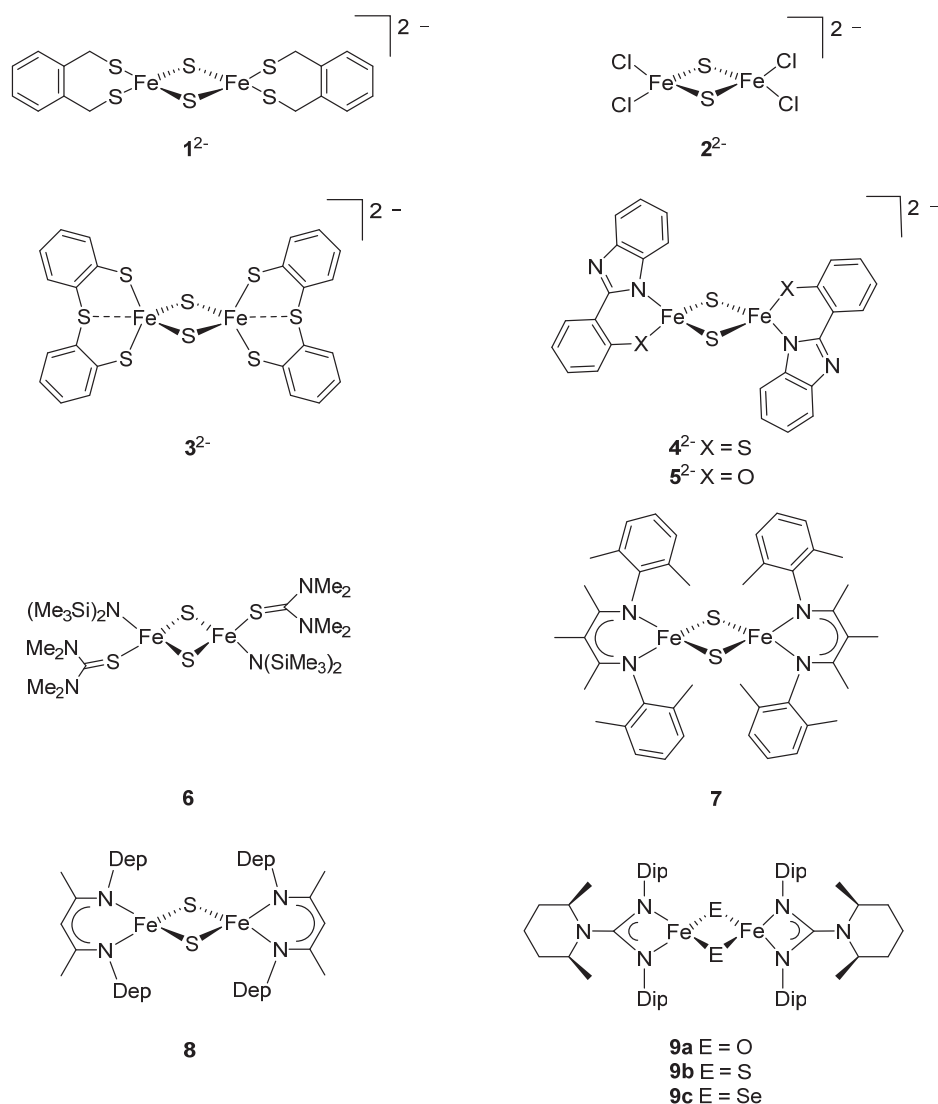


**Figure 1.5:** Synthetic  $[2\text{Fe}-2\text{S}]$  clusters: The first synthetic  $[2\text{Fe}-2\text{S}]$  cluster  $1^{2-}$ , tetrachloro-coordinated cluster  $2^{2-}$  serving as a precursor for new synthetic model systems, thiolate ligated cluster  $3^{2-}$  featuring five-coordinate iron centers, benzimidazole based clusters  $4^{2-}$  and  $5^{2-}$ , neutral cluster **6** and ketimate ligated clusters **7** and **8** (Dep =  $\text{C}_6\text{H}_3\text{iPr}_2$ ) illustrating various approaches in mimicking the naturally occurring histidine ligand and chalcogene analogues of  $[2\text{Fe}-2\text{S}]$  clusters **9a-c** (Dip =  $\text{C}_6\text{H}_3\text{iPr}_2$ ).

While a number of homoleptic [2Fe–2S] clusters have been prepared *via* different synthetic strategies, the synthesis of heteroleptic [2Fe–2S] clusters is considerably more challenging, since ligand scrambling and formation of homoleptic side products have to be suppressed.

The first synthetic analogue **11**<sup>2-</sup> mimicking the heteroleptic {N<sub>2</sub>} {S<sub>2</sub>} coordination found in Rieske proteins was only reported in 2008 (Figure 1.6).<sup>[144]</sup> This heteroleptic cluster can be viewed as a combination of all-N-ligated cluster **10**<sup>2-</sup> and all-thiolate ligated cluster **1**<sup>2-</sup> and was prepared in a stepwise ligand exchange reaction starting from precursor **2**<sup>2-</sup>. The average *g* value of *g*<sub>av</sub> = 1.92 found in the mixed valent form is in good agreement with the *g*<sub>av</sub> found in Rieske Proteins (about 1.90–1.91).<sup>[77,145,146]</sup>

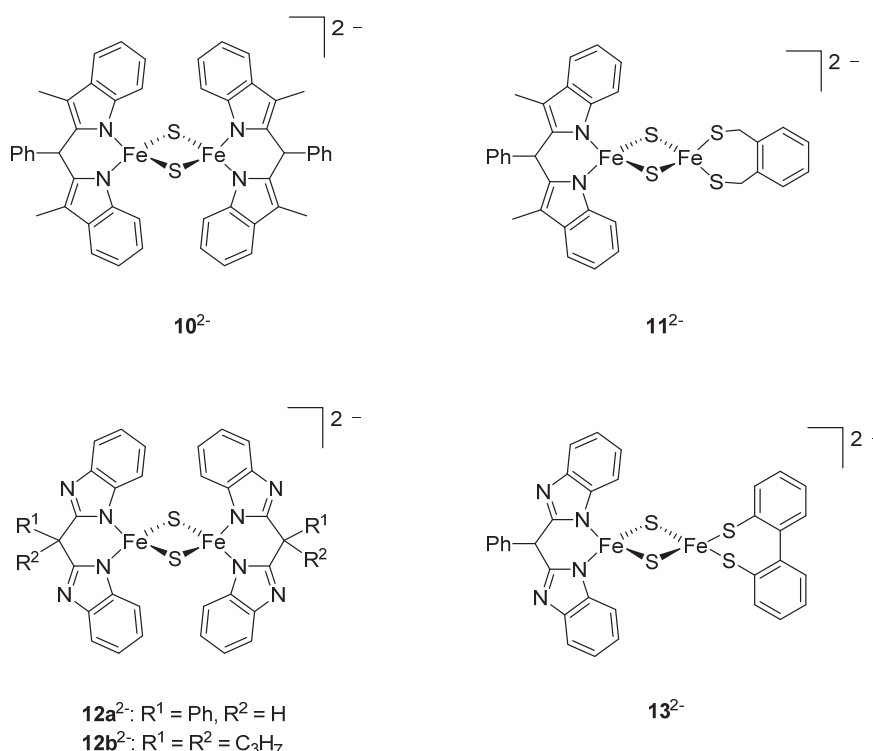
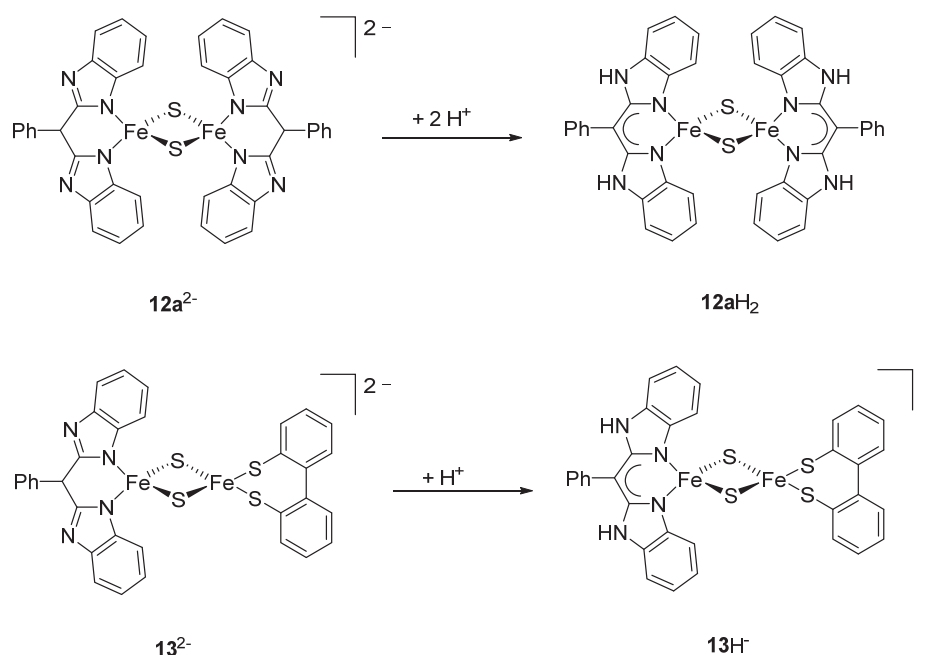


**Figure 1.6:** Evolution of synthetic models for [2Fe–2S] Rieske centers from 2008 to 2014.<sup>[144,147,148]</sup>

Although **10**<sup>2-</sup> proved to be a good structural and spectroscopic model, it lacks a distal N-atom in the ligand's backbone to fully emulate the properties of the histidine as a proton responsive ligand. To enable protonation and thus proton coupled electron transfer (PCET), bis-benzimidazoles were used as ligands and clusters **12**<sup>2-</sup> and **13**<sup>2-</sup> were prepared.<sup>[147–149]</sup>

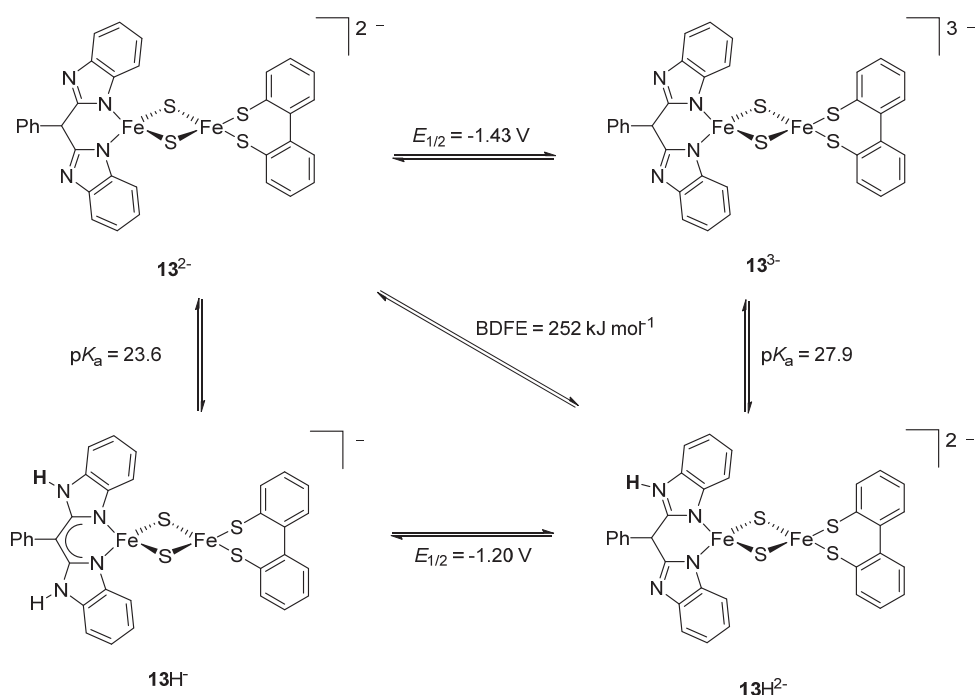
The bis-thiolate ligand was modified from *o*-xylyl- $\alpha$ - $\alpha'$ -dithiol to 2,2-dithio-1,1'-biphenyl in order to improve crystallization properties. The second generation Rieske model **13**<sup>2-</sup> is a high fidelity model that does not only mimic the structural and spectroscopic but also the functional properties of Rieske [2Fe–2S] clusters. The diferric forms of both homoleptic cluster **12a**<sup>2-</sup> and heteroleptic cluster **13**<sup>2-</sup> was shown to undergo tautomerization upon protonation of the N-atoms in the backbone of the benzimidazole-type terminal ligands to

form the fully conjugated ligand system (Scheme 1.8). This tautomerization led to rise of an intense band in the visible absorption spectra of these compounds ( $\lambda_{\max} = 386 \text{ nm}$ ,  $\varepsilon = 60000 \text{ M}^{-1} \text{ cm}^{-1}$  for **12aH<sub>2</sub>** and  $\lambda_{\max} = 385 \text{ nm}$  and  $\varepsilon = 47000 \text{ M}^{-1} \text{ cm}^{-1}$  for **13H<sup>-</sup>**).<sup>[147,148]</sup> No tautomerization was observed upon protonation of the respective mixed valent species **12a<sup>3-</sup>** and **13<sup>3-</sup>**.



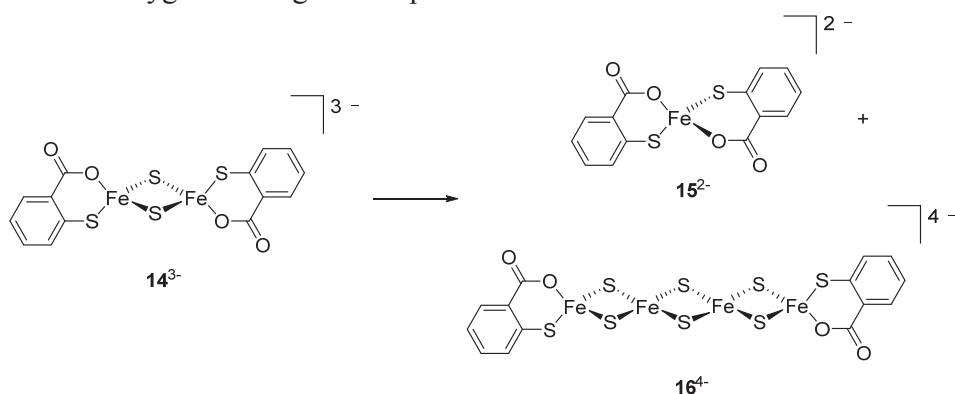
**Scheme 1.8:** Tautomerization observed upon protonation of the benzimidazole-based terminal ligands in diferric clusters **12a<sup>2-</sup>** and **13<sup>2-</sup>**.<sup>[147,148]</sup>

The ability to undergo PCET reactions was demonstrated for **13<sup>2-</sup>** and also for homoleptic models **12a<sup>2-</sup>** and **12b<sup>2-</sup>** and the respective square schemes have been established for **13<sup>2-</sup>** and **12b<sup>2-</sup>**.<sup>[148,150]</sup> In case of **12a<sup>2-</sup>**, all studies had to be carried out in DMF due to solubility issues. Since the  $\text{p}K_{\text{a}}$  values of acids used for protonation are not well defined in DMF, this prevented the summary in a reliable square scheme. Self-exchange between diferric **12b<sup>2-</sup>** and mixed valent **12b<sup>3-</sup>** was monitored by <sup>1</sup>H NMR spectroscopy. Since both species show distinct resonances in <sup>1</sup>H NMR spectra, self-exchange is slow on the NMR time scale and a line shape analysis in mixtures containing varying amount of **12b<sup>2-</sup>** and **12b<sup>3-</sup>** allowed for the determination of a free energy barrier of  $10.5 \text{ kcal mol}^{-1}$ .<sup>[151]</sup> In contrast to electron transfer, proton transfer, *i.e.* self-exchange between the protonated and unprotonated cluster, is fast on the NMR time scale.<sup>[151]</sup> Additionally, **12a<sup>4-</sup>** was the first example of a fully characterized all-ferrous [2Fe–2S] cluster.<sup>[152]</sup>



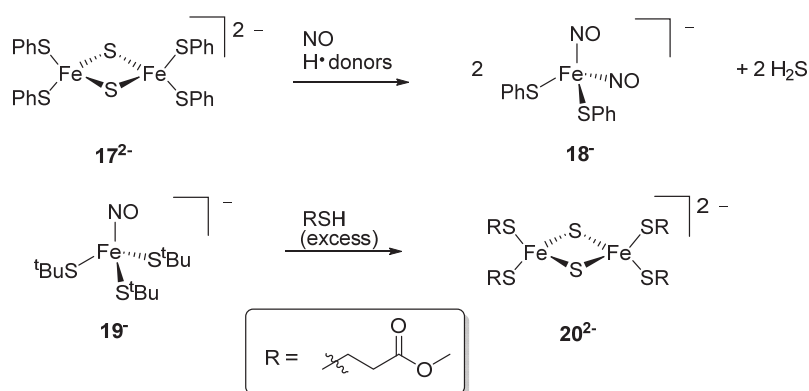
**Scheme 1.8:** Square scheme summarizing thermodynamic parameters of reduction, protonation and PCET for  $13^{2-}$ .<sup>[148]</sup>

An example of cluster rearrangement, which shall be mentioned here, is the decomposition of a mixed valent  $[2\text{Fe}-2\text{S}]$  cluster.  $14^{3-}$  was shown to slowly decompose forming mononuclear ferrous species  $15^{2-}$  and a linear tetra ferric cluster  $16^{4-}$  (Scheme 1.9).<sup>[153]</sup> Even though this reaction takes several days to be complete, it gives some insight into the difficulties of isolating mixed valent  $[2\text{Fe}-2\text{S}]$  clusters. Cluster interconversion between synthetic  $[2\text{Fe}-2\text{S}]$  and  $[4\text{Fe}-4\text{S}]$  clusters has been observed as well. The interconversion was shown to be reversible and to depend on the presence of reductive/oxidative conditions.<sup>[154]</sup> A similar conversion of  $[2\text{Fe}-2\text{S}]$  clusters into  $[4\text{Fe}-4\text{S}]$  clusters has been described for the oxygen sensing transcription factor FNR.<sup>[155]</sup>



**Scheme 1.9:** Decomposition of mixed valent  $[2\text{Fe}-2\text{S}]$  cluster  $14^{3-}$  to mononuclear ferrous  $15^{2-}$  and linear tetra-ferric species  $16^{4-}$ .<sup>[153]</sup>

In recent years, the reactivity of [2Fe–2S] clusters toward nitric oxide (NO) has been investigated in detail. NO is an important biological signaling molecule with iron sulfur proteins being among the possible targets.<sup>[156]</sup> In many cases, reaction of NO with biological iron sulfur centers results in the formation of dinitrosyl iron complexes (DNICs).<sup>[157]</sup> A similar reactivity has been reported for synthetic iron sulfur clusters. Synthetic [2Fe–2S] clusters such as **17**<sup>2-</sup> are converted to the corresponding DNICs upon reaction with NO.<sup>[158,159]</sup> If this transformation is carried out in the presence of acids or formal H donors such as PhSH or <sup>t</sup>Bu<sub>3</sub>PhOH, the formation of MNICs or DNICs respectively is coupled to the release of H<sub>2</sub>S (Scheme 1.10, top).<sup>[160,161]</sup> It has also been shown that mononitrosyl iron complexes (MNICs) can be repaired *i.e.* reconverted into [2Fe–2S] clusters with an excess of cysteine analogues RSH (Scheme 1.10, bottom).<sup>[162,163]</sup> These model studies using synthetic analogues have provided a more thorough understanding of cellular NO signaling pathways.



**Scheme 1.10:** Formation of DNICs from [2Fe–2S] clusters coupled to H<sub>2</sub>S release (top) and repair of MNICs to form [2Fe–2S] clusters by an excess of cysteine analogues RSH (bottom).<sup>[156]</sup>

A multitude of synthetic [4Fe–4S] clusters have been prepared over the past decades.<sup>[132] [164]</sup> A prominent example is thiolate ligated cluster **21**<sup>6-</sup>, which is water soluble due to the presence of carboxylates in the ligands. This cluster also allowed for investigations of the kinetics of ligand exchange.<sup>[165]</sup> It was shown that substitution of ligands in [4Fe–4S] depends on the nucleophilicity of the substrates, the solvent and protonation state.<sup>[166,167]</sup> Using N-heterocyclic carbenes as ligands made the preparation of an all ferrous [4Fe–4S] cluster **22** possible.<sup>[168]</sup> This cluster served as a first model for the fully reduced state of [4Fe–4S] clusters, which has also been recognized to be accessible in a number of proteins and was first proposed to occur in *azotobacter vinelandinii* nitrogenase in 1994.<sup>[169]</sup> Heteroleptic, site differentiated [4Fe–4S] clusters such as **23** can serve as models for Cys<sub>3</sub>His coordinated clusters, which are found in hydrogenases.<sup>[170,171]</sup> Their synthesis was achieved by stepwise ligand exchange reactions starting from [Fe<sub>4</sub>S<sub>4</sub>{N(SiMe<sub>3</sub>)<sub>2</sub>}<sub>4</sub>] and using bulky thiolate ligands. Homoleptic [4Fe–4S] cluster bearing four bulky monodentate thiolate

ligands have been described as models for HiPIPs in their oxidized form  $[4\text{Fe}-4\text{S}]^{3+}$ .<sup>[170,172,173]</sup>

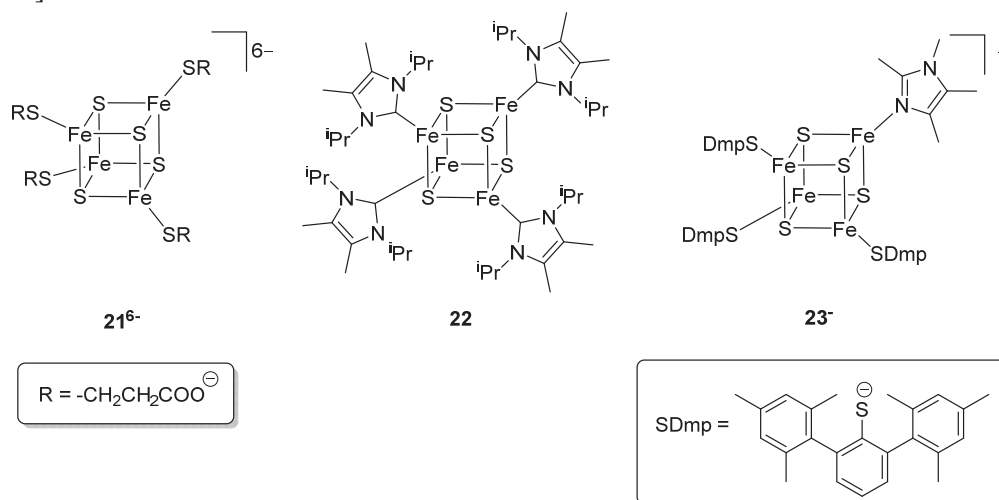
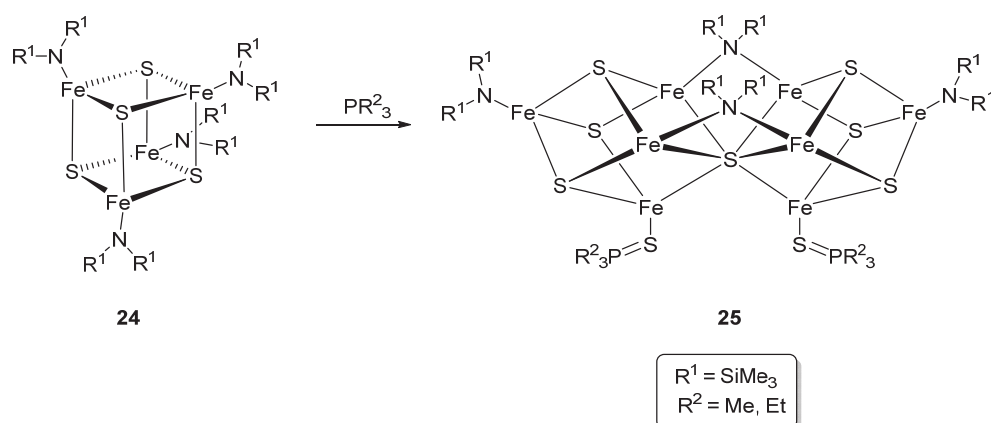


**Figure 1.7:** Synthetic models for  $[4\text{Fe}-4\text{S}]$  clusters: Water soluble cluster  $21^{6-}$  in which ligand exchange was studied, all-ferrous cluster  $22$ , in which low oxidation state is stabilized by N-heterocyclic carbene ligands, and site-differentiated cluster  $23$ .

The synthesis of clusters with higher nuclearity for modeling the  $[8\text{Fe}-7\text{S}]$  cluster of nitrogenase has been achieved by various pathways.<sup>[174-177]</sup> One possible synthesis relies on the reductive fusion of two all-ferric  $[4\text{Fe}-4\text{S}]$  clusters (Scheme 1.11).<sup>[178]</sup>



**Scheme 1.11:** Synthetic analogue of the  $[8\text{Fe}-7\text{S}]$  P-cluster prepared by reductive fusion of two  $[4\text{Fe}-4\text{S}]$  clusters.<sup>[178]</sup>

## 1.7 EPR Spectroscopy in Iron Sulfur Clusters

Electron paramagnetic resonance (EPR) has not only played a central role in the discovery of iron sulfur clusters but has also contributed largely to the understanding of the properties and related function.<sup>[146,179]</sup> EPR spectroscopy is based on the interaction of electromagnetic radiation with a paramagnetic sample in a magnetic field. If an electron with a spin  $S$  is placed in a magnetic field  $B_0$ , the  $\alpha$ - and  $\beta$ -states are no longer degenerate but are energetically split according to:<sup>[180]</sup>

$$\Delta E = g\mu_B B_0$$

Therein,  $g$  is the so called Landé factor which is  $g = 2.002319$  for a free electron and  $\mu_B$  is the Bohr magneton  $\mu_B = 9.724 \cdot 10^{-24} \text{ J T}^{-1}$ . Absorption of electromagnetic radiation can occur under the resonance condition in which  $h$  is the Planck constant  $h = 6.626 \cdot 10^{-34} \text{ J s}$ :

$$h\nu = \Delta E$$

The magnetic moment  $\mu_e$  is comprised of spin and orbit contributions with the orbit quantum number  $l$ :

$$\mu_e = \mu_B S + \mu_B l$$

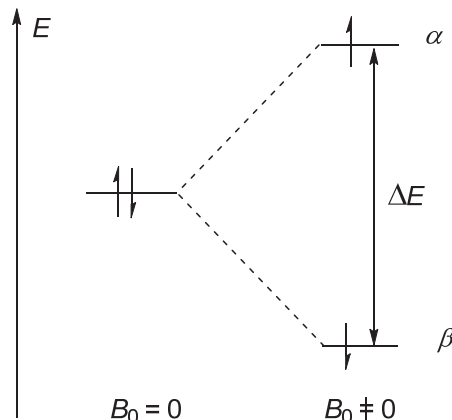


**Figure 1.8:** Energetic splitting of  $\alpha$  and  $\beta$  states of an electron in an external magnetic field (Zeeman effect).<sup>[180]</sup>

The spin and orbit contributions are however not independent on each other and spin orbit coupling (SOC) occurs especially when heavy atoms such as metal centers are present. This results in deviations of the observed  $g$  value from the  $g$  value of the free electron. Since SOC is anisotropic the  $g$ -value depends on the orientation of the magnetic field with respect to the axes of the molecular system and must be described as a tensor. The principal axes of the tensor are chosen in a way which leaves only the diagonal elements of the tensor  $g_{xx}$ ,  $g_{yy}$  and  $g_{zz}$  non-zero. When an EPR spectrum is recorded in frozen solution, the three different  $g$



values can be determined. If all three  $g$ -values are different, a rhombic spectrum is observed whereas an axial spectrum is obtained if two of the principal  $g$ -values are identical. When an EPR spectrum is obtained in solution, the free movement of the individual molecules is too fast and only the average  $g$ -value can be observed.<sup>[180]</sup>

$$g_{av} = \frac{1}{3} \sum_i g_i$$

EPR spectroscopy also allows for the determination of other parameters useful in describing the molecular system: the zero field splitting parameters  $D$  and  $E$  and the hyperfine coupling constant  $A$ , which may be anisotropic as well and describes the interaction of the unpaired electron with the nuclear spin  $I$  of atoms.

Since this thesis focuses on [2Fe–2S] clusters and relies on their characterization by EPR spectroscopy, the typical features of their EPR spectra will be briefly introduced here. Due to antiferromagnetic coupling between the iron centers, [2Fe–2S] clusters in their diferric form have an  $S = 0$  ground state and are thus EPR silent. In their mixed valent form the antiferromagnetic coupling results in an  $S = 1/2$  ground state and a characteristic rhombic EPR spectrum can be observed. As a Robin and Day class II compound, they feature a partially delocalized unpaired electron.<sup>[181]</sup> One of the three principal  $g$  values is typically larger than 2 while the other two  $g$  values are smaller than 2, usually between 1.95 and 1.85. This can be rationalized by considering the two single iron centers which make up the [2Fe–2S] cluster: High spin Fe<sup>III</sup> constitutes the major contribution to the overall spin of the system. In its tetrahedral coordination with a  $d^5$  configuration is almost isotropic with an average  $g$ -value close to  $g = 2$ . High spin Fe<sup>II</sup> with a  $d^6$  configuration in a tetrahedral environment has a much more pronounced anisotropy and features  $g$  values  $>2$ , as evidenced by analysis of the energy levels and spin orbit coupling constants. It has been shown that coupling of two spins  $S_1$  with  $g_1$  and  $S_2$  with  $g_2$  resulting in a total spin  $S_{tot}$  the effective  $g$  value can be calculated, assuming that the principal axes of the  $g$  tensors are the same.<sup>[182]</sup>

$$g = \frac{g_1 + g_2}{2} + \frac{(g_1 - g_2)}{2S_{tot}(S_{tot} + 1)} [S_1(S_1 + 1) - S_2(S_2 + 1)]$$

For mixed valent [2Fe–2S] clusters with  $S_1 = 5/2$ ,  $S_2 = 2$  and  $S_{tot} = 1/2$  an effective average  $g$ -value of  $g < 2$  can be calculated:

$$g = \frac{7g_1 - 4g_2}{3}$$

Based on DFT studies, Orio and Mouesca have shown that there is a general relation between the degree of delocalization and the average  $g$ -value in iron sulfur clusters. For [2Fe–2S] clusters it was shown that the average  $g$ -value increases toward the free electron value  $g_e = 2.002319$  with increasing delocalization of the unpaired electron.<sup>[183]</sup> Indeed, an unusually low average  $g$ -value of  $g_{av} = 1.91$  has been reported for Rieske [2Fe–2S] cluster isolated from *Thermus Thermophilus*<sup>[145]</sup> in contrast to  $g_{av} \approx 1.95$ – $1.97$  observed in all-cysteine coordinated ferredoxines.<sup>[1,184]</sup> This low  $g_{av}$  reflects the strong localization of the unpaired electron on the iron center coordinated by the two histidine ligands. In fact, the very low  $g_3$ -value has been attributed to orthorhombic distortion on the {N<sub>2</sub>} {S<sub>2</sub>} coordinated iron center, which gives further evidence for localization of the unpaired electron on this iron site. A similar trend has been observed in synthetic [2Fe–2S] clusters. Heteroleptic Rieske model **13**<sup>3-</sup> shows a lower  $g_{av}$  of 1.935 than homoleptic model **12a**<sup>3-</sup> ( $g_{av} = 1.946$ ).<sup>[148,149]</sup> This is in good agreement with an increased localization of the distinct ferrous and ferric sites, which was confirmed by Mößbauer spectroscopy.

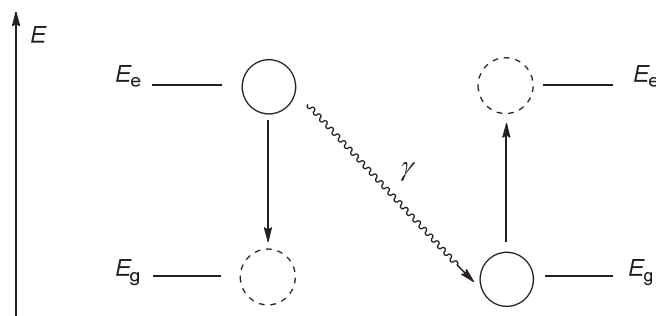
## 1.8 Mößbauer Spectroscopy in Iron Sulfur Clusters

Mößbauer spectroscopy is a valuable tool for probing key properties particularly of iron containing species such as formal oxidation states, and coordination geometry.<sup>[185,186]</sup> It has been used in the study of iron sulfur clusters since the discovery of these cofactors and in combination with EPR spectroscopy has turned out to be a powerful tool in both discovering new iron sulfur clusters as well as in detailed investigation of their electronic structures.<sup>[187]</sup>

Mößbauer spectroscopy is based on recoilless emission and resonance absorption of nuclear  $\gamma$  radiation as described by Rudolf Mößbauer in 1958.<sup>[188]</sup> If an excited nuclear state  $E_e$  of one nucleus (source) decays to its ground state  $E_g$ ,  $\gamma$  radiation is emitted with a wavelength corresponding to the energy gap between the two states (Scheme 1.12, left). This  $\gamma$  radiation can lead to excitation of a second nucleus if its wavelength matches the required resonance energy (Scheme 1.12, right). However, emission of  $\gamma$  radiation from decay of a nuclear excited state is generally accompanied by recoil leading to an increased wave length of the emitted radiation which then no longer matches the energy necessary to cause excitation in the sample nucleus. The recoil energy  $E_R$  is given related to the energy of emitted  $\gamma$  radiation  $E_\gamma$ , the mass  $m$  of the emitting particle or atom, and the speed of light  $c$ , according to:

$$E_R = \frac{E_\gamma^2}{2mc^2}$$

To achieve recoilless emission and resonance absorption of radiation, the experiment must be carried out in solid state or frozen solution. Thereby the nuclei no longer move independently but collectively, increasing  $m$  in the equation given above from the mass of a single nucleus to the mass of the whole particle thus drastically decreasing the recoil energy. The fraction of recoilless processes is then described by the Lamb-Mössbauer factor  $f$ . The isotope most widely studied by Mössbauer spectroscopy is  $^{57}\text{Fe}$  for which  $^{57}\text{Co}$  is used as a source of radiation, which has a half life time of 270 days. The natural abundance of  $^{57}\text{Fe}$  is only 2.1% which means that in order to achieve suitable intensities isotopically enriched samples have to be prepared when only little amounts of sample are available or when the iron: ligand or iron:protein ratio is low, as it is usually the case in samples of enzymes. Other isotopes for which Mössbauer spectroscopy is frequently used include  $^{119}\text{Sn}$  and  $^{121}\text{Sb}$ .<sup>[185]</sup>



**Scheme 1.12:** Emission of  $\gamma$  radiation upon decay of a nuclear excited state and subsequent excitation of a second nucleus.<sup>[185]</sup>

Since the nucleus in the sample is found in a slightly different chemical environment than the nuclei in the source, the energies and thus the energy gap between the ground and excited state differ from those in the source. Thus the emitted frequency must be modulated by moving the source at different velocities ( $v$  ( $\text{mm s}^{-1}$ )) in order to achieve the respective resonance frequencies for excitation of the sample nucleus (Doppler effect). In the absence of an additional external magnetic field, two main parameters can be obtained from a Mössbauer spectrum: the isomer shift  $\delta_{\text{IS}}$  and the quadrupole splitting  $\Delta E_{\text{Q}}$  (Figure 1.10).

The isomer shift  $\delta_{\text{IS}}$  is a result of the electric monopole interaction between the nuclear charge and the charge of the  $s$ -electrons at the nucleus. This interaction results in a different ground state energy of the  $I=1/2$  and  $I=3/2$  states in the sample in relation to the emitting source (Figure 1.10). The resulting isomer shift  $\delta$  contains valuable information on the  $s$  electron density at the respective  $^{57}\text{Fe}$  nucleus. It contains contributions from  $4s$  electrons, which are affected by their participation in bonding, and by shielding effects from  $3p$  and  $3d$  electrons. In general, a more negative isomer shift indicates a higher electron density at the nucleus and thus often coincides with a higher formal oxidation state. However, the isomeric shift also gives information regarding the spin state, the number of ligands and the nature of the Fe-ligand bond, *i.e.* on the degree of covalency or multiple bonding. For example, ferrous

species usually show a higher isomer shift than ferric species due to a decreased s-electron density at the  $^{57}\text{Fe}$  nucleus, as more d-electrons are present, which shield the nucleus from the s-electrons. Furthermore, harder, *i.e.* more ionic ligands generally cause higher isomer shifts as they lead to more covalent metal-ligand interactions and high spin complexes show a higher isomer shifts than their low spin analogues, as the s-electron density at the nucleus is smaller in the high spin case.<sup>[185]</sup>

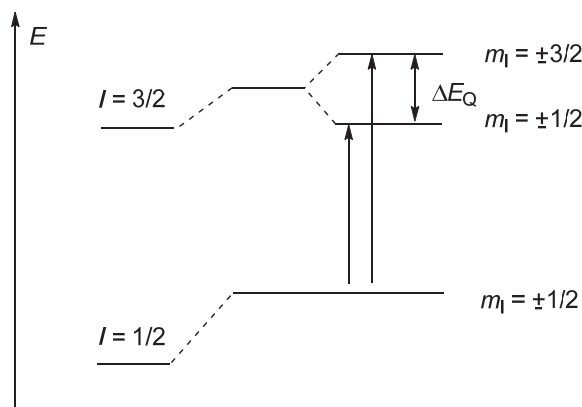


**Figure 1.10:** Mössbauer transitions in the absence of an applied field and origin of the observable quadrupole splitting  $\Delta E_Q$ .<sup>[185]</sup>

Since the excited  $I = 3/2$  state has a non-spherical charge distribution, it causes a quadrupole moment which interacts with the non-homogenous electrical field at the nucleus. This causes an energetic splitting of the  $m_l = \pm 3/2$  and  $m_l = \pm 1/2$  sub-states of the  $I = 3/2$  state. As a consequence, transitions from the ground state can occur to these energetically distinct states at different resonance energies, causing a line splitting in the Mössbauer spectrum (Figure 1.10). Both transitions are equally allowed as the selection rule for Mössbauer transitions is  $\Delta m_l = 0; \pm 1$ . The observed quadrupole splitting contains information on the coordination geometry, especially on the degree of symmetry, including information on chemically non-equivalent ligands coordinating a single nucleus (ligand or lattice contribution). Additionally, the quadrupole splitting is affected by non-cubic distribution of  $d$  electrons in the valence orbitals (valence contribution). One example is the observed difference in quadrupole splitting observed when comparing low spin ferrous ions, which usually show a small quadrupole splitting due to the highly symmetric distribution of electrons over all  $3d$  orbitals in an octahedral ligand field, to high spin ferrous ions, which typically show a large quadrupole splitting due to asymmetric distributions of  $3d$  electrons.<sup>[185]</sup>

Since all  $^{57}\text{Fe}$  nuclei of a sample are detected, Mössbauer spectroscopy is useful in determining the over-all composition of the sample. The integral of each doublet observed in the Mössbauer spectrum directly corresponds to the ratio at which this species is present in the sample. Since both the isomer shift and the quadrupole splitting as well as Lamb-



## 1 Introduction

---

Möbbauser factors can be temperature dependent, it is important to compare spectra recorded at the same temperature when comparing spectra of related compounds.<sup>[185,187]</sup>

In studies of biological and synthetic iron sulfur clusters, Möbbauser spectroscopy has played an essential role in discovering new clusters, determining their composition, describing their electronic properties and formal oxidation states, and analyzing the role of the cluster during transformations as observed in radical SAM enzymes.<sup>[187]</sup> For example, Möbbauser spectroscopy has helped in establishing Histidine coordination in Rieske centers. While diferric all-cysteine coordinated [2Fe–2S] clusters display only one doublet with an isomer shift of  $\delta = 0.27 \text{ mm s}^{-1}$  and a quadrupole splitting of  $\Delta E_Q = 0.60 \text{ mm s}^{-1}$ ,<sup>[189]</sup> diferric [2Fe–2S] Rieske centers show two distinct doublets with  $\delta = 0.24$  and  $0.32 \text{ mm s}^{-1}$  and a quadrupole splitting of  $\Delta E_Q = 0.32$  and  $0.91 \text{ mm s}^{-1}$ .<sup>[145]</sup> Due to the presence of the two histidine ligands, the N<sub>2</sub>S<sub>2</sub> coordinated site displays a larger quadrupole splitting and a larger isomer shift than the S<sub>4</sub> coordinated site.<sup>[145]</sup>

Möbbauser spectroscopy also provides insights into the degree of valence localization in mixed valent [2Fe–2S] clusters. Based on theoretical considerations, the maximum difference in isomer shift for fully localized, distinct ferrous and ferric sites, both found in a tetrahedral coordination environment, has been predicted to be  $\Delta\delta = 0.4 \text{ mm s}^{-1}$ . In mixed valent Rieske clusters from *Thermus thermophilus*, two distinct doublets with  $\delta = 0.31$  and  $0.74 \text{ mm s}^{-1}$  and  $\Delta E_Q = 0.63$  and  $3.05 \text{ mm s}^{-1}$ , respectively have been observed.<sup>[145]</sup> The difference in isomer shift is thus  $\Delta\delta = 0.43 \text{ mm s}^{-1}$ , indicating strong localization of the unpaired electron. In comparison, the difference in isomer shift in mixed valent all-cysteine coordinated [2Fe–2S] clusters is typically around  $\Delta\delta = 0.25 \text{ mm s}^{-1}$ .<sup>[189]</sup> At higher temperatures (typically 200 K) some examples of mixed valent [2Fe–2S] clusters no longer show two doublets corresponding to distinct ferrous and ferric sites.<sup>[147]</sup> In this case electron hopping between both sites becomes faster than the Möbbauser time scale ( $10^{-7} \text{ s}$ ), while in mixed valent [2Fe–2S] clusters with a higher localization of the unpaired electron both distinct doublets are still visible in Möbbauser spectra recorded at 200 K.<sup>[147,148]</sup>

Möbbauser spectroscopy can also be used to distinguish between smaller and larger clusters as well as between the cuboidal and linear forms of [3Fe–4S] clusters.<sup>[190,191]</sup> In radical SAM enzymes Möbbauser spectroscopy has played a crucial role in identifying key intermediates such as the mixed valent [2Fe–2S] intermediate in BioB or the [3Fe–4S] intermediate observed during turn-over of LipA. Under SAM-limited conditions, the reaction was allowed to proceed only until the first thiolation had occurred. The Möbbauser parameters of the thus formed intermediate were strongly dependent on the presence of an external magnetic field, revealing the presence of a paramagnetic species. Additionally, they closely resembled those of well-known [3Fe–4S]<sup>0</sup> clusters, giving first evidence for the loss on one iron ion of the cluster upon formation of the enzymes previously elusive intermediate state.<sup>[123]</sup>

## 2 Thesis Outline

This thesis focuses on establishing new biomimetic [2Fe–2S] model systems with one or more imidazole-type terminal ligands that provide valuable insights into the structure and most intriguingly into the function of their biological blueprints. Three different synthetic [2Fe–2S] clusters are prepared and their properties and reactivity in various bio-inspired processes are explored (Figure 2.1).

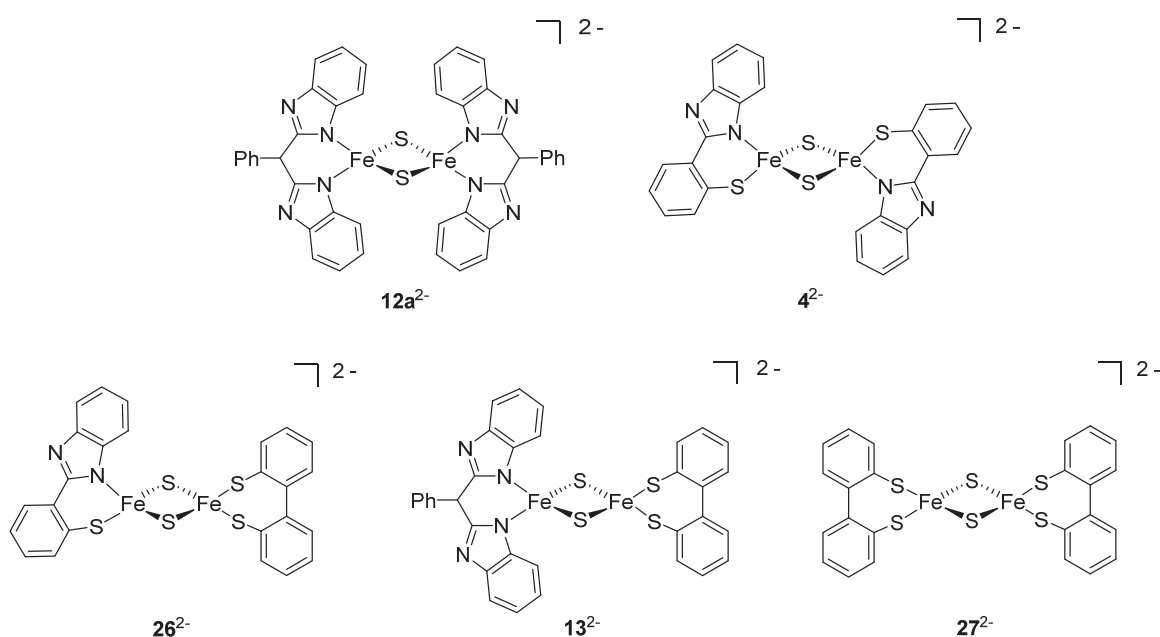


**Figure 2.1:** Synthetic [2Fe–2S] model clusters investigated in this thesis: {N<sub>2</sub>} {N<sub>2</sub>} ligated cluster **12a<sup>2-</sup>**,<sup>[139]</sup> {SN} {SN} ligated cluster **4<sup>2-</sup>**,<sup>[139]</sup> heteroleptic {S<sub>2</sub>} {SN} ligated cluster **26<sup>2-</sup>**,<sup>[192]</sup> {N<sub>2</sub>} {S<sub>2</sub>} ligated Rieske model **13<sup>2-</sup>**,<sup>[148]</sup> and thiolate ligated cluster **27<sup>2-</sup>**.

Cluster **4<sup>2-</sup>** has already been reported by Beardwood and Gibson in 1992.<sup>[139]</sup> This thesis presents a full characterization of this cluster including crystallographic data of the diferric and mixed valent species (Chapter 3). Since two geometric isomers of this cluster are present in solution, kinetic investigations of the rearrangement process were carried out to determine the mechanism of this transformation. These studies aimed at providing insight into the factors controlling ligand rearrangement and cluster transfer processes in nature (Chapter 4).

Since no synthetic model for [2Fe–2S] clusters with a Cys<sub>3</sub>His coordination had previously been reported, heteroleptic cluster **26<sup>2-</sup>** was designed by combining the mixed S/N–donating ligand of **4<sup>2-</sup>** and the thiolate ligand previously used in the synthesis of Rieske model **13<sup>2-</sup>**.

**26**<sup>2-</sup> was successfully synthesized and its spectroscopic properties in the diferric, mixed valent, and protonated forms were analyzed (Chapter 5).

The successful synthesis of heteroleptic cluster **26**(NEt<sub>4</sub>)<sub>2</sub> furthermore provides a valuable member in a series of [2Fe–2S] clusters featuring an {N<sub>x</sub>S<sub>4-x</sub>} coordination. Temperature dependent electrochemistry of four clusters of this series allows for the determination of thermodynamic parameters of electron transfer. The results of this study will be presented in chapter 6 and provide insight into trends within this series. They highlight the role of non-cysteine ligands in modulating the cluster's redox potential and show how asymmetric ligation affects the entropy changes associated with one-electron reduction.

Both clusters **4**<sup>2-</sup> and **26**<sup>2-</sup> may potentially mediate PCET processes, since they feature a benzimidazole moiety as a proton responsive ligand. Their PCET reactivity is presented in chapter 7. Full square schemes were established for both species and the kinetics of PCET were investigated for both **4H**<sup>-</sup> and **26H**<sup>-</sup> by double-mixing stopped flow techniques. These experiments in conjunction with previously reported PCET reactivity of **12b**<sup>2-</sup> and **13**<sup>2-</sup> aimed at establishing a series of [2Fe–2S] clusters and their PCET reactivity. These efforts were directed at gaining insight into the intrinsic factors, which determine PCET reactivity in [2Fe–2S] clusters. Additionally, they point toward a potential role of mitoNEET proteins in PCET reactions.

Since redox inert cations Li<sup>+</sup> and Na<sup>+</sup> are omnipresent in biological systems, their potential interaction with iron sulfur cofactors was studied in his thesis. Chapter 8 introduces first insights into the role of the benzimidazole ligand in coordinating these cations. Binding constants and stoichiometry are established and the effect of cation binding on the properties of [2Fe–2S] clusters is explored.

The role of auxiliary iron sulfur clusters as sulfur donors in radical SAM enzymes is of special interest since it differs drastically from the roles of iron sulfur clusters described in catalysis, electron transport and sensing. As part of this thesis, the development of a functional model system was intended (chapter 9). Therefore, synthetic model clusters **4**<sup>2-</sup> and **12a**<sup>2-</sup>, as well as neutral [2Fe–2S] cluster provided by the group of Prof. Marc Walter (TU Braunschweig)<sup>[193]</sup> were tested in reactions with organic radicals. Two different approaches for generating a suitable organic radical were pursued.

All these diverse insights into the structure, properties and reactivity of synthetic [2Fe–2S] clusters highlight the breadth of roles non-cysteine ligation can play in iron sulfur cofactors and are directed toward the deciphering of functions of iron sulfur cofactors bearing alternative ligands.

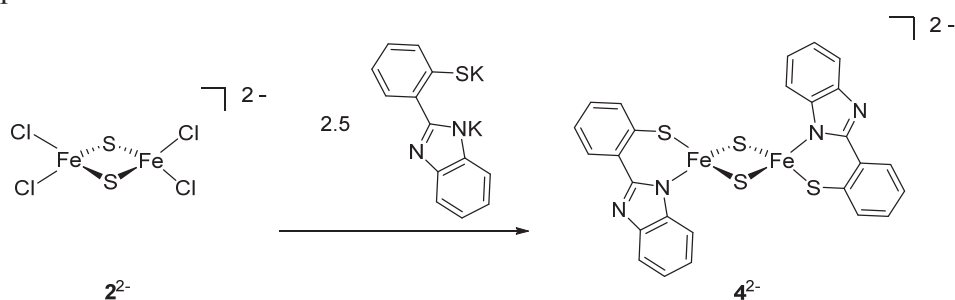
### 3 Characterization of a Biomimetic [2Fe–2S] Cluster in its Diferric, Mixed Valent and Protonated State

#### 3.1 Introduction

Homoleptic cluster  $4(\text{NEt}_4)_2$  has originally been described by Beardwood and Gibson in 1992.<sup>[139]</sup> It features an asymmetric S/N-donating ligand  $\text{L}^{\text{SN}}$ , which is well suited to mimic the mixed coordination by histidine and cysteine residues that is found in biological iron-sulfur clusters (see chapter 1). Since this cluster is central to many of the reactivity studies in this thesis, a complete overview of its properties and spectroscopic features in different oxidation and protonation states will be given in this chapter, even though some of these (UV-vis, CV, and EPR) have already been reported by Beardwood and Gibson previously. Some parts of this chapter have been adapted from recent publications.<sup>[192,194]</sup>

#### 3.2 Synthesis and Structural Characterization of Diferric Cluster $4(\text{NEt}_4)_2$

Synthesis of  $4(\text{NEt}_4)_2$  was adapted from literature.<sup>[139]</sup> The homoleptic cluster was prepared in a simple ligand exchange reaction by adding a solution of 2.5 eq deprotonated ligand  $\text{L}^{\text{SN}}\text{K}_2$  in THF to a solution of precursor complex  $[\text{Fe}_2\text{S}_2\text{Cl}_4](\text{NEt}_4)_2$  ( $2(\text{NEt}_4)_2$ ) in MeCN at low temperature.



**Scheme 3.1:** Synthetic approach toward homoleptic  $[\text{2Fe-2S}] 4^{2-}$  using excess  $\text{L}^{\text{SN}}\text{K}_2$ .<sup>[139,194]</sup>

Slow diffusion of diethyl ether into a solution of  $4(\text{NEt}_4)_2$  led to crystals suitable for X-ray diffraction. Figure 3.1 shows the molecular structure of the anion of diferric  $4(\text{NEt}_4)_2$  in the solid. Key metric parameters such as the  $\text{Fe}\cdots\text{Fe}$  distance (2.695 Å) and  $\text{Fe}-\mu\text{S}$  distance (2.19 – 2.20 Å) are in the range typical for  $[\text{2Fe-2S}]$  clusters.<sup>[132]</sup> A comparison with related diferric  $[\text{2Fe-2S}]$  clusters  $12\text{a}(\text{NEt}_4)_2$ , featuring four benzimidazole-type terminal ligands and  $27(\text{NEt}_4)_2$ , featuring four terminal thiolate ligands, shows that the  $\text{Fe}\cdots\text{Fe}$  distance decreases

slightly with the presence of more terminal thiolate ligands. However, the overall structural changes in the [2Fe–2S] upon exchanging the terminal ligands appear to be very small (Table 3.1).

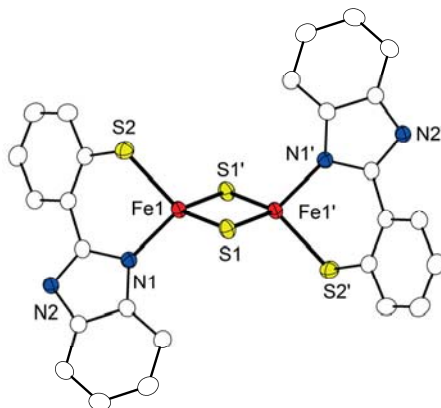


**Figure 3.1:** Molecular structure of  $4^{2-}$  in solid state. Hydrogen atoms and counter ions have been omitted for clarity.<sup>[194]</sup>

**Table 3.1:** Selected bond lengths (Å) and angles (°) of diferric cluster  $4(\text{NEt}_4)_2$  and related clusters  $12a(\text{NEt}_4)_2$ <sup>[149]</sup> and  $27(\text{NEt}_4)_2$ <sup>[195]</sup>

	$4(\text{NEt}_4)_2$ <sup>[194]</sup> {SN} <sub>2</sub>	$12a(\text{NEt}_4)_2$ <sup>[149]</sup> {NN} <sub>2</sub>	$27(\text{NEt}_4)_2$ <sup>[195]</sup> {SS} <sub>2</sub>
$d(\text{Fe}\cdots\text{Fe})$	2.69479(5)	2.7019(5)	2.6772(4)
$d(\text{Fe}-\mu\text{S})$	2.1898(5)-2.2026(5)	2.1938(5)-2.2081(5)	2.1969(5)-2.2094(5)
$d(\text{Fe}-\text{S}_{\text{lig}})$	2.2770(5)	–	2.2989(4)-2.2864(4)
$d(\text{Fe}-\text{N}_{\text{lig}})$	1.9905(13)	1.9776(14)-1.9905(12)	–
$\angle(\text{Fe}-\mu\text{S}-\text{Fe})$	74.144(16)	75.727(16)	74.665(15)

### 3.3 Spectroscopic Characterization of Diferric Cluster $4^{2-}$

#### 3.3.1 Spectroscopy in Solid State

The zero-field Mößbauer spectrum of solid  $4(\text{NEt}_4)_2$  shows a single doublet with an isomeric shift of  $\delta = 0.27 \text{ mm s}^{-1}$  and a quadrupole splitting of  $\Delta E_Q = 0.81 \text{ mm s}^{-1}$  at 80 K. These values are characteristic for diferric [2Fe–2S] clusters, in which both high spin  $\text{Fe}^{\text{III}}$  ( $S = 5/2$ ) ions feature a tetrahedral coordination environment.<sup>[187]</sup>

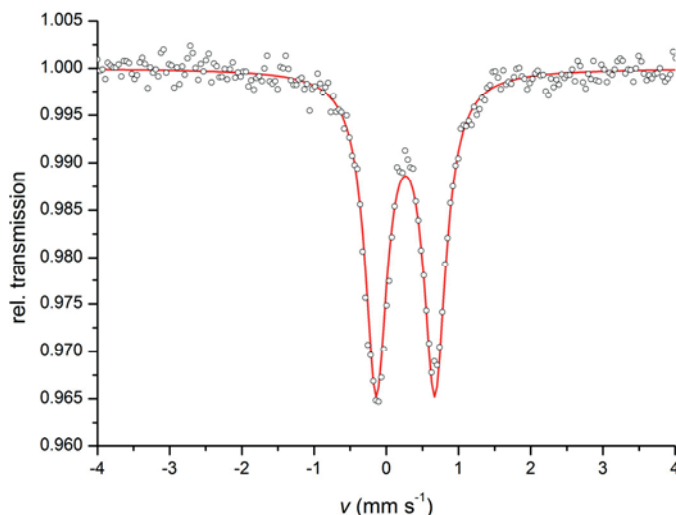


**Figure 3.2:** Zero-field Mößbauer spectrum of solid  $4(\text{NEt}_4)_2$  at 80 K. Simulation of the experimental data resulted in the parameters given in the text.<sup>[192]</sup>

Magnetic measurements (SQUID) of solid  $4(\text{NEt}_4)_2$  confirmed an  $S = 0$  ground state due to strong antiferromagnetic coupling of the two hs  $\text{Fe}^{\text{III}}$  centers with a coupling constant of  $J = -151 \text{ cm}^{-1}$  (Figure 3.3). Experimental data for  $4(\text{NEt}_4)_2$  were modelled by using a fitting procedure to the appropriate Heisenberg-Dirac-van-Vleck (HDvV) spin Hamiltonian for isotropic exchange coupling and Zeeman splitting:

$$\hat{H} = -2J\hat{S}_1 \cdot \hat{S}_2 + g\mu_B(\vec{S}_1 + \vec{S}_2)B.$$

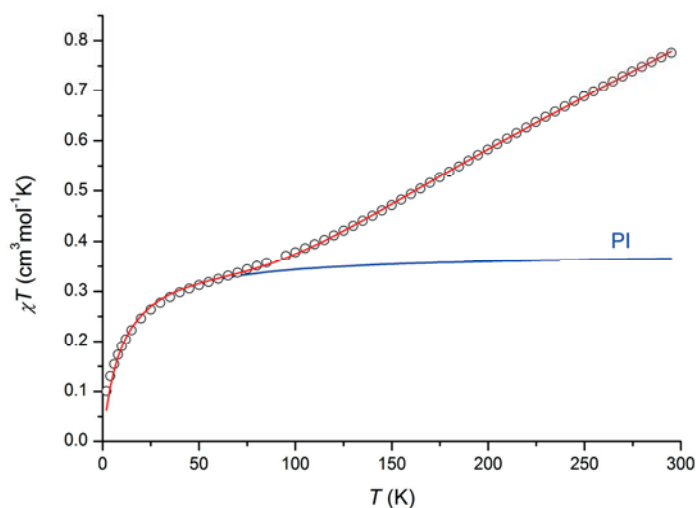


**Figure 3.3:** Temperature dependence of  $\chi_M T$  for homoleptic  $4(\text{NEt}_4)_2$ . The solid red line represents the calculated curve fit with the parameters  $g = 1.90$  (fixed),  $J = -151 \text{ cm}^{-1}$ ,  $P = 8.6 \%$  and  $TIP = 2610 \cdot 10^{-6} \text{ cm}^3 \text{ mol}^{-1}$ . The solid blue line represents contributions from traces of a paramagnetic impurity (8.6%).<sup>[192]</sup>

Temperature-independent paramagnetism (*TIP*) and a Curie-behaved paramagnetic impurity (*PI*) with spin  $S = 5/2$  were included according to:

$$\chi_{\text{calc}} = (1 - PI) \cdot \chi + PI \cdot \chi_{\text{mono}} + TIP.$$

### 3.3.2 Spectroscopy in Solution

The spectroscopic features of  $4(\text{NEt}_4)_2$  observed in solution are in good agreement with those reported by Beardwood and Gibson. Although only one isomer of  $4(\text{NEt}_4)_2$  was found in the crystalline material,  $^1\text{H}$  NMR spectroscopy at 293 K revealed that two isomers which differ by the relative arrangement of the capping ligands exist in solution (Figure 3.4). This behavior had already been described by Beardwood and Gibson.<sup>[139]</sup> Even though the antiferromagnetic coupling of the two iron centers leads to an  $S = 0$  ground state, all resonances in the  $^1\text{H}$  NMR spectrum are slightly broadened due to residual paramagnetism.  $^1\text{H}$  NMR spectroscopy allowed for quantification of the ratio of both isomers present in solution and for kinetic investigations of the isomerization process which will be described in detail in chapter 4. The signal for the proton which is closest to the  $S = 5/2$  iron center is broadened in a way that makes it unobservable. Because of these broad lines, no couplings between the individual protons are visible in the one dimensional  $^1\text{H}$  NMR spectrum.<sup>[194]</sup>

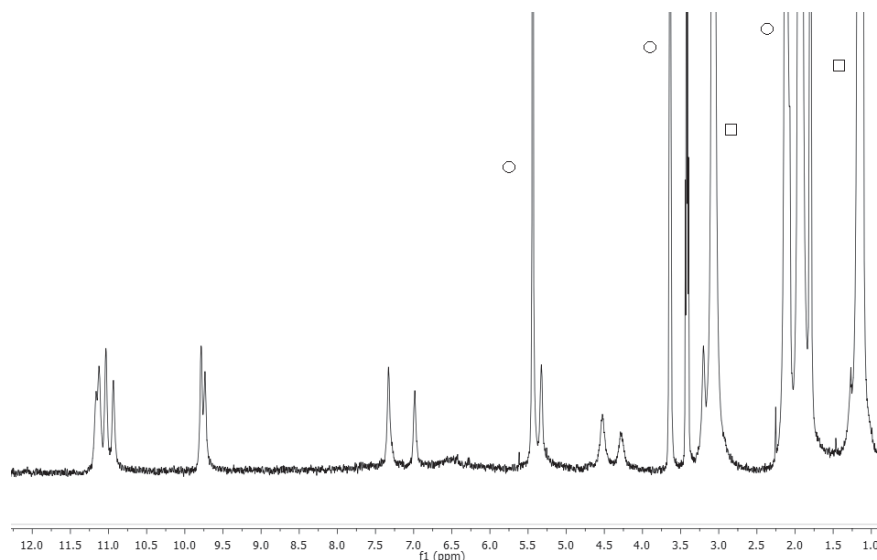


**Figure 3.4:**  $^1\text{H}$  NMR spectrum of  $4(\text{NEt}_4)_2$  in  $\text{MeCN-d}_3$  at 293 K showing two sets of signals due to the presence of two geometrical isomers. Signals from residual solvent (O), and  $\text{NEt}_4^+$  counterions (□) are labelled.

$^1\text{H}$  COSY NMR spectroscopy and comparison with related Rieske Model  $13^{2-}$  now allowed for assignment of the individual resonances to the protons present in  $4(\text{NEt}_4)_2$  (Figure 3.5).  $^1\text{H}$

### 3 Characterization of a Biomimetic [2Fe–2S] Cluster in its Diferric, Mixed Valent and Protonated State

COSY experiments were carried out at 243 K. At this temperature all signals are slightly shifted in comparison to those observed at 293 K. However, couplings between neighboring protons can be observed *via* two dimensional  $^1\text{H}$  COSY NMR spectroscopy (Figure 3.6.). The resonances of the protons of the ligand alternate between higher and lower chemical shifts which can be attributed to a Fermi-contact interaction starting from the iron centers.<sup>[196]</sup>

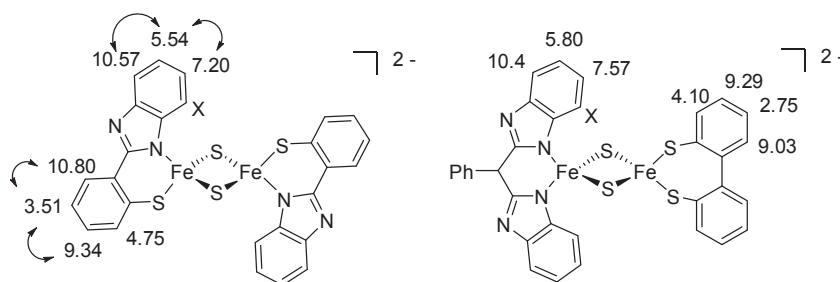


**Figure 3.5:** Assignment of the single resonances  $\delta$  (ppm) to the individual protons of one isomer of cluster  $4(\text{NEt}_4)_2$  at 243 K (left), and related Rieske model  $13^{2-}$  (right).<sup>[148]</sup> Arrows mark couplings between protons as observed in  $^1\text{H}$  COSY NMR. Protons whose resonances cannot be observed in  $^1\text{H}$  NMR are labeled X.

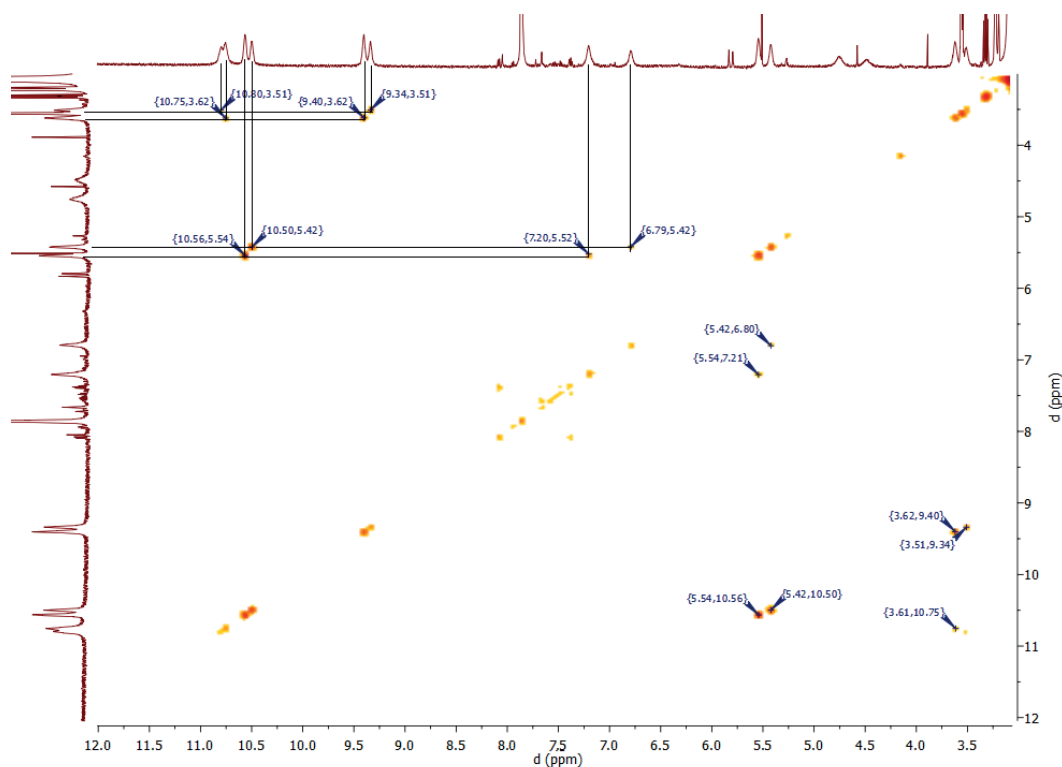


**Figure 3.6:**  $^1\text{H}$  COSY spectrum of  $4(\text{NEt}_4)_2$  MeCN- $d_3$ , two independent sets of couplings are visible corresponding to the two distinct isomers present in solution at 243 K.

The cyclic voltammogram (CV) of  $4(\text{NEt}_4)_2$  obtained in 0.25 M solution of  $\text{NBu}_4\text{PF}_6$  in MeCN at  $-15\text{ }^\circ\text{C}$  shows two distinct reversible redox events which correspond to the formation of mixed valent  $4^{3-}$  (at  $E_{1/2} = -1.407\text{ vs. Fc/Fc}^+$ ) and diferrous  $4^{4-}$  (at  $E_{1/2} = -2.227\text{ vs. Fc/Fc}^+$ ) (Figure 3.7).<sup>[192]</sup> Since they are separated by 820 mV the mixed valent cluster should be chemically accessible and relatively stable. Decamethylcobaltocene  $\text{CoCp}^*_2$  was chosen as chemical reductant since its reducing potential ( $E_{1/2}\text{ vs. Fc/Fc}^+ = -1.95\text{ V}$ )<sup>[197]</sup> is in between the two redox waves observed in the CV of  $4(\text{NEt}_4)_2$ .

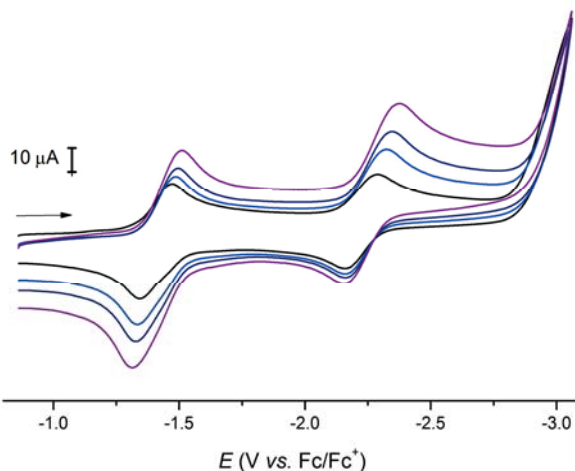


**Figure 3.7:** CV of  $4(\text{NEt}_4)_2$  recorded in 0.25 M  $\text{NBu}_4\text{PF}_6$  solution in MeCN at 258 K.  $E_{1/2} = -1.407\text{ V}$  and  $-2.227\text{ V vs. Fc/Fc}^+$  at scan rates of  $100\text{ mV s}^{-1}$  (black),  $200\text{ mV s}^{-1}$  (blue),  $400\text{ mV s}^{-1}$  (dark blue) and  $600\text{ mV s}^{-1}$  (purple).<sup>[192]</sup>

## 3.4 Mixed Valent Cluster $4^{3-}$

### 3.4.1 Characterization and Spectroscopy in the Solid State

Solid material of  $4^{3-}$  was obtained by addition of 1.0 eq  $\text{CoCp}^*_2$  to a solution of  $4(\text{NEt}_4)_2$  in MeCN at  $-30\text{ }^\circ\text{C}$  and subsequent precipitation of the product by addition of diethyl ether. Crystals suitable for X-ray diffraction were obtained by slow diffusion of diethyl ether into a solution of redissolved  $4(\text{NEt}_4)_x(\text{CoCp}^*_2)_{(3-x)}$  ( $x = 1, 2$ ) in MeCN.  $4(\text{NEt}_4)(\text{CoCp}^*_2)_2$  crystallizes in the triclinic space group  $P\bar{1}$  without solvent molecules present in the cell. The structure shows that there are almost no changes in bond lengths and angles upon one-electron reduction of the [2Fe–2S] cluster core. The  $\text{Fe}\cdots\text{Fe}$  distance and the  $\text{Fe}-\mu\text{S}$  distance remain essentially unchanged, while the Fe-ligand bonds are slightly elongated in comparison to the diferric cluster. The Fe–N bond changes the most by elongating from  $1.9905\text{ \AA}$  in  $4(\text{NEt}_4)_2$  to  $2.029\text{ \AA}$  in  $4(\text{NEt}_4)(\text{CoCp}^*_2)$ . The most prominent structural change seems to concern the terminal ligands, which are twisted by about  $20^\circ$  when going from the

### 3 Characterization of a Biomimetic [2Fe–2S] Cluster in its Diferric, Mixed Valent and Protonated State

diferric to the mixed valent form (Figure 3.8). This observed twist is most likely the result of packing effects due to the presence of the  $[\text{CoCp}^*_2]^+$  counter-ions in the cell.

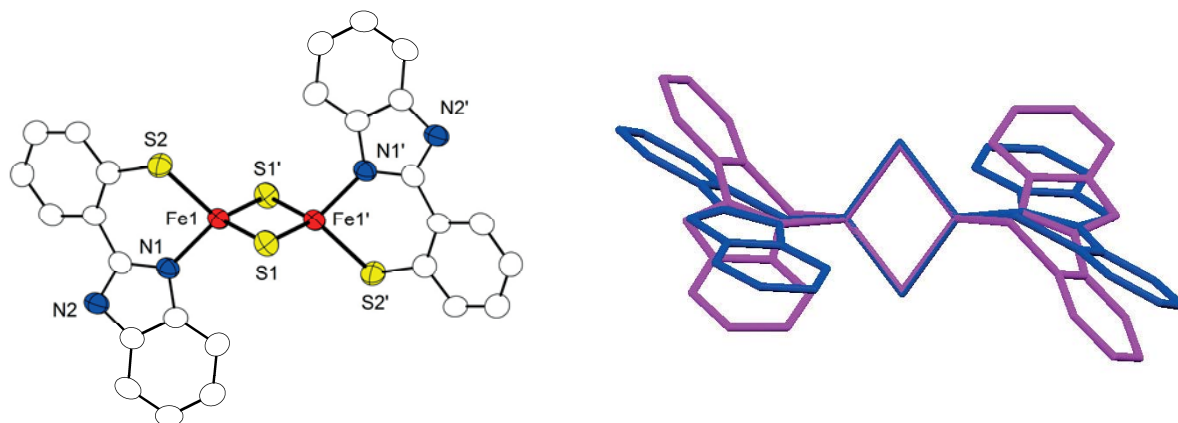


**Figure 3.8:** Molecular structure of the anion of  $4(\text{NEt}_4)(\text{CoCp}^*_2)_2$  in solid state (left) and overlay of structures (right) of the anions of diferric  $4(\text{NEt}_4)_2$  (pink) and mixed valent  $4(\text{NEt}_4)(\text{CoCp}^*_2)_2$  (blue) show only minor structural changes of the central  $\{\text{Fe}_2\text{S}_2\}$  core upon one-electron reduction.<sup>[194]</sup>

**Table 3.2:** Selected bond lengths (Å) and angles (°) of diferric cluster  $4(\text{NEt}_4)_2$  and mixed valent cluster  $4(\text{NEt}_4)(\text{CoCp}^*_2)$ .<sup>[194]</sup>

	$4(\text{NEt}_4)_2$	$4(\text{NEt}_4)(\text{CoCp}^*_2)$
$d(\text{Fe}\cdots\text{Fe})$	2.69479(5)	2.6500(11)
$d(\text{Fe}-\mu\text{S})$	2.1898(5)-2.2026(5)	2.222(4)-2.2225(12)
$d(\text{Fe}-\text{S})$	2.2770(5)	2.3238(11)
$d(\text{Fe}-\text{N}_{\text{His}})$	1.9905(13)	2.029(3)
$\angle(\text{C1}-\text{S2}-\text{Fe})$	97.71(6)	107.33
$\angle(\text{N}_{\text{His}}-\text{Fe}-\text{S}_{\text{Cys}})$	95.79(4)	92.16(9)
$\angle(\text{Fe}-\mu\text{S}-\text{Fe})$	74.144(16)	73.20(4)

Zero-field Mößbauer spectra of  $4(\text{NEt}_4)(\text{CoCp}^*_2)$  were obtained at 12 K and 200 K (Figure 3.9, Table 3.3). The spectrum at 12 K displays two distinct doublets corresponding to one  $\text{Fe}^{\text{III}}$  site (with  $\delta = 0.35 \text{ mm s}^{-1}$  and  $\Delta E_{\text{Q}} = 1.20 \text{ mm s}^{-1}$ ) and one  $\text{Fe}^{\text{II}}$  site (with  $\delta = 0.62 \text{ mm s}^{-1}$  and  $\Delta E_{\text{Q}} = 3.09 \text{ mm s}^{-1}$ ). The difference in isomer shift is about  $0.37 \text{ mm s}^{-1}$ . For fully localized  $\text{Fe}^{\text{III}}$  and  $\text{Fe}^{\text{II}}$  sites a difference in isomer shift of  $0.4 \text{ mm s}^{-1}$  has been predicted.<sup>[198]</sup> While the spectrum at 12 K shows two distinct doublets, the spectrum recorded at 200 K shows only one doublet (with  $\delta = 0.41 \text{ mm s}^{-1}$  and  $\Delta E_{\text{Q}} = 1.39 \text{ mm s}^{-1}$ ) showing that at higher temperatures electron hopping between the two iron centers is faster than the Mößbauer timescale (Figure 3.9).<sup>[192]</sup>

### 3 Characterization of a Biomimetic [2Fe–2S] Cluster in its Diferric, Mixed Valent and Protonated State

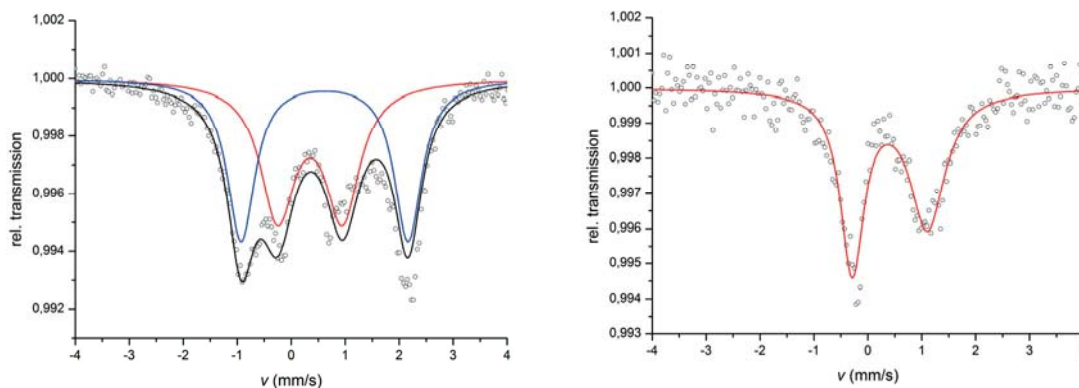


**Figure 3.9:** Mößbauer spectra of solid  $4(\text{NEt}_4)_2(\text{CoCp}^*_2)$  at 12 K (left), and 200 K (right). Simulation of the experimental data resulted in the parameters given in table 3.1.<sup>[192]</sup>

**Table 3.3:** Mößbauer parameters for solid  $4(\text{NEt}_4)_2$  and  $4(\text{NEt}_4)(\text{CoCp}^*_2)_2$ .<sup>[192]</sup>

	$4(\text{NEt}_4)_2$ (80 K)	$4(\text{NEt}_4)_2(\text{CoCp}^*_2)$ (12 K)	$4(\text{NEt}_4)_2(\text{CoCp}^*_2)$ (200 K)
$\delta$ (mm s <sup>-1</sup> )	0.27	0.35	0.41
$\delta$ (mm s <sup>-1</sup> )	--	0.62	--
$\Delta E_Q$ (mm s <sup>-1</sup> )	0.81	1.20	1.39
$\Delta E_Q$ (mm s <sup>-1</sup> )	--	3.09	--
fwhm (mm s <sup>-1</sup> )	0.37	0.87	0.80
fwhm (mm s <sup>-1</sup> )	--	0.56	--
Fe <sup>III</sup> :Fe <sup>II</sup>	--	51:49	--

It should be mentioned here, that a two-electron reduction of  $4^{2-}$  generating diferrous  $4^{4-}$  is also feasible, as the second reduction wave observed in cyclic voltammetry is still well defined and reversible. Indeed it was possible to generate  $4^{4-}$  *in situ* by addition of an excess of  $\text{CoCp}^*_2$  (6.0 eq) in DMF at  $-35^\circ\text{C}$ . A Mößbauer spectrum of this solution at 13 K clearly shows full conversion to diferrous  $4^{4-}$  with  $\delta = 0.76 \text{ mm s}^{-1}$  and  $\Delta E_Q = 2.72 \text{ mm s}^{-1}$  (Figure 3.10). The Mößbauer parameters of  $4^{4-}$  are very similar to those of  $12\mathbf{a}^{4-}$  ( $\delta = 0.79 \text{ mm s}^{-1}$  and  $\Delta E_Q = 2.67 \text{ mm s}^{-1}$ ).<sup>[152]</sup> However, no structural data for  $4^{4-}$  and no pure solid material could be obtained due to partial reoxidation upon addition of diethylether or evaporation of solvent.

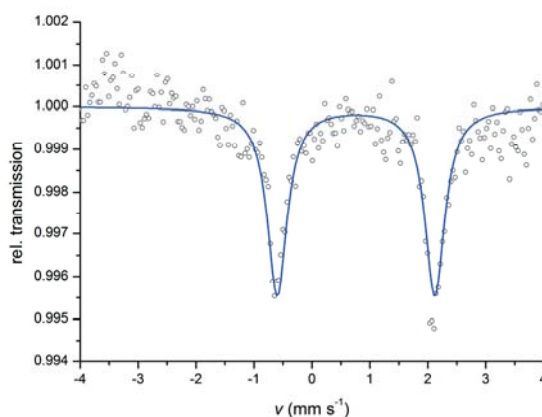


**Figure 3.10:** Mössbauer spectrum of *in situ* prepared  $4^{4-}$  in frozen solution in DMF at 13 K. Simulation of the experimental data resulted in the parameters given in the text.

At 23 °C, a mononuclear ferrous species  $28(\text{CoCp}^*_2)_2$  (Figure 3.11) crystallized from a solution of  $4^{3-}$  in MeCN indicating the propensity for decomposition of the mixed valent species, similar to what has previously been observed for synthetic mixed valent [2Fe–2S] clusters (see chapter 1.6).<sup>[153]</sup>

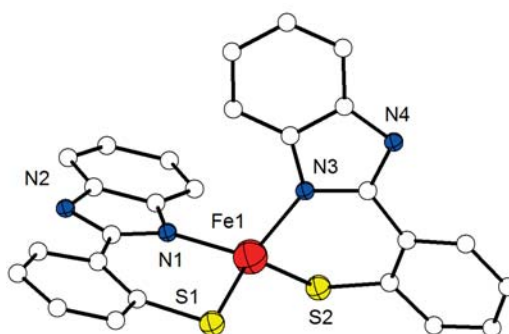


**Figure 3.11:** Molecular structure of the anion of mononuclear  $\text{Fe}^{\text{II}}$  complex  $28(\text{CoCp}^*_2)$  in solid state. Hydrogen atoms and counter cations have been omitted for clarity.

### 3.4.2 Spectroscopy in Solution

Chemical reduction of  $4(\text{NEt}_4)_2$  by addition of 1.0 eq  $\text{CoCp}^*_2$  is accompanied by changes in the visible absorption spectrum recorded in MeCN. An overall decrease in intensity is observed and the bands at 434, 510 and 584 nm disappear while a new band at 565 nm appears (Figure 3.12). Subsequent addition of  $[\text{CoCp}_2]\text{PF}_6$  ( $E_{1/2}$  vs.  $\text{Fc}/\text{Fc}^+ = -1.31 \text{ V}$ )<sup>[197]</sup> proves the chemical reversibility of the reduction. Attempts to gain insight into the kinetics of the chemical re-oxidation by single-mixing stopped flow both with 1.0 eq and excess (5.0 eq)  $[\text{CoCp}_2]\text{PF}_6$  were unsuccessful. Even at low temperatures ( $-30 \text{ °C}$ ) the reaction was found to be too fast to be monitored by stopped-flow kinetic measurements since it was already complete after the initial mixing time of 1 ms.<sup>[192]</sup>

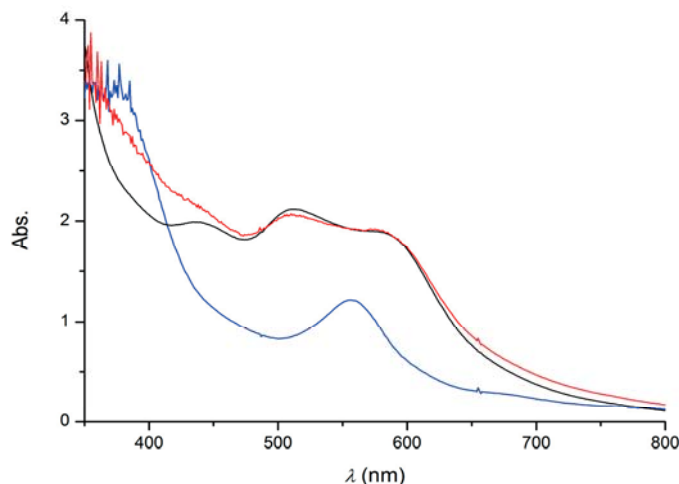


**Figure 3.12:** Visible absorption spectra of  $4(\text{NEt}_4)_2$  (black),  $4(\text{NEt}_4)_2(\text{CoCp}_2^*)$  prepared *in situ* by addition of  $\text{CoCp}_2^*$  (blue) and after re-oxidation by addition of  $[\text{CoCp}_2]\text{PF}_6$  (red) in MeCN.

Since both iron centers are antiferromagnetically coupled, the mixed valent cluster has an  $S = 1/2$  ground state which gives rise to a characteristic rhombic EPR spectrum. The EPR spectrum of chemically reduced  $4^{3-}$  was obtained in frozen solution in MeCN at 160 K and can be simulated with the  $g$ -values  $g_1 = 2.010$ ,  $g_2 = 1.932$ ,  $g_3 = 1.882$ , and  $g_{\text{av}} = 1.941$  (Figure 3.13).<sup>[199,200]</sup> As shown in chapter 1.7 an average  $g$ -value smaller than 2 is characteristic of mixed valent [2Fe–2S] clusters, and the average  $g$ -value of mixed valent [2Fe–2S] clusters increases with decreasing localization of the unpaired electron. The average  $g$ -value of  $g_{\text{av}} = 1.94$  observed in  $4^{3-}$  indicates increased delocalization in comparison with heteroleptic Rieske model  $13^{2-}$  and homoleptic  $\{\text{N}_4\}$  ligated cluster  $12\text{a}^{3-}$ .<sup>[148,150]</sup>

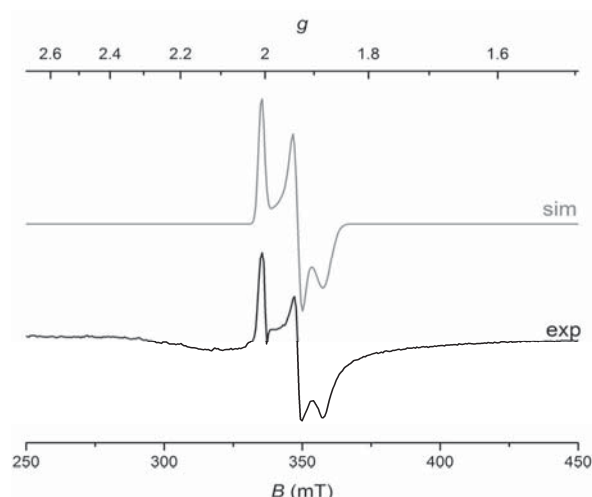


**Figure 3.13:** EPR spectrum of  $4^{3-}$  prepared *in situ* by addition of 1.03 eq  $\text{CoCp}_2^*$  to a solution of  $4(\text{NEt}_4)_2$  in MeCN; recorded in frozen solution in MeCN at 160 K. The grey line is a simulation yielding  $g_1 = 2.010$ ,  $g_2 = 1.932$ ,  $g_3 = 1.882$  and  $g_{\text{av}} = 1.941$ .<sup>[192]</sup>

### 3 Characterization of a Biomimetic [2Fe-2S] Cluster in its Diferric, Mixed Valent and Protonated State

The  $^1\text{H}$  NMR spectrum of  $4^{3-}$  was recorded in  $\text{MeCN-d}_3$  at varying temperatures. All resonances are slightly shifted in comparison to the resonances observed in the diferric cluster spanning a slightly bigger range of chemical shift values due to increased paramagnetism. All resonances slightly shift with temperature in line with classical Curie behavior (Figure 3.14).

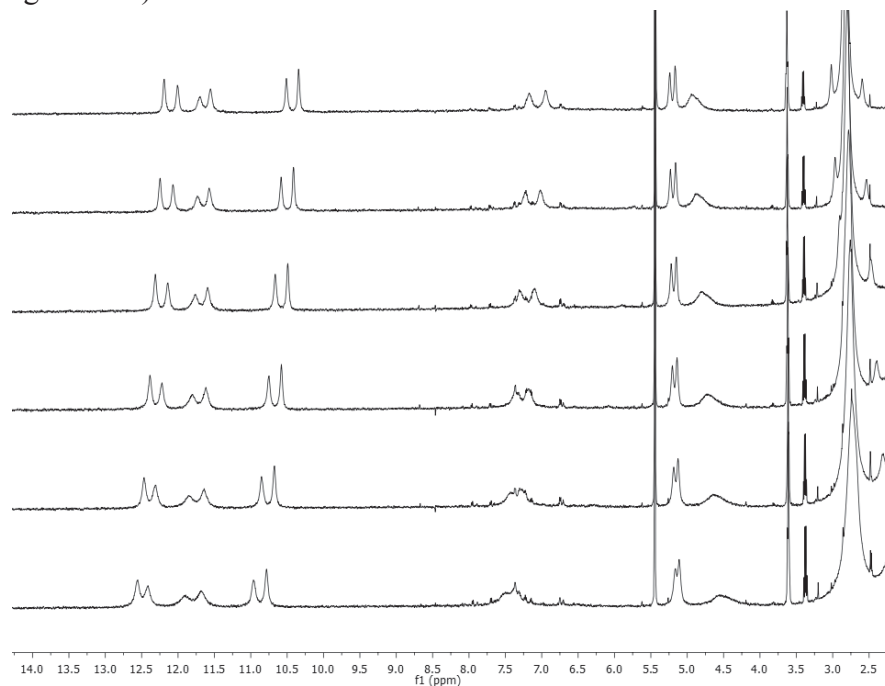


**Figure 3.14:**  $^1\text{H}$  NMR spectra of mixed valent  $4^{3-}$  in  $\text{MeCN-d}_3$  generated *in situ* by addition of 1.05 eq  $\text{CoCp}_2^*$  to a solution of  $4(\text{NEt}_4)_2$ ; spectra recorded at varying temperatures in steps of 10 K from 243 K (bottom) to 293 K (top).

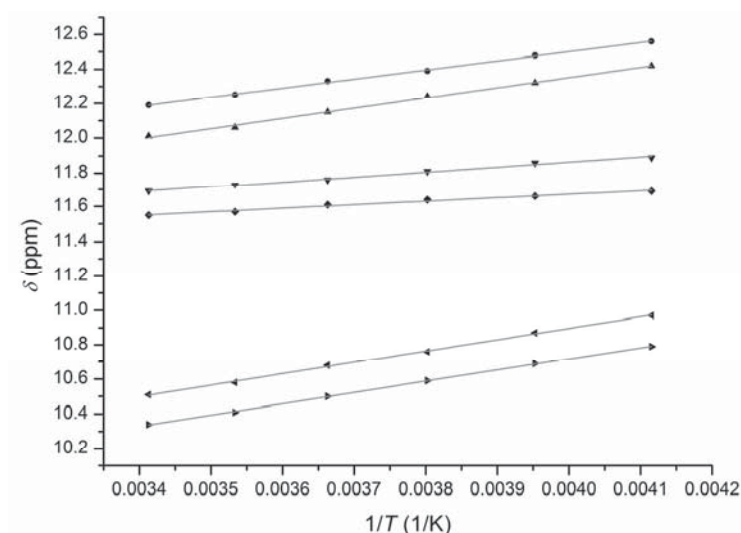


**Figure 3.15:** Chemical shift  $\delta$  (ppm) vs.  $1/T$  ( $\text{K}^{-1}$ ) of the single resonances observed in  $^1\text{H}$  NMR and linear fit (grey), showing classical Curie behavior.

## 3.5 Protonation of the Diferric and Mixed Valent Cluster

### 3.5.1 Protonation of the Diferric Cluster

Similar to previously reported bis(benzimidazole)ligands, ligand  $[L^{SN}]^{2-}$  offers a potential protonation site in the backbone of the ligand. 2,6-dimethylpyridium tetrafluoroborate ( $[DMPH]BF_4$ ) was chosen as acid to protonate  $4(NEt_4)_2$  and diazabicycloundecene (DBU) was used as base in subsequent deprotonation experiments (Figure 3.16).<sup>[201]</sup>

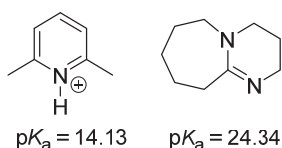


**Figure 3.16:** Molecular structures and  $pK_a$  values of  $[DMPH]^+$  (left)<sup>[201]</sup> and DBU (right).

Protonation of  $4(NEt_4)_2$  was monitored by UV-vis spectroscopy (Figure 3.16). Addition of 1.0 eq of  $[DMPH]BF_4$  leads to an overall decrease in intensity. The band at 434 nm disappears and the bands at 510 nm and 584 nm are shifted to 504 nm and 579 nm respectively. At low temperatures ( $-30^\circ C$ ) a second protonation step is possible, which is accompanied by a further decrease of the absorption at 434 nm while the bands at 504 nm and 579 nm shift back to their original positions. Addition of further equivalents of  $[DMPH]BF_4$  lead to no further changes in the visible spectra, indicating that cluster  $4^{2-}$  offers only two possible protonation sites. Most likely these protonation steps occur on the N-atoms in the backbone of the benzimidazole moiety of the two ligands. While protonation at the bridging sulfides cannot be fully excluded, support for protonation at the benzimidazole-N was obtained from NMR spectroscopy (see below). Subsequent addition of DBU restores the initial spectrum, even though the intensity could not be completely recovered probably due to minor decomposition of the doubly protonated species. Since the doubly protonated species is electronically neutral, its solubility in polar solvents such as MeCN is very low. Thus no further experiments on the doubly protonated compound  $4H_2$  such as  $^1H$  NMR were performed.

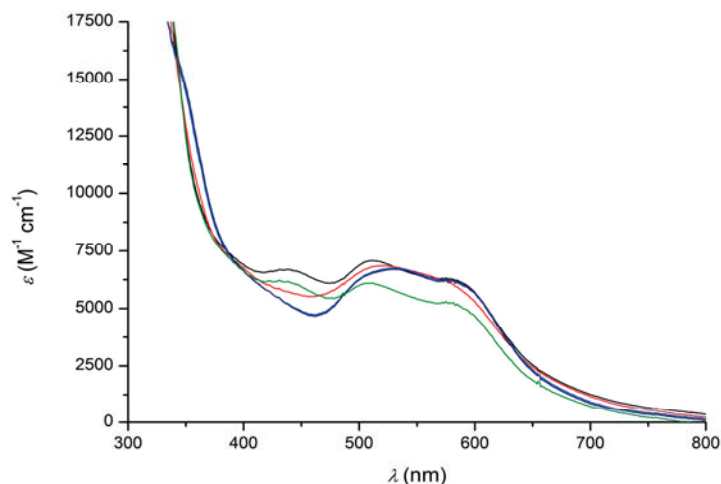


**Figure 3.17:** UV-vis absorption spectra of  $4(\text{NEt}_4)_2$  (black) in MeCN after addition of 1.0 eq  $[\text{DMPH}]^+$  (red), 2.0 eq  $[\text{DMPH}]^+$  (blue), 3.0 eq  $[\text{DMPH}]^+$  (dark blue) and excess DBU (green) at  $-30\text{ }^\circ\text{C}$ .<sup>[192]</sup>

The  $\text{p}K_a$  of  $4\text{H}^-$  was determined by back-titration experiments performed at  $-30\text{ }^\circ\text{C}$  under inert conditions monitored by UV-vis spectroscopy. Therefore  $4\text{H}^-$  was generated *in situ* by addition of 1.0 eq of  $[\text{DMPH}]\text{BF}_4$ . DBU was then added in steps of 0.2 eq and the reappearing band at 434 nm was used to quantify the amount of protonated and unprotonated species present in solution. According to mass balance, the  $\text{p}K_a$  was derived from the equations given below in which  $[\text{Fe}]$  corresponds to the concentration of deprotonated cluster  $4^{2-}$ ,  $[\text{FeH}]$  to the concentration of singly protonated cluster  $4\text{H}^-$ ,  $[\text{BH}]$  to the concentration of  $\text{DBUH}^+$ , and  $[\text{B}]$  to the concentration of free base (DBU) (Figure 3.18). The value given below is the average of three independent runs.<sup>[192]</sup>

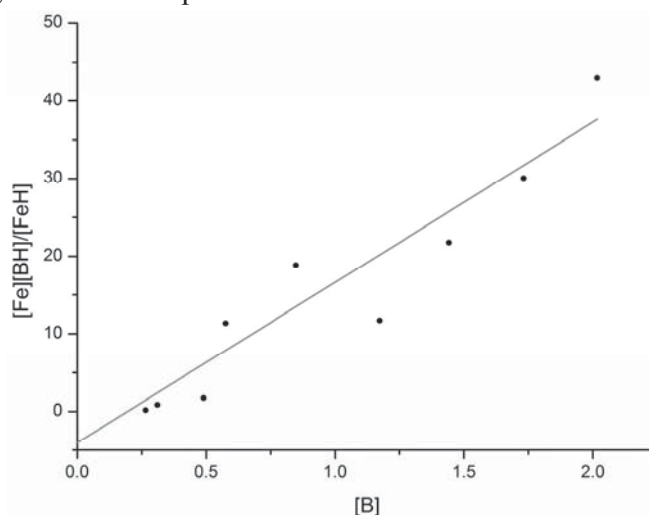


**Figure 3.18:** Plot of  $[\text{Fe}][\text{BH}]/[\text{FeH}]$  vs.  $[\text{B}]$  derived from backtitration experiments of  $4\text{H}^-$  (obtained by protonation of  $4(\text{NEt}_4)_2$  in MeCN solution) using DBU as the base,<sup>[201]</sup> monitored by UV-vis spectroscopy. The slope equals the equilibrium constant  $K$ .

### 3 Characterization of a Biomimetic [2Fe-2S] Cluster in its Diferric, Mixed Valent and Protonated State

$$K = \frac{[\text{Fe}][\text{BH}]}{([\text{Fe-H}][\text{B}])}$$

$$K[\text{B}] = \frac{[\text{Fe}][\text{BH}]}{[\text{Fe-H}]}$$

$$\text{p}K_{\text{a}} = \text{p}K_{\text{a}}(\text{BH}) - \log(K)$$

$$\text{p}K_{\text{a}}(\text{DBU}) = 24.34^{[201]}$$

$$K = 22.4 \pm 0.7$$

$$\text{p}K_{\text{a}} = 24.34 - \log(22.4) = 23.0 \pm 0.1$$

Protonation of  $4(\text{NEt}_4)_2$  was also monitored by  $^1\text{H}$  NMR spectroscopy. Therefore samples containing  $4(\text{NEt}_4)_2$  and varying amounts of  $[\text{DMPH}]\text{BF}_4$  were prepared and  $^1\text{H}$  NMR spectra were measured at room temperature. All resonances observed for both isomers of the cluster shift upon protonation, the biggest shift occurs for the signals at 5.25 and 5.50 ppm (Figure 3.19).

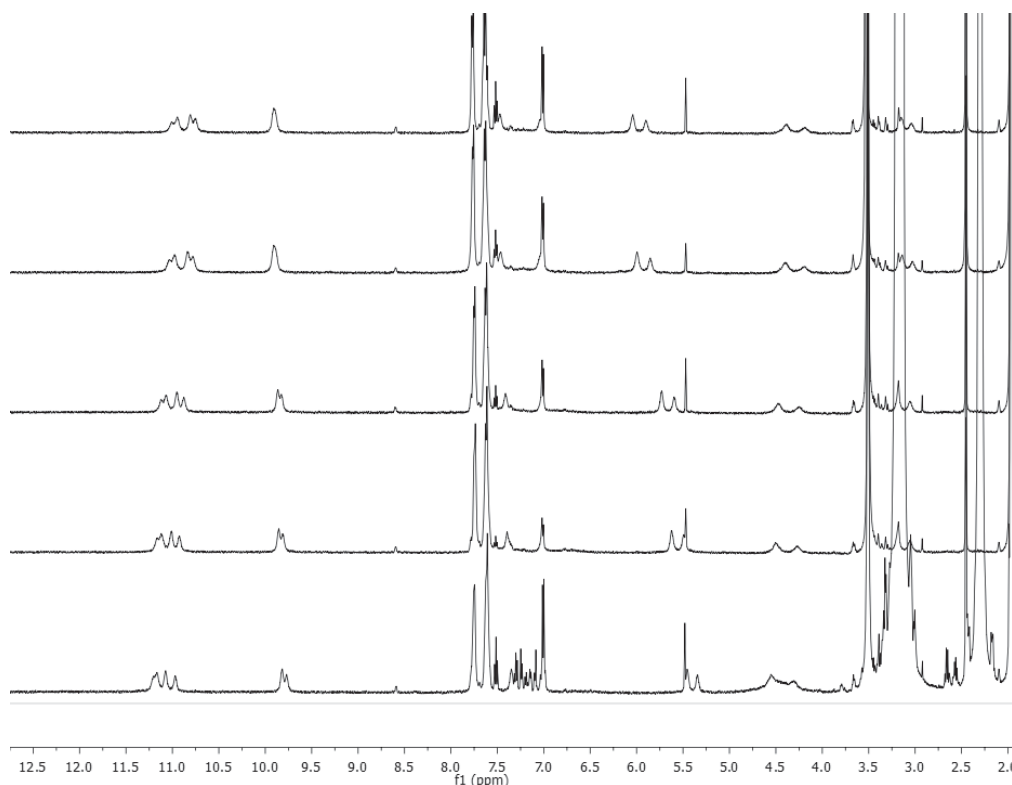


**Figure 3.19:**  $^1\text{H}$  NMR spectra during the stepwise protonation of  $4(\text{NEt}_4)_2$  at room temperature. Addition of 0.25, 0.5, 0.8 and 1.0 eq  $[\text{DMPH}]^+$  (second from bottom to top) gradually shifts all resonances. Addition of 1.5 eq DBU restores the spectrum of the unprotonated cluster (bottom), proving the reversibility of the process.<sup>[192]</sup>

### 3 Characterization of a Biomimetic [2Fe–2S] Cluster in its Diferric, Mixed Valent and Protonated State

The shift of each signal is proportional to the ratio of deprotonated: protonated cluster in the sample which shows that proton transfer between clusters is fast on the NMR timescale. In fact, the system is in a fast-exchange regime and the exchange is too fast to be measured accurately by  $^1\text{H}$  NMR spectroscopy.<sup>[202][203]</sup> Since only one set of peaks is observed even in a mixture of both the protonated and unprotonated cluster, the self-exchange rate between these two species must be at least as high as the rate that is just necessary to achieve coalescence. This rate can be determined as:<sup>[151]</sup>

$$k_{obs} = \frac{\pi \cdot \Delta\delta}{\sqrt{2}}$$

The largest peak separation observed in the spectra of both species is 0.58 ppm for the resonance which shifts from 5.48 ppm to 6.05 ppm (Figure 3.19 and 3.20). From this peak separation an observed rate constant of  $k_{obs} = 633 \text{ s}^{-1}$  can be determined. Since the NMR experiments were performed at a concentration of  $c = 0.00335 \text{ M}$ , this corresponds to a rate constant of  $1.9 \cdot 10^5 \text{ M}^{-1} \text{ s}^{-1}$ . This can be considered a conservative lower limit for the rate constant of self-exchange between  $4^{2-}$  and  $4\text{H}^-$ . Since the signals corresponding to the two distinct isomers shift simultaneously, it can be concluded that protonation of one of the isomers is not favored over protonation of the other isomer. A lower limit of  $10^4 \text{ M}^{-1} \text{ s}^{-1}$  for the self-exchange between the protonated and unprotonated species has been reported for  $12\text{b}^{2-} / 12\text{bH}^-$ .<sup>[151]</sup>

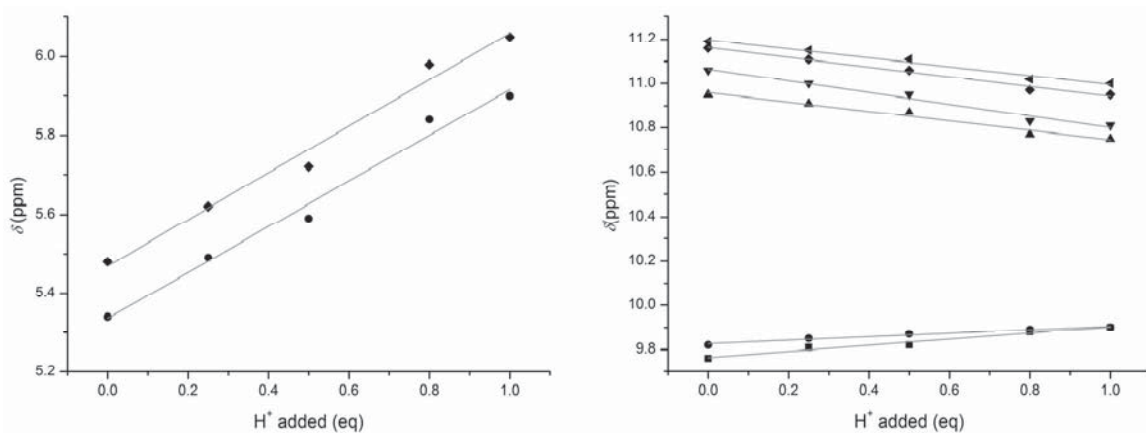


**Figure 3.20:** Chemical shifts observed in  $^1\text{H}$  NMR vs. amount of protons added, grey lines represent linear fits.

No resonance attributable to the presence of an N–H proton could be observed at room temperature probably due to broadening caused by rapid exchange with solvent molecules. At low temperature however a broad signal at 15.68 ppm was observed (Figure 3.21). This signal is found at very similar shift in comparison with the signal attributed to an N–H proton in cluster  $12\text{aH}^-$ .<sup>[147]</sup> Structural information from X-ray crystallography had established the

benzimidazole-N as the site of protonation in this case. It is thus assumed that protonation in  $4^{2-}$  also occurs on the benzimidazole-N rather than on the bridging sulfides.<sup>[192]</sup>

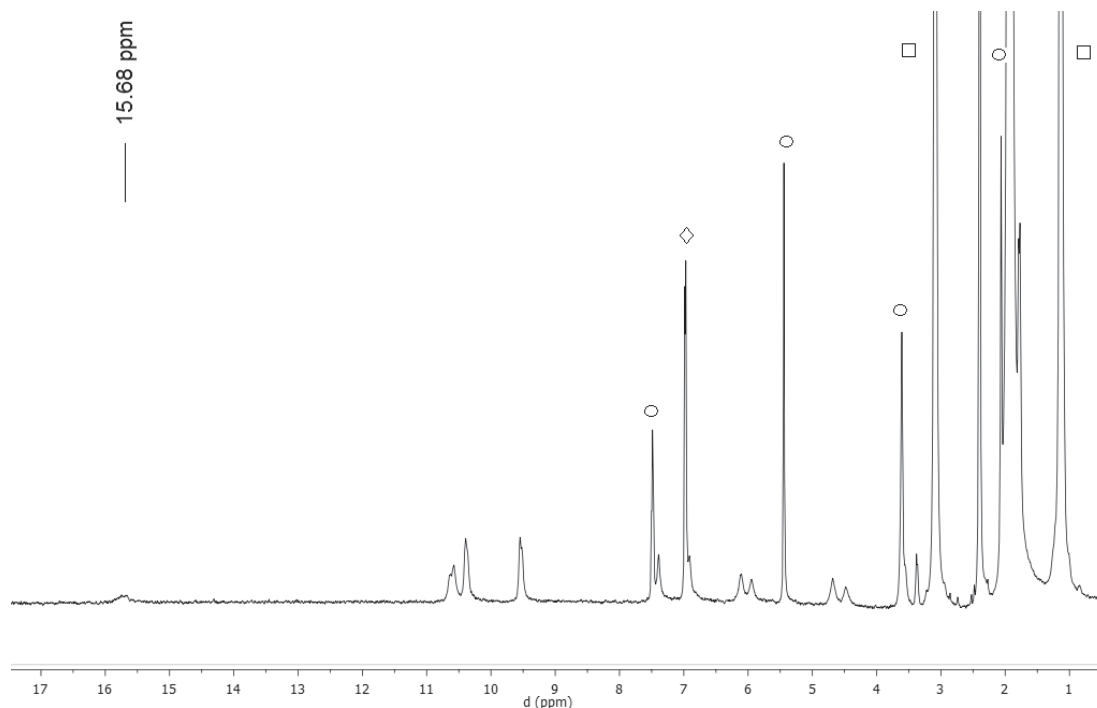


**Figure 3.21:** <sup>1</sup>H NMR spectrum of  $4\text{H}(\text{NEt}_4)$  at 243 K generated *in situ* by addition of 1.0 eq  $[\text{DMPH}]^+$ . The resonance at 15.68 ppm is similar to the one observed for closely related  $12\text{aH}_2$  and can be attributed to an N-H proton. Signals from residual solvent (O), DMP (◇) and counter ions  $\text{NEt}_4^+$  (□) are labelled.<sup>[192]</sup>

### 3.5.2 Protonation of the Mixed Valent Cluster

Protonation of mixed valent cluster  $4^{3-}$  was significantly more challenging due to the low stability of the species involved.  $4^{3-}$  was prepared *in situ* by addition of 1.0 eq  $\text{CoCp}^*_2$  to a solution of  $4(\text{NEt}_4)_2$  in MeCN. Protonation and deprotonation were then monitored by UV-vis spectroscopy at  $-30\text{ }^\circ\text{C}$  (Figure 3.22). Addition of 1.0 eq  $[\text{DMPH}]^+$  only led to minor changes in the visible absorption spectrum of the cluster (Figure 3.22). Protonation is accompanied by a slight increase in overall intensity and the rise of a shoulder at 530 nm. Upon addition of DBU, this shoulder vanishes and the overall intensity decreases below the initially observed intensity of  $4^{3-}$  indicating about 17 % decomposition (Figure 3.22). Thus the mixed valent protonated species appears to be rather unstable. In general the changes observed in UV-vis spectroscopy are not informative to unambiguously establish whether protonation of the mixed valent species occurs on the nitrogen atoms of the ligand, and whether it is reversible.

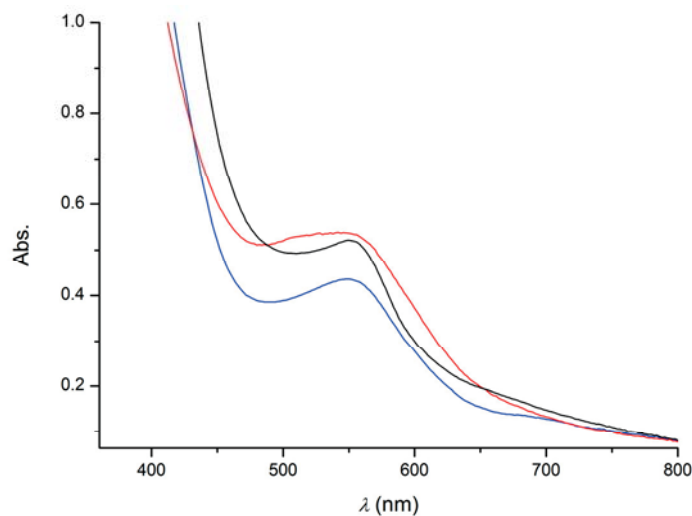


**Figure 3.22:** UV-vis absorption spectra of  $4^{3-}$  (black) in MeCN solution after addition of 1.0 eq [DMPH] $^+$  (red) and subsequent addition of 4.0 eq DBU (blue) at  $-30^\circ\text{C}$ .<sup>[192]</sup>

The redox potential of the protonated cluster was studied by cyclic voltammetry. Therefore a cyclic voltammogram of  $4(\text{NEt}_4)_2$  was recorded at  $-15^\circ\text{C}$  in 0.25 M  $\text{NBu}_4\text{PF}_6$  solution in MeCN. Subsequent addition of 1.0 eq [DMPH] $\text{BF}_4$  led to a shift of the cathodic peak potential of the first redox wave by  $-65\text{ mV}$ , corresponding to a redox potential of  $E_{1/2} = -1.342\text{ V vs. Fc/Fc}^+$  for  $4\text{H}^-$  assuming that a shift in peak potential corresponds to an equal shift in  $E_{1/2}$ .<sup>[192]</sup> Protonation of the ligand changes its overall charge from twofold to singly negative. Consequently, the ligand in its protonated form is better suited for stabilization of a ferrous species than the ligand in its unprotonated form. Thus the reduction potential of the [2Fe–2S] cluster is shifted to higher, *i.e.* less negative, values. However, the observed shift is rather small in comparison to shifts commonly reported for protonation of benzimidazole-N atoms in terminal ligands of [2Fe–2S] clusters which are about  $-200\text{ mV}$ .<sup>[147,148,150]</sup> No explanation for the small shift in this case could be found so far. Subsequent addition of DBU only partially restored the initial spectrum, which indicates that decomposition occurs upon protonation and deprotonation or during the course of the electrochemical measurements. (Figure 3.23).

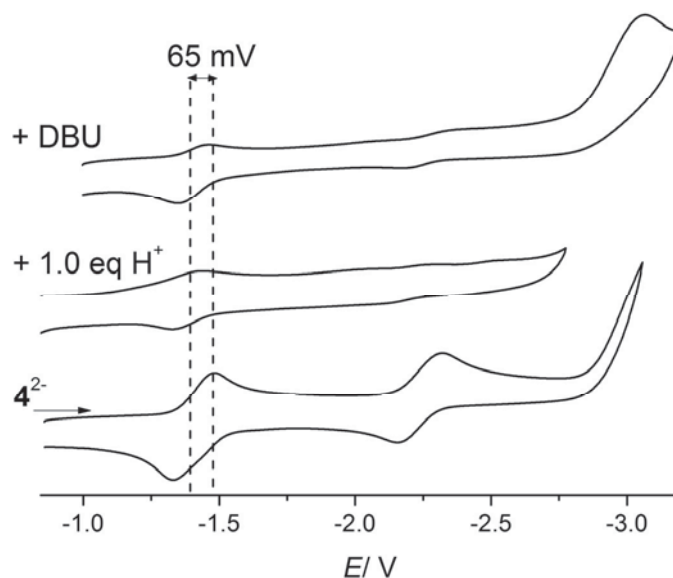


**Figure 3.23:** Effect of protonation on cyclic voltammogram of  $4(\text{NEt}_4)_2$  in 0.25 M  $\text{NBu}_4\text{PF}_6$  at  $-15^\circ\text{C}$  vs.  $\text{Fc}/\text{Fc}^+$  at a scan rate of 400 mV/s. The first reduction of  $4^{2-}$  (bottom) is shifted upon addition of 1.0 eq of acid (middle); addition of DBU partially restores the initial spectrum (top).<sup>[192]</sup>

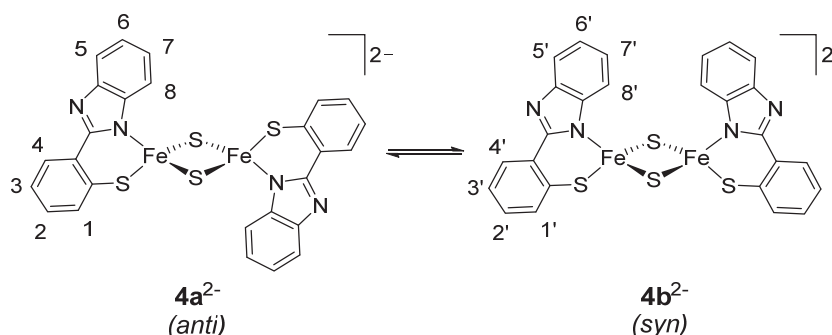
### 3.6 Conclusion

In conclusion this chapter presents a detailed characterization of a homoleptic [2Fe–2S] cluster bearing a mixed S/N-donor ligand. The cluster was prepared and fully characterized in its diferric and mixed valent form including structural characterization by X-ray diffraction in both cases. Some indications for the possibility of isolating a diferrous species were found. All resonances observed in  $^1\text{H}$  NMR spectra were assigned to the individual protons in both geometric isomers of the cluster. Additionally it was shown that  $4^{2-}$  can be reversibly protonated twice with the benzimidazole-N of both ligands as protonation site, similar to the proton responsive histidine ligands found in biological iron sulfur cofactors. By back titration a  $\text{p}K_a$  value of 23.0(1) was determined for  $4\text{H}^-$ . Electrochemical investigations have shown that the  $E_{1/2}$  for the first reduction of the cluster is affected by the cluster's protonation state. These findings establish  $4^{2-}$  as a suitable candidate to be used in reactivity studies modelling the functionality of biological [2Fe–2S] clusters with alternative ligands, which will be presented in the following chapters.

## 4 Slow Isomerization in a Synthetic [2Fe–2S] Cluster

### 4.1 Introduction

As shown in chapter 1.2, ligand exchange and rearrangement play a crucial role in iron sulfur cluster biosynthesis. Furthermore ligand rearrangement processes may be related to the function of iron sulfur clusters in sensing of protons and redox conditions. This chapter presents the first example of a [2Fe–2S] model complex in which slow isomerization *via* ligand rearrangement could be observed. Parts of this chapter have been adapted from a recent publication.<sup>[194]</sup> Although only one isomer of cluster **4**(NEt<sub>4</sub>)<sub>2</sub> was found in the crystalline material, two isomers are present in solution which differ by the relative arrangement of the mixed S/N-donating ligands, namely the *anti* isomer **4a**<sup>2-</sup> and the *syn* isomer **4b**<sup>2-</sup> (Scheme 4.1). Both isomers display a distinct <sup>1</sup>H NMR spectrum, which allows for quantification of the ratio of both species present in solution. While NMR spectra of the two isomers differ, no change in visible absorption spectra or cyclic voltammetry could be detected upon isomerization. This is likely due to the effect that the observed absorption bands arise mainly from charge transfer (LMCT) processes within the [2Fe–2S] core of the cluster, which remains intact during the isomerization process.



**Scheme 4.1:** Molecular structures of isomers **4a**<sup>2-</sup> and **4b**<sup>2-</sup> present in solution.

Several different mechanistic scenarios for the isomerization process are feasible: One possibility is full or partial dissociation of one of the ligands as an initial step. Full dissociation of the bidentate chelating ligand is most unlikely whereas dissociation of one binding site, rotation of the ligand around the remaining bond and re-coordination are more likely. The isomerization might also proceed *via* ligand exchange between two clusters. In this scenario the formation of a transient dimer of two clusters, possibly involving sulfide bridges formed by the thiolate functions of the ligand, might take place. Since the cluster in its diferric state bears a total of two anionic charges a scenario in which two clusters form an adduct might be energetically disfavored due to electronic repulsion. As a third possible

scenario an associative mechanism involving the coordination of a solvent molecule to one of the iron centers is conceivable as well. This would result in an intermediate with five-coordination on one of the iron centers, reminiscent of the situation described for  $\mathbf{3}^{2-}$  in chapter 1.6. The other isomer might then be formed from this intermediate upon solvent de-coordination. A combined experimental and computational approach presented in this chapter provides unprecedented insight into the mechanism of this isomerization process and give implications for ligand dynamics in natural iron sulfur systems.

## 4.2 Isomerization in MeCN- $d_3$

Since isomerization between the two species  $\mathbf{4a}^{2-}$  and  $\mathbf{4b}^{2-}$  was found to be slow at  $-30\text{ }^\circ\text{C}$ , solutions of pure  $\mathbf{4a}^{2-}$  (0.514 mM) could be prepared by rapidly dissolving crystalline material in MeCN- $d_3$  at  $-35\text{ }^\circ\text{C}$  and immediate freezing of the sample at  $-200\text{ }^\circ\text{C}$ . These samples were transferred to the NMR spectrometer and after an equilibration time of 5 min  $^1\text{H}$  NMR spectra were recorded every 6 min for a total of 16 h at varying temperatures ( $-25$ ,  $-20$ ,  $-15$ ,  $-10$ ,  $-5\text{ }^\circ\text{C}$ ) (Figure 4.1 and 4.2).<sup>[194]</sup>

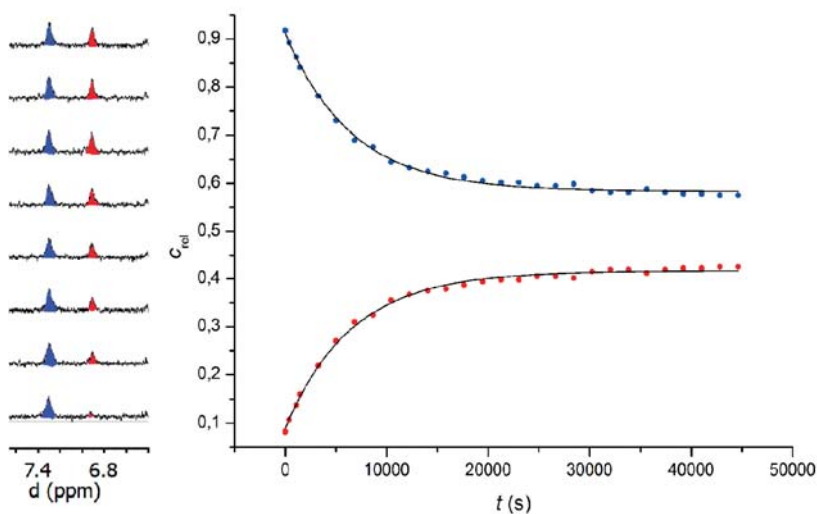


**Figure 4.1:**  $^1\text{H}$  NMR spectral changes monitored over 14 h at  $-25\text{ }^\circ\text{C}$ . A growing signal at 6.9 ppm corresponding to H-7' (red) was observed and quantified in relation to the signal at 7.3 ppm corresponding to H-7 (blue) to determine the relative concentration of both species in solution. The black line serves as a guide for the eye. Details of spectra on the left represent intervals of 2 h.<sup>[194]</sup>

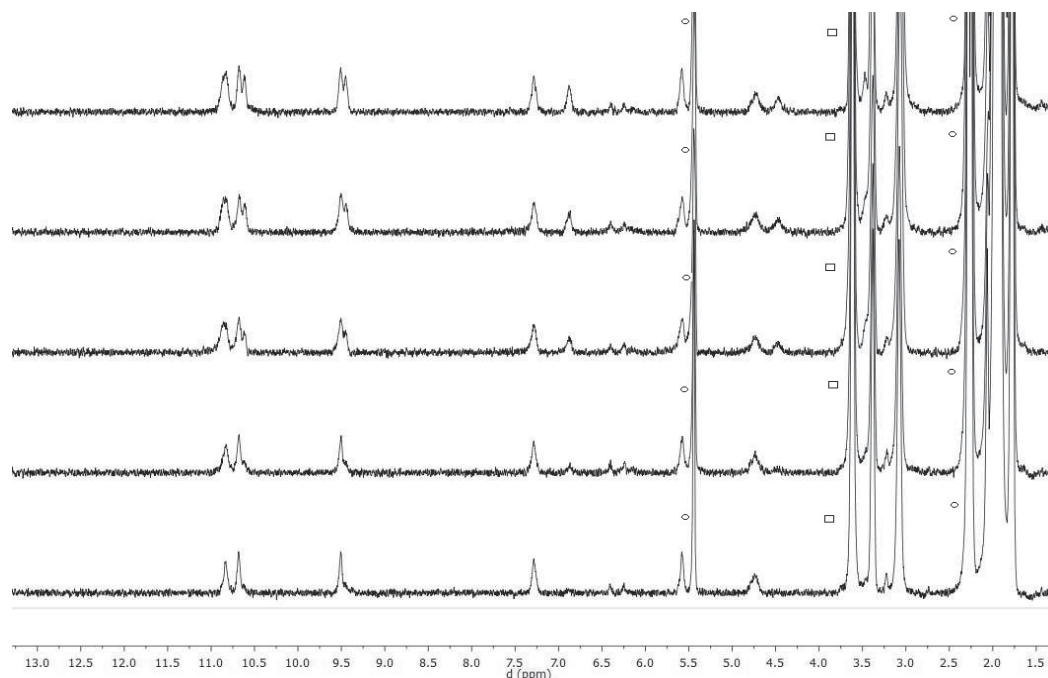


**Figure 4.2:** Full  $^1\text{H}$  NMR spectrum observed during the isomerization of  $4^{2-}$  in  $\text{MeCN-d}_3$ . Spectra recorded at  $-20^\circ\text{C}$  and shown here in intervals of 4 h. Signals arising from solvent molecules or counter ions are marked  $\circ$  and  $\square$ , respectively. <sup>[194]</sup>

At higher temperatures the isomerization was found to be too fast to be monitored by  $^1\text{H}$  NMR. After phasing and baseline correction in MestreNova 10.0 the signal at 7.3 ppm (corresponding to  $\text{H}^7$  in  $4\mathbf{a}^{2-}$ ) and the growing signal at 6.9 ppm (corresponding to  $\text{H}^{7'}$  in  $4\mathbf{b}^{2-}$ ) were used to quantify the ratio of both species. It should also be noted here that no signals corresponding to the free ligand were observed during the reaction. This means that the isomerization most likely does not include full dissociation of one of the ligands as an intermediate step. The equilibrium ratio of compounds  $4\mathbf{a}^{2-}$  and  $4\mathbf{b}^{2-}$  as determined by relative integration of the corresponding signals for  $\text{H}^7$  and  $\text{H}^{7'}$  is almost invariant with temperature over a range of almost 50 K ranging from 1 : 0.71 at 248 K to 1 : 0.75 at 293 K (Table 4.1). <sup>[194]</sup>

**Table 4.1:** Equilibrium constant  $K_{\text{eq}} = c(4\mathbf{b}^{2-})/c(4\mathbf{a}^{2-})$  for the isomerization process in  $\text{MeCN-d}_3$  at different temperatures.

$T$ (K)	$K_{\text{eq}}$
248	0.707
253	0.7128
258	0.726
263	0.718
268	0.738
293	0.75

#### 4 Slow Isomerization in a Synthetic [2Fe-2S] Cluster

The almost invariant equilibrium constants suggest very low differences in ground state energies of the two isomers. Indeed, thermodynamic parameters  $\Delta H^0 = 0.73 \text{ kJ mol}^{-1}$ ,  $\Delta S^0 = -0.08 \text{ J mol}^{-1} \text{ K}^{-1}$  and thus  $\Delta G^0 = 0.75 \text{ kJ mol}^{-1}$  at 293 K were obtained from the slope and intercept of a van t'Hoff plot (Figure 4.3) according to the equations given below.<sup>[204,205]</sup>

$$\Delta G^0 = \Delta H^0 - T\Delta S^0$$

$$\Delta G^0 = -RT \ln K_{eq}$$

$$\ln K_{eq} = -\frac{\Delta H^0}{RT} + \frac{\Delta S^0}{R}$$

$$\Delta H^0 = -R \cdot \text{slope}$$

$$\Delta S^0 = R \cdot \text{intercept}$$

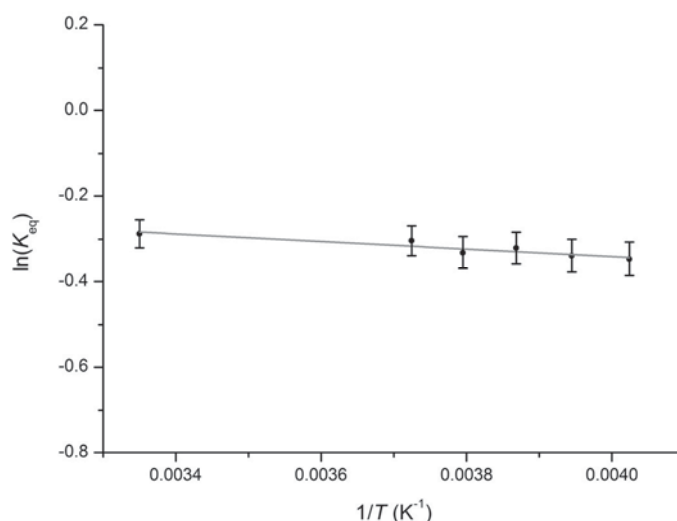


**Figure 4.3:** Van t'Hoff plot for the isomerization process monitored in MeCN-d<sub>3</sub>. Error bars were determined from the resulting integrals in <sup>1</sup>H NMR spectra after applying different baseline corrections. A linear fit yields an intercept of  $-(6.93 \cdot 10^{-5} \pm 0.064)$  and a slope of  $-(84.77 \pm 17.0)$ , thus  $\Delta H^0 = (0.73 \pm 0.15) \text{ kJ mol}^{-1}$  and  $\Delta S^0 = (0.08 \pm 0.6) \text{ J mol}^{-1} \text{ K}^{-1}$ .<sup>[194]</sup>

For a first order reaction that reaches an equilibrium, rate constants for the forward and backward reactions can be derived from the slope of a linearized plot (Figure 4.4) according to the equations given below

$$\ln((c_0 - c_{\text{final}})/(c_t - c_{\text{final}})) = k_{\text{observed}} \cdot t$$

With the equilibrium constant  $K_{\text{eq}} = [\mathbf{4b}_{\text{final}}]/[\mathbf{4a}_{\text{final}}]$  the individual first order rate constants for the forward and backward reaction can be extracted from the observed rate constants and are summarized in Table 4.2.

$$K_{\text{eq}} = k_{\text{forward}}/k_{\text{backward}}$$

$$k_{\text{observed}} = k_{\text{backward}} - k_{\text{forward}}$$

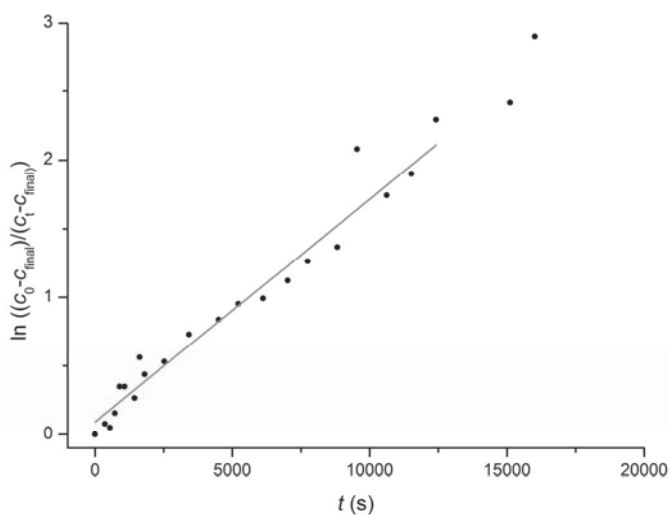


**Figure 4.4:** Linearized plot of  $\ln((c_0 - c_{\text{final}})/(c_t - c_{\text{final}}))$  vs.  $t$  (shown for the isomerization at  $c_0 = 0.514$  mM and  $T = 258$  K), yielding a slope corresponding to  $k_{\text{observed}} = 1.625 \cdot 10^{-4} \text{ s}^{-1}$ .<sup>[194]</sup>

**Table 4.2:** First order rate constants for the isomerization of  $\mathbf{4}^{2-}$  in MeCN- $d_3$  at various temperatures at  $c_0 = 0.514$  mM.<sup>[194]</sup>

$T$ (K)	$k_{\text{forward}}$ ( $10^{-4} \text{ s}^{-1}$ )	$k_{\text{backward}}$ ( $10^{-4} \text{ s}^{-1}$ )	$k_{\text{observed}}$ ( $10^{-4} \text{ s}^{-1}$ )
263	5.814	7.857	2.043
258	4.625	6.25	1.625
253	4.113	5.558	1.445
248	3.674	4.965	1.291

The first order rate constants determined for the forward reaction were used to derive the activation parameters for the forward reaction of  $\Delta S^\ddagger = -(253 \pm 9) \text{ J mol}^{-1} \text{ K}^{-1}$ ,  $\Delta H^\ddagger = (14.0 \pm 2.3) \text{ kJ mol}^{-1}$ , and  $\Delta G^\ddagger = (88.1 \pm 4.9) \text{ kJ mol}^{-1}$  at 293 K from an Eyring plot (Figure 4.5) according to the Eyring equation given below:<sup>[194,204,205]</sup>

$$\ln\left(\frac{k}{T}\right) = \frac{-\Delta H}{R} \cdot \frac{1}{T} + \ln\left(\frac{k_B}{h}\right) + \frac{\Delta S}{R}$$

$$\Delta H = -\text{slope} \cdot R$$

$$\Delta S = \left( \text{intercept} - \ln\left(\frac{k_B}{h}\right) \right) \cdot R$$

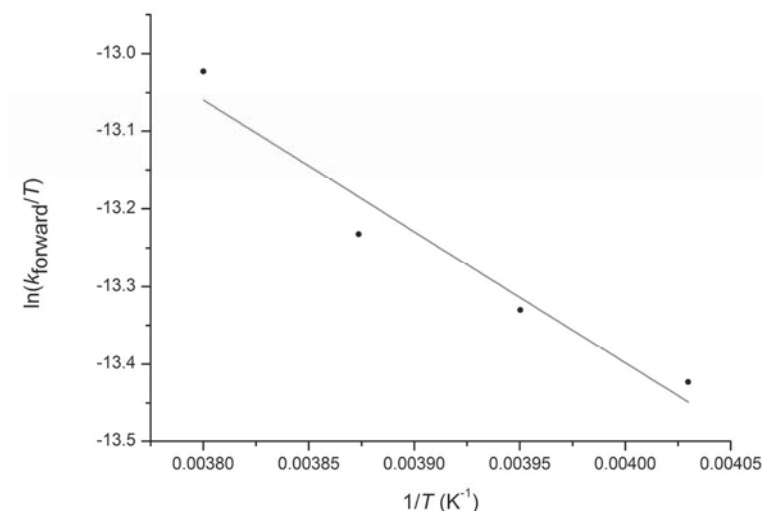


**Figure 4.5:** Eyring plot for the isomerization at  $-25^{\circ}\text{C}$  to  $-10^{\circ}\text{C}$  at  $c_0(\mathbf{4a}^{2-}) = 0.51 \text{ mM}$ . Linear fit (grey) yields a slope of  $-1689.7 \text{ K}$  and an intercept of  $-6.39$ .<sup>[194]</sup>

From the values obtained in these kinetic studies first conclusions about the underlying mechanism of the reaction can be drawn. Since there is almost no difference in ground state energies of  $\mathbf{4a}^{2-}$  and  $\mathbf{4b}^{2-}$  and the activation entropy is the main contribution to the activation free energy  $\Delta G^{\ddagger}$  at 293 K, the isomerization barrier is mainly a kinetic barrier. The relatively large negative value of the activation entropy ( $\Delta S^{\ddagger} = -(253 \pm 9) \text{ J mol}^{-1} \text{ K}^{-1}$ ) may point toward an associative mechanism of the observed reaction. An associative mechanism may be either a scenario involving solvent coordination or dimer formation. To further elucidate whether this mechanism involves the formation of a dimeric species, isomerization experiments at different concentrations were performed. In case of dimer formation, the isomerization is expected to be second order in cluster concentration, which would result in a linear dependency on the square of the initial concentration. Therefore solid compound  $\mathbf{4a}(\text{NEt}_4)_2$  was rapidly dissolved in  $\text{MeCN-d}_3$  at  $-35^{\circ}\text{C}$  and samples of different concentrations were prepared. The isomerization process in these samples was then monitored by  $^1\text{H}$  NMR spectroscopy at  $-15^{\circ}\text{C}$  and the initial rate of the reaction was determined from a linear fit of the concentration of isomer  $\mathbf{4b}^{2-}$  vs. time for the first 25% conversion of the reaction (Figure 4.6). This part of the reaction was chosen, since it was assumed that during these first 25% only the forward reaction is relevant. Not enough product  $\mathbf{4b}^{2-}$  is assumed to have been formed by then so the backward reaction does not yet contribute significantly to the observed rate.

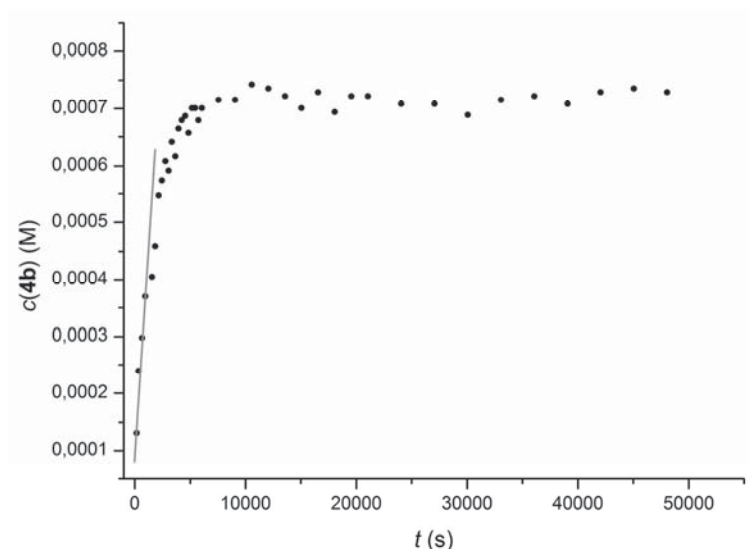


**Figure 4.6:** Linear fit (grey) of the first 25% of the reaction at 258 K with  $c_0 = 2.0$  mM giving a slope of  $2.97 \cdot 10^{-7} \text{ M s}^{-1}$ .<sup>[194]</sup>

**Table 4.3:** Initial rates for the isomerization of  $4^{2-}$  in MeCN at 258 K with varying concentrations of  $4(\text{NEt}_4)_2$ .<sup>[194]</sup>

$c$ (mM)	$v_{\text{initial}}$ ( $10^{-7} \text{ M s}^{-1}$ )
0.514	0.482
1.06	2.16
1.77	3.00
2.0	2.97
2.28	4.38
4.0	7.73

Since the initial rate of the reaction increases linearly when increasing the initial concentration of  $4\mathbf{a}(\text{NEt}_4)_2$  (Figure 4.7), the observed isomerization must be first-order in cluster concentration. If the reaction were second-order in cluster concentration, the initial rate would be expected to show a behavior proportional to a polynomial function upon increasing the temperature. It can thus be concluded that the isomerization thus not occur *via* the formation of a dimer of two [2Fe–2S] clusters as an intermediate step. A second possible associative mechanistic scenario involves the coordination of solvent molecules to the [2Fe–2S] cluster. To investigate this possibility more closely, experiments in different solvents need to be carried out, which will be presented in the following chapter.

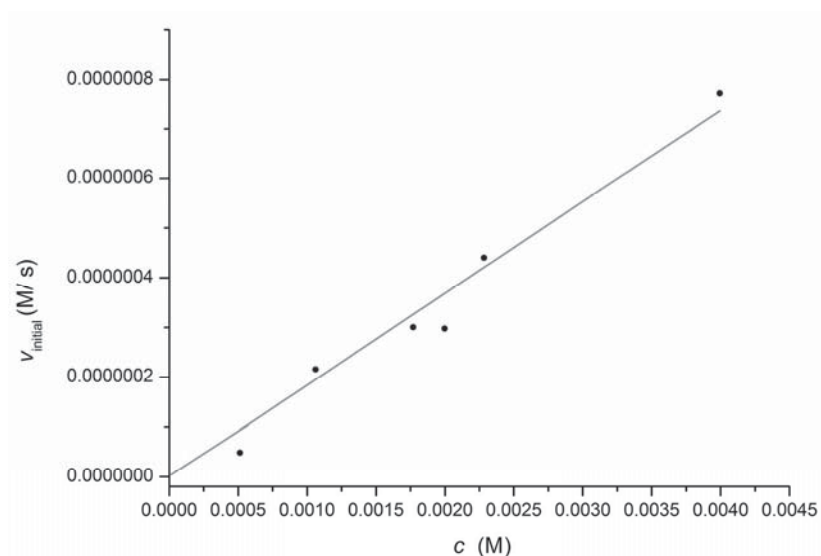


**Figure 4.7:** Plot of  $v_{\text{initial}}$  ( $\text{M}\cdot\text{s}^{-1}$ ) vs  $c_0$  (M) in MeCN- $\text{d}_3$  at  $-15^\circ\text{C}$  and linear fit (grey).<sup>[194]</sup>

### 4.3 Isomerization in DMF

To investigate a possible involvement of solvent molecules in the isomerization process, kinetic studies in DMF- $\text{d}_7$  were carried out and compared to the results obtained for MeCN- $\text{d}_3$ . Both DMF and MeCN are potentially coordinating solvents. To investigate whether coordination of solvent molecules is necessary to achieve isomerization, experiments would have to be conducted in non-coordinating solvents. However, due to the low solubility of  $4(\text{NEt}_4)_2$  in unpolar and non-coordinating solvents such as toluene or hexanes, this was not possible and experiments concerning the effect of solvent could only be carried out in DMF. Similar to the experiments described in chapter 4.2 an Eyring plot and a van t'Hoff plot were used to determine the thermodynamic parameters of the reaction and to gain insight into the mechanism. Similar to what was observed in MeCN- $\text{d}_3$ , the differences in ground state energy of  $4\mathbf{a}^{2-}$  and  $4\mathbf{b}^{2-}$  are very small in DMF- $\text{d}_7$ . Thermodynamic parameters of  $\Delta H^0 = (0.62 \pm 0.22) \text{ kJ mol}^{-1}$  and  $\Delta S^0 = -(0.58 \pm 0.86) \text{ J mol}^{-1} \text{ K}^{-1}$  were derived from a van't Hoff plot (Figure 4.8) and activation parameters of  $\Delta S^\ddagger = -(250.3 \pm 10.3) \text{ J mol}^{-1} \text{ K}^{-1}$ ,  $\Delta H^\ddagger = (17.17 \pm 2.69) \text{ kJ mol}^{-1}$  and  $\Delta G^\ddagger = (90.51 \pm 5.71) \text{ kJ mol}^{-1}$  at 293 K were derived from an Eyring plot (Figure 4.9).<sup>[194]</sup>

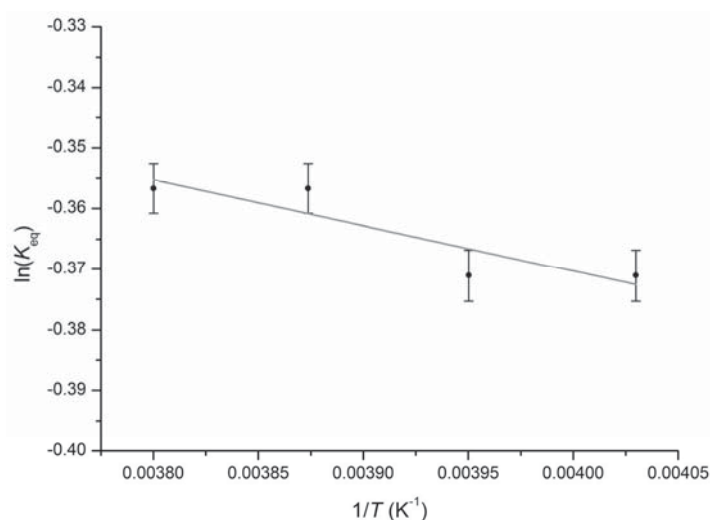


**Figure 4.8:** Van t'Hoff plot for the isomerization process monitored in DMF-d<sub>7</sub>. Error bars were determined from the resulting integrals in <sup>1</sup>H-NMR spectra after applying different baseline corrections. A linear fit yields an intercept of  $-(0.06973 \pm 0.104)$  and a slope of  $-(75.15 \pm 26.58)$ , thus  $\Delta H^0 = (0.62 \pm 0.22)$  kJ mol<sup>-1</sup> and  $\Delta S^0 = -(0.58 \pm 0.86)$  J mol<sup>-1</sup> K<sup>-1</sup>.<sup>[194]</sup>

**Table 4.4:** First order rate constants for the isomerization of **4**<sup>2-</sup> in DMF-d<sub>7</sub> at various temperatures at  $c = 1.27$  mM.

$T$ (K)	$k_{\text{forward}}$ ( $10^{-4}$ s <sup>-1</sup> )	$k_{\text{backward}}$ ( $10^{-4}$ s <sup>-1</sup> )	$k_{\text{observed}}$ ( $10^{-4}$ s <sup>-1</sup> )
263	1.803	2.613	0.81
258	1.564	2.268	0.7031
253	1.191	1.726	0.535
248	1.091	1.581	0.49

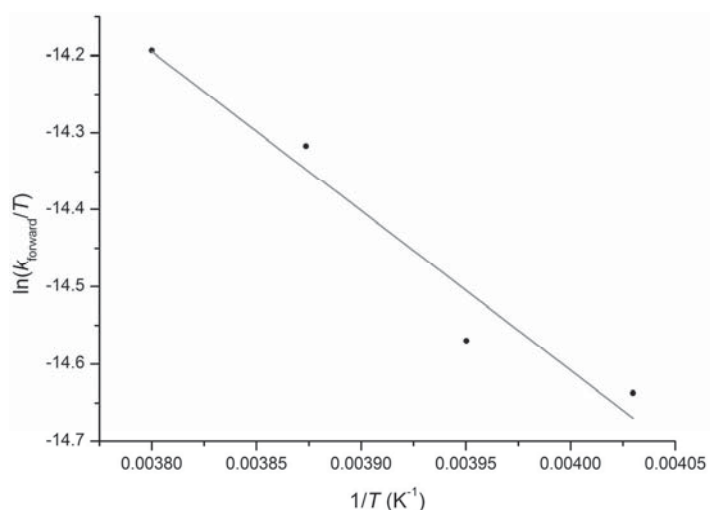


**Figure 4.9:** Eyring Plot for the isomerization process monitored in DMF-d<sub>7</sub>. A linear fit yields the intercept of  $(6.347 \pm 1.26)$  and slope of  $-(2065 \pm 323)$ , thus  $\Delta S^\ddagger = -(250.3 \pm 10.3)$  J mol<sup>-1</sup> K<sup>-1</sup>,  $\Delta H^\ddagger = (17.17 \pm 2.69)$  kJ mol<sup>-1</sup> and  $\Delta G^\ddagger = (90.51 \pm 5.71)$  kJ mol<sup>-1</sup> at 293 K.

#### 4 Slow Isomerization in a Synthetic [2Fe–2S] Cluster

Similar to what had already been observed in MeCN-d<sub>3</sub>, the initial rate of the reaction shows a linear dependence on the starting concentration  $c_0(\mathbf{4a}^{2-})$ . These findings show that the mechanistic pathway to achieve an equilibrium between  $\mathbf{4a}^{2-}$  and  $\mathbf{4b}^{2-}$  is the same in both solvents. While the activation parameters differ only slightly, the observed rates of the reaction are somewhat different. The isomerization proceeds with an initial rate of  $3.0 \cdot 10^{-7} \text{ M s}^{-1}$  at  $c = 1.77 \text{ mM}$  in MeCN-d<sub>3</sub> while the rate observed in DMF-d<sub>7</sub> was only  $1.62 \cdot 10^{-7} \text{ M s}^{-1}$  at a concentration of  $c = 1.73 \text{ mM}$ . Thus the reaction is about two times slower in DMF-d<sub>7</sub> than in MeCN-d<sub>3</sub>, which may indeed indicate involvement of solvent molecules in the isomerization process.<sup>[194]</sup>

**Table 4.5:** Initial rates for the isomerization of  $\mathbf{4}^{2-}$  in DMF-d<sub>7</sub> at 258 K at different concentrations of starting material.

$c \text{ (mM)}$	$v_{\text{initial}} (10^{-7} \text{ M s}^{-1})$
0.831	0.322
1.04	0.51
1.27	1.01
1.73	1.62

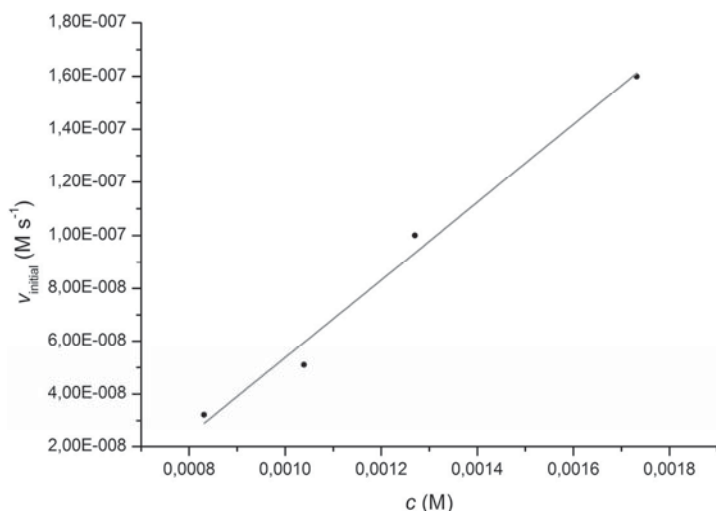


**Figure 4.10:** Plot of  $v_{\text{initial}} \text{ (M s}^{-1}\text{)}$  vs  $c_0 \text{ (M)}$  at  $-15^\circ\text{C}$  and linear fit (grey).<sup>[194]</sup>

Isomerization experiments were also performed in MeOD-d<sub>4</sub>. However, in these experiments the cluster was found already isomerized to the final equilibrium when the first <sup>1</sup>H NMR spectrum was recorded. Methanol is not only a coordinating solvent but may also be involved in the formation of hydrogen bonds, which may contribute to an accelerated isomerization. A similar effect can be anticipated in the presence of protons and will be discussed in chapter 4.5.

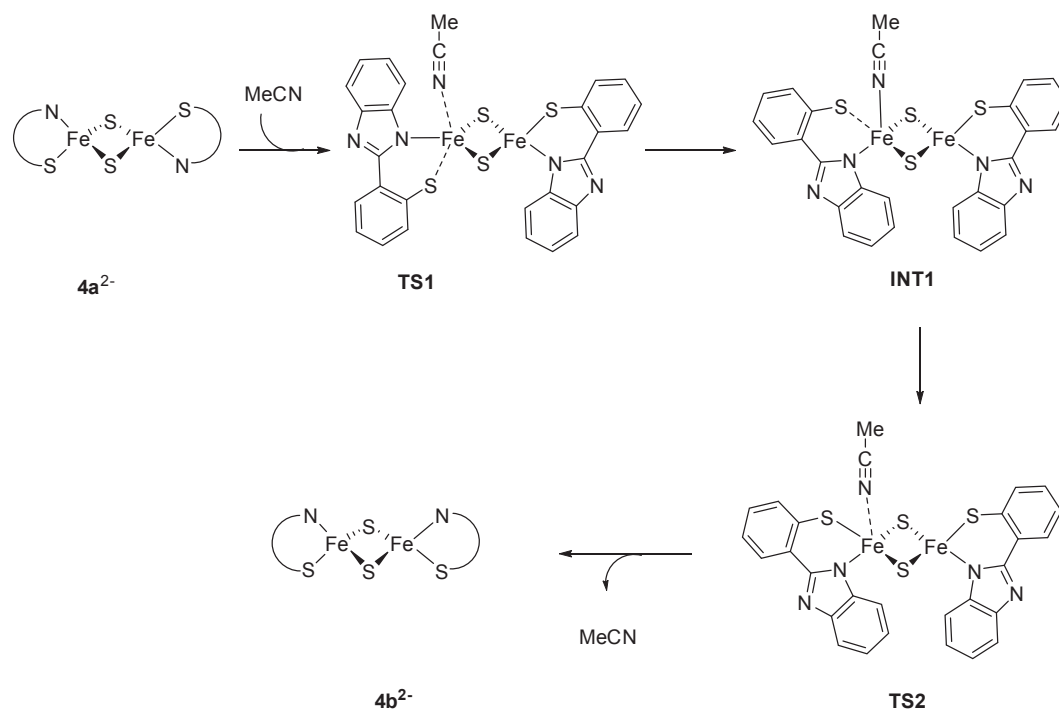
## 4.4 Density Functional Theory (DFT) Calculations

To rationalize the experimental results and verify the conclusions drawn from them, computational studies were performed. These calculations were carried out in collaboration with Dr. Shengfa Ye and Prof. Frank Neese at the Max-Planck Institute in Mülheim, and details of these computational studies can be found in a recent joint publication.<sup>[194]</sup> A broken symmetry approach was used with the ORCA software program.<sup>[206]</sup> Optimizations were performed with the hybrid B3LYP density functional in combination with triple- $\zeta$  quality TZVP basis set on all atoms.<sup>[207,208]</sup> These calculations confirmed that  $\mathbf{4a}^{2-}$  and  $\mathbf{4b}^{2-}$  have almost identical ground state energies reflected by very small values of  $\Delta H^\circ$  and  $\Delta G^\circ$ . The geometry optimized structure for  $\mathbf{4a}^{2-}$  is in good agreement with the structure determined by X-ray crystallography, showing that the chosen approach is suitable for describing the given diferric [2Fe–2S] system. Most importantly, the calculations support a mechanism in which one solvent molecule (MeCN) coordinates to one of the ferric iron centers of the cluster, leading to the formation of five-coordinate intermediate INT1 with a distorted square pyramidal geometrical coordination, while the second iron center retains its tetrahedral coordination. The Fe–NCMe interaction weakens the bond Fe–S bond between the metal and the thiolate donor of  $[\mathbf{L}^{\text{SN}}]^{2-}$  as evidenced by a considerably elongated Fe–S bond in the first transition state TS1 in comparison to the bond length found in the initial ground state structure  $\mathbf{4a}^{2-}$ . The solvent molecule then dissociates from intermediate INT1 *via* a second transition state TS2 upon which the *syn*-isomer  $\mathbf{4b}^{2-}$  is formed. The calculated free energy barrier for TS1 (98.0 kJ mol<sup>-1</sup>) is in reasonable agreement with the value observed experimentally (88.1 kJ mol<sup>-1</sup> in MeCN-d<sub>3</sub>). Starting from INT1, the forward or backward transformation proceeds with equal probability, since the respective barrier is nearly identical (about 10 kJ mol<sup>-1</sup>). This is consistent with an equilibrium ratio of both species in solution of almost 1:1.

**Table 4.6:** Experimental (in MeCN-d<sub>3</sub> and DMF-d<sub>7</sub>) and calculated (for MeCN) thermodynamic parameters for the observed isomerization process between  $\mathbf{4a}^{2-}$  and  $\mathbf{4b}^{2-}$ .<sup>[194]</sup>

	MeCN-d <sub>3</sub>	DMF-d <sub>7</sub>	MeCN <sub>calc</sub>
$\Delta H^\circ$ /kJ mol <sup>-1</sup>	0.73 ± 0.15	0.62 ± 0.22	4.7
$\Delta S^\circ$ /J mol <sup>-1</sup> K <sup>-1</sup>	- 0.08 ± 0.6	-0.58 ± 0.86	28.2
$\Delta G^\circ$ /kJ mol <sup>-1</sup>	0.75 ± 0.32	0.79 ± 0.47	-3.0
$\Delta H^\ddagger$ /kJ mol <sup>-1</sup>	14.0 ± 2.3	17.2 ± 2.7	62.7
$\Delta S^\ddagger$ /J mol <sup>-1</sup> K <sup>-1</sup>	- 253 ± 9.2	- 250 ± 10.3	- 164.0
$\Delta G^\ddagger$ /kJ mol <sup>-1</sup>	88.1 ± 4.9	90.51 ± 5.71	98.0

## 4 Slow Isomerization in a Synthetic [2Fe-2S] Cluster



**Scheme 4.2:** Proposed mechanism for the isomerization of  $4a^{2-}$  to  $4b^{2-}$  as based on DFT calculations.

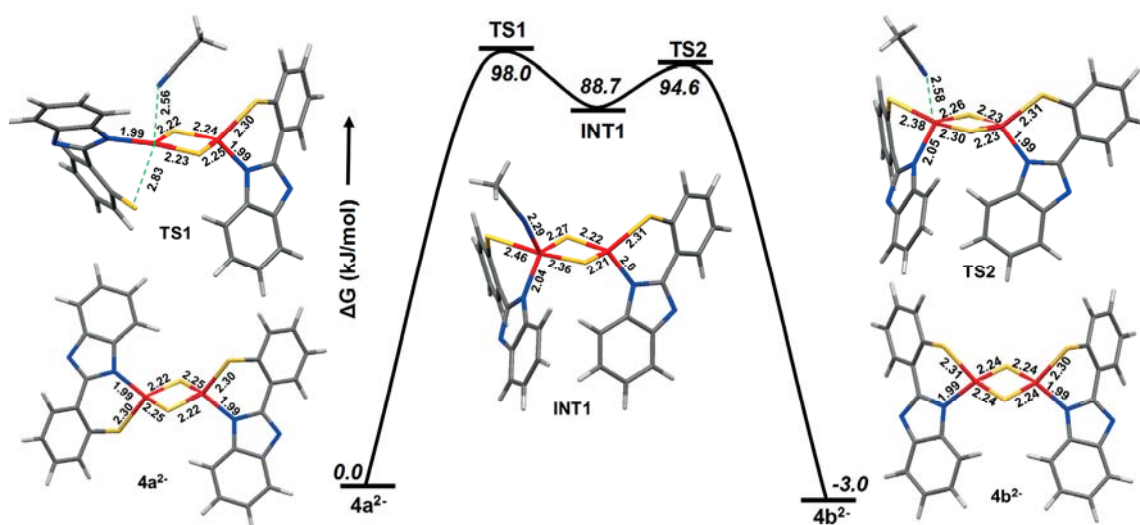


**Figure 4.13:** Free energy profile diagram for the isomerization of  $4a^{2-}$  to  $4b^{2-}$ . Optimized geometries of the intermediate and transition states are shown. Bond distances are reported in units of Å. Color code: Fe(red), S(yellow), N(blue), C(grey) and H(white).<sup>[194]</sup>

## 4.5 Effect of Protonation and Cluster Redox State

To gain further insight into the mechanism of the observed isomerization, the effect of cluster redox state and protonation was observed. Therefore crystalline  $\mathbf{4}(\text{NEt}_4)_2$  was rapidly dissolved in  $\text{MeCN-d}_3$  at  $-35^\circ\text{C}$  and reduced *in situ* by addition of  $\text{CoCp}^*_2$ . The solution was transferred to an NMR-tube and immediately frozen at  $-200^\circ\text{C}$ . After transfer to the NMR spectrometer, temperature equilibration at  $-30^\circ\text{C}$  and shimming (a total time of about 5 min) both isomers were already found to be present in their final ratio of about 1: 0.9. This indicates that one-electron reduction of the cluster makes the isomerization process faster by at least one order of magnitude. The ratio of both isomers does not change with varying temperature over a temperature range from  $-30^\circ\text{C}$  to  $20^\circ\text{C}$  (see Figure 3.14) consistent with identical ground state energies of both isomers.<sup>[194]</sup> For a first-order reaction the integrated rate law is given as:

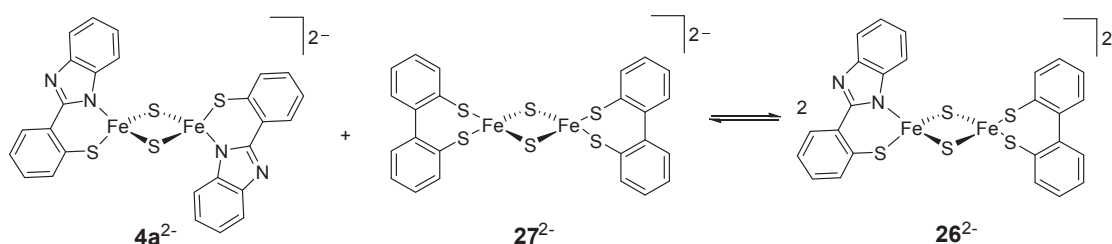
$$\ln(c_{eq}) = -kt + \ln(c_0)$$

With  $c_0(\mathbf{4a}^{3-}) = 1.27\text{ mM}$ ,  $c_{eq}(\mathbf{4a}^{3-}) = 0.668\text{ mM}$  and  $t = 300\text{ s}$ , a lower limit for the observed rate constant can be determined as  $k_{\text{obs,min}} = 2.14 \cdot 10^{-3}\text{ s}^{-1}$  at  $-30^\circ\text{C}$  whereas  $k_{\text{obs}} = 1.29 \cdot 10^{-4}$  for  $\mathbf{4}^{2-}$  in  $\text{MeCN-d}_3$  at  $-30^\circ\text{C}$ .

The effect of protonation was studied by dissolving  $\mathbf{4}(\text{NEt}_4)_2$  in  $\text{MeCN-d}_3$  that already contained 1.0 eq of  $[\text{DMPH}](\text{BF}_4)$  at  $-35^\circ\text{C}$ . Again the isomerization was already complete by the time the first  $^1\text{H-NMR}$  spectrum could be recorded and both isomers were present in their final ratio of 1:0.73 (final ratio at  $23^\circ\text{C}$ : 1:0.71, see Figures 3.19 and 3.21). With  $c_0(\mathbf{4aH}^-) = 1.27\text{ mM}$ ,  $c_{eq}(\mathbf{4aH}^-) = 0.73\text{ mM}$  and  $t = 300\text{ s}$ , a lower limit for the observed rate constant can be determined as  $k_{\text{obs,min}} = 1.85 \cdot 10^{-3}\text{ s}^{-1}$  at  $-30^\circ\text{C}$ . The very similar ratios of both isomers at  $-30^\circ\text{C}$  and  $23^\circ\text{C}$  are identical within error, consistent with identical ground state energies of the two isomers. A fast isomerization of the protonated cluster can be rationalized in the following way: Protonation of the benzimidazole ligand changes its properties from a doubly negatively charged to a singly negatively charged ligand. This considerably weakens the Fe–N bond which facilitates dissociation of this bond and leads to rapid isomerization in solution. As described in chapter 4.3, in  $\text{MeOD-d}_4$  the isomerization of unprotonated  $\mathbf{4a}^{2-}$  was already complete when the first  $^1\text{H NMR}$  spectrum was recorded at  $-30^\circ\text{C}$ . This may be due to possible H–/D– bonds formed, which facilitate the isomerization in a similar way as protonation. These findings may point toward a possible strategy of iron sulfur cofactors in sensing of oxidative or pH conditions, since these factors seem to facilitate rearrangements in the clusters coordination environment.<sup>[194]</sup>

## 4.6 Ligand Exchange Between Different Homoleptic [2Fe–2S] Clusters

If the isomerization would proceed *via* ligand exchange between two clusters, ligand exchange with another related [2Fe–2S] cluster should occur at a rate in the same order of magnitude. For comparison, ligand exchange experiments were performed by mixing cluster  $4^{2-}$  and homoleptic  $\{S_4\}$  coordinated cluster  $27^{2-}$  at  $-35^\circ\text{C}$  and monitoring the spectral properties of the obtained solutions over time.



**Scheme 4.3:** Possible ligand exchange between homoleptic clusters  $4^{2-}$  and  $27^{2-}$  to yield heteroleptic compound  $26^{2-}$ .

No changes in both  $^1\text{H-NMR}$  and UV-vis spectra of the solution containing both clusters were detected neither at  $-30^\circ\text{C}$  nor at  $20^\circ\text{C}$  over a period of 16 h, indicating that no ligand exchange between the two clusters takes place. The UV-vis absorption spectra of a 1:1 mixture of clusters  $4^{2-}$  and  $27^{2-}$  is largely dominated by the contributions of  $27^{2-}$ , as the extinction coefficients of this cluster are much higher than those observed for  $4^{2-}$ . However, the visible absorption spectrum did not change over the course of about 3 h, indicating that no exchange reaction takes place.

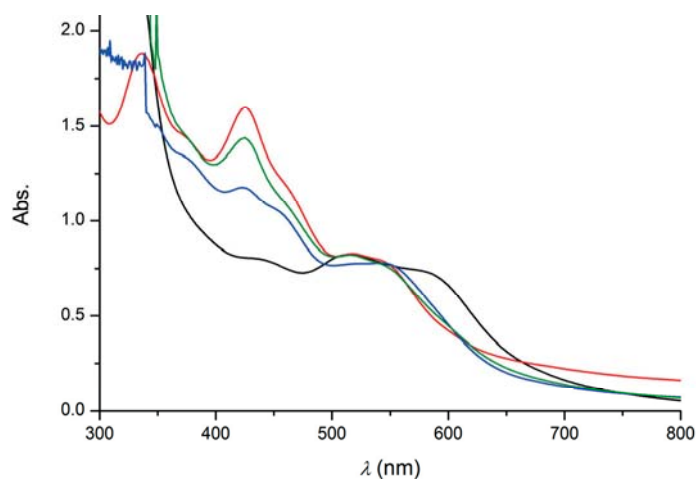


**Figure 4.14:** UV-vis absorption spectra of  $4^{2-}$  (black),  $27^{2-}$  (red), heteroleptic compound  $26^{2-}$  (blue), and a mixture of  $4^{2-}$  and  $27^{2-}$  (green).



Although formation of the heteroleptic cluster in a solution of a 1:1 mixture of both clusters after 5 h was observed by ESI MS, it can be assumed that this exchange takes place after injection into the spectrometer during the ionization. This observation provides additional evidence that isomerization between  $4\mathbf{a}^{2-}$  and  $4\mathbf{b}^{2-}$  does not proceed *via* intermolecular ligand exchange between two clusters.

## 4.7 Conclusion

In conclusion a detailed experimental and computational investigation of the mechanism of the isomerization of a biomimetic [2Fe–2S] cluster has been presented in this chapter. It was shown that the isomerization in MeCN and DMF most probably proceeds *via* an associative mechanism involving the coordination of a solvent molecule to one of the iron centers. This results in five-coordination of one of the iron centers, while the other iron center retains its tetrahedral coordination environment. The structure of this five-coordinate intermediate is reminiscent of the structure of five-coordinate cluster  $3^{2-}$  (see chapter 1.6).<sup>[138]</sup> Due to low solubility, studies in less polar and less coordinating solvents were not possible. One electron reduction as well as protonation were shown to increase the rate of the observed isomerization process by at least one order of magnitude. For the first time these studies provide insights into ligand rearrangement at [2Fe–2S] clusters that may be relevant for the understanding of biological cluster transfer or sensing processes.<sup>[194]</sup>

To obtain a broader view of the factors facilitating ligand rearrangement or exchange, various studies in the presence of catalytic amounts of protons or in the presence of coordinating alkali metal ions may be carried out. Additionally, using clusters which are soluble in non-coordinating solvents may yield further evidence for involvement of coordination of solvent molecules in the isomerization process. Finally, the design of less bulky ligands could make systems, in which ligand exchange between two clusters can be studied, available and provide further useful insight in regard to cluster transfer processes occurring during iron sulfur cluster biogenesis.



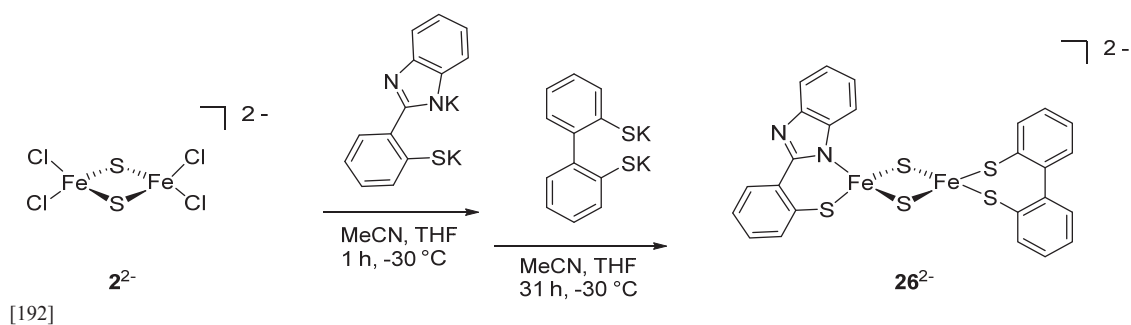
## 5 A Structural Model System for the [2Fe–2S] Cluster in MitoNEET Proteins

### 5.1 Introduction

Among [2Fe–2S] clusters featuring alternative ligands, *i.e.* ligands different from cysteine, histidine is the most commonly found ligand. Three different classes of [2Fe–2S] clusters featuring a Cys<sub>3</sub>His coordination are known to date, as introduced in chapter 1.4.<sup>[73]</sup> In the widely studied mitoNEET cluster, the role of the alternative ligand has not yet been understood and no synthetic model system mimicking this special asymmetric coordination motif is known to date. This chapter introduces the first structural model system for the [2Fe–2S] cluster in mitoNEET and related proteins along with its spectroscopic properties in the diferric, mixed valent and protonated forms. Parts of this chapter have been adapted from a recent publication.<sup>[192]</sup>

### 5.2 Synthesis and Crystallographic Characterization in the Solid State

Diferric **26**(NEt<sub>4</sub>)<sub>2</sub> was prepared *via* a stepwise ligand exchange pathway starting from [Fe<sub>2</sub>S<sub>2</sub>Cl<sub>4</sub>](NEt<sub>4</sub>)<sub>2</sub> (**2**(NEt<sub>4</sub>)<sub>2</sub>) similar to the synthesis of the recently reported Rieske models **11**<sup>2-</sup> and **13**<sup>2-</sup>.<sup>[144,148]</sup> This synthesis proved to be challenging since the formation of homoleptic side products must be suppressed by optimizing the reaction conditions, *i.e.* reaction time, temperature and amount of ligand used. Additionally, several recrystallization steps were found to be necessary in order to obtain the pure product. Diffusion of diethyl ether into a solution of **26**(NEt<sub>4</sub>)<sub>2</sub> in MeCN at 8 °C led to growth of crystals suitable for X-ray diffraction. The molecular structure of the diferric cluster anion is shown in figure 5.1.



**Scheme 5.1:** Synthetic approach toward heteroleptic cluster **26**<sup>2-</sup> *via* stepwise ligand exchange.

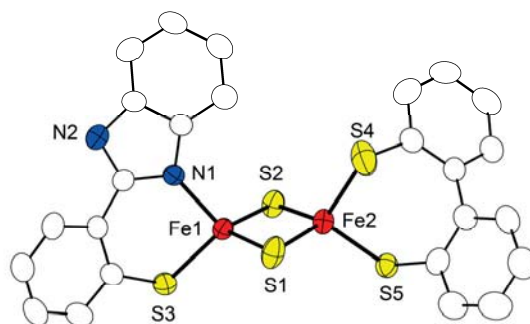


**Figure 5.1:** Molecular structure of the anion of diferric mitoNEET model  $\mathbf{26}(\text{NEt}_4)_2$  in the solid, hydrogen atoms, solvent molecules and counter ions have been omitted for clarity.<sup>[192]</sup>

$\mathbf{26}(\text{NEt}_4)_2$  crystallizes in the triclinic space group  $P-1$  with 0.5 molecules of MeCN per cluster. Selected geometric parameters and corresponding structural parameters for a selected biological mitoNEET cluster are shown in table 5.1. While the all cysteine ligated iron site in the biological mitoNEET cluster features a nearly ideal tetrahedral coordination sphere, the His/Cys ligated iron site is coordinated in a distorted tetrahedral mode with a  $\text{N}_{\text{His}}\text{-Fe-S}_{\text{Cys}}$  angle of  $98.9\text{--}99.9^\circ$ . The heteroleptic model complex  $\mathbf{26}(\text{NEt}_4)_2$  nicely emulates this property with an  $\text{N-Fe-S}$  angle of  $95.64^\circ$ .<sup>[192]</sup>

**Table 5.1:** Selected bond lengths (Å) and angles ( $^\circ$ ) of diferric cluster  $\mathbf{26}(\text{NEt}_4)_2$  and human mitoNEET.

	$\mathbf{26}(\text{NEt}_4)_2$ <sup>[192]</sup>	mitoNEET <sup>[94]</sup>
$d(\text{Fe}\cdots\text{Fe})$	2.692(1)	2.75
$d(\text{Fe}-\mu\text{S})$	2.2001(15)–2.2047(16)	2.20 – 2.23
$d(\text{Fe}-\text{S})$	2.278(2) – 2.2965(15)	2.21 – 2.34
$d(\text{Fe}-\text{N}_{\text{His}})$	2.009(4)	2.22 – 2.18
$(\text{S}_{\text{Cys}}\text{-Fe-S}_{\text{Cys}})$	103.81(6)	103.2 (av)
$(\text{N}_{\text{His}}\text{-Fe-S}_{\text{Cys}})$	95.64(12)	98.8 – 99.9
$(\text{Fe}-\mu\text{S}-\text{Fe})$	75.19(5) av	76.7 (av)

## 5.3. Spectroscopy in the Solid State and in Solution

### 5.3.1 Spectroscopy in the Solid State

A zero-field Mößbauer spectrum of solid  $\mathbf{26}(\text{NEt}_4)_2$  was recorded at 80 K (Figure 5.2). The experimental spectrum was simulated with two doublets with relatively similar parameters,

which results in complete overlay of the two subspectra. One doublet with  $\delta = 0.28 \text{ mm s}^{-1}$  and  $\Delta E_Q = 0.77 \text{ mm s}^{-1}$  (blue subspectrum in Figure 5.2) most likely corresponds to the {SN} ligated  $\text{Fe}^{\text{III}}$  ion while the second doublet with  $\delta = 0.29 \text{ mm s}^{-1}$  and  $\Delta E_Q = 1.01 \text{ mm s}^{-1}$  (red subspectrum in Figure 5.2) probably corresponds to the {S<sub>2</sub>} ligated  $\text{Fe}^{\text{III}}$  ion. This assignment can be proposed based on comparison with the Mößbauer parameters of related homoleptic clusters  $\mathbf{4}^{2-}$  and  $\mathbf{27}^{2-}$  ( $\delta = 0.28 \text{ mm s}^{-1}$  and  $\Delta E_Q = 0.86 \text{ mm s}^{-1}$  in {S<sub>2</sub>} {S<sub>2</sub>} coordinated  $\mathbf{27}^{2-}$  and  $\delta = 0.27 \text{ mm s}^{-1}$  and  $\Delta E_Q = 0.81 \text{ mm s}^{-1}$  in {SN} {SN} coordinated  $\mathbf{4}^{2-}$ )<sup>[195]</sup> but cannot be established unambiguously.<sup>[192]</sup> An alternative fit of the Mößbauer spectrum of solid  $\mathbf{26}(\text{NEt}_4)_2$  can be proposed in which the two doublets show relatively similar quadrupole splittings ( $\Delta E_Q = 0.87$  and  $0.89 \text{ mm s}^{-1}$ ) but differ in their isomer shifts ( $\delta = 0.22$  and  $0.34 \text{ mm s}^{-1}$ , respectively). However, considering Mößbauer spectra of related clusters  $\mathbf{27}(\text{NEt}_4)_2$  and  $\mathbf{4}(\text{NEt}_4)_2$ , the isomer shift does not seem to be largely affected by replacing thiolate for N-donating ligands. The spectrum of  $\mathbf{26}(\text{NEt}_4)_2$  is thus probably best described by two doublets with similar isomer shifts and different quadrupole splitting.

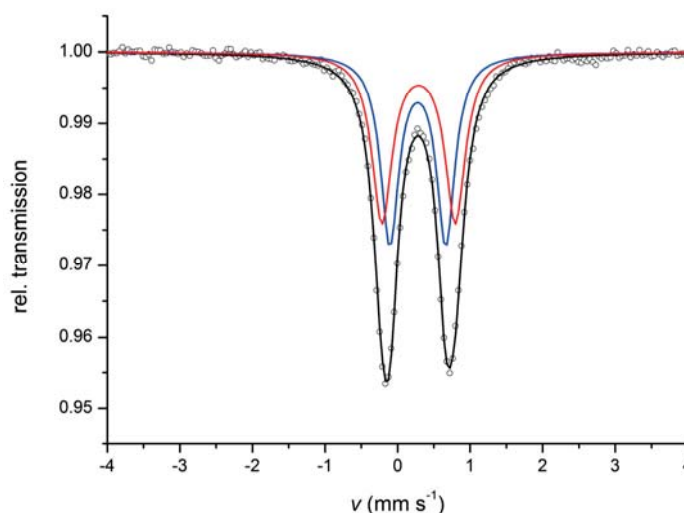


**Figure 5.2:** Zero-field Mößbauer spectrum of solid  $\mathbf{26}(\text{NEt}_4)_2$  at 80 K. Simulation led to the parameters summarized in the text.<sup>[192]</sup>

SQUID magnetometry of solid  $\mathbf{26}(\text{NEt}_4)_2$  confirmed an  $S = 0$  ground state due to strong antiferromagnetic coupling of the two high spin  $\text{Fe}(\text{III})$  centers with a coupling constant of  $J = -123 \text{ cm}^{-1}$  (Figure 5.3). This value is significantly smaller than the coupling observed in diferric homoleptic  $\mathbf{4}^{2-}$ . The reason for the decrease in the strength of the antiferromagnetic coupling is not clear but may be due to differences in geometrical parameters, such as the angle  $\text{Fe}-\mu\text{S}-\text{Fe}$  which increases from  $74.1$  to  $75.2^\circ$  when going from the homoleptic to the heteroleptic model system, or to the increasing number of thiolate ligands. Experimental data for  $\mathbf{26}(\text{NEt}_4)_2$  were modelled to the appropriate

Heisenberg-Dirac-van-Vleck (HDvV) spin Hamiltonian for isotropic exchange coupling and Zeeman splitting:

$$\hat{H} = -2J\hat{S}_1 \cdot \hat{S}_2 + g\mu_B(\vec{S}_1 + \vec{S}_2)B$$

Simulation of the experimental magnetic data was performed with the *julX* program. Temperature-independent paramagnetism (*TIP*) and a Curie-behaved paramagnetic impurity (*PI*) with spin  $S = 5/2$  were included according to  $\chi_{\text{calc}} = (1 - PI) \cdot \chi + PI \cdot \chi_{\text{mono}} + TIP$ .

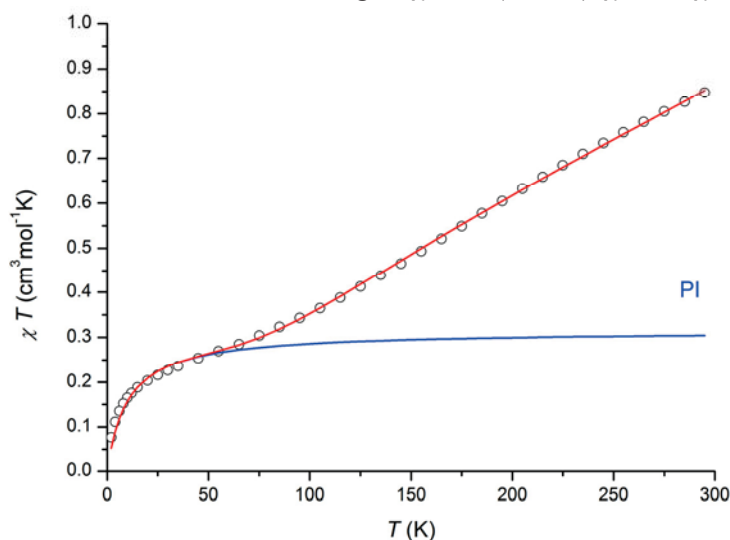


**Figure 5.3:** Temperature dependence of  $\chi_M T$  for heteroleptic **26**(NEt<sub>4</sub>)<sub>2</sub>. The solid red line represents the calculated fit with the parameters  $g = 1.90$  (fixed),  $J = -124 \text{ cm}^{-1}$ ,  $PI = 7.2 \%$  and  $TIP = 3520 \cdot 10^{-6} \text{ cm}^3 \text{ mol}^{-1}$ . The solid blue line represents traces of paramagnetic impurity (7.2 %).<sup>[192]</sup>

### 5.3.2 Spectroscopy in Solution

The <sup>1</sup>H-NMR spectrum of **26**(NEt<sub>4</sub>)<sub>2</sub> was obtained in MeCN-d<sub>3</sub> at 243 K and coupling between neighboring protons was observed by <sup>1</sup>H COSY NMR spectroscopy (Figures 5.4 and 5.5). Based upon the observed couplings and on comparison with related [2Fe–2S] cluster **4**<sup>2-</sup> and **13**<sup>2-</sup>, the resonances in the <sup>1</sup>H NMR spectrum were assigned to the corresponding protons (Figure 5.6). A number of couplings is visible in the region of 8.70–9.00 ppm/ 3.15–3.35 ppm, which arise from couplings within the aromatic rings of the bis(thiolate)ligand. Both aromatic rings are chemically inequivalent but relatively similar. An exact assignment of the resonances to the individual protons in these two rings is thus rather challenging and can only be preliminary at this point. The resonance corresponding to the proton closest to the paramagnetic Fe<sup>III</sup> center is not visible, likely due to strong broadening. Similar behavior has been observed in related benzimidazole ligated clusters **4**<sup>2-</sup>, **12a**<sup>2-</sup>, **12b**<sup>2-</sup>, and **13**<sup>2-</sup>.<sup>[147,148,150,192]</sup>

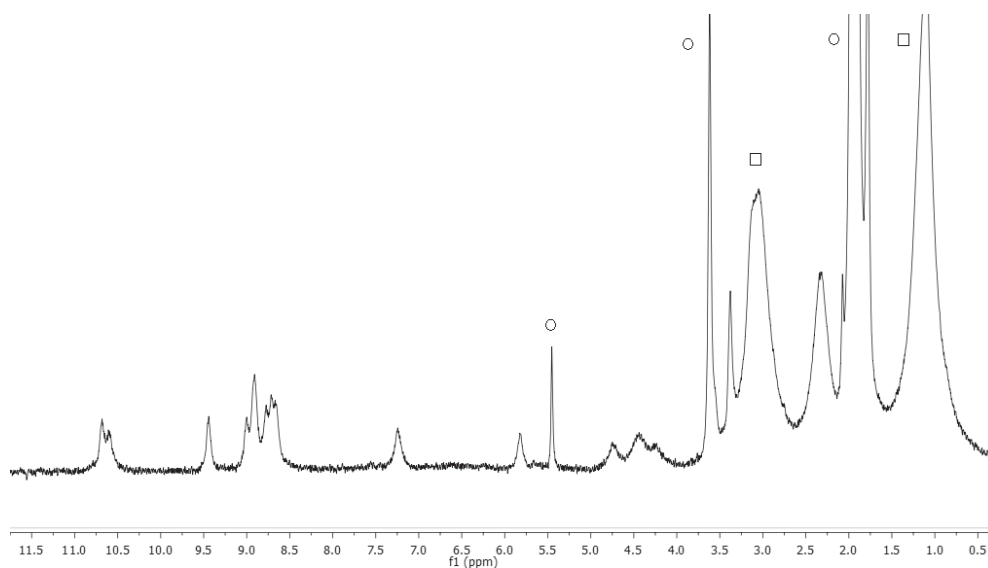


**Figure 5.4:**  $^1\text{H}$  NMR spectrum of  $26(\text{NEt}_4)_2$  in  $\text{MeCN-d}_3$  at 243 K. Signals from residual solvent (O), and counterions  $\text{NEt}_4^+$  (□) are labelled.<sup>[192]</sup>

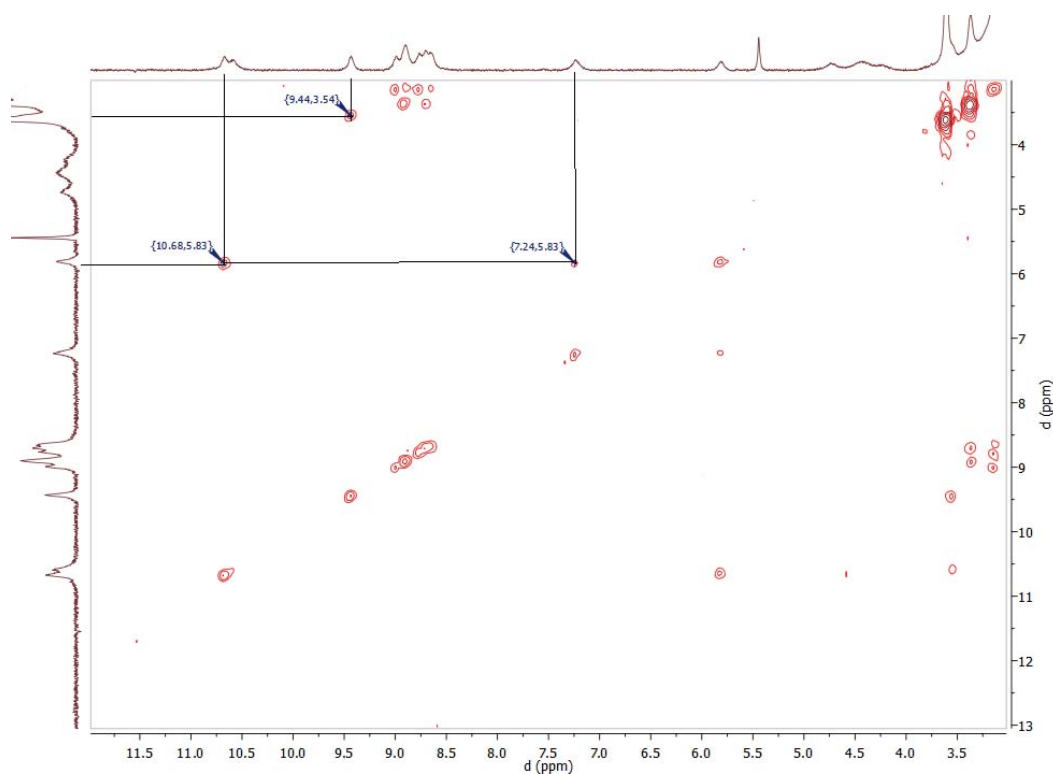


**Figure 5.5:**  $^1\text{H}$  COSY spectrum of  $26(\text{NEt}_4)_2$  in  $\text{MeCN-d}_3$  at 243 K.

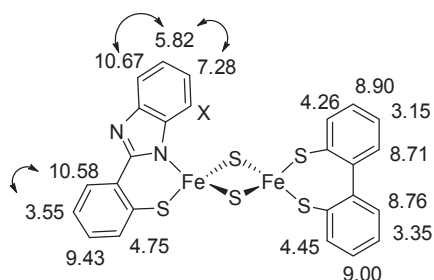


**Figure 5.6:** Assignment of the observed resonance  $\delta$  (ppm) to the respective protons in cluster  $\mathbf{26}(\text{NEt}_4)_2$ . Arrows mark couplings between protons as observed in  $^1\text{H}$  COSY NMR. The proton, for which no resonance can be observed in  $^1\text{H}$  NMR spectrum is labeled X.

Electrochemical properties of  $\mathbf{26}(\text{NEt}_4)_2$  were studied by cyclic voltammetry in 0.25 M  $\text{NBu}_4\text{PF}_6$  solution in MeCN at  $-15^\circ\text{C}$ . The spectrum shows two cathodic redox events. The first one, occurring at  $-1.647\text{ V vs. Fc/Fc}^+$ , is attributed to the formation of mixed valent  $\mathbf{26}^{3-}$ , whereas the second redox event at  $-2.375\text{ V vs. Fc/Fc}^+$  indicates the formation of diferrous  $\mathbf{26}^{4-}$ . Both redox events are separated by 730 mV indicating that mixed valent species  $\mathbf{26}^{3-}$  should be chemically accessible and relatively stable. The peak-to-peak distance for the first reduction is about 63 mV, which shows that the reduction is a reversible process. The  $E_{1/2}$  values of both redox events are shifted cathodically by about 150 mV in comparison to the homoleptic model  $\mathbf{4}(\text{NEt}_4)_2$  due to the presence of the relatively hard thiolate donor functions. Since these are strong donor ligands, the Fe(III) state is favored over Fe(II) making the reduction of the cluster more difficult, which results in a lower *i.e.* more negative redox potential.<sup>[192]</sup>

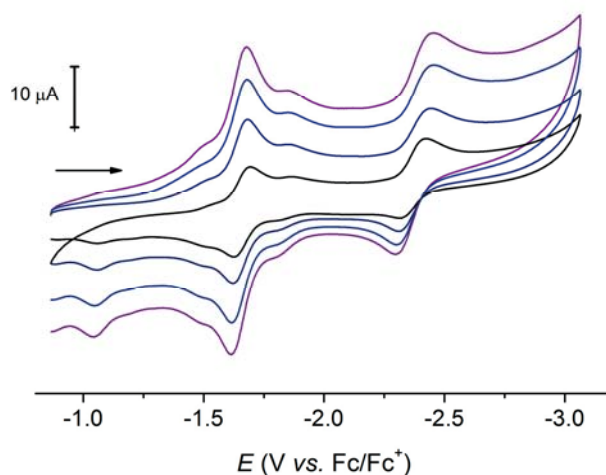


**Figure 5.7:** Cyclic voltammogram of  $\mathbf{26}(\text{NEt}_4)_2$  recorded at  $-15^\circ\text{C}$  in MeCN/ 0.25 M  $\text{Bu}_4\text{PF}_6$  vs.  $\text{Fc/Fc}^+$ .  $E_{1/2} = -1.647\text{ V}$  and  $E_{1/2} = -2.375\text{ V}$  at various scan rates ( $\nu = 50, 100, 200, 500\text{ mV s}^{-1}$ ).<sup>[192]</sup>

## 5.4 Mixed Valent Cluster $26^{3-}$ : Spectroscopy in Solid State and in Solution

Mixed valent cluster  $26^{3-}$  can be prepared by addition of 1.0 eq  $\text{CoCp}^*_2$  ( $E_{1/2}$  vs.  $\text{Fc}/\text{Fc}^+ = -1.91$  V)<sup>[197]</sup> in MeCN at  $-30$  °C. Solid material was obtained by addition of diethyl ether at  $-30$  °C. One-electron reduction of  $26^{2-}$  is accompanied by changes in the UV-vis spectrum, which are very similar to those observed for related homoleptic model  $4^{2-}$  (chapter 3.4.2). An overall decrease in intensity is observed upon formation of the mixed valent species, the characteristic bands at 422, 455, and 550 nm decrease and a new band at 565 nm is formed (Figure 5.8). These changes can be reversed by addition of  $[\text{CoCp}_2]\text{PF}_6$  as a chemical oxidant ( $E_{1/2}$  vs.  $\text{Fc}/\text{Fc}^+ = -1.34$  V)<sup>[197]</sup>, which confirms the reversibility of the reduction process as observed in CV.<sup>[192]</sup>

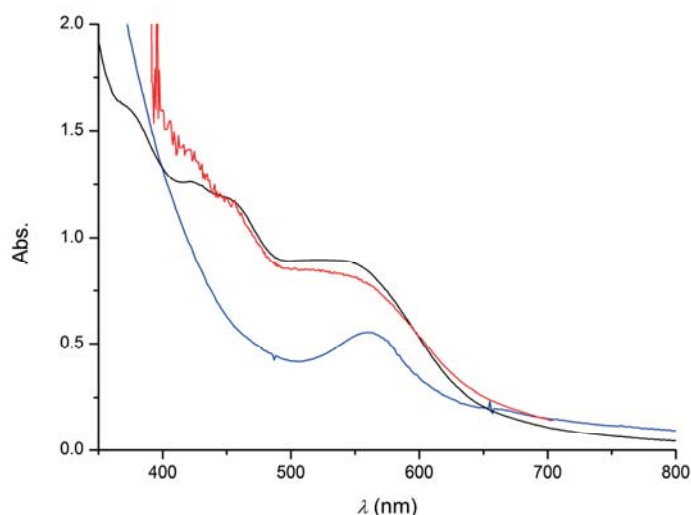


**Figure 5.8:** Visible absorption spectra of  $26(\text{NEt}_4)_2$  (black),  $26(\text{NEt}_4)_2(\text{CoCp}^*_2)$  prepared *in situ* by addition of  $\text{CoCp}^*_2$  (blue) and after re-oxidation by addition of  $[\text{CoCp}_2]\text{PF}_6$  (red) in MeCN.<sup>[192]</sup>

An EPR spectrum of  $26^{3-}$  generated *in situ* was recorded at 160 K in frozen solution in MeCN. It shows a rhombic signal typical for mixed valent [2Fe–2S] clusters and confirms an  $S = 1/2$  ground state. Simulation of the experimental spectrum yielded the following parameters:  $g_1 = 2.005$ ,  $g_2 = 1.932$ ,  $g_3 = 1.875$  and  $g_{\text{av}} = 1.937$ . The average  $g$ -value of  $g_{\text{av}} = 1.937$  is lower than  $g_{\text{av}} = 1.941$  observed in  $4^{3-}$ . It has been shown by Mousesca and Orio that a lower  $g_{\text{av}}$  in mixed valent [2Fe–2S] clusters corresponds to more pronounced localization of the unpaired electron (see chapter 1.6).<sup>[183]</sup> A higher localization in the heteroleptic mixed valent cluster may be rationalized by considering the cluster's asymmetric ligation pattern. While one iron center is coordinated in an  $\{\text{S}_4\}$  environment, the other iron center features  $\{\text{NS}_3\}$  coordination. N-donation on one of the iron centers favors localization

of the unpaired electron on this {NS<sub>3</sub>} coordinated site, since N-donating ligands are better suited to stabilize the lower oxidation state than the dithiolate ligand.

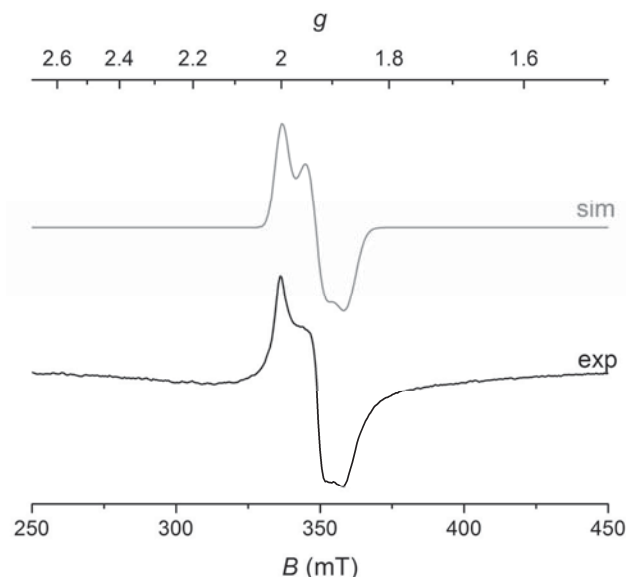


**Figure 5.9:** EPR spectrum of  $26^{3-}$  prepared by addition of 1.03 eq  $\text{CoCp}^*_2$  to a solution of  $26(\text{NEt}_4)_2$  in MeCN; recorded in frozen MeCN at 160 K. The grey line is a simulation yielding  $g_1 = 2.005$ ,  $g_2 = 1.932$ ,  $g_3 = 1.875$  and  $g_{\text{av}} = 1.937$ .<sup>[192]</sup>

The  $^1\text{H}$  NMR spectrum of  $26^{3-}$  reflects the cluster's paramagnetic ground state with 15 resonances spanning a total range of  $\Delta\delta = 18$  ppm, of which two are found at negative chemical shift values ( at  $-5.9$  and  $-6.1$  ppm), along with some decomposition products and signals corresponding to  $\text{CoCp}^*_2$  (Figure 5.10).

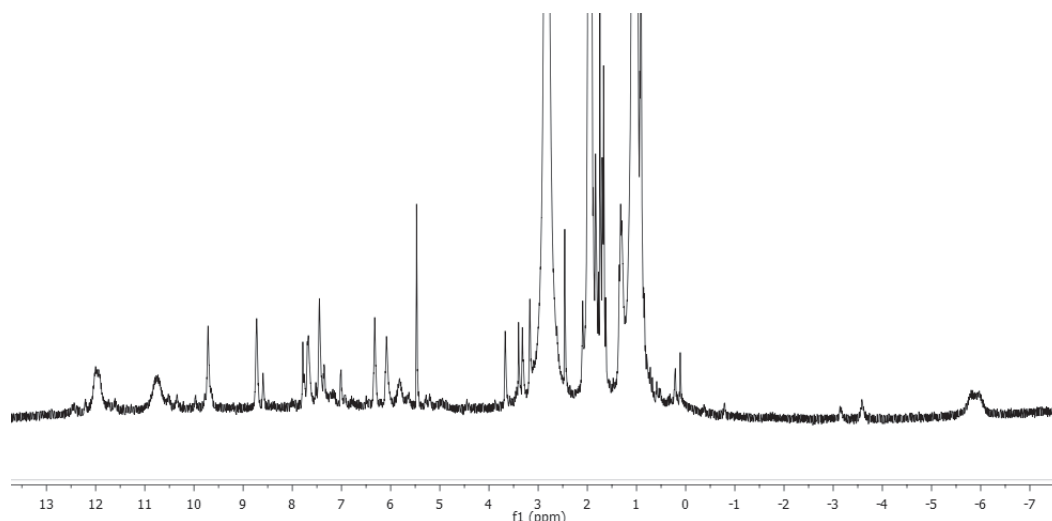


**Figure 5.10:**  $^1\text{H}$  NMR spectra of mixed valent  $26^{3-}$  in  $\text{MeCN-d}_3$  at 293 K, generated *in situ* by addition of 1.05 eq  $\text{CoCp}^*_2$  to a solution of  $26(\text{NEt}_4)_2$ .<sup>[192]</sup>

Solid material of  $\mathbf{26}(\text{NEt}_4)_2(\text{CoCp}^*_2)$  was obtained by addition of 1.03 eq  $\text{CoCp}^*_2$  to a solution of  $\mathbf{26}(\text{NEt}_4)_2$  in MeCN at  $-30\text{ }^\circ\text{C}$ . After 15 min the solvent was removed under reduced pressure. Zero-field Mößbauer spectra of solid  $\mathbf{26}(\text{NEt}_4)_2(\text{CoCp}^*_2)$  were recorded at 13 K, 80 K and 230 K (Figure 5.11). All three spectra show two distinct doublets corresponding to the presence of one high spin  $\text{Fe}^{\text{III}}$  center (red subspectra in figure 5.11) and one high spin  $\text{Fe}^{\text{II}}$  center (blue subspectra in figure 5.11), each in a tetrahedral coordination environment. The parameters obtained by simulation of the experimental spectra are summarized in table 5.2. The  $\text{Fe}^{\text{III}}:\text{Fe}^{\text{II}}$  ratio differs slightly from the expected 50:50 value depending on the temperature; this is likely due to a combination of the different temperature dependence of Lamb-Mößbauer factors for  $\text{Fe}^{\text{III}}$  and  $\text{Fe}^{\text{II}}$  and line broadening that most probably is caused by slow magnetic relaxation. In contrast to the behavior observed for mixed valent  $\mathbf{4}(\text{NEt}_4)(\text{CoCp}^*_2)_2$  (chapter 3.4.1) the two distinct doublets are still visible at 230 K. These findings support the conclusions drawn from EPR spectroscopy since they are consistent with a more pronounced localization of the unpaired electron in the asymmetric heteroleptic model, which prevents fast electron hopping between the two iron sites on the Mößbauer time scale.<sup>[192]</sup>

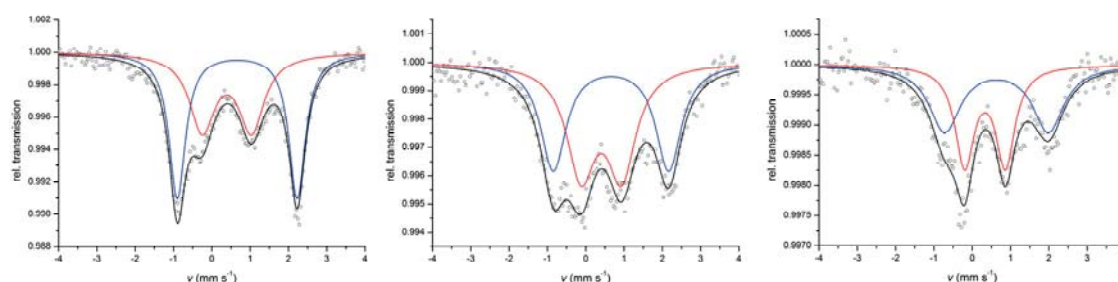


**Figure 5.11:** Mößbauer spectra of solid  $\mathbf{26}(\text{NEt}_4)_2(\text{CoCp}^*_2)$  at 13 K (left), 80 K (middle) and 230 K (right). Simulation led to the parameters summarized in table 5.2.

**Table 5.2:** Mößbauer parameters for solid  $\mathbf{26}(\text{NEt}_4)_2(\text{CoCp}^*_2)$ .<sup>[192]</sup>

	13 K	80 K	230 K
$\delta(\text{mm s}^{-1})$	0.39	0.41	0.33
$\delta(\text{mm s}^{-1})$	0.66	0.66	0.63
$\Delta E_Q(\text{mm s}^{-1})$	1.29	1.06	1.06
$\Delta E_Q(\text{mm s}^{-1})$	3.13	3.01	2.71
fwhm ( $\text{mm s}^{-1}$ )	0.81	0.91	0.60
fwhm ( $\text{mm s}^{-1}$ )	0.52	0.81	0.98
$\text{Fe}^{\text{III}}:\text{Fe}^{\text{II}}$	44:56	53:47	48:52

## 5.5 Protonation of Diferric and Mixed Valent Clusters

### 5.5.1 Protonation of Diferric Cluster $26^{2-}$

Similar to related homoleptic cluster  $4^{2-}$ ,  $26^{2-}$  offers a potential protonation site on the benzimidazole-N of the S/N-donating ligand. Protonation was carried out with  $[\text{DMPH}]^+$  and the reaction was followed by UV-vis and  $^1\text{H}$  NMR spectroscopy. Addition of 1.0 eq  $[\text{DMPH}]\text{BF}_4$  leads to the formation of  $26\text{H}^-$ . Since only one benzimidazole ligand is present in the heteroleptic model, only one protonation event is possible and addition of more than 1.0 eq of  $[\text{DMPH}]\text{BF}_4$  led to no further changes in the UV-vis absorption spectra. Addition of DBU as a base afforded the initial spectrum proving the reversibility of the protonation process (Figure 5.12).<sup>[192]</sup>

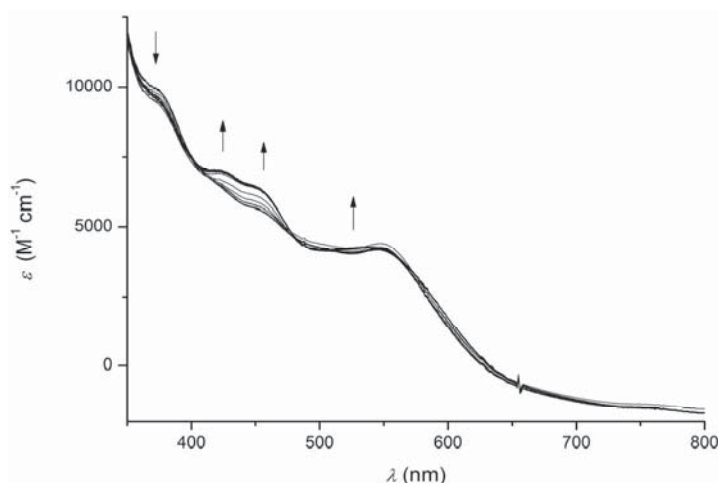


**Figure 5.12:** UV-vis absorption spectra for the titration experiment using  $26\text{H}^-$  (generated *in situ* by addition of 1.0 eq of  $[\text{DMPH}]\text{BF}_4$  to a solution of  $26(\text{NEt}_4)_2$  in MeCN) and DBU at  $-30\text{ }^\circ\text{C}$ . Each line represents the addition of 0.2 eq of DBU.<sup>[192]</sup>

The  $\text{p}K_a$  value of the protonated diferric cluster was determined *via* backtitration experiments using DBU.<sup>[201]</sup> According to the conservation of mass balance, a  $\text{p}K_a$  of = 23.7(2) was derived from a linearized plot of  $[\text{Fe}][\text{BH}]/[\text{FeH}]$  vs.  $[\text{B}]$  (Fe corresponds to the unprotonated cluster, BH to the protonated base, FeH to the protonated cluster and B to the free base, Figure 5.13). The reappearing band at 443 nm was used to quantify the amount of unprotonated cluster in the solution.

$$\text{p}K_a = \text{p}K_a(\text{BH}) - \log(K)$$

$$K = 4.28 \pm 1.43$$

$$\text{p}K_a = 24.34 - \log(4.28) = 23.7 \pm 0.2$$

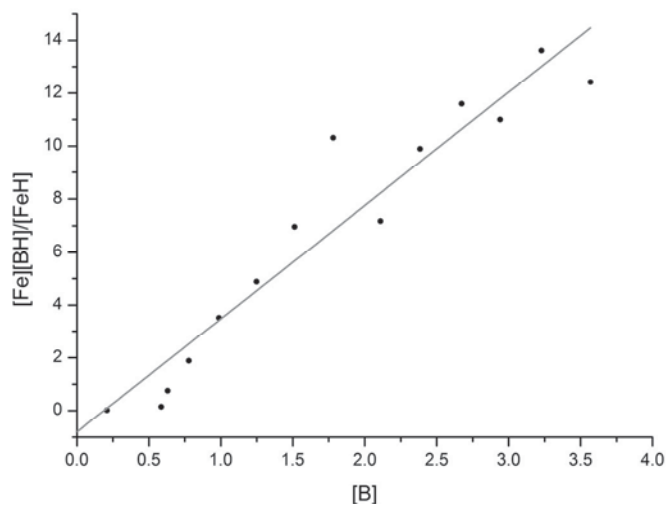


**Figure 5.13:** Plot of  $[\text{Fe}][\text{BH}]/[\text{FeH}]$  vs.  $[\text{B}]$  derived from backtitration experiments of  $26\text{H}^-$  (obtained by *in situ* protonation of  $26(\text{NEt}_4)_2$  by addition of 1.0 eq  $[\text{DMPH}]\text{BF}_4$  in MeCN solution) using DBU as the base, monitored by UV-vis spectroscopy at  $-30\text{ }^\circ\text{C}$ . The slope equals the equilibrium constant  $K$ .

In  $^1\text{H}$  NMR, protonation leads to a shift of all proton signals proportional to the ratio of protonated/ unprotonated species present in solution. This indicates that proton transfer is fast on the NMR time scale, similar to what was observed for homoleptic cluster  $4\text{H}^-$  (chapter 3) and cluster  $12\text{bH}^-$ .<sup>[151,192]</sup> In fact, the system is found in a fast-exchange regime in which the exchange is too fast to be measured accurately by  $^1\text{H}$  NMR spectroscopy.<sup>[202,203]</sup> Since only one set of peaks is observed even in a mixture of both the protonated and unprotonated cluster, the self-exchange rate between these two species must be at least as high as the rate that is required to just achieve coalescence. This rate can be determined as:<sup>[151]</sup>

$$k_{\text{obs}} = \frac{\pi \cdot \Delta\delta}{\sqrt{2}}$$

The largest peak separation observed in the spectra of both species is 1.13 ppm for the resonance, which shifts from 5.66 ppm to 6.79 ppm (Figure 5.14 and 5.15). From this peak separation a rate constant  $k_{\text{obs}} = 1255\text{ s}^{-1}$  can be determined. Since the NMR experiments were performed at a concentration of  $c = 0.00163\text{ M}$ , this corresponds to a rate constant of  $7.7 \cdot 10^5\text{ M}^{-1}\text{ s}^{-1}$  at  $25\text{ }^\circ\text{C}$ . This value can be considered a conservative lower limit for the rate constant of proton self-exchange between  $26^{2-}$  and  $26\text{H}^-$ . A lower limit of  $10^4\text{ M}^{-1}\text{ s}^{-1}$  for the self-exchange between the protonated and unprotonated species has been reported for  $12\text{b}^{2-}/12\text{bH}^-$ .<sup>[151]</sup> For self-exchange between homoleptic clusters  $4^{2-}$  and  $4\text{H}^-$  a lower limit for the rate constant of  $1.9 \cdot 10^5\text{ M}^{-1}\text{ s}^{-1}$  was determined in chapter 3.5. Heteroleptic model  $26^{2-}/26\text{H}^-$  shows the largest shift of the resonances between the protonated and unprotonated species. However, the values determined by  $^1\text{H}$  NMR spectroscopy can only be considered as

lower limits for the actual rate of self-exchange. Whether the trend observed for these lower limits actually holds for the true self-exchange rates cannot be predicted.

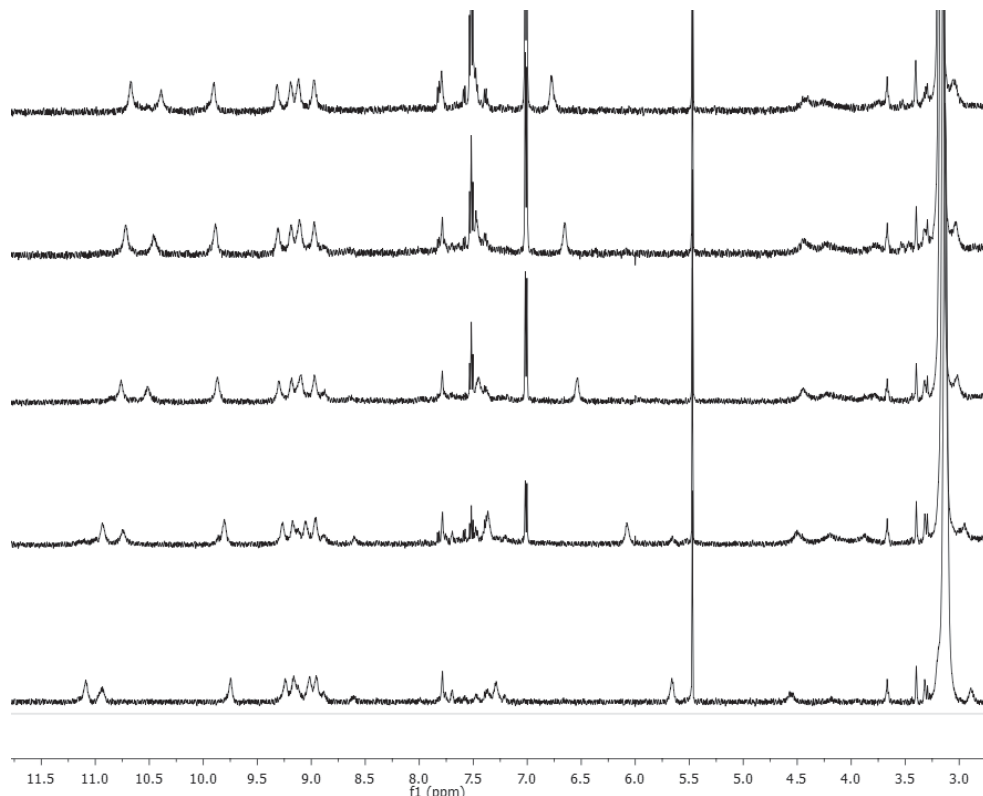


**Figure 5.14:**  $^1\text{H}$  NMR spectra in  $\text{MeCN-d}_3$  during stepwise protonation of  $26(\text{NEt}_4)_2$  at  $25\text{ }^\circ\text{C}$ . Addition of 0.25, 0.5, 0.8 and 1.0 eq  $[\text{DMPH}]\text{BF}_4$  (second from bottom to top) gradually shifts all resonances. Addition of 1.5 eq DBU restores the spectrum of the unprotonated cluster (bottom).<sup>[192]</sup>

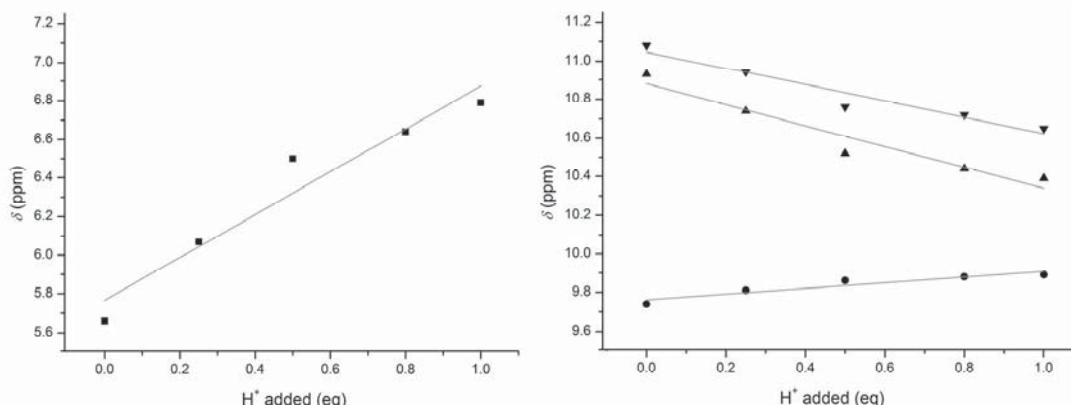


**Figure 5.15:** Chemical shifts  $\delta(\text{ppm})$  observed in  $^1\text{H}$  NMR vs. amount of protons added during protonation of  $26^{2-}$ , grey lines represent linear fits.

### 5.5.2 Protonation of Mixed Valent Cluster $26^{3-}$

Similar to protonation of  $4^{3-}$  (see chapter 3.5.2) protonation of mixed valent cluster  $26^{3-}$  proved to be difficult due to the low stability and solubility of the species involved.  $26^{3-}$  was prepared *in situ* by addition of 1.0 eq  $\text{CoCp}^*_2$  to a solution of  $26(\text{NEt}_4)_2$  in MeCN at  $-30\text{ }^\circ\text{C}$ . Protonation and deprotonation experiments were then performed at  $-25\text{ }^\circ\text{C}$  and monitored by UV-vis spectroscopy (Figure 5.16)

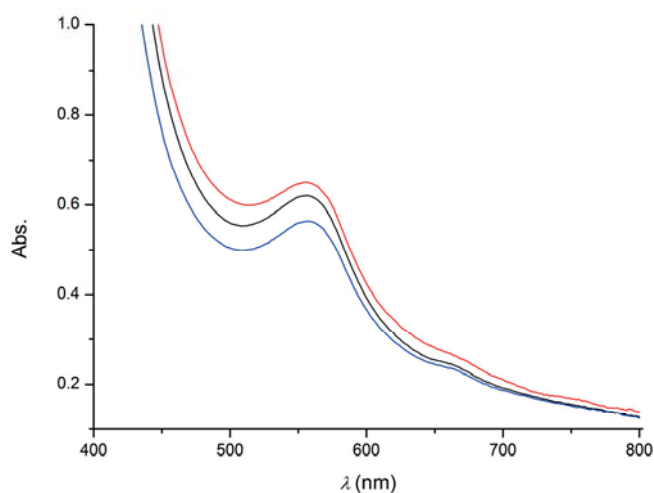


**Figure 5.16:** UV-vis absorption spectra of  $26^{3-}$  (black) in MeCN solution after addition of 1.0 eq  $[\text{DMPH}]^+$  (red) and subsequent addition of 4.0 eq DBU (blue) at 247 K.<sup>[192]</sup>

Addition of 1.0 eq  $[\text{DMPH}]\text{BF}_4$  to form protonated mixed valent cluster  $26\text{H}^{2-}$  only led to minor changes in the visible absorption spectrum of the cluster namely an overall increase in intensity and a slight broadening of the band at 565 nm and broadening of the shoulder at 670 nm. Subsequent addition of DBU in order to deprotonate  $26\text{H}^{2-}$  led to a decrease in intensity and the weak band at 670 nm reappeared. The overall intensity decreased after the protonation and deprotonation experiment to about 90 % of the initial intensity, which is attributed to decomposition of the cluster. Since the changes observed in UV-vis are not significant, it cannot be established unambiguously whether protonation of mixed valent  $26^{3-}$  is a reversible process.

The redox potential of the protonated cluster was studied by cyclic voltammetry.  $26(\text{NEt}_4)_2$  was recorded at  $-15\text{ }^\circ\text{C}$  in 0.25 M  $\text{NBU}_4\text{PF}_6$  solution in MeCN. Addition of 0.9 eq  $[\text{DMPH}]\text{BF}_4$  led to a shift of the cathodic peak potential of the first redox wave by  $-235\text{ mV}$  which corresponds to an  $E_{1/2} = -1.407\text{ vs. Fc/Fc}^+$  for protonated cluster  $26\text{H}^-$  assuming that a shift in peak potential directly translates into an equal shift of  $E_{1/2}$ . However, reversibility of the redox process is partially lost. Since the intensity of the observed waves was relatively low and the waves were rather broad, the first derivative of the current was used to determine the

peak position of the waves more accurately. Subsequent addition of DBU did not lead to complete reversion of these changes (Figure 5.17).

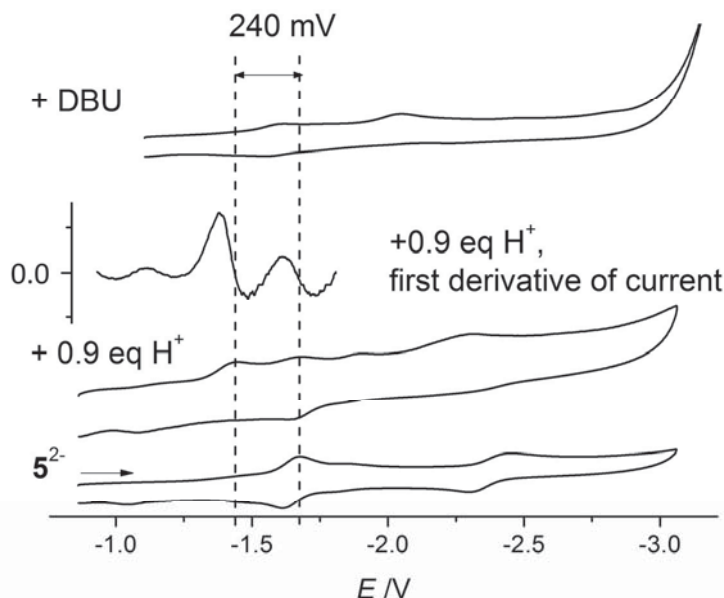


**Figure 5.17:** Effect of protonation on cyclic voltammograms of  $26(\text{NEt}_4)_2$  in 0.25 M  $\text{NBu}_4\text{PF}_6$  in MeCN at  $-15\text{ }^\circ\text{C}$  vs.  $\text{Fc}/\text{Fc}^+$  at a scan rate of  $400\text{ mV s}^{-1}$ . The first reduction of  $26^{2-}$  (bottom) is shifted upon addition of 0.9 eq of acid (middle); addition of DBU partially restores the initial spectrum (top).<sup>[192]</sup>

The observed shift is in good agreement to shifts typically reported for protonation of [2Fe–2S] clusters featuring benzimidazole ligands, which are 230 mV and 245 mV in related clusters  $13^{2-}$  and  $12b^{2-}$ , respectively. The shift observed upon protonation of mitoNEET proteins was reported to be 200 mV.<sup>[100]</sup> Protonation of the benzimidazole moiety turns the ligand from a dianionic into a monoanionic ligand. This monoanionic ligand is better suited for stabilizing a lower oxidation state (ferrous iron) and thus makes reduction of the cluster easier to achieve, which is reflected by an anodically shifted (*i. e.* less negative) reduction potential. Since the initial peak position could not be completely restored upon deprotonation, it cannot be unambiguously established whether protonation is indeed reversible. Cyclic voltammetry provides some indication of protonation occurring on the nitrogen atoms in the ligand's backbone rather than on the bridging sulfides, but does not yield final proof. However, based upon comparison with related cluster, protonation on the backbone of the benzimidazole moieties will be assumed in the following chapter.



## 5.6 Conclusion

In this chapter a first structural and spectroscopic model **26**<sup>2-</sup> for the Cys<sub>3</sub>His coordinated [2Fe–2S] cluster in mitoNEET proteins is presented. It mimics the special {SN}{S<sub>2</sub>} coordination environment and features a possible protonation site in the backbone of the ligand, similar to the naturally occurring histidine ligand. The synthetic model emulates the structural and spectroscopic features of the natural cofactor very well. EPR and Mößbauer spectroscopy have provided insight into a significantly more pronounced localization of the unpaired electron in the cluster's mixed valent state when compared to related homoleptic cluster **4**<sup>2-</sup>. Additionally, **26**<sup>2-</sup> can be protonated, presumably on the ligand's benzimidazole moiety, and a p*K*<sub>a</sub> value of 23.7(2) was determined by titration experiments. Moreover, proton transfer between clusters was shown to be fast on the NMR time scale. In cyclic voltammetry, a shift of 235 mV was observed upon protonation, which compares very well with a shift of 200 mV observed in mitoNEET proteins but reversibility of the redox process is partially lost upon protonation and the protonation itself appears not to be completely reversible. These characteristics make **26**<sup>2-</sup> a promising candidate to investigate a possible involvement of mitoNEET type [2Fe–2S] clusters in PCET reactions. These studies will be presented in chapter 7.



---

## 6 Temperature Dependent Electrochemistry in a Series of [2Fe–2S] Clusters

### 6.1 Introduction

Temperature dependent electrochemistry is an easily accessible tool to obtain valuable information about the thermodynamics and kinetics of redox processes. However, this method has been widely underappreciated in the investigation of synthetic bioinorganic model systems.<sup>[209]</sup> The free energy change  $\Delta G^\circ$  of a redox process is related to the difference in electrochemical potential  $\Delta E^\circ$  of the two reaction partners which can be determined as  $E_{1/2}$  from cyclic voltammetry *via* the Faraday constant  $F$  ( $F = 96\,485\text{ C mol}^{-1}$ ) and the number of electrons  $n$  transferred in this process:

$$\Delta G^\circ = -nF\Delta E^\circ$$

This free energy change is temperature dependent and is comprised of contributions from the changes in entropy  $\Delta S^\circ$  and enthalpy  $\Delta H^\circ$ :

$$\Delta G^\circ = \Delta H^\circ - T\Delta S^\circ$$

The changes in entropy  $\Delta S^\circ$  and enthalpy  $\Delta H^\circ$  associated with a redox process can be calculated according to:

$$\Delta S^\circ = nF \left( \frac{\partial E}{\partial T} \right)$$

$$\Delta H^\circ = nF \left[ T \left( \frac{\partial E}{\partial T} \right) - E \right]$$

Measuring the potential at which a redox process occurs at various temperatures thus allows for the determination of these thermodynamic parameters.<sup>[209,210]</sup> However, “absolute” thermodynamic values such as  $\Delta G^\circ$ ,  $\Delta H^\circ$ , and  $\Delta S^\circ$  obtained from electrochemical measurements have to be considered with great care. In all electrochemical measurements, no absolute potentials but rather potential differences in relation to a given reference electrode are measured. Therefore the thermodynamics of the redox partner *i.e.* of the reference electrode have to be considered as well.<sup>[211]</sup> The absolute potential of the standard hydrogen electrode (SHE) at 25 °C has been determined by a variety of groups using a number of different techniques and IUPAC now recommends working with a value of

$E^\circ(\text{SHE}) = (4.44 \pm 0.02) \text{ V}$ .<sup>[212–214]</sup> For the determination of the entropy  $\Delta S^\circ$  only the change of the redox potential with varying temperature is considered, thus no absolute potentials are needed to calculate an absolute value of  $\Delta S^\circ$ . However, these calculations must assume that the electrode set-up used in the experiments does not show any temperature-dependent behavior itself.<sup>[209]</sup> No data on the temperature dependence of the glassy carbon and platinum electrodes exists. However, their potential can be assumed as relatively invariant upon changes in temperature. In conclusion, even though absolute values determined from them have to be treated with great care, obtaining temperature dependent electrochemical data is most useful to compare general trends within a series of compounds measured under the same conditions, and to derive relationships between their structural and electrochemical features.

Temperature dependent electrochemical measurements have been used in studies of biological electron transfer proteins such as cytochrome c, in which they have revealed a conformational change of cytochrome c<sub>533</sub> from *Bacillus pasteurii* at higher temperature ( $T > 35^\circ\text{C}$ ) and shed light on the pH dependent nature of the redox process.<sup>[215–217]</sup> A number of iron sulfur proteins have also been investigated by this method including mononuclear rubredoxines, Rieske [2Fe–2S] clusters, and [4Fe–4S] ferredoxines.<sup>[218–220]</sup> All these clusters show a linear temperature dependency of their reduction potentials, both in their protonated and unprotonated forms. However, studies on Rieske cluster from *Thermus thermophilus* have shown that the entropy change associated with one-electron reduction is smaller in case of the unprotonated form in comparison to the protonated species ( $\Delta S^\circ = -(35 \pm 2) \text{ J mol}^{-1} \text{ K}^{-1}$  at pH 14 and  $\Delta S^\circ = -(56 \pm 8) \text{ J mol}^{-1} \text{ K}^{-1}$  at pH 7).<sup>[83]</sup> These studies have also emphasized the role of solvent ordering effects. An increase in overall charge upon reduction entails a higher degree of solvent ordering. As a consequence, clusters that are more accessible to solvent molecules show higher absolute values for the entropy associated with one-electron reduction.<sup>[83]</sup>

Synthetic efforts reported previously<sup>[139,148]</sup> and work presented in this thesis have established a series of synthetic [2Fe–2S] clusters with varying ligation (Figure 6.1). Both the number of N- and S- donors as well as the degree of localization in the mixed valent form are varied throughout this series, while the overall coordination number on each iron site as well as the fundamental coordination motifs are kept constant. The number of N- donors decreases from four in **12a**<sup>2-</sup> to only one in **26**<sup>2-</sup>. The degree of localization increases when changing from homoleptic to heteroleptic ligation and is proposed to be at a maximum in Rieske model **13**<sup>2-</sup> based on Mößbauer and EPR spectroscopy. Temperature dependent electrochemical measurements of this series of clusters can provide valuable insight into the effect of asymmetric ligation and alternative ligands on the redox properties of iron sulfur clusters relevant in biological electron transfer reactions.

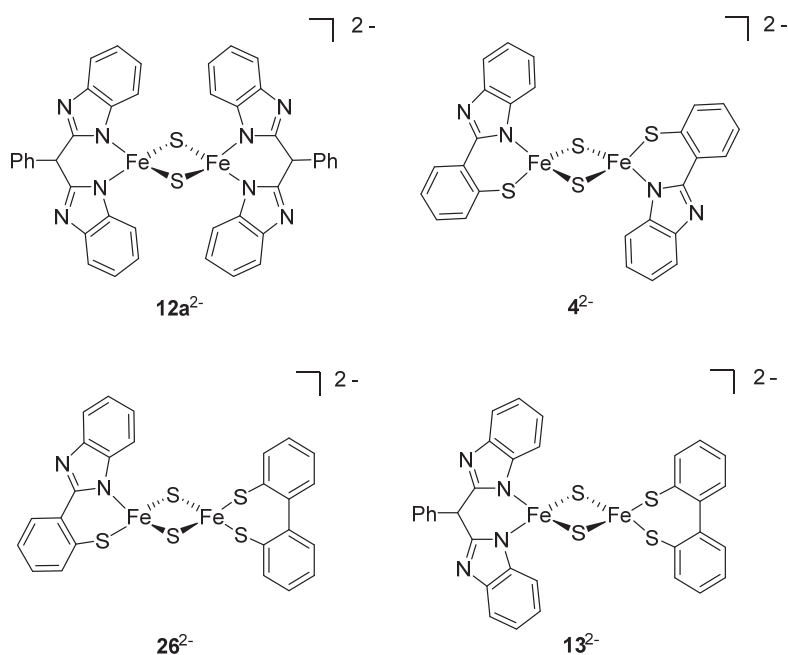


**Figure 6.1:** A series of synthetic [2Fe–2S] clusters studied by temperature dependent electrochemistry.

## 6.2 Determination of Reaction Entropy of Electrochemical One Electron Reduction

Cyclic voltammograms of all four [2Fe–2S] clusters were measured at variable temperatures in a range of about 40 K (–15 °C to +25 °C) in a 0.1 M NBu<sub>4</sub>PF<sub>6</sub> solution in MeCN. Three independent runs were performed for each compound and ferrocene was added for referencing at the end of each run (details are given in section 12.4).

In the homoleptic {N<sub>2</sub>} {N<sub>2</sub>} coordinated cluster **12a**<sup>2–</sup> a relatively small shift in potential of about 20 mV was observed when lowering the temperature from 25 °C to –15 °C (Figure 6.2). The reduction potential is shifted to a higher value, which indicates that reduction of the cluster is more easily achieved at lower temperatures. The observed reduction potential  $E_{1/2}$  shows a linear dependence on the chosen temperature  $T$  and a linear fit yields the slope  $\delta E/\delta T$  from which the entropy change  $\Delta S^\circ$  associated with one electron reduction of the cluster can be calculated (Figure 6.3). Three independent runs yielded a slope of  $\delta E/\delta T = -(5.34 \pm 0.73) \cdot 10^{-4} \text{ V K}^{-1}$  and thus a reaction entropy of  $\Delta S^\circ = -(51.5 \pm 7.1) \text{ J mol}^{-1} \text{ K}^{-1}$ .

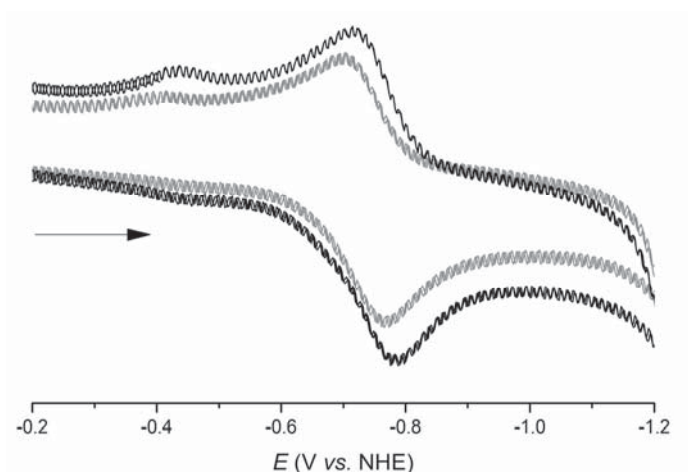


**Figure 6.2:** Cyclic voltammogram for homoleptic model  $12a^{2-}$  at  $-15\text{ °C}$  (grey) and  $25\text{ °C}$  (black) shows only small changes in  $E_{1/2}$  (V vs. NHE) upon lowering the temperature.

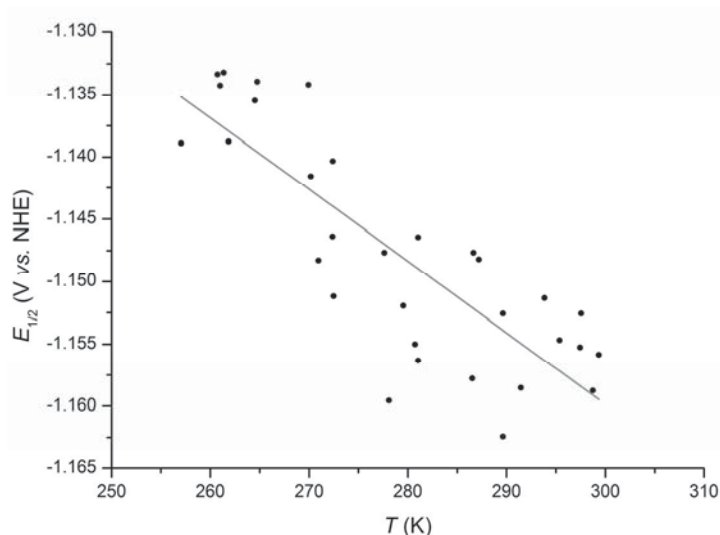


**Figure 6.3:** Temperature dependence of  $E_{1/2}$  (V vs. NHE) for homoleptic model  $12a^{2-}$ . A linear fit (grey) gives a slope of  $\delta E/\delta T = -(5.34 \pm 0.73) \cdot 10^{-4} \text{ V K}^{-1}$ .

In the homoleptic {SN} {SN} coordinated cluster  $4^{2-}$  the changes in reduction potential upon varying the temperature are even smaller. A total shift of 10 mV is observed when lowering the temperature from  $25\text{ °C}$  to  $-15\text{ °C}$  (Figure 6.4). Consequently, a very small entropy change is associated with one electron reduction of the cluster. An average slope of  $\delta E/\delta T = -(2.28 \pm 0.25) \cdot 10^{-4} \text{ V K}^{-1}$  was obtained from the linear fit (Figure 6.5) of three independent runs and thus an entropy change of  $\Delta S^\circ = -(21.9 \pm 2.4) \text{ J mol}^{-1} \text{ K}^{-1}$  was determined.

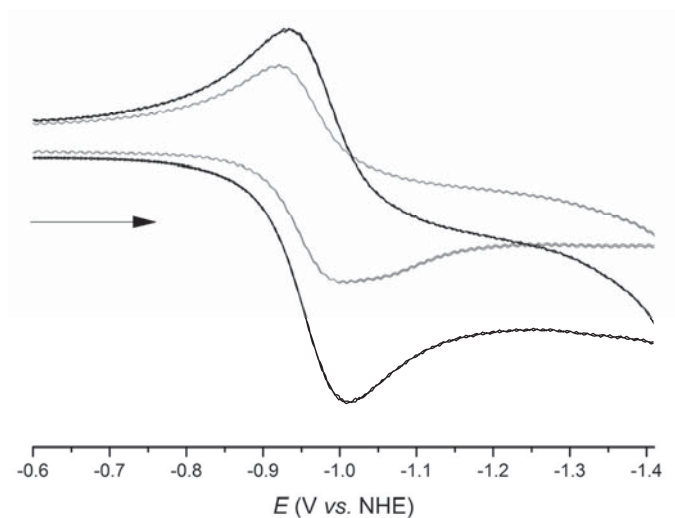


**Figure 6.4:** Cyclic voltammogram for homoleptic model  $4^{2-}$  at  $-15\text{ }^{\circ}\text{C}$  (grey) and  $25\text{ }^{\circ}\text{C}$  (black) shows only small changes in  $E_{1/2}$  (V vs. NHE) upon lowering the temperature.

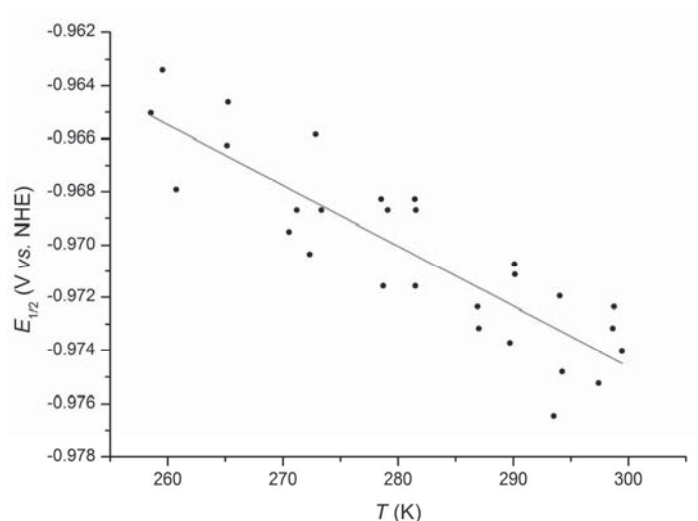


**Figure 6.5:** Temperature dependence of  $E_{1/2}$  (V vs. NHE) for homoleptic model  $4^{2-}$ . A linear fit (grey) yields a slope of  $\delta E/\delta T = -(2.28 \pm 0.25) \cdot 10^{-4} \text{ V K}^{-1}$ .

Heteroleptic mitoNEET model  $26^{2-}$  shows a stronger dependency of the observed  $E_{1/2}$  reduction potential on temperature than the two homoleptic models described above. The potential  $E_{1/2}$  for the first reduction is shifted by about 45 mV (Figure 6.6). This is about four times larger than the shift observed in related homoleptic model  $4^{2-}$ . The average slope of a linear fit of the temperature dependence of  $E_{1/2}$  was determined as  $\delta E/\delta T = -(9.25 \pm 2.4) \cdot 10^{-4} \text{ V K}^{-1}$  (Figure 6.7). From this value an entropy change of  $\Delta S^{\circ} = -(89.2 \pm 23.5) \text{ J mol}^{-1} \text{ K}^{-1}$  was calculated.

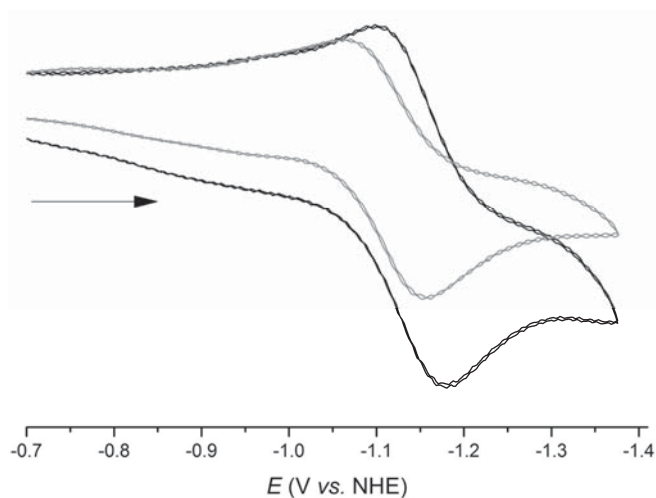


**Figure 6.6:** Cyclic voltammogram for heteroleptic model  $26^{2-}$  at  $-12\text{ °C}$  (grey) and  $20\text{ °C}$  (black) shows a shift in  $E_{1/2}$  (V vs. NHE) of about 45 mV upon lowering the temperature.

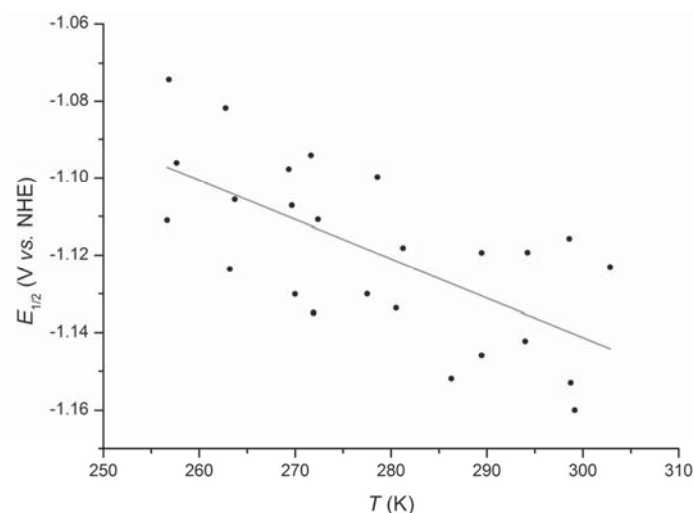


**Figure 6.7:** Temperature dependence of  $E_{1/2}$  (V vs. NHE) for heteroleptic model  $26^{2-}$ . A linear fit (grey) yields a slope of  $\delta E/\delta T = -(9.25 \pm 2.4) \cdot 10^{-4} \text{ V K}^{-1}$ .

In heteroleptic  $\{N_2\}\{S_2\}$  coordinated Rieske model  $13^{2-}$  a shift of about 55 mV can be observed upon lowering the temperature from  $25\text{ °C}$  to  $-16\text{ °C}$ . This is the biggest shift observed among the four clusters studied in this chapter. Consequently, the change in entropy associated with one electron reduction of  $13^{2-}$  is the largest of the values determined in this series of [2Fe–2S] clusters. An average slope  $\delta E/\delta T = -(10.9 \pm 0.9) \cdot 10^{-4} \text{ V K}^{-1}$  was determined from three independent runs and a value of  $\Delta S^\circ = -(105.2 \pm 8.6) \text{ J mol}^{-1} \text{ K}^{-1}$  was calculated.

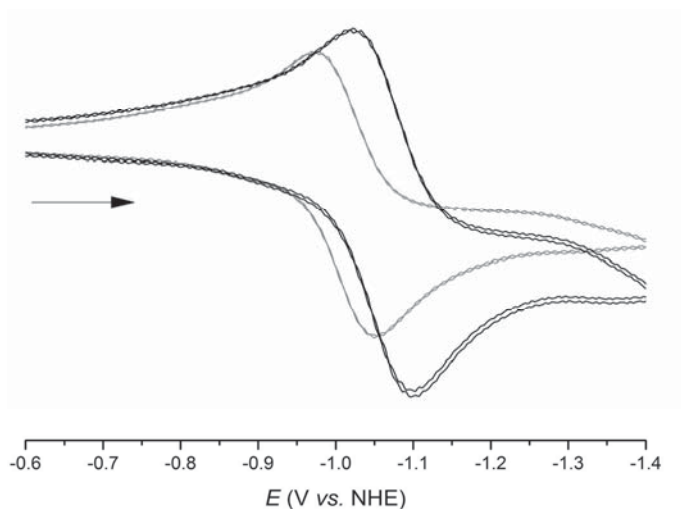


**Figure 6.8:** Cyclic voltammogram for heteroleptic model  $\mathbf{13}^{2-}$  at  $-16\text{ }^{\circ}\text{C}$  (grey) and  $25\text{ }^{\circ}\text{C}$  (black) shows a pronounced shift of 55 mV in  $E_{1/2}$  (V vs. NHE) upon lowering the temperature.

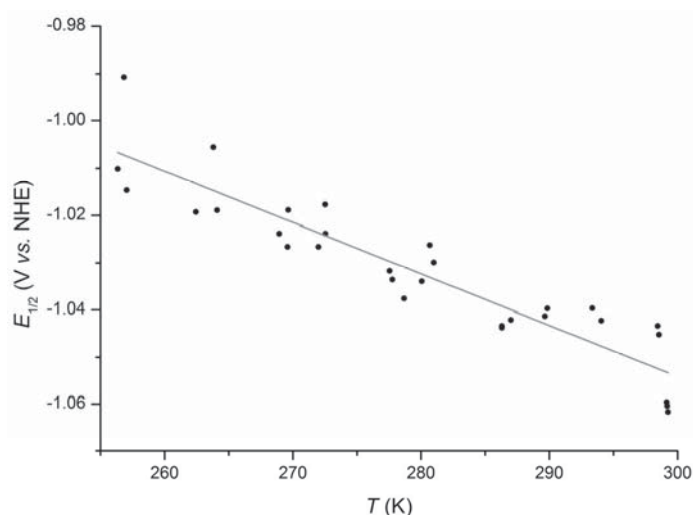


**Figure 6.9:** Temperature dependence of  $E_{1/2}$  (V vs. NHE) for heteroleptic model  $\mathbf{13}^{2-}$ . A linear fit (grey) yields a slope of  $\delta E/\delta T = -(10.9 \pm 0.9) \cdot 10^{-4}\text{ V K}^{-1}$ .

A comparison of the determined entropies (summarized in Table 6.1) reveals a general trend: The entropy change associated with one electron reduction of the [2Fe–2S] core increases significantly when moving from a symmetric homoleptic model to an asymmetric heteroleptic model. This difference in entropy can be due to both inner-sphere and outer-sphere reorganization. Outer-sphere reorganization, *i.e.* rearrangements of solvent molecules are expected to be very similar for all [2Fe–2S] clusters of this series, as all of them are dianionic in their diferric state and have ligands of comparable size. Due to the steric bulk of the phenyl group in the backbone of bis(benzimidazole) ligand  $[\mathbf{L}^{\text{NN}}]^{2-}$ , there may be larger outer-sphere rearrangements upon one-electron reduction of clusters  $\mathbf{12a}^{2-}$  and  $\mathbf{13}^{2-}$ , which may partly explain the larger values for the difference in entropy observed upon reduction of

$12a^{2-}$  when compared to  $4^{2-}$ . However, a larger molecular volume also decreases the overall charge density, causing weaker interactions between the charged molecule and the surrounding solvent. The trend observed for the differences in entropy can more easily be rationalized based upon differences in inner-sphere reorganizations. Thus bigger structural changes, *i.e.* a larger inner-sphere reorganization, accompany the reduction of the more asymmetrically ligated clusters. This is well in line with a stronger localization of the unpaired electron in the mixed valent form of these clusters as compared to homoleptic clusters. A more pronounced localization in the heteroleptic mixed valent clusters has been proposed based on EPR and Mößbauer spectroscopy (see chapters 3 and 5). Indeed, cluster  $13^{2-}$ , for which the highest degree of localization was proposed based on the relatively low  $g_{av}$  of 1.935, shows the largest negative value of the reaction entropy in electron transfer. In line with this rationalization, homoleptic cluster  $4^{2-}$  shows the lowest absolute value for  $\Delta S^\circ$ , *i.e.* the least pronounced inner-sphere rearrangements. Based on the observed indicators for a less pronounced localization of the unpaired electron in mixed valent homoleptic cluster  $12a^{3-}$ , an even smaller absolute value of the reaction entropy for one-electron reduction would have been anticipated. However, the inner-sphere reorganization is not only associated with structural changes within the [2Fe–2S] core but also in differences in bond lengths to the terminal capping ligands. As crystallographic data for both  $4(NEt_4)_2$  and  $4(NEt_4)(CoCp^*_2)_2$  as well as for  $12a(NEt_4)_2$  and  $12a(NEt_4)_2(CoCp^*_2)$  exist, the difference in metal-ligand bond lengths upon one-electron reduction can be examined. In  $\{N_2\}\{N_2\}$  ligated cluster  $12a(NEt_4)_2/12a(NEt_4)_2(CoCp^*_2)$ , the Fe–N bond length increases by an average of 0.0634 Å upon one-electron reduction, which is about 3.2 % of the total initial bond length.<sup>[149]</sup> In  $\{SN\}\{SN\}$  ligated cluster  $4(NEt_4)_2/4(NEt_4)(CoCp^*_2)_2$ , the Fe–N bond length increases by 0.0385 Å (1.93% of the total initial bond length) while the Fe–S<sup>thiolate</sup> bond length increases by 0.0468 Å (2.01% of the total initial bond length).<sup>[194]</sup> The more pronounced elongation of metal–terminal ligand bonds observed in  $\{N_2\}\{N_2\}$  ligated cluster  $12a(NEt_4)_2(CoCp^*_2)$  may at least partly explain the larger negative value of the difference in entropy associated with one-electron reduction in this cluster. The general trend of larger entropic changes associated with the reduction of asymmetrically ligated clusters and the importance of inner-sphere reorganization are clearly established from these experiments.

**Table 6.1:** Slope of variation of  $E_{1/2}$  with  $T$  and entropy change  $\Delta S^\circ$  derived for one electron reduction of diferric [2Fe–2S] clusters and selected biological examples.

	$\delta E/\delta T$ ( $10^{-4}$ V K <sup>-1</sup> )	$\Delta S^\circ$ (J mol <sup>-1</sup> K <sup>-1</sup> )	$g_{av}$ of mixed valent species
$12a^{2-}$ $\{N_2\}\{N_2\}$	$-(5.34 \pm 0.74)$	$-(51.5 \pm 7.1)$	1.945
$4^{2-}$ $\{SN\}\{SN\}$	$-(2.28 \pm 0.25)$	$-(21.9 \pm 2.4)$	1.941
$26^{2-}$ $\{SN\}\{S_2\}$	$-(9.25 \pm 2.4)$	$-(89.2 \pm 21.6)$	1.937
$13^{2-}$ $\{N_2\}\{S_2\}$	$-(10.9 \pm 0.9)$	$-(106.3 \pm 8.6)$	1.935
Rieske <i>bc</i> <sub>1</sub> <sup>[218]</sup>	-9.12	$-(88 \pm 11)$	1.91
FD <sub>Pf</sub> <sup>[219]</sup> [4Fe–4S]	-12.3	-118.7	–



Comparison with a biological [2Fe–2S] cluster is difficult, since measurements on these clusters are typically performed in aqueous media rather than in organic solvents. Additionally, a network of hydrogen bonds is often found within the protein, which tunes the electrochemical properties of the iron sulfur cluster. When considering the reorganization energy associated with electron transfer of an iron sulfur protein, not only structural rearrangements of the cluster core but also rearrangement of the whole protein including the surrounding solvent molecules has to be considered. Nevertheless, the reaction entropy for one electron reduction of the Rieske [2Fe–2S] protein from the bovine heart mitochondrial *bc<sub>1</sub>* complex are found in a similar order of magnitude (Table 6.1). Temperature dependent electrochemical data have also been reported for the [4Fe–4S] ferredoxin extracted from *Pyrococcus furiosus* (FD<sub>Pf</sub>) and a reaction entropy of  $-119 \text{ J mol}^{-1} \text{ K}^{-1}$  can be extracted for the one electron reduction of the [4Fe–4S] cluster. This value is slightly higher than those found for [2Fe–2S] clusters, which may be due to more pronounced rearrangements taking place in the protein environment of a larger cluster. Temperature dependent electrochemistry can indeed be a valuable tool for understanding the effect of alternative ligands on the properties of iron sulfur clusters in biology and of their synthetic analogues. Carrying out similar experiments with protonated model systems may provide further insight into the effect of protonation on the coupling between protonation and electron transfer in iron sulfur clusters bearing alternative ligands.

### 6.3 Determination of Reaction Gibbs Free Energy and Enthalpy of One Electron Reduction

For the determination of  $\Delta G^\circ$  and  $\Delta H^\circ$  the measured potentials were converted to values vs. NHE using  $E^\circ([\text{FeCp}_2]^{0/+}) = +0.40 \text{ V vs. NHE}$ .<sup>[221]</sup> Since they have been determined in relation to a reference electrode, the resulting thermodynamic values should not be considered absolute values. However, they do allow for an examination of a general trend in the properties of the different [2Fe–2S] clusters studied within this work. The enthalpy and Gibbs free energy of the one electron reduction have been calculated according to the formulas given at the beginning of this chapter (see section 6.1) and are summarized in table 6.2. As mentioned previously, the electrochemical potential for the first reduction of synthetic [2Fe–2S] clusters is significantly lower than the potential found in the related biological systems (Table 6.2). This is due to the effect of the protein environment, hydrogen bonding networks and the influence of solvent molecules, since experiment using proteins are usually performed in aqueous solution while synthetic analogues are mostly studied in organic solvents. Additionally, the protein environment of naturally occurring [2Fe–2S] clusters can balance the overall charge of the system making clusters in these systems easier to reduce compared to the synthetic [2Fe–2S] clusters studied herein, all of which are dianionic in their diferric state. As it may have been anticipated, the potential for

electrochemical reduction of the clusters linearly decreases with a decreasing number of N-donor ligands (Figure 6.10). The strongly  $\sigma$ - and potentially  $\pi$ -donating thiolate ligands favor the ferric over the ferrous state and thus make reduction of the cluster more difficult to achieve. This trend is directly translated into larger values for the Gibbs free energies for one-electron reduction at 298 K (Table 6.2).

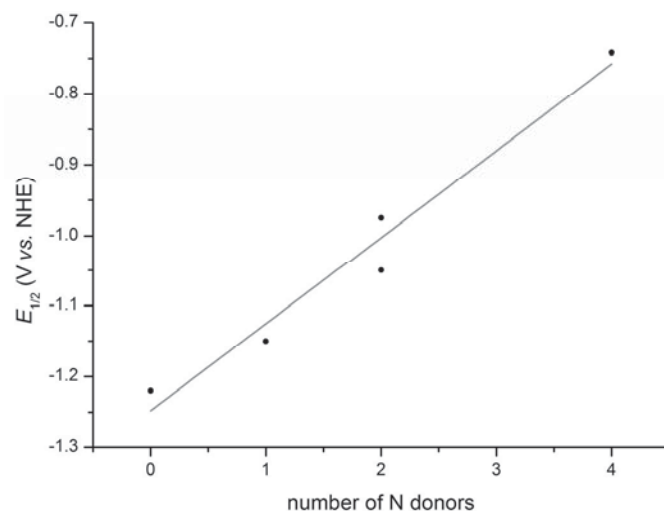


**Figure 6.10:** The reduction potential for the one-electron reduction of diferric [2Fe–2S] clusters ( $E_{1/2}$  in V vs. NHE) depends on the number of N–donors.

**Table 6.2:**  $E_{1/2}$  (V vs. SHE) at 298 K and thermodynamic parameters  $\Delta H^\circ$  and  $\Delta G^\circ$  derived for one electron reduction of diferric [2Fe–2S] clusters and selected biological examples.

	$E_{1/2}$ (V vs. SHE) at 298 K	$\Delta H^\circ$ (kJ mol <sup>-1</sup> )	$\Delta G^\circ$ (kJ mol <sup>-1</sup> ) at 298 K
{N <sub>2</sub> } {N <sub>2</sub> }	-0.742	59.6	71.6
{SN} {SN}	-0.975	88.3	94.1
{N <sub>2</sub> } {S <sub>2</sub> }	-1.048	69.5	101.1
{SN} {S <sub>2</sub> }	-1.146	60.7	110.6
{S <sub>2</sub> } {S <sub>2</sub> } <sup>[195]</sup>	-1.220	not determined	117.7
<i>Rieske bc<sub>1</sub></i> <sup>[218]</sup>	+0.312	-56 ± 4	-30 ± 1

## 6.4 Conclusion

Temperature dependent electrochemical measurements in a series of synthetic [2Fe–2S] clusters reveal the effects of alternative and asymmetric ligation on the thermodynamic properties of electron transfer in these clusters. The number of N- and S- donating ligands serves to tune the potential at which one electron reduction occurs. The degree of asymmetry in these clusters, which is closely connected to the degree of localization in the mixed valent cluster, seems to be directly translated into a larger negative value of the entropy  $\Delta S^\circ$ . This



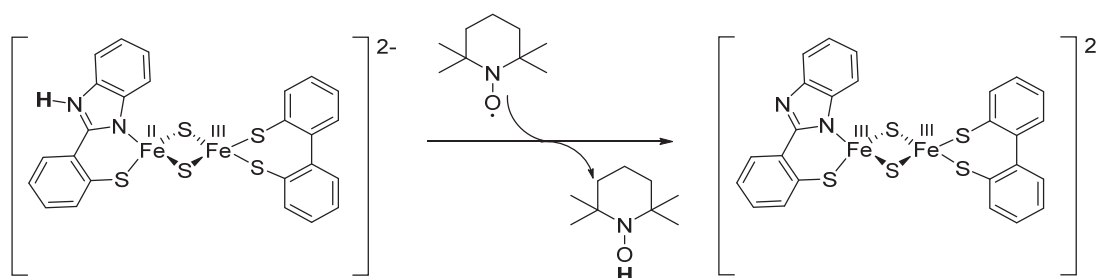
can be rationalized by considering the more pronounced inner-sphere rearrangements of the cluster that are necessary to accommodate for a more localized additional electron. Differing inner-sphere reorganizations are also due to a more pronounced elongation of metal–ligand bonds upon one-electron reduction of the [2Fe–2S] cluster, as observed when comparing clusters  $\mathbf{4}^{2-}$  and  $\mathbf{12a}^{2-}$ . A direct comparison of clusters  $\mathbf{4}^{2-}$  and  $\mathbf{13}^{2-}$  most clearly illustrates these effects of asymmetric ligation and the presence of alternative ligands: Both clusters feature two N- and two S-donors which results in very similar reduction potentials ( $E_{1/2}$  vs. NHE (at 298 K) =  $-0.975$  and  $-1.048$  V, respectively) and consequently in relatively similar Gibbs free energies for the one-electron reduction at 298 K ( $94.1$  and  $101.1$  kJ mol $^{-1}$ , respectively). Homoleptic cluster  $\mathbf{4}^{3-}$ , however, displays a significantly lower degree of localization than heteroleptic cluster  $\mathbf{13}^{3-}$ , which is evident from the  $g_{av}$  of the mixed valent species (table 6.3). Consequently, the determined entropy  $\Delta S^\circ$  for the reduction of  $\mathbf{13}^{2-}$  is almost five times as big as  $\Delta S^\circ$  determined for the reduction of related cluster  $\mathbf{4}^{2-}$ .



## 7 Proton Coupled Electron Transfer in Biomimetic Iron Sulfur Clusters

### 7.1 Introduction

Proton Coupled Electron Transfer (PCET) processes play a crucial role in a multitude of biological processes including photosynthesis and respiration.<sup>[70]</sup> Many of these processes rely on iron sulfur clusters for mediating PCET. One example is the thoroughly investigated Rieske cofactor introduced in chapter 1.4. Synthetic [2Fe–2S] clusters **13**<sup>2-</sup> and **12b**<sup>2-</sup> bearing imidazole based ligands have already been shown to undergo PCET reactivity and full square schemes and thermodynamic parameters have been established.<sup>[148,150]</sup> Heteroleptic Rieske model **13H**<sup>2-</sup> was shown to undergo a very fast PCET reaction with TEMPO at a rate of  $k = 9.5 \cdot 10^4 \text{ M s}^{-1}$  at 293 K. This high rate was attributed to a low reorganization energy due to very minor structural differences between the diferric and mixed valent species. In this chapter, [2Fe–2S] clusters **4**<sup>2-</sup> and **26**<sup>2-</sup> are shown to mediate PCET and the kinetics of these reactions are investigated. This extended series of [2Fe–2S] clusters for which PCET has been studied now allows for insights into the intrinsic factors determining this reactivity and emphasizes the role of reorganization energies. Full square schemes summarizing the thermodynamic parameters for stepwise and concerted proton and electron transfer can be established based upon the values determined in chapters 3 and 5. To obtain insights into the kinetics of the PCET reactions mixed valent protonated clusters **4H**<sup>2-</sup> and **26H**<sup>2-</sup> were prepared and treated with the PCET reagent TEMPO (Scheme 7.1). These reactions were monitored by UV-vis spectroscopy using double-mixing stopped-flow experiments under pseudo first order conditions at varying temperatures with varying amounts of excess TEMPO, and activation parameters for these reaction were determined. Parts of this chapter have been adapted from a recent publication.<sup>[192]</sup>



**Scheme 7.1:** PCET reaction of **26H**<sup>2-</sup> and TEMPO forming **26**<sup>2-</sup> and TEMPOH.

## 7.2 Thermodynamic Square Scheme of Homoleptic Model $4^{2-}$

Based upon the detailed characterization presented in chapter 3, a full square scheme for cluster  $4^{2-}$  can be established (Scheme 7.2). The strength of the N–H bond (bond dissociation free energy (BDFE)) in mixed valent, protonated  $4H^{2-}$  can be calculated according to the equation below (with  $C_{G,sol} = 54.9$  for MeCN,  $E_{1/2} = -1.342$  V and  $pK_a = 23.0$  for  $4H^-$ ).<sup>[64]</sup>

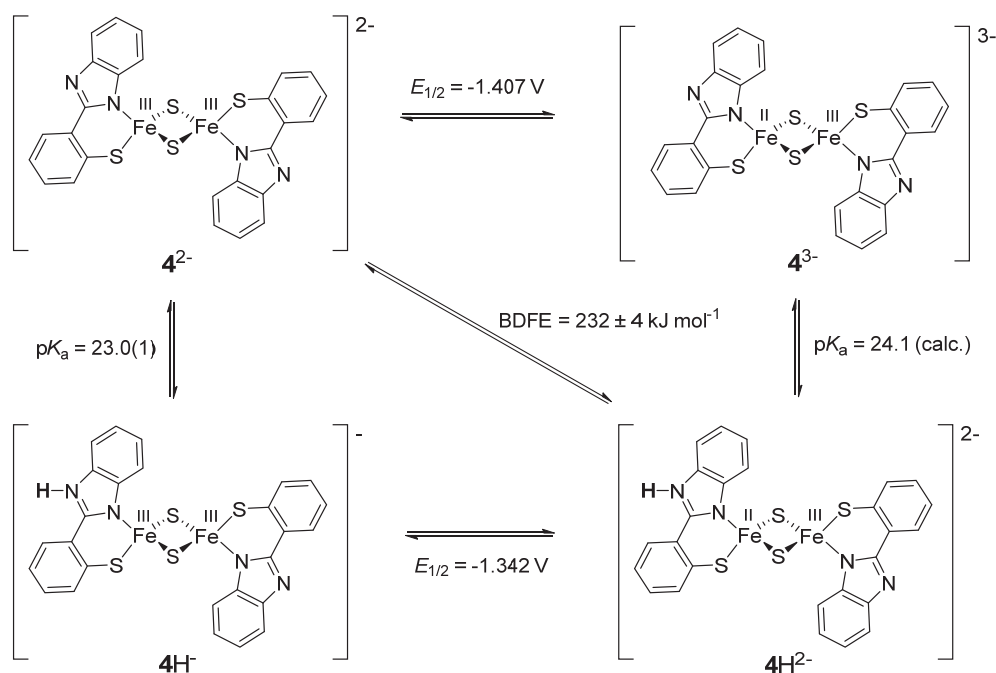
$$\text{BDFE (X-H)} = 1.37 pK_a + 23.06 E_{1/2} + C_{G,sol}$$

$$\text{BDFE (}4H^{2-}\text{)} = (232 \pm 4) \text{ kJ/mol}$$

The  $pK_a$  value of the protonated mixed valent cluster  $4H^{2-}$  could not be directly determined experimentally due to the sensitivity and poor solubility of the species. It can however be calculated according to Hess' law (with  $E_{1/2} = -1.407$  V for  $4^{2-}$ ).<sup>[64]</sup>

$$pK_a = (\text{BDFE} - 23.06 \cdot E_{1/2} - C_{G,sol})/1.37$$

$$pK_a(4H^{2-}) = 24.1$$



**Scheme 7.2:** Square scheme summarizing thermodynamic parameters for the homoleptic model  $4^{2-}$  in MeCN; potentials referenced vs.  $Fc/Fc^+$ .<sup>[192]</sup>

### 7.3 PCET Reactivity in Homoleptic Model $4H^{2-}$

Initial UV-vis experiments in MeCN at  $-30\text{ }^{\circ}\text{C}$  confirmed that unprotonated diferric  $4^{2-}$  is formed upon addition of TEMPO to a solution of *in situ* prepared  $4H^{2-}$  (Figure 7.1), establishing  $4H^{2-}$  as a potential PCET reagent.

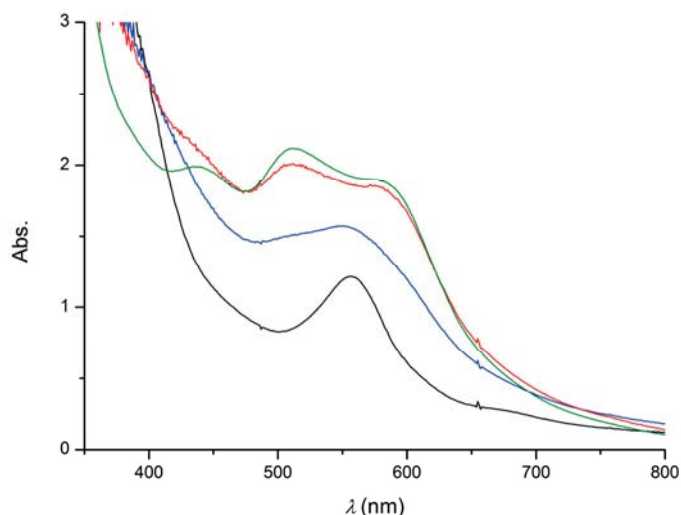


**Figure 7.1:** UV-vis spectra of diferric  $4^{2-}$  (green), mixed valent  $4^{3-}$  (black), *in situ* generated  $4H^{2-}$  (blue). Addition of TEMPO leads back to  $4^{2-}$  (red).

To investigate the kinetics of this PCET reaction, solutions of  $4^{3-}$  (0.738 mM), [DMPH](BF<sub>4</sub>) (0.738 mM), and TEMPO (3.3, 6.4, 9.6, 12.8 and 16.0 mM) were prepared. Relatively large excess of TEMPO was used in all cases to ensure pseudo first-order conditions. Reagents and MeCN were loaded into gas-tight syringes and were attached to gas-tight 2-way valves. The changes in UV-vis absorption spectra of the solution during the reaction was monitored over 2 s. First-order fitting yielded first order rate constants  $k_{\text{obs}}$ . Since all experiments were performed under pseudo first order conditions, these observed rate constants  $k_{\text{obs}}$  can then be plotted vs.  $c(\text{TEMPO})$  to obtain corresponding rate constants  $k$  from a linear fit (Figure 7.2). The individual rate constants  $k$  determined for each temperature can be used to extract the activation parameters of PCET the reaction from an Eyring plot (Figure 7.3). The origin of the large intercepts in some of the  $k_{\text{obs}}$  vs.  $c(\text{TEMPO})$  plots cannot be identified clearly. One possible reason may be a concurrent decomposition of  $4H^{2-}$ . However, independent experiments generating  $4H^{2-}$  in the same way but in the absence of TEMPO did not show significant decay over the timescale of the kinetics experiments (about 2 s). Consequently, the large intercepts cannot be explained by concurrent decomposition of  $4H^{2-}$ .<sup>[192]</sup>

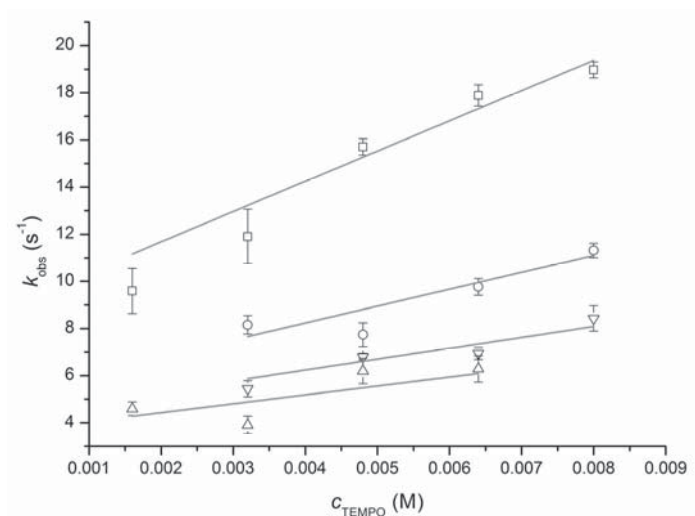


**Figure 7.2:** Linear fits of  $k_{\text{obs}}$  values of the reaction between  $7.38 \cdot 10^{-4}$  M  $4\text{H}^{2-}$  (generated *in situ*) and excess TEMPO in MeCN at various temperatures ( $\square$   $-30$  °C,  $\circ$   $-15$  °C,  $\nabla$   $0$  °C,  $\Delta$   $20$  °C).<sup>[192]</sup>

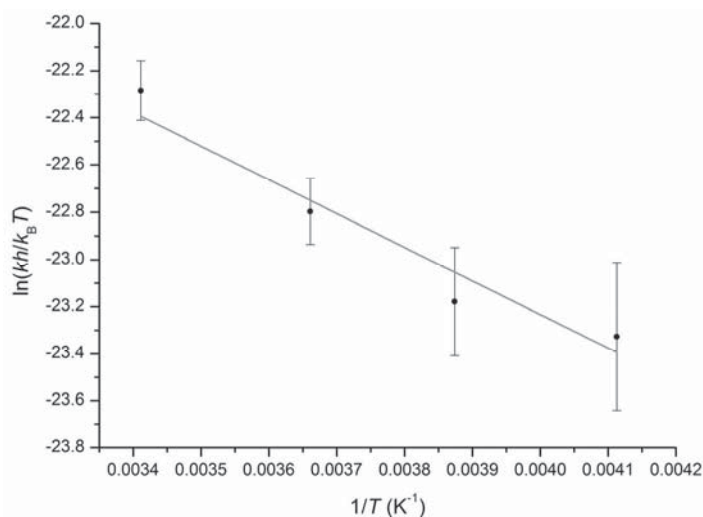


**Figure 7.3:** Eyring plot for the reaction of  $4\text{H}^{2-}$  with excess TEMPO in MeCN.<sup>[192]</sup>

The transition state parameters as determined from the Eyring plot are:<sup>[192]</sup>

$$\begin{aligned}\Delta H^\ddagger &= (14.2 \pm 3.3) \text{ kJ mol}^{-1} \\ \Delta S^\ddagger &= - (132 \pm 12) \text{ J mol}^{-1} \text{ K}^{-1}\end{aligned}$$

With the rate at 293 K  $k_{293} = 1281 \text{ M s}^{-1}$ ,  $\Delta G^\ddagger$  at 293 K can be determined from the Eyring equation:<sup>[192]</sup>

$$\Delta G^\ddagger = (54.3 \pm 0.2) \text{ kJ mol}^{-1}$$

## 7.4 Thermodynamic Square Scheme of MitoNEET model $26^{2-}$

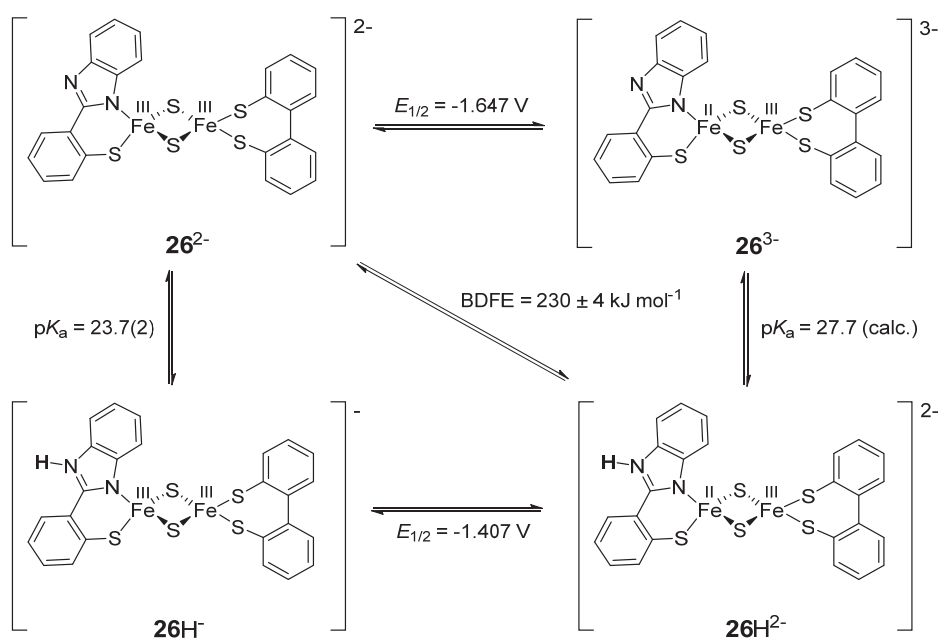
The N–H bond dissociation free energy and the  $pK_a$  value of mixed valent protonated  $26H^{2-}$  were determined as described in chapter 7.2 and a full square scheme can be established based upon these values (Scheme 7.3).<sup>[64]</sup> A BDFE of  $230 \text{ kJ mol}^{-1}$  was determined, which is relatively low compared to a BDFE of  $280 \text{ kJ mol}^{-1}$  reported for mitoNEET proteins.

$$\text{BDFE (X-H)} = 1.37 pK_a + 23.06 E_{1/2} + C_{G,\text{sol}}$$

$$\text{BDFE (}26H^{2-}\text{)} = (230 \pm 4) \text{ kJ/mol}$$

$$pK_a = (\text{BDFE} - 23.06 E_{1/2} - C_{G,\text{sol}})/1.37$$

$$pK_{a\text{ mv}} = 27.7$$



**Scheme 7.3:** Square scheme summarizing thermodynamic parameters for mitoNEET model  $26^{2-}$  in MeCN, potentials referenced vs.  $\text{Fc}/\text{Fc}^+$ .<sup>[192]</sup>

## 7.5 Kinetics of PCET in MitoNEET Model $26^{2-}$

The formation of  $26^{2-}$  after addition of TEMPO to *in situ* generated  $26H^{2-}$  was established by preliminary UV-vis experiments in MeCN at  $-30\text{ }^{\circ}\text{C}$  (Figure 7.4). Kinetics of this PCET reactivity were then investigated as described for  $4H^{2-}$  in chapter 6.5 using solutions of  $26^{3-}$  (0.738 mM), [DMPH](BF<sub>4</sub>) (0.738 mM), and TEMPO (3.3, 6.4, 9.6, 12.8 and 16.0 mM) under pseudo first-order conditions and using double mixing stopped-flow experiments. Individual rates  $k_{\text{obs}}$  for each concentration and temperature were determined by first order fitting.

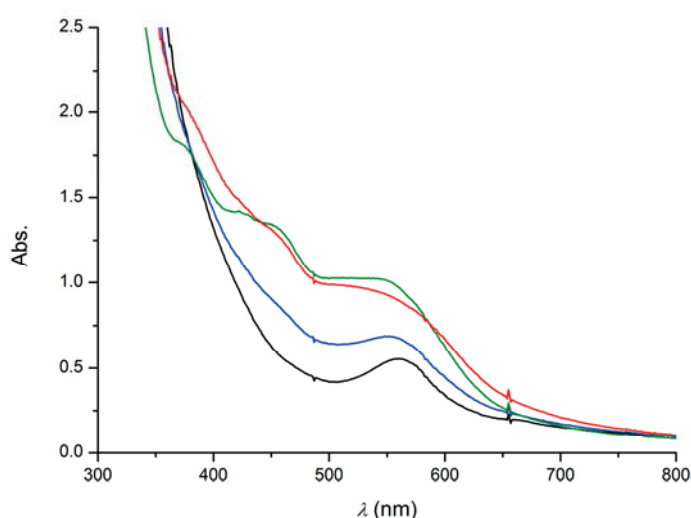


**Figure 7.4:** UV-vis spectra of diferric  $26^{2-}$  (green), mixed valent  $26^{3-}$  (black), *in situ* prepared  $26H^{2-}$  (blue). Addition of TEMPO led back to diferric unprotonated  $26^{2-}$  (red).

Since all reactions were carried out under pseudo first-order conditions by using an excess of TEMPO, the rate constants  $k$  at each temperature can be obtained from linear fits of  $k_{\text{obs}}$  vs.  $c(\text{TEMPO})$  (Figure 7.5). They were then used to derive the activation parameters from an Eyring plot (Figure 7.6). The following activation parameters for the PCET reaction were thus obtained:<sup>[192]</sup>

$$\begin{aligned}\Delta H^{\ddagger} &= (17.6 \pm 3.0) \text{ kJ mol}^{-1} \\ \Delta S^{\ddagger} &= - (143 \pm 11) \text{ J mol}^{-1} \text{ K}^{-1}\end{aligned}$$

With the rate constant  $k = 134 \text{ M s}^{-1}$  at 293 K, the activation Gibbs energy  $\Delta G^{\ddagger}$  can be determined from the Eyring equation, at 293K:<sup>[192]</sup>

$$\Delta G^{\ddagger} = (59.8 \pm 0.5) \text{ kJ mol}^{-1}$$

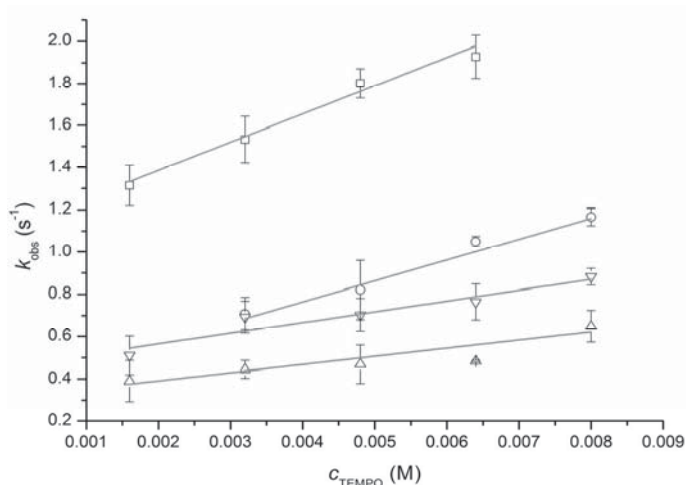


**Figure 7.5:** Linear fits of  $k_{\text{obs}}$  values of the reaction between  $7.38 \cdot 10^{-4}$  M  $26\text{H}^{2-}$  (generated *in situ*) and excess TEMPO in MeCN at various temperatures ( $\square$   $-30$  °C,  $\circ$   $-15$  °C,  $\nabla$   $0$  °C,  $\Delta$   $20$  °C). The slope of each line gives the corresponding rate constant  $k$ .<sup>[192]</sup>

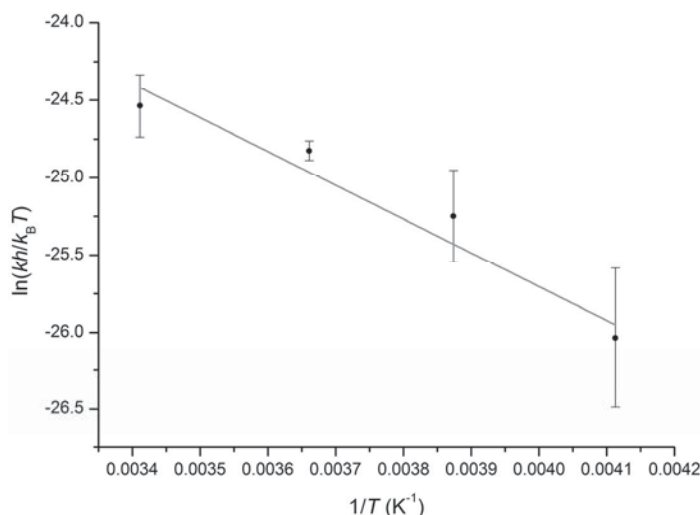


**Figure 7.6:** Eyring plot for the reaction of  $26\text{H}^{2-}$  with excess TEMPO in MeCN.<sup>[192]</sup>

The driving force (*i.e.* the Gibbs free energy)  $\Delta G^\circ_{\text{CPET}}$  for the concerted proton and electron transfer reaction can be calculated as:<sup>[64]</sup>

$$\Delta G^\circ_{\text{CPET}} = \text{BDFE}(26\text{H}^{2-}/4\text{H}^{2-}) - \text{BDFE}(\text{TEMPO-H})$$

With a value of  $66.5 \text{ kcal mol}^{-1}$  for  $\text{BDFE}(\text{TEMPO-H})$  in MeCN the driving force for the reaction of either  $4\text{H}^{2-}$  or  $26\text{H}^{2-}$  can be calculated as:<sup>[64]</sup>

$$\Delta G^\circ_{\text{CPET}} = -46.3 \text{ kJ mol}^{-1} \text{ for } 4\text{H}^{2-}$$

$$\Delta G^\circ_{\text{CPET}} = -48.4 \text{ kJ mol}^{-1} \text{ for } 26\text{H}^{2-}$$

Even though the BDFE and thus the driving forces for the reactions of  $4\text{H}^{2-}$  and  $26\text{H}^{2-}$  are very similar, the activation parameters for the reaction of  $26\text{H}^{2-}$  with TEMPO are higher than those determined for the reaction of  $4\text{H}^{2-}$ . Both reactions differ most clearly when considering the individual rate constants  $k$ . At 23°C the reaction of homoleptic model  $4\text{H}^{2-}$  occurs with a rate of  $1281 \text{ M s}^{-1}$  while the reaction of  $26\text{H}^{2-}$  proceeds with a rate constant of  $134.8 \text{ M s}^{-1}$  (Table 7.1). According to Marcus theory, the rate of a PCET process depends on the driving force and the reorganization energy associated with this reaction. Since the driving force is essentially the same for both reactions, the drastic difference in rate must be attributed to a higher reorganization energy in the reaction of heteroleptic  $26\text{H}^{2-}$ . A higher reorganization energy in the heteroleptic model can be rationalized as a consequence of the higher localization of the unpaired electron in the mixed valent form of the heteroleptic cluster when compared to the homoleptic cluster. This higher localization is associated with higher structural changes accompanying reactions involving electron transfer. As a consequence of these structural changes, the reorganization energy is higher, which leads to a decreased rate for the PCET reaction. It is however evident from further comparison with related clusters  $12\text{bH}^{2-}$  and  $13\text{H}^{2-}$  that an increased localization is not the only factor determining the rate of PCET in  $[2\text{Fe}-2\text{S}]$  clusters. The highest PCET rate was found in  $13\text{H}^{2-}$ , even though the highest degree of localization is assumed for this cluster based on EPR and Mößbauer spectroscopy and thus the lowest rate for PCET would have been predicted. Other factors may include the steric accessibility of the proton, as well as effects arising from tautomerization of the ligand.

**Table 7.1:** Thermodynamic parameters for the reaction of  $4\text{H}^{2-}$  and  $26\text{H}^{2-}$  and previously reported Rieske models  $12\text{bH}^{2-}$  and  $13\text{H}^{2-}$  with TEMPO.

	$12\text{bH}^{2-}$ [150]	$13\text{H}^{2-}$ [148]	$4\text{H}^{2-}$ [192]	$26\text{H}^{2-}$ [192]
$\Delta H^\ddagger$ (kJ mol <sup>-1</sup> )	$6.7 \pm 1.3$	$8.7 \pm 1.0$	$14.16 \pm 3.28$	$17.6 \pm 2.95$
$\Delta S^\ddagger$ (J mol <sup>-1</sup> K <sup>-1</sup> )	$-159 \pm 10$	$-120 \pm 5$	$-131.9 \pm 11.8$	$-142.9 \pm 11.1$
$k$ (M <sup>-1</sup> s <sup>-1</sup> ) at 293K	$2200 \pm 350$	$95000 \pm 12000$	$1281 \pm 116$	$134.8 \pm 27.2$
BDFE (kJ mol <sup>-1</sup> )	$253 \pm 4$	$252 \pm 2$	$232 \pm 4$	$230 \pm 4$
$\Delta G^\ddagger$ (kJ mol <sup>-1</sup> ) at 293 K	54.0	43.8	54.3	59.8
$\Delta G^\circ\text{CPET}$ (kJ mol <sup>-1</sup> )	-25.1	-26.4	-46.3	-48.4

## 7.6 Comparison of Stepwise and Concerted Pathways

As shown in chapter 1.3, the observed PCET reaction can either follow a stepwise or a concerted mechanism. These mechanistic scenarios can be distinguished by examining the thermodynamics of the single steps. If the free energy differences of the single PT and ET steps are larger than the observed activation barrier, the reaction cannot follow a stepwise pathway.

A stepwise mechanism with proton transfer as initial step would lead to  $4^{3-}$  or  $26^{3-}$  and TEMPOH<sup>+</sup>. The Gibbs free energy for proton transfer can be calculated as:

$$\Delta G^{\circ}_{\text{PT}} = -RT \ln(\text{p}K_{\text{a}})$$

For  $4\text{H}^{2-}$  (with  $\text{p}K_{\text{a}} = 24.1$  ( $4\text{H}^{2-}$ ),  $\text{p}K_{\text{a}}(\text{TEMPOH}^+) = -4$ ):<sup>[64]</sup>

$$\Delta G^{\circ}_{\text{PT}} = 2.303 RT (\Delta\text{p}K_{\text{a}}) = 161 \text{ kJ mol}^{-1}$$

For  $26\text{H}^{2-}$  (with  $\text{p}K_{\text{a}}(26\text{H}^{2-}) = 27.7$ ):

$$\Delta G^{\circ}_{\text{PT}} = 2.303 RT (\Delta\text{p}K_{\text{a}}) = 182 \text{ kJ mol}^{-1}$$

The values of  $\Delta G^{\circ}_{\text{PT}} = 161 \text{ kJ mol}^{-1}$  and  $182 \text{ kJ mol}^{-1}$  are much larger than the activation energy for the concerted pathway of the reaction of  $4\text{H}^{2-}$  and  $26\text{H}^{2-}$  with TEMPO ( $\Delta G^{\ddagger} = 54.3$  and  $59.8 \text{ kJ mol}^{-1}$  respectively). Thus proton transfer as an initial step can be excluded.<sup>[64,192]</sup>

A stepwise mechanism with electron transfer as initial step would lead to  $4\text{H}^{\cdot}$  or  $26\text{H}^{\cdot}$  and TEMPO<sup>•</sup>. The Gibbs free energy for electron transfer can be calculated as:<sup>[64]</sup>

$$\Delta G^{\circ}_{\text{ET}} = -F \cdot \Delta E^{\circ} = -(96.48 \text{ kJ mol}^{-1} \text{ V}^{-1}) \Delta E^{\circ}$$

For  $4\text{H}^{2-}$  (with  $E_{1/2} = -1.34 \text{ V}$ ) and  $E^{\circ}(\text{TEMPO}) = -1.95 \text{ V}$ ):<sup>[64]</sup>

$$\Delta G^{\circ}_{\text{ET}} = 58.8 \text{ kJ mol}^{-1}$$

For  $26\text{H}^{2-}$  (with  $E_{1/2} = -1.41 \text{ V}$ ):

$$\Delta G^{\circ}_{\text{ET}} = 52.1 \text{ kJ mol}^{-1}$$

The values of  $\Delta G^{\circ}_{\text{ET}} = 58.8 \text{ kJ mol}^{-1}$  and  $52.1 \text{ kJ mol}^{-1}$  are very similar to the activation energy for the concerted pathway of the reaction of  $4\text{H}^{2-}$  and  $26\text{H}^{2-}$  with TEMPO making initial electron transfer thermodynamically possible.<sup>[192]</sup> However, electron transfer as initial step is unlikely. Initial electron transfer in this case would require  $\Delta G^{\circ}_{\text{ET}}$  to be equal to the intrinsic barrier for electron transfer, since according to Marcus Theory  $\Delta G^{\ddagger} = (\Delta G^{\circ}_{\text{ET}} +$



$\lambda)^2/4$ ).<sup>[64]</sup> Since values of the reorganization energy  $\lambda$  for electron transfer reactions in MeCN are typically larger than  $60 \text{ kJ mol}^{-1}$ ,<sup>[222] [223]</sup> it is more likely that the observed reactions follow a concerted rather than a stepwise pathway.

### 7.7 Conclusion

The studies presented in this chapter show that proton coupled electron transfer is a general possibility and should be considered as one feasible function of [2Fe–2S] clusters in the mitoNEET family. PCET reactivity of clusters **4H**<sup>2-</sup> and **26H**<sup>2-</sup> were studied in double-mixing stopped-flow and comparison of the obtained kinetic parameters to the single steps of potential stepwise scenarios indicate that the observed PCET reactions follow a concerted rather than a stepwise mechanism. Furthermore, the comparison of the rates of PCET reactions of closely related synthetic [2Fe–2S] clusters emphasizes the role of reorganization energies in this process. Even though the driving force for the reaction of **4H**<sup>2-</sup> and **26H**<sup>2-</sup> with TEMPO are almost identical, heteroleptic model **26H**<sup>2-</sup> reacts much slower. A reason for the slowing down of the reaction with TEMPO may be the asymmetric ligation of **26H**<sup>2-</sup> and the resulting higher localization of the unpaired electron in the mixed valent form of the cluster. The findings presented in this chapter thus indicate that asymmetric ligation leads to higher localization of the unpaired electron which in turn leads to an increased reorganization energy in PCET processes which in turn results in a decreasing rate of the observed reaction.<sup>[192]</sup> However, comparing the rates observed for clusters **26H**<sup>2-</sup>, and **4H**<sup>2-</sup> to those previously reported in related clusters **12bH**<sup>2-</sup>, and **13H**<sup>2-</sup> shows that other factors such as properties of the ligands and the steric accessibility of the protonation site also play an important role in tuning a cluster's PCET reactivity.

---

## 8 Weak Binding Interactions Between Alkali Metal Cations and Synthetic [2Fe–2S] Clusters

### 8.1 Introduction

Alkali metal cations are ubiquitous and occur in the earth's crust as well as in biology. Lithium is found as an essential trace element in plants, animals and humans and has been used in psychiatric medication since the nineteenth century, as for example in the treatment of bipolar disorder.<sup>[224–226]</sup> Sodium and potassium are present in the human body at high concentrations where they have a multitude of functions (140 mM K<sup>+</sup> and 15 mM Na<sup>+</sup> inside cells and 5 mM K<sup>+</sup> and 150 mM Na<sup>+</sup> outside of cells).<sup>[227]</sup> For example, neuronal communication within the brain depends on voltage-gate sodium channels, making sodium an essential element for life.<sup>[228]</sup> Deficiencies or excess in the concentration of these alkali metal cations thus has severe consequences for every living organism. Since they are often spectroscopically silent, much effort has been made in the last decades to develop sensors for visualizing the presence of these cations.<sup>[229]</sup> Therefore a variety of chelating agents have been developed, which for example exploit the fluorescence properties of the sensing agents upon binding of these alkali metal ions.<sup>[230,231]</sup> Crown ethers such as 12-crown-4 for Li<sup>+</sup>,<sup>[232]</sup> 15-crown-5 for Na<sup>+</sup>, and 16-crown-6 for K<sup>+</sup>, as well as cryptands such as cryptofix-[2.2.2] have been described as efficient binding agents for alkali metal cations, which can be used to remove these metal ions from contact-ion pairs.<sup>[233,234]</sup> While these alkali metal cations themselves are redox inert, it has been shown that their presence can play a significant role in modulating the redox properties of complexes containing redox active metals or organic compounds.<sup>[235]</sup> Monovalent cations Li<sup>+</sup>, Na<sup>+</sup>, and K<sup>+</sup> were shown to shift the electrochemical potentials of the reduction in dinuclear copper-oxo compounds.<sup>[236,237]</sup> Divalent cations M<sup>2+</sup> such as Ca<sup>2+</sup> and Sr<sup>2+</sup> were reported to strongly influence the reactivity and oxygen-release from a mononuclear non-heme iron(II) peroxo complex.<sup>[238]</sup> In both cases the redox inert cation binds to the oxo unit and thus modulates the redox properties of the whole system. Divalent redox inactive metal cations were also found to modulate the reduction potential in heterometallic manganese-oxido clusters.<sup>[239]</sup>

“Crowned” [4Fe–4S] clusters such as **29**<sup>2-</sup> bearing crown ethers in their ligand backbones have been shown to bind alkali metal cations leading to shifts of the redox potentials of the observed Fe<sup>II</sup>/Fe<sup>III</sup> redox pair (Figure 9.1).<sup>[240]</sup> This anodic shift was reported to be up to 190 mV depending on the nature of the cation. These clusters were thus proposed to be suitable electrochemical sensors for the presence of otherwise spectroscopically silent alkali metal cations. Additionally interaction modes are possible in iron sulfur clusters with alternative ligands, as well as potential interactions with the bridging sulfides and terminal thiolates.

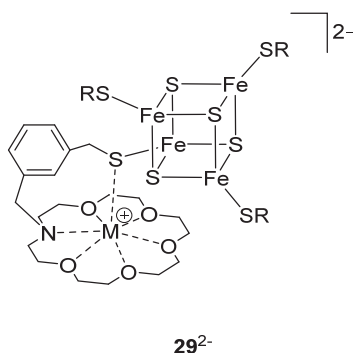


**Figure 8.1:** “Crowned” [4Fe–4S] clusters as electrochemical sensors for alkali metal cations.<sup>[240]</sup>

The benzimidazole ligands of clusters  $12a^{2-}$ ,  $4^{2-}$  and  $26^{2-}$  offer two (in case of  $12a^{2-}$  and  $4^{2-}$ ) or a single (in case of  $26^{2-}$ ) potential site for coordination of alkali metal ions (Figure 9.2) at the N-atom in the backbone of the terminal ligand. These interactions are expected to lead to similar spectroscopic changes as protonation, since they are expected to occur at the same binding sites. However, interactions occurring at the bridging sulfides or the thiolates are feasible as well. This chapter describes weak binding interactions between the aforementioned [2Fe–2S] clusters, the determination of binding constants and the effect of cation binding on spectroscopic and electrochemical properties.

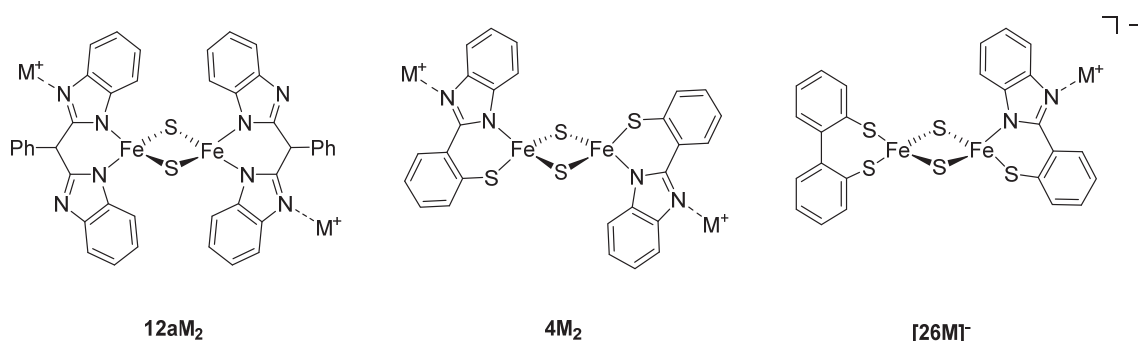


**Figure 8.2:** Possible binding interactions between N-atoms of benzimidazole-type ligands of [2Fe–2S] clusters  $12a^{2-}$ ,  $4^{2-}$ , and  $26^{2-}$  and alkali metal cations ( $M^+ = Li^+, Na^+, K^+$ ).

## 8.2 Binding of Alkali Metal Cations to Homoleptic Cluster $4^{2-}$

### 8.2.1 Determination of Binding Stoichiometry with $Li^+$

Homoleptic cluster  $4^{2-}$  offers two potential binding sites for alkali metal ions, similar to the two potential binding sites for protons in the backbone of the two identical benzimidazole ligands. Indeed, addition of LiOTf to a solution of  $4^{2-}$  in MeCN leads to changes in the UV-vis absorption spectra (Figure 9.3), which are similar to the changes observed during

protonation experiments (see chapter 3.5.1). The bands at 510 nm and 584 nm are slightly shifted upon addition of LiOTf and the band at 434 nm disappears. After addition of about 40.0 eq LiOTf no further spectroscopic changes were observed. Subsequent addition of 15-crown-5 or 12-crown-4 does not reverse these changes but leads to additional minor shifts of the observed bands, indicating that the crown ether does not remove the  $\text{Li}^+$  cation from the cluster but rather binds additionally (Figure 9.4). A similar structure will be reported for binding between  $\text{Li}^+$  and cluster  $\mathbf{12a}^{2-}$  in section 9.4.

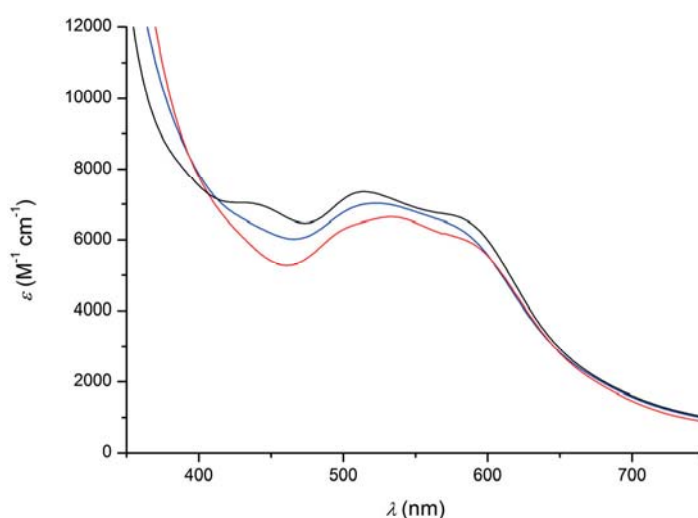


**Figure 8.3:** UV-vis absorption spectra of  $\mathbf{4}^{2-}$  (black) upon addition of 40.0 eq LiOTf (blue), subsequent addition of 12-crown-4 (red).

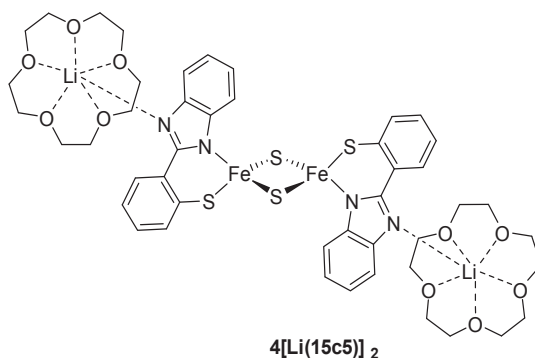


**Figure 8.4:** Proposed complex of  $\mathbf{4}^{2-}$ , 2.0 eq  $\text{Li}^+$  and 15-crown-5.

To obtain first indications whether one or two  $\text{Li}^+$  cations bind to the iron sulfur cluster a Job Plot was obtained following the method of continuous variation.<sup>[241]</sup> Therefore solutions of  $\mathbf{4}(\text{NEt}_4)_2$  and LiOTf in MeCN with equal concentrations were prepared. Samples containing these two solutions in varying ratios, keeping the total concentration  $c(\mathbf{4}(\text{NEt}_4)_2) + c(\text{LiOTf})$  constant were then prepared and UV-vis absorption spectra were recorded. Three independent runs were performed and the vanishing band at 434 nm was used to indicate the

presence of product  $4\text{Li}_n^{(2-n)-}$  ( $n = 1$  or  $2$ ). The difference in extinction at 434 nm was used as a measure for the presence of the product and  $\Delta\epsilon(434\text{nm}) \cdot (1-r_{\text{Li}})$  ( $r_{\text{Li}} = \text{molar ratio of Li}^+$ ) was plotted vs.  $r_{\text{Li}}$ . The resulting Job plots show maxima at about  $r_{\text{Li}} = 0.59, 0.63$  and  $0.64$  (an exemplary Job Plot is shown in figure 8.5). The interaction of  $\text{Li}^+$  and  $4^{2-}$  is thus most likely a 2:1 bonding interaction. For a 1:1 binding event, a Job plot typically is expected to show a maximum at  $r_{\text{Li}} = 0.5$ .<sup>[241,242]</sup> The rather flat shape of the resulting plot already indicates weak binding interactions. For strong binding interactions, steeper slopes and a well-defined peak position are usually observed.

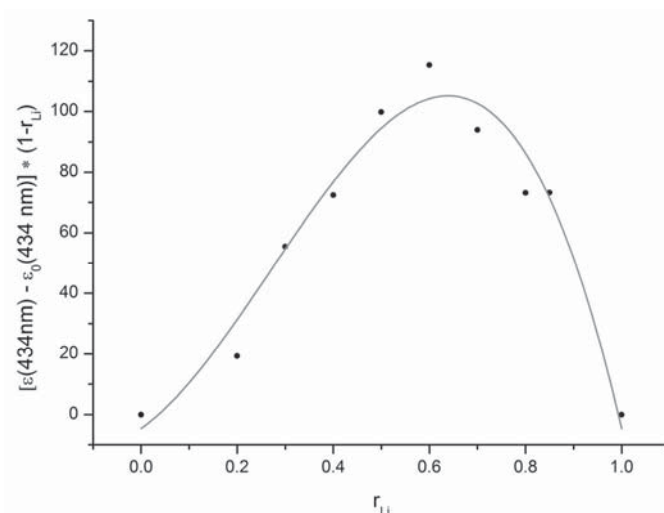
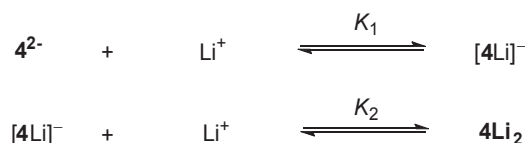


**Figure 8.5:** Job plot for the interaction of  $4^{2-}$  and  $\text{Li}^+$  indicates a 1:2 bonding mode. The grey line serves as a guide for the eye.

### 8.2.2 Determination of Binding Constants with $\text{Li}^+$

A 1:2 bonding interaction between the cluster and the binding  $\text{Li}^+$  cations makes the determination of binding constants more challenging than a simple 1:1 interaction, since two equilibria and thus two binding constants  $K_1$  and  $K_2$  must be considered.<sup>[243,244]</sup>



Three independent titration experiments were performed and the binding constants were determined using bindfit v0.5 available *via* supramolecular.org (Figure 8.6).<sup>[244]</sup> These independent runs yielded average values of  $K_1 = (279 \pm 23) \text{ M}^{-1}$  and  $K_2 = (131 \pm 67) \text{ M}^{-1}$ . The error of the obtained values is relatively large, especially the error of the second binding

constant  $K_2$ . This might be due to the very small changes in extinction coefficient between the species, which make an accurate determination of the bonding constants challenging. However, both binding constants are in the same order of magnitude, showing that binding of a second  $\text{Li}^+$  is only slightly less favorable than binding of the first  $\text{Li}^+$ . The two binding sites in the cluster therefore seem to be almost independent from each other, which supports the assumption of  $\text{Li}^+$  binding to the peripheral N-atoms of the benzimidazole-type capping ligands.

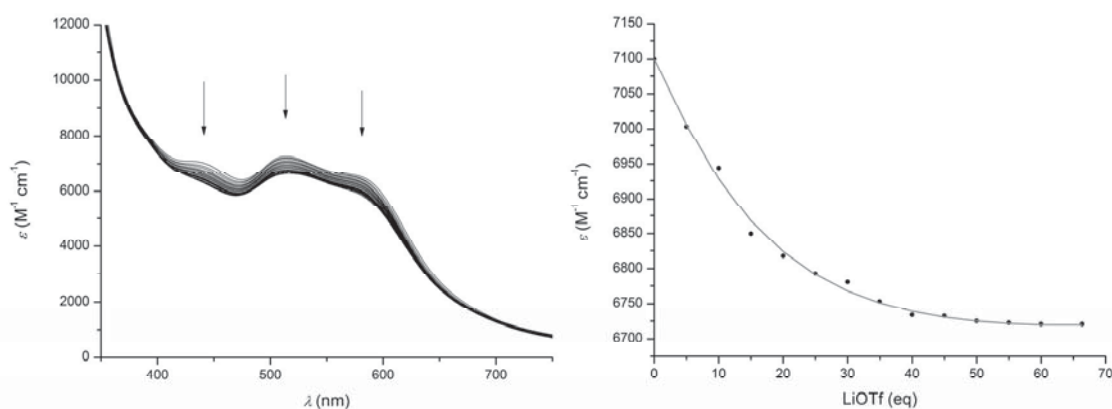


**Figure 8.6:** Left: UV-vis spectral changes observed during the addition of LiOTf to  $\mathbf{4}(\text{NET}_4)_2$  in MeCN, each line represents the addition of 4 eq. Right: Extinction coefficient for the band at 438 nm observed after addition of varying amounts of LiOTf and fit obtained by bindfit v0.5 (grey).

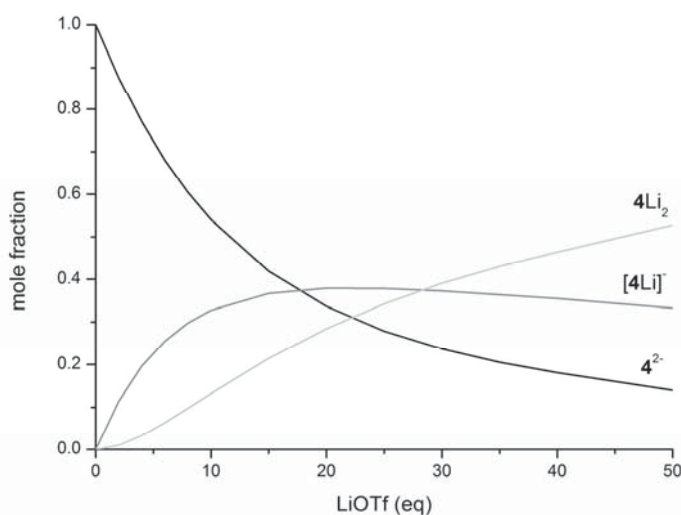


**Figure 8.7:** Mole fractions of  $\mathbf{4}^{2-}$ ,  $[\mathbf{4}\text{Li}]^+$  and  $\mathbf{4}\text{Li}_2$  present in solution vs. amount of LiOTf added (eq), determined using bindfit v0.5.

Bindfit v0.5 also allows for the determination of the mole fractions of all species involved in the equilibrium after the addition of a certain amount of LiOTf (Figure 8.7).<sup>[244]</sup> The resulting mole fraction plot shows that even after the addition of 50 eq LiOTf, when no further

changes can be observed in UV-vis absorption spectra, only about 50 % of the cluster are actually binding two  $\text{Li}^+$  cations. 20 % of the cluster is still present as “free”  $\mathbf{4}^{2-}$  without any cation binding. This may shed light on the difficulties encountered in crystallization attempts. Attempts to crystallize  $\mathbf{4Li}_2$  from solutions of MeCN, DMF or mixtures of MeCN with DME, THF, EtOH or 12-crown-4 by slow diffusion of diethyl ether into these solution only yielded crystals of “free”  $\mathbf{4}^{2-}$  with two  $\text{NEt}_4^+$  counter ions. These findings suggest that either even though in solution  $\mathbf{4Li}_2$  exists in equilibrium with  $\mathbf{4}^{2-}$  and  $[\mathbf{4Li}]^-$ , crystallization in the solid favors the presence of two  $\text{NEt}_4^+$  cations over  $\text{Li}^+$  cations or an increased solubility of the cluster due to interaction with  $\text{Li}^+$  prevents it from crystallizing.

Addition of 40.0 eq of LiOTf to a solution of  $\mathbf{4}(\text{NEt}_4)_2$  in MeCN leads to shifts in the cluster’s  $^1\text{H}$  NMR spectrum (Figure 8.8), which are very similar to the shifts observed during protonation experiments. All resonances are slightly shifted with the most pronounced shift observable for the resonances at 4.25 and 4.48 ppm. This shift is smaller than the shift observed upon protonation which might be due to a weaker binding interaction between the cluster and a  $\text{Li}^+$  cation compared to the binding of a proton. Furthermore, the free cluster, *i.e.* without  $\text{Li}^+$  bound, is still present in solution, so a smaller observable shift was expected. Notably, the resonances corresponding to the two distinct isomers are shifted by the same  $\Delta\delta$  (ppm) and the ratio of isomers is conserved. Thus binding of alkali metal cations does not shift the equilibrium between the isomers, but it may have an effect on the rate of isomerization, similar to what has been observed upon protonation of the cluster (see chapter 4.5). In analogy to the determination of the self-exchange rate between protonated and unprotonated clusters presented in chapter 3.5, a lower limit for the rate at which the bound  $\text{Li}^+$  ions are exchanged between clusters can be calculated according to:

$$k_{obs} = \frac{\pi \cdot \Delta\delta}{\sqrt{2}}$$

From the shift of 0.23 ppm an observed rate  $k_{obs} = 255 \text{ s}^{-1}$  can be determined. Since the experiment was carried out at a concentration of  $c = 0.002 \text{ M}$ , this corresponds to a lower limit for the rate for cation exchange of about  $k = 1.3 \cdot 10^5 \text{ M}^{-1} \text{ s}^{-1}$ . This value is very similar to the one determined for proton exchange between clusters ( $k_{PT} = 1.9 \cdot 10^5 \text{ M}^{-1} \text{ s}^{-1}$ ).

To verify whether the observed effects are indeed due to coordinating  $\text{Li}^+$  cations,  $^7\text{Li}$  NMR spectra of free LiOTf and of a mixture of LiOTf and 0.071 eq  $\mathbf{4}(\text{NEt}_4)_2$  were obtained (Figure 8.9). In the presence of  $\mathbf{4}(\text{NEt}_4)_2$  the single signal observed in  $^7\text{Li}$  NMR is shifted by about 0.209 ppm from  $-2.354$  to  $-2.145$  ppm and broadened (Figure 9.9). This effect is relatively small, since about 90 % of the  $\text{Li}^+$  cations are free and do not bind to the iron sulfur cluster. Nevertheless, it proves that  $\text{Li}^+$  cations do interact with the iron sulfur cluster. No differences

## 8 Weak Binding Interactions Between Alkali Metal Cations and Synthetic [2Fe–2S] Clusters

in  $^{19}\text{F}$  NMR were observed, showing that the  $\text{TfO}^-$  ions are not involved in any interaction with the iron sulfur cluster.

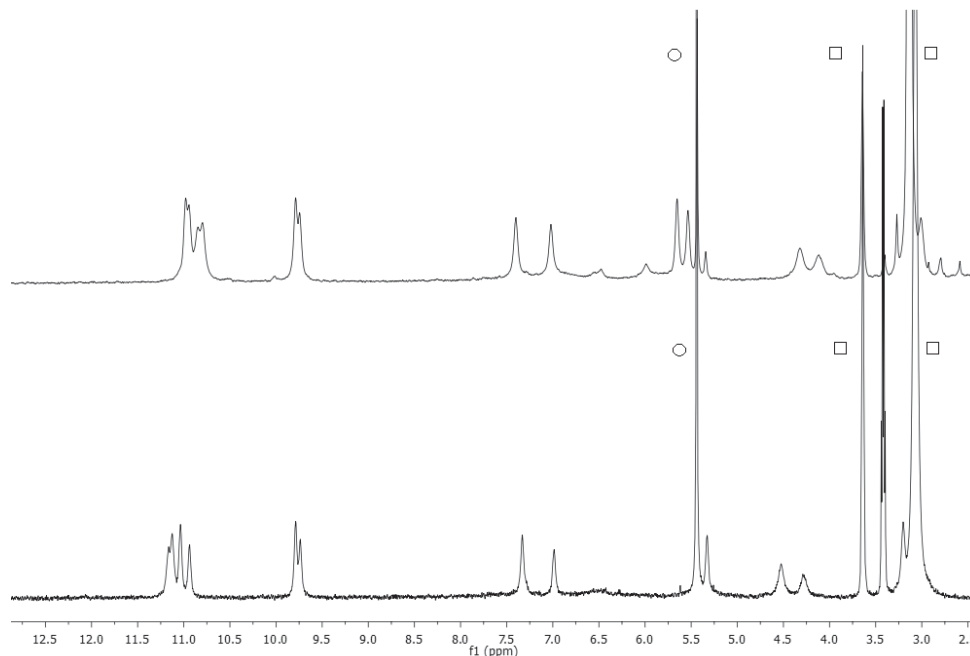


**Figure 8.8:**  $^1\text{H}$  NMR spectrum of  $4(\text{NEt}_4)_2$  at 298 K (bottom) and after addition of 30 eq.  $\text{LiOTf}$  (top). Signals from residual solvent (○) and counter ions  $\text{NEt}_4^+$  (□) are labelled.

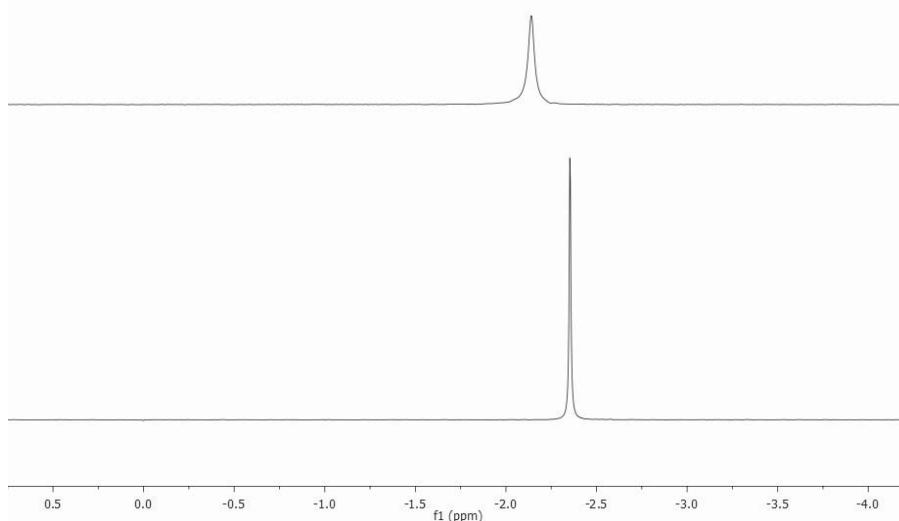


**Figure 8.9:**  $^7\text{Li}$  NMR of free  $\text{LiOTf}$  in  $\text{MeCN-d}_3$  (bottom) and of a 14:1 mixture of  $4(\text{NEt}_4)_2$  and  $\text{LiOTf}$  (top) measured at room temperature.

### 8.2.3 Effect of Li<sup>+</sup> Binding on Electrochemical Properties of 4<sup>2-</sup>

The effect of coordinated lithium ions on the redox properties of 4<sup>2-</sup> was studied by cyclic voltammetry at room temperature. Therefore a cyclic voltammogram of 4(NEt<sub>4</sub>)<sub>2</sub> was recorded in 0.1 M NBu<sub>4</sub>PF<sub>6</sub> solution in MeCN in the absence of LiOTf and after addition of 11.0 eq LiOTf and after addition of a total of 30.0 eq LiOTf (Figure 9.10). Addition of LiOTf leads to a significant broadening of the observed redox wave for the Fe<sup>III</sup>Fe<sup>III</sup>/Fe<sup>III</sup>Fe<sup>II</sup> couple with the peak-to-peak separation increasing from 110 mV to 450 mV when measured at a scan rate of 200 mV s<sup>-1</sup>. This broadening is accompanied by a very small shift (-20 mV) of the position of the wave with  $E_{1/2}$  increasing from -1.378 V vs. Fc/Fc<sup>+</sup> to -1.358 V vs. Fc/Fc<sup>+</sup>. It must be taken into consideration that the addition of 30.0 eq LiOTf increases the total salt concentration in the electrochemical cell from 0.1 M to 0.136 M which corresponds to an increase of 36%. The observed broadening and slight shift of the redox wave may at least in some part be a result of this change in experimental conditions. The observed broadening of the wave, *i.e.* the reduced rate of electron transfer may be due to an EC mechanism. Reduction results in an additional negative charge on the [2Fe–2S] cluster, which might lead to a stronger bonding interaction between the cluster and Li<sup>+</sup> due reasons of electrostatics. The structural changes associated with binding of Li<sup>+</sup> might lead to the observed partial loss of reversibility.

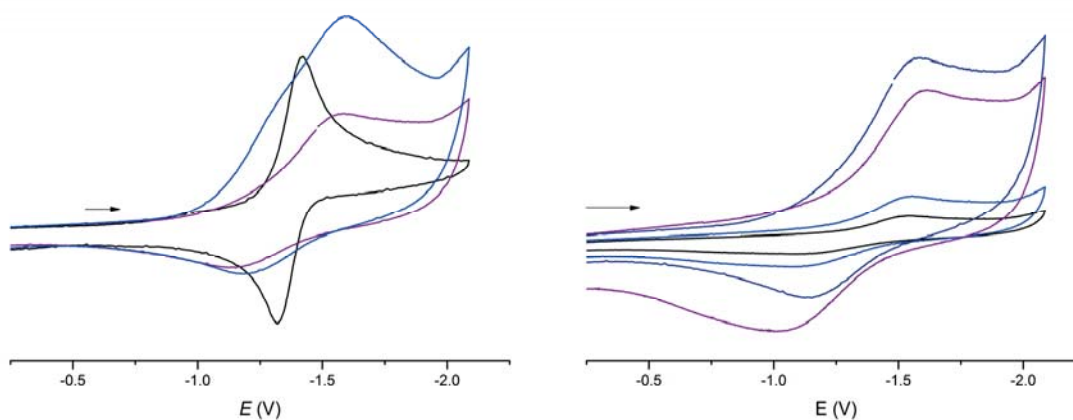


**Figure 8.10:** Left: Cyclic voltammograms of 4<sup>2-</sup> (black) in 0.1 M NBu<sub>4</sub>PF<sub>6</sub> solution in MeCN at 23 °C after addition of 11 eq LiOTf (blue) and 30 eq LiOTf (purple) at 200 mV s<sup>-1</sup> shows a pronounced broadening and a slight shift of the observed reduction wave. Right: Cyclic voltammogram of 4<sup>2-</sup> (in 0.1M NBu<sub>4</sub>PF<sub>6</sub> in MeCN at 23 °C) after addition of 30 eq LiOTf at different scan rates: 50 (black), 100 (blue), 200 (dark blue) and 400 (purple) mV s<sup>-1</sup>.

### 8.2.4 Binding of Na<sup>+</sup> to Homoleptic Cluster 4<sup>2-</sup>

To investigate the effect of different cation sizes, binding experiments using Na<sup>+</sup> were performed. Addition of NaOTf to a solution of 4<sup>2-</sup> in MeCN shows similar effects compared

to the observed changes upon addition of LiOTf. However, in case of Na<sup>+</sup> as coordinating cation, about 600 eq of NaOTf are needed to reach the final equilibrium (Figure 8.11). This is well in line with a proposed binding strength decreasing with an increasing radius of the cation following  $r(\text{H}^+) < r(\text{Li}^+) < r(\text{Na}^+) < r(\text{K}^+)$ .<sup>[234]</sup> Due to the limited solubility of NaOTf in MeCN this makes it impossible to study the effect of Na<sup>+</sup> binding on the electrochemical properties of **4**<sup>2-</sup>. It is also not possible to obtain a reliable Job plot or to investigate the final equilibrium state by <sup>1</sup>H NMR spectroscopy due to the same reasons. Since the spectroscopic changes are very similar to those observed for the addition of Li<sup>+</sup> it can be assumed that the binding site and stoichiometry are the same when using Li<sup>+</sup> or Na<sup>+</sup>. Thus a 1:2 binding interaction was assumed and data from UV-vis titration experiments were fit to yield two binding constants  $K_1$  and  $K_2$ :

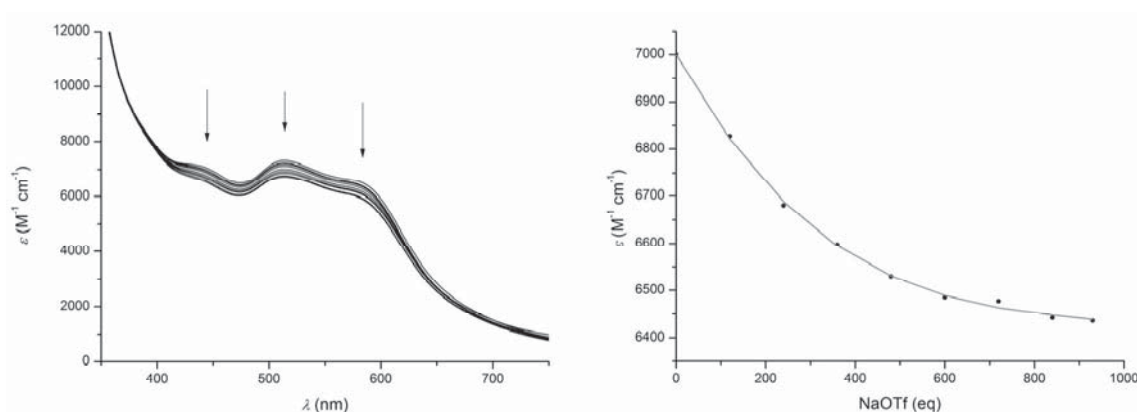
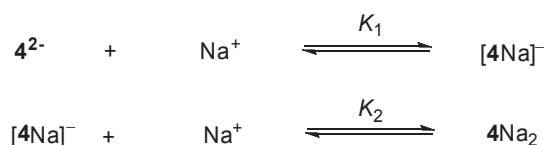


**Figure 8.11:** Left: UV-vis spectral changes observed during the addition of NaOTf to **4**(NEt<sub>4</sub>)<sub>2</sub> in MeCN, each line represents the addition of 100 eq. Right: Extinction coefficient for the band at 434 nm observed after addition of varying amounts of NaOTf and fit obtained by bindfit v0.5 (grey).

Three independent titration experiments were performed using NaOTf and binding constants were determined using bindfit v0.5 available *via* supramolecular.org.<sup>[244]</sup> These independent runs yielded average values of  $K_1 = (4.42 \pm 1.5) \text{ M}^{-1}$  and  $K_2 = (4.74 \pm 4.5) \text{ M}^{-1}$ . These binding constants are almost two orders of magnitude smaller than those determined for the interaction of **4**<sup>2-</sup> and Li<sup>+</sup>. As already mentioned in the case of LiOTf, the error of the obtained values is large, especially the error of  $K_2$ . Within their error, both binding constants  $K_1$  and  $K_2$  are identical which might indicate that binding of Na<sup>+</sup> to each of the possible binding sites occurs independent from the other.

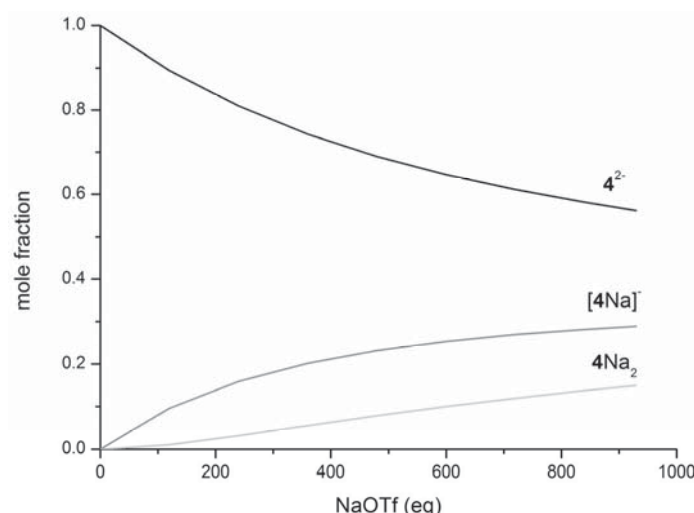


**Figure 8.12:** Mole fractions of  $4^{2-}$ ,  $[4Na]^-$  and  $4Na_2$  present in solution vs. eq NaOTf added, determined using bindfit v0.5.

A plot of the mole fractions of the species present in solution (obtained from bindfit v0.5) shows that even when saturation is reached in the visible absorption spectra, “free” cluster  $4^{2-}$  is the main species present in solution (Figure 8.12). The assumed product of the 1:2 binding interaction,  $4Na_2$ , is present only as about 16 %. As a consequence, it was impossible to obtain crystalline material of this product suitable for X-ray crystallography. Since binding of  $Na^+$  is already rather weak, no experiments concerning the binding of  $K^+$  were performed. Since the strength of the interaction seems to decrease with an increasing radius of the respective alkali metal cation, very high amounts of  $K^+$ , which can hardly be achieved due to solubility issues, are expected to be necessary in order to observe any effect on the properties of cluster  $4^{2-}$ .

### 8.3 Binding Alkali Metal Ions to Heteroleptic Cluster $26^{2-}$

Since it is bearing only one benzimidazole moiety, heteroleptic cluster  $26^{2-}$  offers only a single potential N-atom in the peripheral ligand for binding of an alkali metal ion. Addition of LiOTf was monitored by UV-vis spectroscopy in MeCN at room temperature. The decrease in intensity of the band at 424 nm upon addition of increasing amounts of LiOTf is very similar to the changes in UV-vis spectra which were observed during protonation experiments (see chapter 6.5.1). However, about 250 eq of LiOTf are necessary to reach saturation (Figure 8.13). Since the binding is assumed to be a 1:1 interaction the association constant is defined as:

$$K_a = \frac{[26Li]^-}{([26^{2-}][Li])}$$

The disappearing band at 424 nm can be used to quantify the amount of “free” cluster and of the complex  $[26\text{Li}]^-$ . The dissociation constant can be determined by fitting the titration data to a 1:1 model using bindfit v0.5.<sup>[244]</sup>

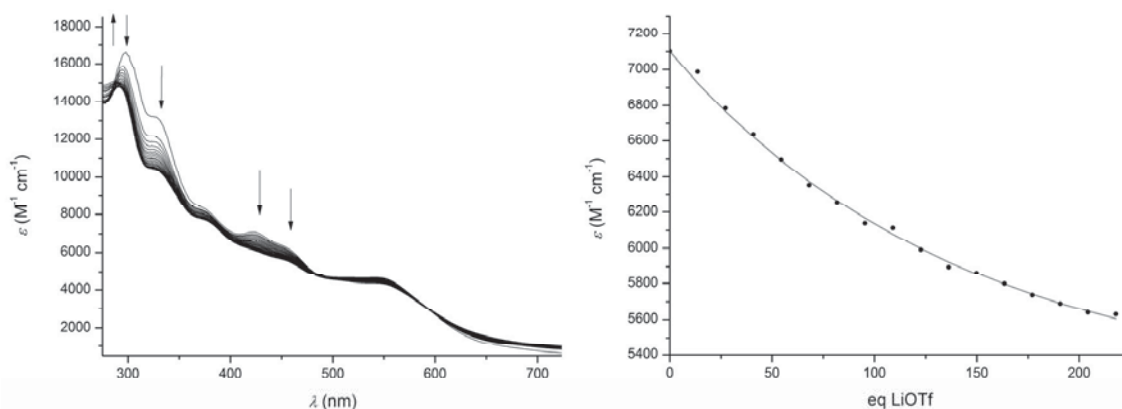


**Figure 8.13:** Left: UV-vis absorption spectra during a typical titration experiment of  $26^{2-}$  and LiOTf. Each line represents the addition of 14 eq LiOTf. Right: Extinction of the band at 424 nm vs. amount of LiOTf added and fit (red) obtained using bindfit v0.5.

Three independent runs were performed ( $K_a = 1.232, 0.140, 0.292 \text{ M}^{-1}$ ) and an average association constant of  $K_a = (0.555 \pm 0.45) \text{ M}^{-1}$  was obtained. Exemplary spectra and a linear fit of a typical run are shown in figure 8.11. Since about 250 eq LiOTf are needed to reach the final equilibrium, it was not possible to obtain  $^1\text{H}$  NMR spectra of the species in this equilibrium or to obtain reliable data on electrochemical behavior of  $[26\text{Li}]^-$ . Since the changes in UV-vis absorption spectra upon addition of the first 15 eq are negligible, it was not possible to verify the proposed 1:1 binding interaction *via* a Job plot. No further experiments using  $\text{Na}^+$  or  $\text{K}^+$  were performed. The smaller binding constant determined for the interaction of  $26^{2-}$  with Li compared to the ones for  $4^{2-}$  with  $\text{Li}^+$  cannot be easily rationalized. For binding of  $\text{Li}^+$  on the N-atom of the peripheral benzimidazole-type ligand, relatively similar binding constants would have been expected for both clusters.

**Table 8.1:** Binding constants determined for the interaction of clusters  $4^{2-}$  and  $26^{2-}$  with  $\text{Li}^+$  and  $\text{Na}^+$ .

	$4^{2-}$	$26^{2-}$
$K(\text{Li}^+) (\text{M}^{-1})$	279; 131	0.55
$K(\text{Na}^+) (\text{M}^{-1})$	4.42; 4.74	–

Thus, to get further insight into whether the observed interaction is indeed due to binding of  $\text{Li}^+$  to the N-atoms of the benzimidazole moiety rather than to the bridging sulfides or thiolate donors, titration experiments were performed using thiolate coordinated cluster  $27^{2-}$

and LiOTf. However, even after addition of 340 eq of LiOTf to a solution of **27**(NEt<sub>4</sub>)<sub>2</sub> in MeCN, no significant changes were observed in the visible absorption spectra (Figure 8.14, left). These findings further support the assumption of Li<sup>+</sup> binding to the N-atoms in the backbone of the ligand rather than to the bridging sulfides or terminal thiolates. However, cluster **27**<sup>2-</sup> seems to be unstable in presence of large amounts of LiOTf, as all bands in the visible absorption spectrum decreased over the course of 40 minutes (Figure 8.14, right).

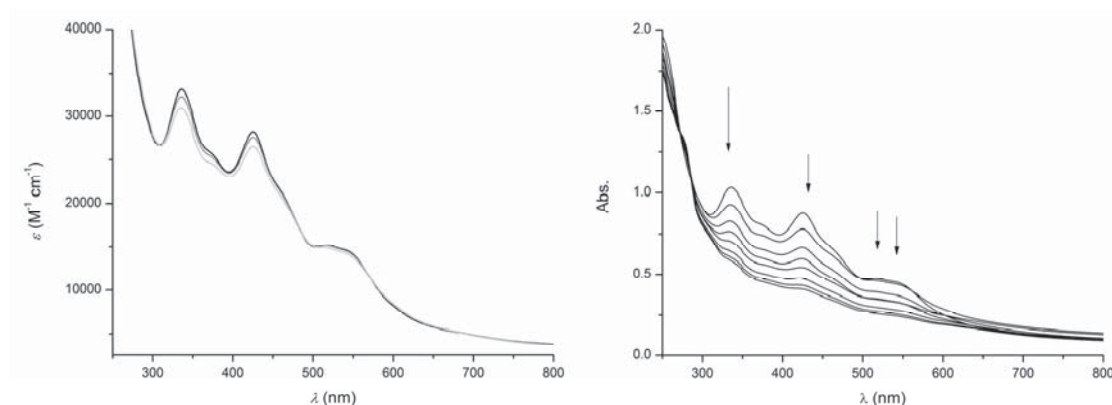


**Figure 8.14:** Left: UV-vis absorption spectra of **27**<sup>2-</sup> and after addition of 170 eq (red) and 340 eq (blue) LiOTf. Right: Decay of **27**<sup>2-</sup> after addition of 340 eq LiOTf over 40 min.

## 8.4 Binding Alkali Metal Cations with Homoleptic Cluster **12a**<sup>2-</sup>

Addition of LiOTf to homoleptic cluster **12a**<sup>2-</sup> led to changes in the cluster's UV-vis absorption spectra, similar to what has previously been observed in protonation experiments. Upon addition of LiOTf a band at 380 nm rises. However, this change does not occur immediately but over a period of about 10 minutes (Figure 8.15): the band at 380 nm rises until it almost reaches a maximum after 11 min, after which the rate of the observed increase is slowed down. After 30 min formation of a precipitate was observed. This behavior makes titration experiments, as described in chapters 8.2 and 8.3., impossible and thus no bonding constant was determined. One reason for this behavior may be a rapid initial binding of the alkali metal cation followed by slow tautomerization of the ligand, which then leads to the emergence of the characteristic band at 380 nm as described in chapter 1.6. Addition of more than 2.0 eq did not lead to an increase in the rate with which this band grows, or its final intensity.

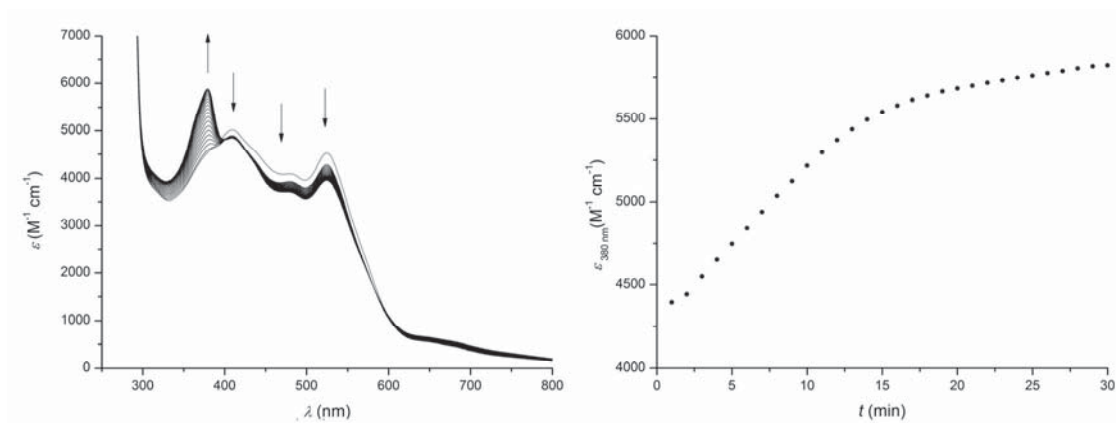


**Figure 8.15:** Left: UV-vis absorption spectra of  $12a^{2-}$  before and after addition of 2.0 eq LiOTf, (black, each line represents an interval of 1 min). Right: The extinction coefficient of the band at 380 nm rises until reaching a maximum after 30 min. After more than 30 min precipitation of solid material was observed.

Addition of NaOTf to a solution of  $12a(NEt_4)_2$  in MeCN lead to similar changes in UV-vis absorption spectroscopy (Figure 8.16). The characteristic band at 380 nm rises over a period of 12 min, followed by slow decomposition of the cluster. However, the final extinction of this band is significantly lower in comparison to what has been observed in experiments with LiOTf. This may indicate a weaker M–N bond when comparing Na–N to the Li–N, which would be well in line with the findings described for experiments using clusters  $4^{2-}$ . Indeed, the capability of binding to the [2Fe–2S] cluster’s ligand seems to decrease with an increasing radius of the respective cation.

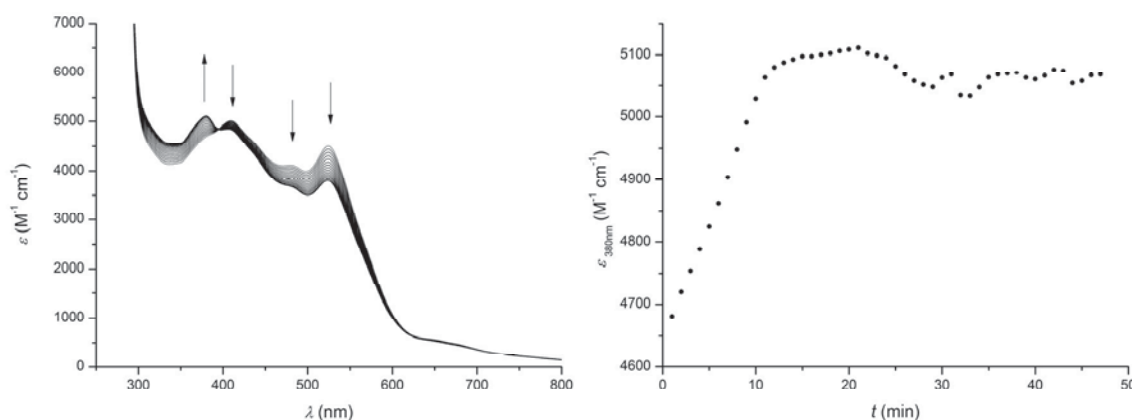


**Figure 8.16:** Left: UV-vis absorption spectra of  $12a^{2-}$  and after addition of 4.0 eq NaOTf monitored for 12 min, (black, each line represents an interval of 1 min). Right: The extinction coefficient of the band at 380 nm rises until reaching a maximum after 10 min and then slowly decreases.

Addition of 13.0 eq LiOTf to a solution of  $12a(NEt_4)_2$  in a 0.1 M solution of  $NBu_4PF_6$  led to an anodic shift in the cyclic voltammogram of about  $-120$  mV (Figure 8.17). This shift is

smaller than the shift of  $-200$  mV observed upon protonation. The additional positive charges provided by (presumably) two binding  $\text{Li}^+$  cations make it easier to accommodate for an additional electron. This makes reduction of the cluster easier and thus shifts the first reduction wave to a higher (*i.e.* less negative) potential. However, the compound decayed during the measurement and the formation of brown solid material was observed. Consequently, the exact nature of the species analyzed by cyclic voltammetry remains unclear.

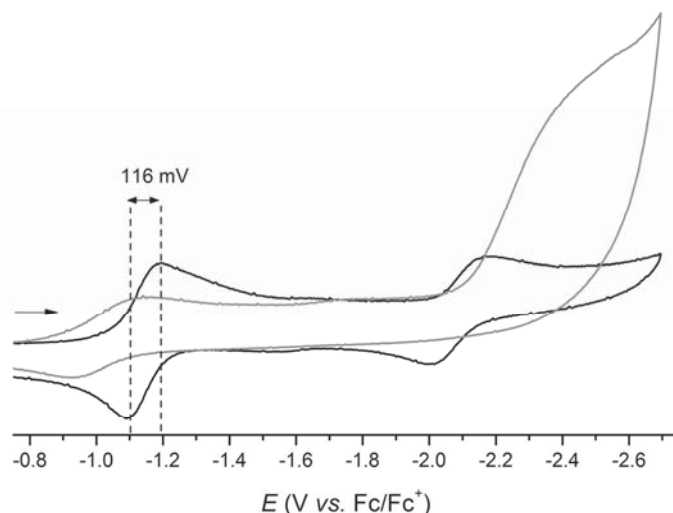


**Figure 8.17:** Cyclic voltammograms (in 0.1M  $\text{NBu}_4\text{PF}_6$  in MeCN at 23 °C) of  $\mathbf{12a}^{2-}$  (black) after addition of 13.0 eq LiOTf (grey) at  $200 \text{ mV s}^{-1}$  shows a pronounced broadening and a shift of 116 mV of the first observed reduction wave. Arrow indicates the direction of scans.

By serendipity, single crystals suitable for X-ray crystallography were obtained from a solution of  $\mathbf{12a}(\text{NEt}_4)_2$  in DMF in the presence of  $\text{Na}^+$  cations complexated by 15-crown-5 and bis(catechol)silicates at  $-20$  °C, initially prepared for investigating potential radical reactions (see chapter 9.2). The structure shows, that two sodium cations complexated by 15-crown-5 are bound to the benzimidazole moieties in the ligand's backbone with a N–Na distance of 2.40 Å (Figure 8.18). The [2Fe–2S] core is slightly compressed by the interactions with the two  $[(15\text{-crown-5})\text{Na}]^+$  cations as indicated by slightly decreased bond lengths and a decreased  $\text{Fe}\cdots\text{Fe}$  distance, as well as a smaller  $\text{Fe}-\mu\text{S}-\text{Fe}$  angle (Table 8.2). No tautomerization of the ligand is observed in this structure, which may be due to the steric bulk of the crown ether preventing geometrical rearrangement of the ligand. Addition of a solution of 1.5 eq  $[(15\text{-crown-5})\text{Na}]\text{bis(catechol)silicates}$  in MeCN to a solution of  $\mathbf{12a}^{2-}$  in MeCN led to immediate rise of the characteristic band at 380 nm. However, this band along with all other bands of the typical cluster spectrum rapidly decreased over 13 minutes (Figure 8.19). This rapid concurrent decomposition or rearrangement makes any possible titration experiment unreliable and thus no binding constants could be determined.

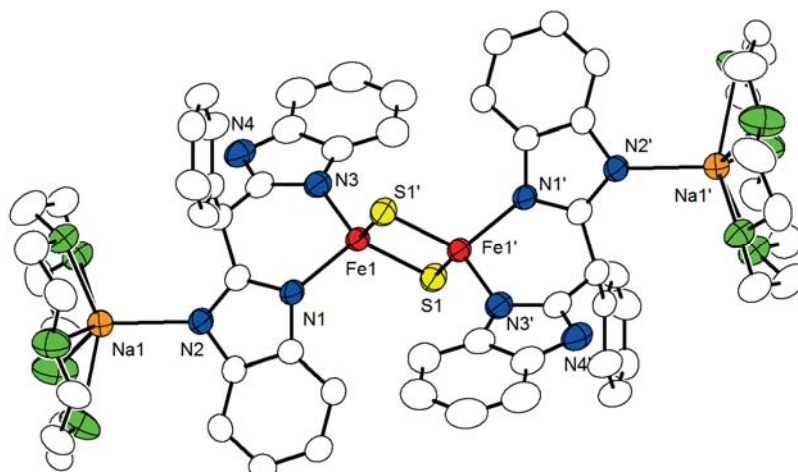


**Figure 8.18:** Molecular structure of the complex of  $12a^{2-}$  and 2.0 eq  $Na[15\text{-crown-}5]^+$  in the solid, hydrogen atoms have been omitted for clarity.

**Table 8.2:** Selected bond lengths (Å) and angles ( $^\circ$ ) of diferric cluster  $12a(NEt_4)_2$  and  $12a[(15\text{-crown-}5)Na]_2$ .

	$12a(NEt_4)_2^{[149]}$	$12a[(15\text{-crown-}5)Na]_2$
$d(Fe\cdots Fe)$	2.7019(5)	2.67474(7)
$d(Fe-\mu S)$	2.1938(5)–2.2081(5)	2.1831(8)–2.1922(8)
$d(Fe-N_{lig})$	1.9776(14)–1.9905(12)	1.980(2)–1.991(2)
$\angle(Fe-\mu S-Fe)$	75.727(16)	74.47(3)

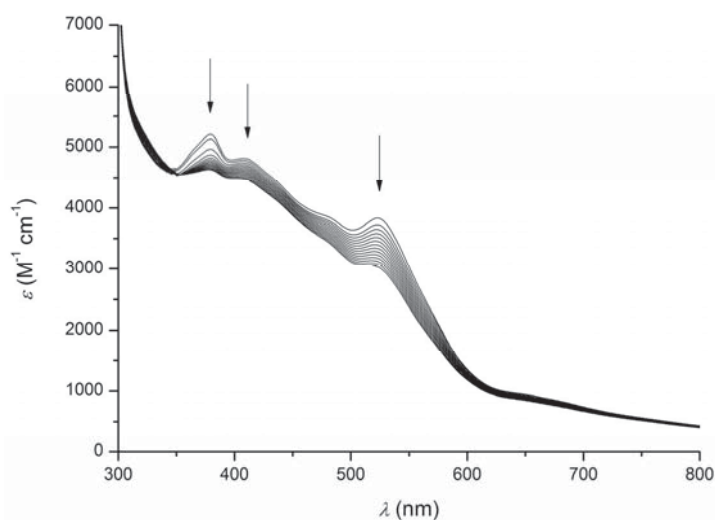


**Figure 8.19:** UV-vis absorption spectra of  $12a^{2-}$  after addition of 1.5 eq  $[(15\text{-crown-}5)Na]$ benzyl-bis(catechol)silicate, monitored for 13 min (each line represents an interval of 1 min).



## 8.5 Conclusion

In this chapter alkali metal cations  $\text{Li}^+$  and  $\text{Na}^+$  have been shown to bind to synthetic [2Fe–2S] clusters, likely to the N-atoms in the backbone of the benzimidazole-based terminal ligands. The UV-vis and  $^1\text{H}$  NMR spectroscopic changes observed upon coordination are similar to those observed during protonation experiments, suggesting that both events occur on the same binding site in the cluster. The interaction of diferric clusters  $\mathbf{4}^{2-}$  and  $\mathbf{26}^{2-}$  with  $\text{Li}^+$  and  $\text{Na}^+$  cations is however very weak and depends on the size of the cation. No similar spectroscopic changes were observed in experiments using  $\{\text{S}_2\}\{\text{S}_2\}$  coordinated cluster  $\mathbf{27}^{2-}$ , supporting the assumption that cation binding takes place on the N-atoms of the benzimidazole-type capping ligands. This chapter has shown that interactions of redox-inert alkali metal ions with iron-sulfur clusters are possible when so called alternative ligands are present to offer a potential binding site. These findings may suggest both a role of iron sulfur clusters in sensing of those biologically relevant metal ions and a role of these omnipresent metal ions in modulating the properties and reactivity of the respective iron sulfur cofactors.

## 9 Biomimetic [2Fe–2S] Clusters in Radical Reactions

### 9.1 Introduction

Reactions involving iron sulfur clusters and organic radicals are key steps in several biological processes including biotin biosynthesis as a prominent example (see chapter 1.5). To date, no functional model mimicking this very special reactivity of iron sulfur clusters has been reported. First studies on potential functional model systems will be presented in this chapter. Various iron sulfur clusters have therefore been investigated with respect to their reactivity toward different organic radicals.

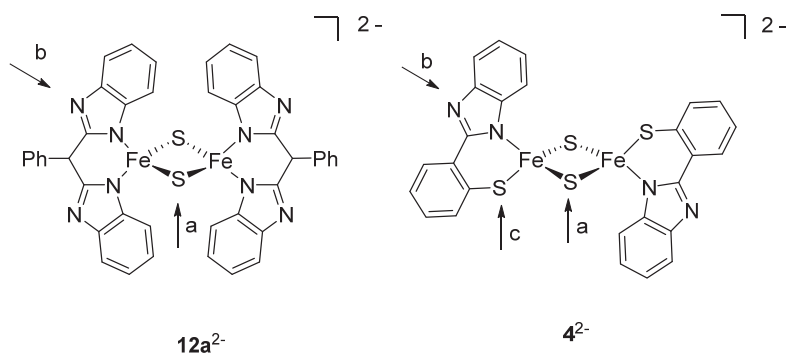


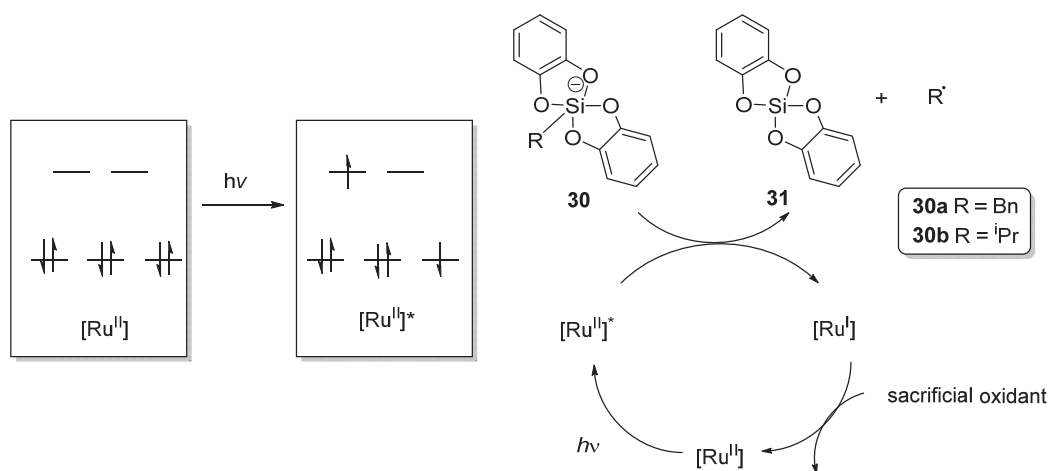
**Figure 9.1:** Possible sites for attack by an organic radical (as indicated by arrows) in synthetic [2Fe–2S] clusters  $12a^{2-}$  and  $4^{2-}$ .

As a first possible reactant cluster  $12a^{2-}$  was chosen due to its easy accessibility, its relatively high stability and advantageous crystallization properties. Since cluster  $12a^{2-}$  features a distal nitrogen atom in the ligand backbone, different positions for radical attack are possible: The radical may either attack on one of the bridging sulfides of the cluster core (*a* in Figure 9.1) or at the nitrogen atoms in the backbone (*b* in Figure 9.1). During protonation of cluster  $12a^{2-}$  on the distal nitrogen atoms, tautomerization to the fully conjugated ligand was observed as evidenced by the formation of a new band in the visible absorption spectrum at  $\lambda_{\max} = 380 \text{ nm}$  ( $\epsilon = 64\,000 \text{ M}^{-1} \text{ cm}^{-1}$ ), as shown in chapter 1.6. The same behavior was observed during protonation of the free ligand  $L^{NN}H_2$ .<sup>[147]</sup> A similar tautomerization might occur upon radical attack on the nitrogen atom in the backbone of the ligand.

Cluster  $4^{2-}$  was shown to have similar properties regarding accessibility, stability and solubility. Similar to  $12a^{2-}$  it offers three distinct possible sites for radical attack, namely the distal N atoms of the ligand (*b* in Figure 9.1), the thiolates of the terminal ligand (*c* in Figure 9.1), and the bridging sulfides (*a* in Figure 9.1). In contrast to  $12a^{2-}$ , cluster  $4^{2-}$  cannot undergo tautomerization of the ligand. Additionally the slightly smaller ligand in  $4^{2-}$  provides

less steric hindrance and might thus make the bridging sulfides more easily accessible in a radical reaction.

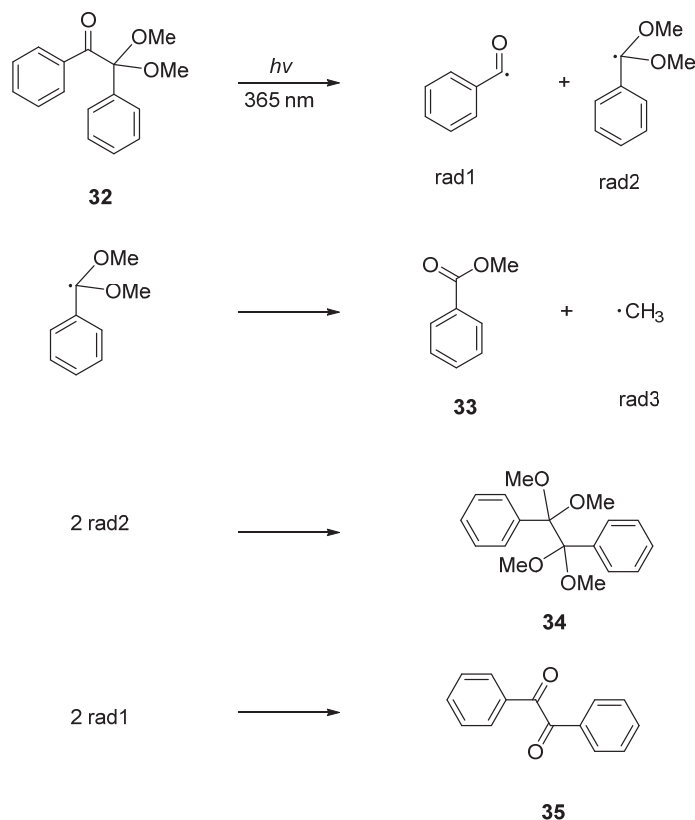
The choice of organic radical proved to be both challenging and crucial in performing the desired reactions with synthetic iron sulfur clusters. While many thermic radical starters have been described, they cannot be used in combination with iron sulfur clusters since they require heating to temperatures above 23 °C at which the clusters themselves or the products of the radical reaction are not stable. The formation of very stable radicals is also undesired since these might not be reactive enough to attack the iron sulfur cluster. The ideal radical would be a reactive, C-centered organic radical which can be generated with good yields at low temperatures and does not display any redox chemistry by itself, *i.e.* does not act as a simple electron-transfer reagent. For a photochemical radical start, the homolytic bond cleavage must be inducible by irradiation with wavelengths at which the iron sulfur cluster itself does not absorb to prevent competing reactions. In this work, two distinct methods for generating organic radicals have been used and will be presented in the following.



**Scheme 9.1:** Simplified scheme for generation of C-centered radicals from silicates using  $[Ru(bpy)_3]^{2+}$  as a photocatalyst as described by Fensterbank.<sup>[245,246]</sup>

Bis(catechol)silicates bearing organic residues as precursors in photolytic radical initiation have been described by Fensterbank and coworkers in 2015 (Scheme 9.1).<sup>[245]</sup> Therefore the presence of a photocatalyst is necessary to achieve oxidation of the silicate and thus cleavage of the Si–C bond to release the organic residue as an organic radical. The most common photocatalyst is  $[Ru(bpy)_3](PF_6)_2$ . Irradiation of this photocatalyst leads to an excited state  $Ru^{2+*}$ , which can act as a strong reductant (due to the presence of an unpaired electron in an orbital, which is high in energy) and as a strong oxidant (due to the resulting “hole” in the lower lying orbital) at the same time.<sup>[246]</sup> A sacrificial oxidant is then necessary to re-oxidize the resulting  $Ru^I$  species to the  $Ru^{II}$  species and perform the reaction in a catalytic way. In the

absence of a sacrificial oxidant, 1.0 eq of the chosen photocatalyst would be needed for full turn-over.



**Scheme 9.2:** Fragmentation of 2,2-dimethoxy-2-phenylacetophenone **32** (DMPA) upon irradiation and selected possible recombination products.

Photolytical radical generation, which does not require the additional presence of oxidants or photosensitizers, appeared to be more promising and 2,2-dimethoxy-2-phenylacetophenone **32** (DMPA) was chosen as a radical starter due to its high solubility in MeCN, its good quantum yield upon irradiation and because it does not release oxygen upon radical initiation. DMPA has been used in laser induced polymerization reactions such as methyl methacrylate homo polymerization.<sup>[247]</sup> Irradiation with light of a wavelength of 365 nm leads to bond cleavage and further rearrangements to yield various organic radicals (Scheme 9.2). While radical rad2 has been described to undergo recombination or further fragmentation releasing a  $\text{CH}_3\cdot$  radical, radical rad1 has been found to act as the initiator for polymerization of methyl methacrylate. Additionally, several recombination products have been observed to occur after radical initiation (Scheme 9.2).<sup>[248]</sup>

## 9.2 Reactions Using Silicates as Radical Starters

### 9.2.1 Cluster $12a^{2-}$ and Radicals Generated from Silicates

If only catalytic amounts of  $[\text{Ru}(\text{bpy})_3]^{2+}$  are to be used for the photochemical generation of radicals from silicates **30a** and **30b**, a sacrificial oxidant is needed. In this work,  $\text{Co}^{\text{III}}$  was chosen as a sacrificial oxidant and reaction mixtures containing **12a**(NEt<sub>4</sub>)<sub>2</sub>, 0.1 eq  $[\text{Ru}(\text{bpy})_3]^{2+}$ , 1.0 eq  $[\text{Co}(\text{NH}_3)_6]\text{Cl}_3$  and 1.5 eq of the respective silicate were prepared in DMF. The formation of insoluble salts from  $[\text{Ru}(\text{bpy})_3]^{2+}$  and **12a**<sup>2-</sup> prevented the use of MeCN as a solvent. Upon irradiation of the resulting reaction mixtures with LEDs emitting with a maximum at 365 nm, a rhombic EPR signal, which may correspond to a reduced [2Fe–2S] cluster was observed. However, the intensity of this signal is very low and the overall spectrum is dominated by a very intense signal at  $B \approx 160$  mT, *i.e.* with a  $g$ -value of about 4.2 (Figure 9.2). This signal may arise from the presence of paramagnetic cobalt species. The same results were found when using *iso*-propyl silicate **30b** instead of **30a**.

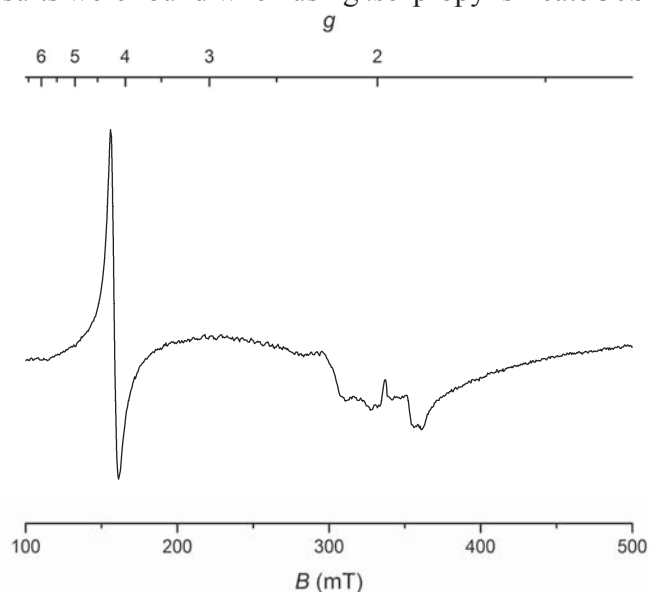


**Figure 9.2:** EPR spectrum recorded after irradiation of **12a**(NEt<sub>4</sub>)<sub>2</sub>, 1.0 eq  $[\text{Co}(\text{NH}_3)_6]\text{Cl}_3$ , 0.15 eq  $[\text{Ru}(\text{bpy})_3](\text{PF}_6)_2$  and 1.5 eq benzyl silicate **30a** in DMF; recorded in frozen solution at 144 K.

The reaction was also followed by UV-vis spectroscopy (Figure 9.3). Upon irradiation, the characteristic absorption bands of the cluster decrease while a new band at 400 nm is rising, which is reminiscent of the band at 390 nm which was previously observed upon tautomerization of the ligand during protonation experiments. After 20 min a shoulder at 587 nm is visible. Even though the intensity of this shoulder is very low, it may indicate the presence of a mixed valent [2Fe–2S] species.

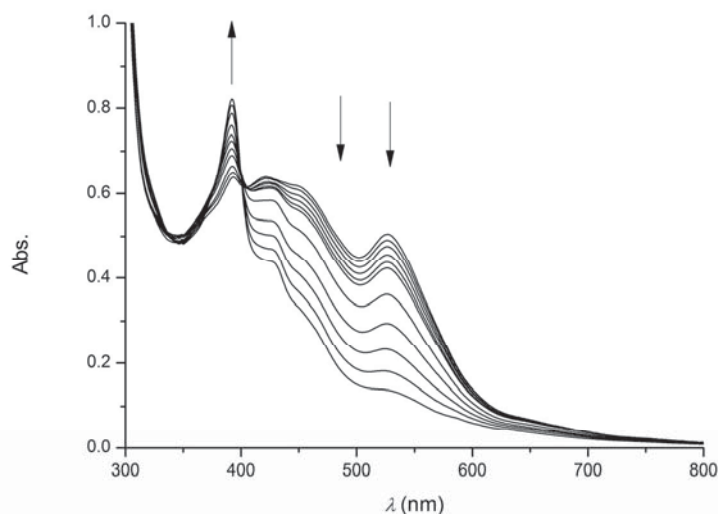


**Figure 9.3:** UV-vis spectral changes observed upon irradiation of a 1:1 mixture of **12a**(NEt<sub>4</sub>)<sub>2</sub>, 1.0 eq [Co(NH<sub>3</sub>)<sub>3</sub>]Cl<sub>3</sub> and 0.15 eq [Ru(bpy)<sub>3</sub>](PF<sub>6</sub>)<sub>2</sub> and 1.5 eq benzyl silicate **30a** in DMF at –20°C. Each line represents an irradiation time of 2 min.

Since the presence of a sacrificial oxidant may not only lead to re-oxidation of the excited ruthenium species but may also cause oxidation of the supposedly very sensitive product of a possible radical reaction occurring on the iron sulfur cluster, subsequent experiments were carried out in the absence of a sacrificial oxidant by using 1.0 eq [Ru(bpy)<sub>3</sub>](PF<sub>6</sub>)<sub>2</sub>. A Solution of **12a**(NEt<sub>4</sub>)<sub>2</sub> containing 1.0 eq [Ru(bpy)<sub>3</sub>](PF<sub>6</sub>)<sub>2</sub> and 1.5 eq benzyl silicate **30a** were prepared in DMF and irradiated with LEDs emitting at 365 nm. A rhombic signal with  $g_1 = 2.01$ ,  $g_2 = 1.918$ ,  $g_3 = 1.87$ , and  $g_{av} = 1.932$  was observed in the EPR spectrum recorded in frozen solution at 160 K and indicates the presence of a mixed valent [2Fe–2S] species (Figure 9.4). The intensity of the signal at  $B = 150$  mT is significantly decreased by avoiding the presence of Co<sup>III</sup> species. However, the observed rhombic signal showed a very low intensity even though relatively high concentrations (about 10 mg/mL) were used. One of the problems occurring in this type of reaction might be the presence of the excited [Ru(bpy)<sub>3</sub>]<sup>\*2+</sup>, which can act as a strong oxidant not only in generating an organic radical but also in re-oxidizing the mixed valent [2Fe–2S] cluster formed upon radical attack. The excited molecule [Ru(bpy)<sub>3</sub>]<sup>2+\*</sup> also acts as a strong reducing agent with a reduction potential of –0.568 V vs. NHE. Since the potential for reduction of **12a**<sup>2–</sup> is –0.742 V vs. NHE, excited [Ru(bpy)<sub>3</sub>]<sup>2+\*</sup> should not be a strong enough reducing agent to achieve reduction of **12a**(NEt<sub>4</sub>)<sub>2</sub>. To fully exclude reduction of **12a**(NEt<sub>4</sub>)<sub>2</sub> by excited [Ru(bpy)<sub>3</sub>]<sup>2+\*</sup> under the conditions used herein, a sample containing only **12a**(NEt<sub>4</sub>)<sub>2</sub> and 1.0 eq [Ru(bpy)<sub>3</sub>](PF<sub>6</sub>)<sub>2</sub> in DMF was prepared and irradiated with LEDs emitting at 365 nm for 5 min. No signal was detected in the EPR spectrum of this sample, showing that the reduction observed in the previous experiments must arise from a reaction with an organic radical rather than from simple one electron reduction by [Ru(bpy)<sub>3</sub>]<sup>2+\*</sup>.

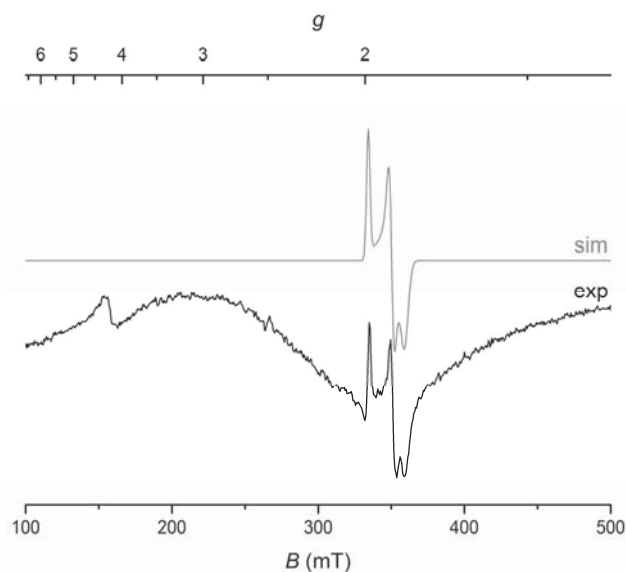


**Figure 9.4:** Experimental EPR spectrum recorded after irradiation ( $\lambda = 365$  nm) of **12a**(NEt<sub>4</sub>)<sub>2</sub>, 1.0 eq [Ru(bpy)<sub>3</sub>](PF<sub>6</sub>)<sub>2</sub>, and 1.5 eq benzyl silicate **30a** in DMF; recorded in frozen solution at 160 K (black) and simulation using the parameters given in the text (grey).

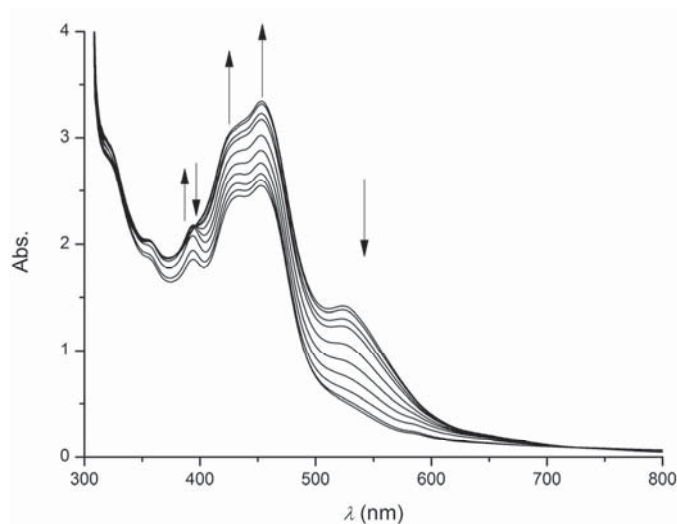


**Figure 9.5:** UV-vis absorption spectra during the irradiation of a mixture of **12a**(NEt<sub>4</sub>)<sub>2</sub>, 1.0 eq Ru(bpy)<sub>3</sub>(PF<sub>6</sub>)<sub>2</sub>, and 1.5 eq benzyl silicate **30a** in DMF at  $-20^{\circ}\text{C}$ . Each line represents an irradiation time of 3 min.

The reaction was also monitored by UV-vis spectroscopy. After an irradiation time of about 15 min, a shoulder at 587 nm indicative of the mixed valent [2Fe–2S] cluster is visible with low intensity. The overall spectrum is more difficult to interpret since bands arising from absorptions of the ruthenium complex and those arising from the [2Fe–2S] cluster are overlaid (Figure 9.5).

ESI mass spectra of the reaction solutions were obtained, but none of the anticipated products could be observed. Despite efforts to obtain solid material by evaporation of the solvent after the reaction or addition of diethyl ether, Mößbauer spectra of the obtained solids always showed the presence of only one doublet corresponding to a ferric species.

## 9.2.2 Cluster $4^{2-}$ and Benzyl Radicals Generated from Silicates

Experiments using  $4(\text{NEt}_4)_2$  and **30b** in the presence of  $[\text{Ru}(\text{bpy})_3](\text{PF}_6)_2$  as a radical starter were performed in close analogy to the experiments described for  $12\text{a}(\text{NEt}_4)_2$  (see chapter 9.2.1). Solutions of  $4^{2-}$ , 1.0 eq  $\text{Ru}(\text{bpy})_3(\text{PF}_6)_2$  and 1.5 eq **30a** without a sacrificial oxidant were prepared in DMF and irradiated with LEDs emitting at 365 nm for 5 min. A rhombic EPR spectrum was observed indicating the presence of a mixed valent [2Fe–2S] cluster with an  $S = 1/2$  ground state (Figure 9.6). The same EPR signal was observed when *iso*-propyl silicate **30b** was used.

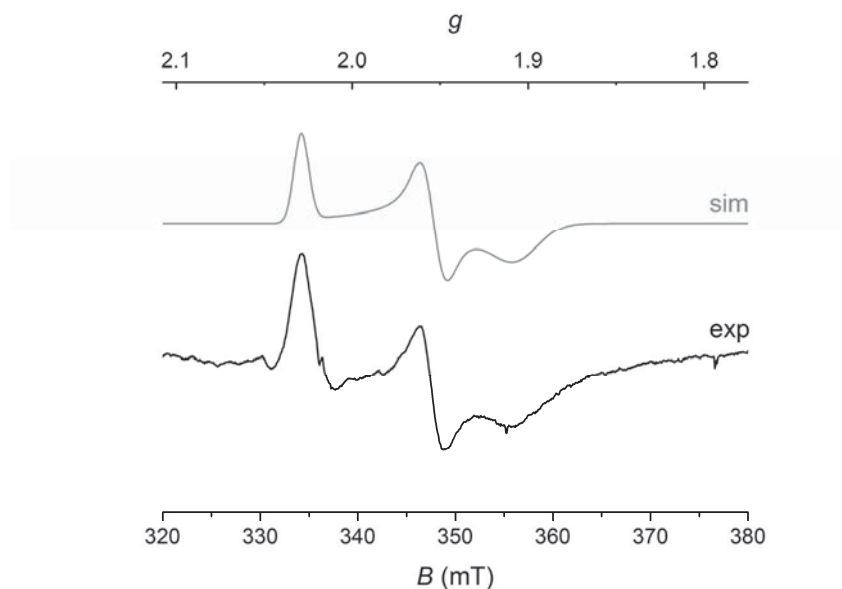


**Figure 9.6:** EPR spectrum recorded after irradiation of  $4(\text{NEt}_4)_2$ , 1.0 eq  $[\text{Ru}(\text{bpy})_3](\text{PF}_6)_2$  and 1.5 eq benzyl silicate **30a** in DMF; recorded in frozen solution at 144 K (black). The grey line is a simulation yielding  $g_1 = 2.012$ ,  $g_2 = 1.936$ ,  $g_3 = 1.89$  and  $g_{\text{av}} = 1.946$ .

A simulation of the experimental EPR spectrum yielded the following parameters:  $g_1 = 2.015$ ,  $g_2 = 1.936$ ,  $g_3 = 1.89$ ,  $g_{\text{av}} = 1.947$  (Figure 9.6). These values are relatively similar to the values found for chemically reduced cluster  $4^{3-}$  ( $g_1 = 2.010$ ,  $g_2 = 1.932$ ,  $g_3 = 1.882$ , and  $g_{\text{av}} = 1.941$ , see chapter 3.4). Similar to what was observed in reactions using cluster  $12\text{a}^{2-}$ , the intensity of the signal was very low, even though high concentrations were used and

different irradiation times were chosen. This might either indicate low stability of the resulting mixed valent species or incomplete turnover.

This reaction was also followed by UV-vis spectroscopy (Figure 9.7). However, the analysis of the resulting spectra is difficult due to overlapping bands arising from cluster  $\mathbf{4}(\text{NEt}_4)_2$  and  $[\text{Ru}(\text{bpy})_3](\text{PF}_6)_2$ . A reaction mixture of  $\mathbf{4}(\text{NEt}_4)_2$ , 1.0 eq  $[\text{Ru}(\text{bpy})_3](\text{PF}_6)_2$  and 1.5 eq  $\mathbf{30a}$  in DMF was irradiated with LEDs emitting at 365 nm and UV-vis spectra were recorded every 3 min. During the reaction all bands corresponding to the presence of cluster  $\mathbf{4}^{2-}$  decrease in intensity while the shoulder at 410 nm is emerging. Full conversion is indicated by the complete vanishing of the cluster spectrum, but no indication for the formation of a mixed valent species can be gained from this experiment.

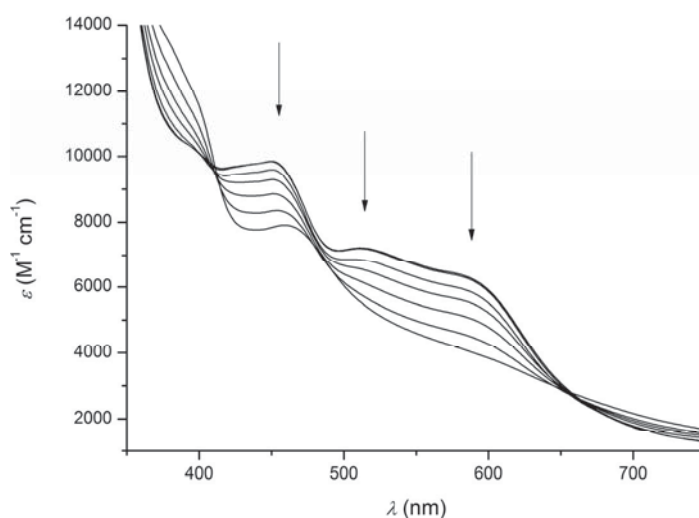


**Figure 9.7:** UV-vis absorption spectra during the irradiation of a 1:1 mixture of  $\mathbf{4}(\text{NEt}_4)_2$ , 1.0 eq  $[\text{Ru}(\text{bpy})_3](\text{PF}_6)_2$  and 1.5 eq benzyl silicate  $\mathbf{30a}$  in DMF at  $-20^\circ\text{C}$ . Each line represents an irradiation time of 3 min.

## 9.3 Reactivity of $12a(\text{NEt}_4)_2$ Toward Organic Radicals Generated from DMPA

### 9.3.1 Spectroscopy in Solution

Cluster  $12a(\text{NEt}_4)_2$  was mixed with 1.0 eq of DMPA in MeCN or DMF and the resulting mixture was irradiated with different light sources at  $-20^\circ\text{C}$  for varying times. Both irradiation with the whole spectral range of 200 – 600 nm as well as irradiation with an LED emitting with a maximum at 365 nm led to the formation of the same characteristic EPR spectrum. A simulation of the experimental spectrum yielded the following parameters:  $g_1 = 2.01$ ,  $g_2 = 1.916$ ,  $g_3 = 1.860$ ,  $g_{\text{av}} = 1.928$  (Figure 9.8).

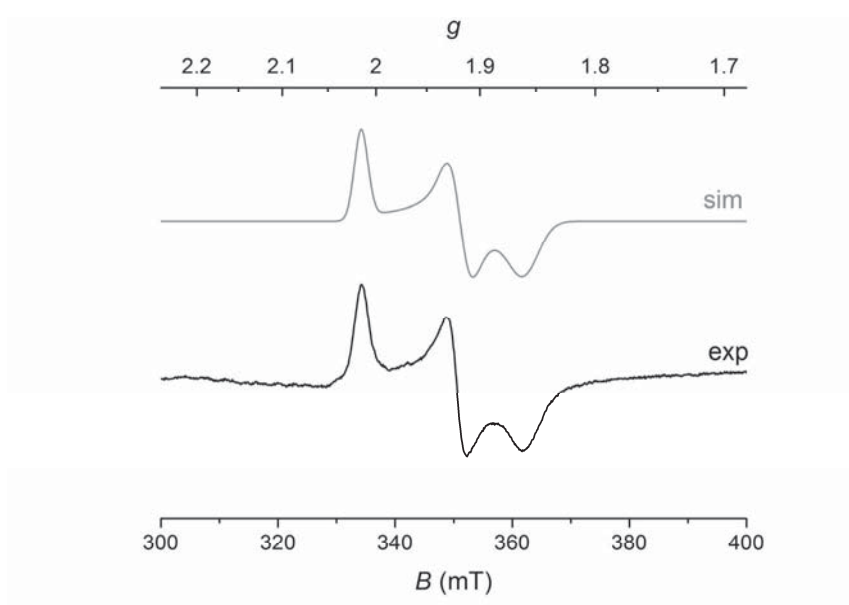


**Figure 9.8:** EPR spectrum after irradiation ( $\lambda = 365$  nm) of  $12a(\text{NEt}_4)_2$  and DMPA in MeCN; recorded in frozen solution at 169 K (black). The blue line is a simulation yielding  $g_1 = 2.01$ ,  $g_2 = 1.915$ ,  $g_3 = 1.850$  and  $g_{\text{av}} = 1.925$ .

**Table 9.1:** EPR parameters of mixed valent [2Fe–2S] cluster  $12a^{3-}$ , and of intermediates observed during radical reactions using  $12a^{2-}$ .

	$12a^{3-}$ in DMF	$12a(\text{NEt}_4)_2$ , Ru(bpy) <sub>3</sub> and $30a$ in MeCN	$12a(\text{NEt}_4)_2$ and DMPA in MeCN
$g_1$	2.016	2.01	2.01
$g_2$	1.935	1.918	1.915
$g_3$	1.885	1.87	1.850
$g_{\text{av}}$	1.945	1.932	1.925

The resulting species proved to be very temperature sensitive and completely decayed over a period of 3 h when kept at 20 °C. This spectrum clearly indicates the presence of a one-electron reduced [2Fe–2S] cluster, similar to what has been observed in BioB. The  $g$  values differ significantly from those of the chemical reduced mixed valent species  $\mathbf{12a}^{3-}$  ( $g_{\text{av}} = 1.945$ , Table 9.1), showing that the photochemically generated radical does not only act as an electron donor in a redox reaction but does attack the cluster under formation of a new species. The average  $g$ -value is very low, suggesting pronounced localization of the unpaired electron on one of the two iron centers. This pronounced localization might give a first hint on radical attack occurring on the ligand's backbone. Radical attack on the ligand's backbone would make the cluster very asymmetric and might thus lead to higher localization of the unpaired electron. In contrast to this, the cluster should still be rather symmetric after radical attack on one of the bridging sulfides and less pronounced localization of the unpaired electron would be expected.

The reaction of cluster  $\mathbf{12a}(\text{NEt}_4)_2$  and organic radicals generated from DMPA was also followed by UV-vis spectroscopy (Figure 9.9). Upon irradiation of the reaction mixture, the whole absorption spectrum decreases in intensity and formation of a new band at 583 nm was observed. The spectrum of the final species closely resembles the spectrum of chemically reduced  $\mathbf{12a}^{3-}$ , proving that reduction of the cluster occurs. During protonation of cluster  $\mathbf{12a}^{2-}$  in DMF, the formation of a new band at about 380 nm with a very high extinction coefficient ( $\varepsilon = 64000 \text{ M}^{-1} \text{ cm}^{-1}$ ) was observed (see chapter 1.6).<sup>[147]</sup> Upon protonation of the free ligand a similar band at 393 nm ( $\varepsilon = 1900 \text{ M}^{-1} \text{ cm}^{-1}$ ) was observed. This was attributed to the tautomerization of the ligand and the formation of a delocalized system.<sup>[147]</sup> No similar band was observed during the photochemically initiated reaction with radicals generated from DMPA. The absence of this band may point toward radical attack on one of the bridging sulfides rather than in the ligand's backbone. For comparison, ligand  $\text{L}^{\text{NN}}\text{H}_2$  was irradiated with LEDs emitting at 365 nm in the presence of 1.0 eq DMPA both in DMF and MeCN and the reaction was followed by UV-vis spectroscopy. No new bands at around 380 nm could be observed during the reaction (Figure 9.10). Consequently, radical attack on the ligand's backbone cannot be excluded based on UV-vis experiments.

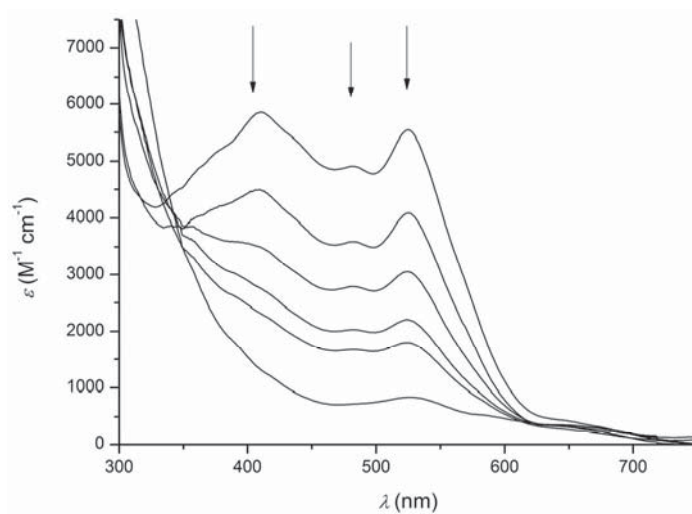


**Figure 9.9:** UV-vis absorption spectra during the irradiation of a 1:1 mixture of **12a**(NEt<sub>4</sub>)<sub>2</sub> and DMPA in MeCN at -20°C. Each line represents an irradiation time of 30 s.

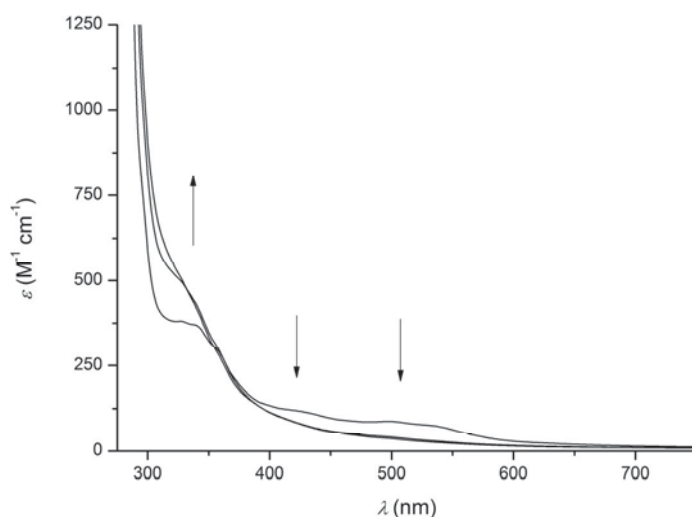


**Figure 9.10:** UV-vis absorption spectra during the irradiation of a 1:1 mixture of L<sup>NN</sup>H<sub>2</sub> and DMPA in MeCN at -20°C, before and after 30 s and 60 s of irradiation.

### 9.3.2 Spectroscopy in Solid State

Solid material of the product of the radical reaction was obtained by irradiating a 1:1 mixture of **12a**(NEt<sub>4</sub>)<sub>2</sub> and DMPA in MeCN at -30 °C, transferring the resulting solution into the glovebox and quickly adding cold diethyl ether (-35 °C). The resulting precipitate was filtered off, washed with cold diethyl ether and dried under reduced pressure. The resulting solid can then be stored at -35°C inside the glove box. Mößbauer spectra were obtained at 12 K, 80 K, and 200 K. At all temperatures these spectra clearly show the presence of mixed valent species (Figure 10.11).

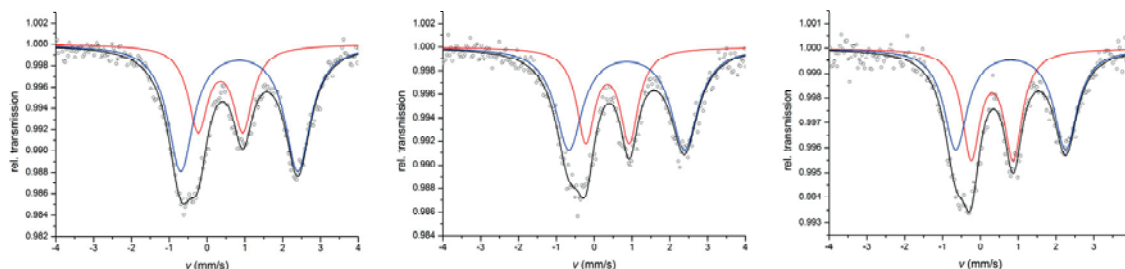


**Figure 9.11:** Zero-field solid state Mössbauer spectra of the solid product of the reaction of **12**(NEt<sub>4</sub>)<sub>2</sub> and DMPA after irradiation ( $\lambda = 365$  nm) for 10 min and subsequent addition of diethyl ether, spectra measured at 12 K, 80 K, 200 K. Simulation with two distinct iron species (red and blue) led to the parameters summarized in Table 9.2.

Two distinct doublets are visible in all three spectra, one corresponding to an Fe<sup>III</sup> center (red in figure 10.11) and the other corresponding to an Fe<sup>II</sup> center (blue in figure 10.11). Mössbauer parameters obtained by simulation are summarized in table 10.2. The difference in isomer shift between the two doublets is relatively large and even larger than the value of 0.4 mm s<sup>-1</sup> predicted for fully localized tetrahedral Fe<sup>II</sup> and Fe<sup>III</sup> sites. This may indicate deviations from tetrahedral coordination geometry either by strong distortions or by formation of a five-coordinate Fe<sup>II</sup> species.

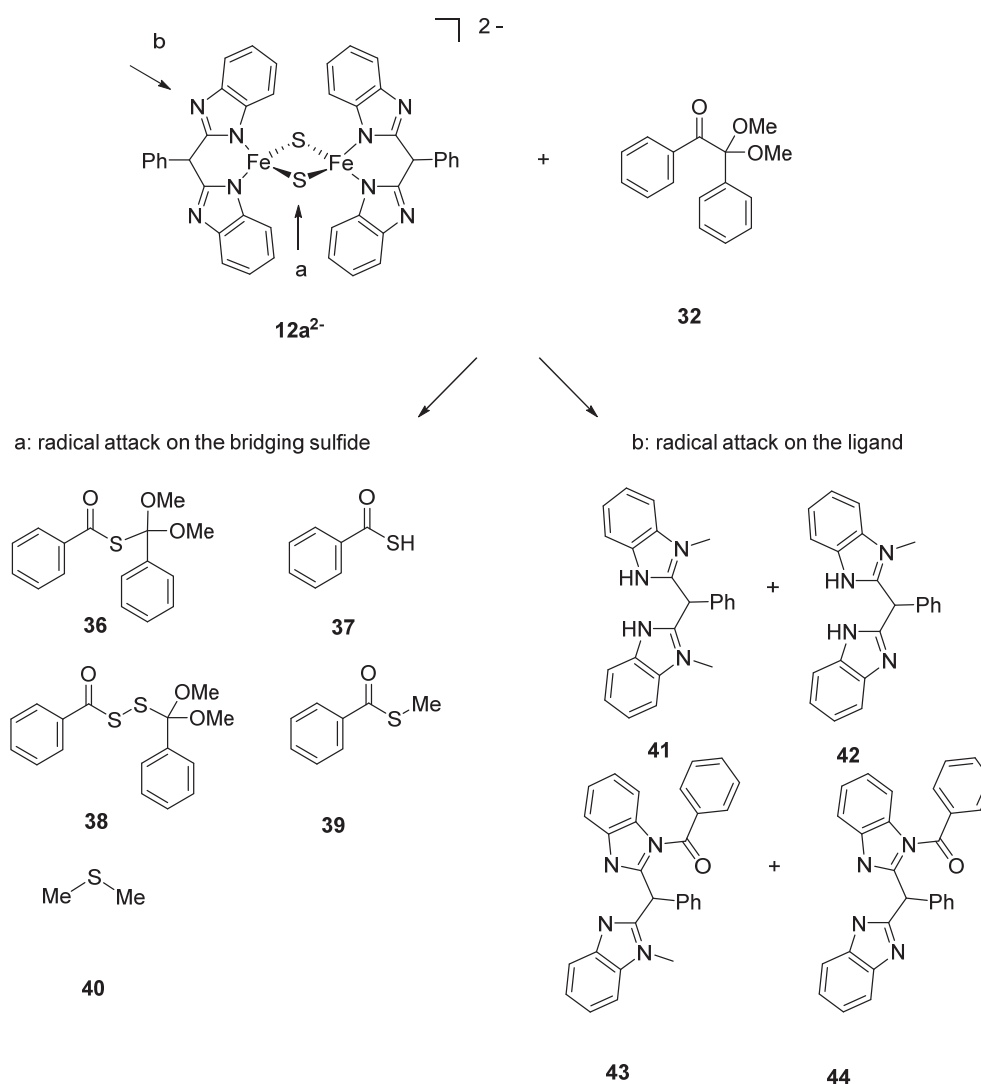
**Table 9.2:** Mössbauer parameters of the product of reaction of DMPA with **12a**(NEt<sub>4</sub>)<sub>2</sub>.

	12 K	80 K	200 K	<b>12a</b> (CoCp* <sub>2</sub> )(NEt <sub>4</sub> ) <sub>2</sub> <sup>[149]</sup> 4.2 K
$\delta$ (mm s <sup>-1</sup> )	0.35	0.35	0.31	0.47
$\delta$ (mm s <sup>-1</sup> )	0.85	0.86	0.80	0.69
$\Delta E_Q$ (mm s <sup>-1</sup> )	1.18	1.15	1.11	1.41
$\Delta E_Q$ (mm s <sup>-1</sup> )	3.10	3.06	2.91	2.90
fwhm (mm s <sup>-1</sup> )	0.63	0.58	0.57	n.d.
fwhm (mm s <sup>-1</sup> )	0.82	0.86	0.74	n.d.
Fe <sup>III</sup> :Fe <sup>II</sup>	34:66	39:61	46:54	45:55

### 9.3.3 Mass Spectrometric Analysis

To get insight into the nature of the radical which attacks the [2Fe–2S] cluster and the position of radical attack, ESI MS experiments were performed. After decomposition of the initial product, *viz* the cluster after radical attack, a multitude of different decomposition products are conceivable, depending on which organic radical attacks the cluster and whether this occurs on the bridging sulfide or on the nitrogen-atom in the backbone of the ligand (Scheme 9.3).

Identifying some of these products in the reaction mixture might thus provide insight into the exact nature of the highly reactive intermediate detected by EPR and UV-vis spectroscopy. Therefore a 1:1 mixture of **12a**(NEt<sub>4</sub>)<sub>2</sub> and DMPA was irradiated at -30 °C for 5 min and then water was added to hydrolyse the iron sulfur core and release possible organic products. The resulting solution was analyzed by ESI MS and the observed fragments *m/z* are summarized in table 9.3 along with a preliminary assignment to a possible species. The only peaks that could be assigned might correspond to the methylated ligand (**42**), suggesting that the methyl radical is the most reactive radical present in solution and that radical attack occurs on the ligand's backbone.



**Scheme 9.3:** Possible decomposition products after attack of different radicals generated from **32** on the bridging sulfides or the ligand.

9 Biomimetic [2Fe–2S] Clusters in Radical Reactions
 

---

**Table 9.3:** Fragments  $m/z$  observed *via* ESI MS in reaction mixtures after irradiation of DMPA + **12a**(NEt<sub>4</sub>)<sub>2</sub> in MeCN.

$m/z$	possible species
+ MS	
223.1	unknown
325.2	[L <sup>NN</sup> + H] <sup>+</sup>
341.2	[L <sup>NN</sup> + Me + 2 H] <sup>+</sup> ( <b>42</b> + 2 H)
– MS	
221.1	unknown
323.1	[L <sup>NN</sup> – H] <sup>–</sup>
339.1	[L <sup>NN</sup> + Me] <sup>–</sup> ( <b>42</b> )
359.1	[L <sup>NN</sup> + 2 Me] <sup>–</sup> ( <b>41</b> )
437.1	unknown

For comparison, free ligand L<sup>NN</sup>H<sub>2</sub> was irradiated with LEDs emitting at 365 nm in the presence of 1.0 eq DMPA and an ESI mass spectrum of the reaction mixture was obtained. For further comparison DMPA (**32**) was irradiated in the absence of any other reagents in MeCN and an ESI mass spectrum was recorded. The fragments observed in each of those experiments are summarized in table 9.4.

**Table 9.4:** Fragments  $m/z$  observed *via* ESI MS in reaction mixtures after irradiation of pure DMPA, and of DMPA + L<sup>NN</sup>H<sub>2</sub> in MeCN.

DMPA ( <b>31</b> ) $m/z$	DMPA + L <sup>NN</sup> H <sub>2</sub> $m/z$	possible species
105 (–MS)	105 (–MS)	rad1
151 (–MS)	151 (–MS)	rad2
165 (+MS)		[rad2 + CH <sub>2</sub> ] <sup>+</sup>
197 (+MS)		
225 (+MS) 5	225 (+MS)	[ <b>32</b> – OMe] <sup>+</sup>
279 (+MS)	279 (+MS)	[ <b>32</b> + Na] <sup>+</sup>
	311 (+MS)	
	323 (–MS)	323 [L <sup>NN</sup> – H] <sup>–</sup>
	341 (+MS)	( <b>42</b> + 2 H <sup>+</sup> ) [L <sup>NN</sup> + Me + 2 H] <sup>+</sup>
	363 (+MS)	
	379 (+MS)	
535.2 (+MS)		[2 · <b>32</b> + Na] <sup>+</sup>

In addition to the fragments observed in the blank reaction after irradiation of DMPA only, the reaction mixture of free ligand and DMPA shows additional fragments at  $m/z = 341$  and

363 which can be assigned to  $[\mathbf{L}^{\text{NN}} + \text{Me} + \text{H}]^+$  and  $[\mathbf{L}^{\text{NN}} + \text{Me} + \text{Na}]^+$ , respectively. A comparison of the results of these ESI MS experiments show that all fragments observed in the ESI mass spectrum after the reaction of  $\mathbf{12a}(\text{NEt}_4)_2$  with DMPA are also present in the ESI mass spectrum recorded of the reaction mixture of free ligand and DMPA under the same conditions. This gives strong indications for a radical attack occurring on the ligand's backbone rather than on the bridging sulfide of the cluster. However, the observed products may also have formed during the aqueous, aerobic work-up. The findings described in this chapter should thus be considered first indications rather than conclusive proof.

## 9.4 Reactivity of $\mathbf{4}^{2-}$ Toward Organic Radicals Generated from DMPA

### 9.4.1 Spectroscopy in Solution

Radical reactions on cluster  $\mathbf{4}^{2-}$  were carried out in close analogy to the experimental conditions described for  $\mathbf{12a}^{2-}$ . Both irradiation with the whole spectral range of 200 – 600 nm as well as irradiation with an LED emitting with a maximum at 365 nm led to the formation of identical characteristic EPR spectra. A simulation of the experimental spectrum yielded the following parameters:  $g_1 = 2.013$ ,  $g_2 = 1.933$ ,  $g_3 = 1.885$ ,  $g_{\text{av}} = 1.943$  (Figure 9.12), which are very similar to the parameters of chemically reduced  $\mathbf{4}^{3-}$  (see chapter 3 and table 9.5). In this case, the average  $g$  values are not lower as those found for chemically reduced cluster  $\mathbf{4}^{3-}$ , but higher. This might suggest less pronounced valence localization and thus radical attack on the bridging sulfides rather than on the ligands, but the differences in average  $g$  values are very small.

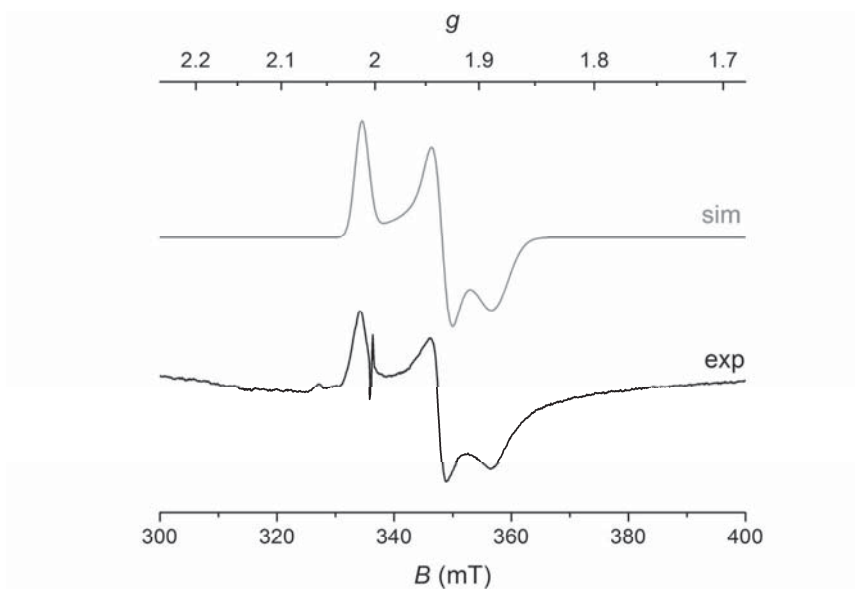


**Figure 9.12:** EPR spectrum obtained after irradiation of  $4(\text{NEt}_4)_2$  and DMPA in DMF; recorded in frozen solution at 168 K (black). The grey line is a simulation using  $g_1 = 2.013$ ,  $g_2 = 1.933$ ,  $g_3 = 1.885$ , and  $g_{\text{av}} = 1.943$ .

**Table 9.5:** EPR parameters of mixed valent [2Fe–2S] cluster  $4^{3-}$ , and of intermediates observed during radical reactions using  $4^{2-}$ .

	$4^{3-}$ in DMF	$4(\text{NEt}_4)_2$ , Ru(bpy) <sub>3</sub> and <b>30a</b> in MeCN	$4(\text{NEt}_4)_2$ and DMPA in MeCN
$g_1$	2.01	2.012	2.01
$g_2$	1.932	1.936	1.933
$g_3$	1.882	1.890	1.885
$g_{\text{av}}$	1.941	1.946	1.943

The reaction of  $4^{2-}$  with DMPA upon irradiation with LEDs emitting with a maximum at 365 nm at  $-20^\circ\text{C}$  was followed by UV-vis spectroscopy (Figure 9.13). All bands decrease in intensity over the course of the reaction but no new bands arise. Notably, the band at 438 nm completely vanishes during the first half of the irradiation experiment, while the bands at 521 and 581 nm are still clearly visible. The band at 438 nm has previously been found to be very sensitive towards protonation and coordination of  $\text{Li}^+$  and  $\text{Na}^+$  cations on the backbone of the ligand. This might indicate that radical attack occurs on the backbone of the ligand rather than on the bridging sulfides.

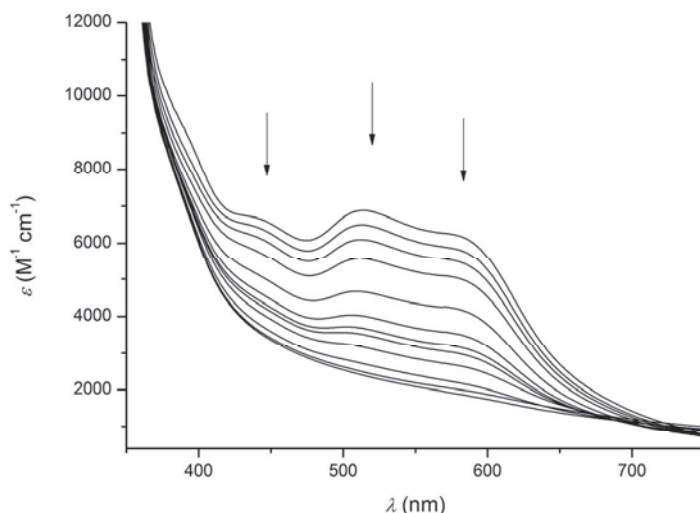


**Figure 9.13:** UV-vis absorption spectra during the irradiation of a 1:1 mixture of  $4(\text{NEt}_4)_2$  and DMPA in MeCN at  $-20^\circ\text{C}$  with LEDs emitting at 365 nm. Each line represents an irradiation time of 15 s.

### 9.4.2 Spectroscopy in Solid State

Solid material of the product of the radical reaction was obtained by addition of cold diethyl ether, filtration of the resulting precipitate and drying under reduced pressure. The solid was stored at  $-35^\circ\text{C}$  in the glove box. A zero-field Mössbauer spectrum was obtained at 13 K and shows the presence of two different iron centers (Figure 9.14). One of these centers with  $\delta = 0.37 \text{ mm s}^{-1}$  and  $\Delta E_Q = 0.90 \text{ mm s}^{-1}$  corresponds to a tetrahedrally coordinated high spin  $\text{Fe}^{\text{III}}$  site and its Mössbauer parameters are in between those of the  $\text{Fe}^{\text{III}}$  site in diferric  $4^{2-}$  and in chemically reduced  $4^{3-}$ . The isomer shift of the doublet corresponding to high spin  $\text{Fe}^{\text{II}}$  is higher than those usually observed for four-coordinate  $\text{Fe}^{\text{II}}$  centers in [2Fe-2S] clusters (typically between  $\delta = 0.60$  and  $0.74 \text{ mm s}^{-1}$ )<sup>[187]</sup> which may indicate coordination of an additional ligand to this iron ion.

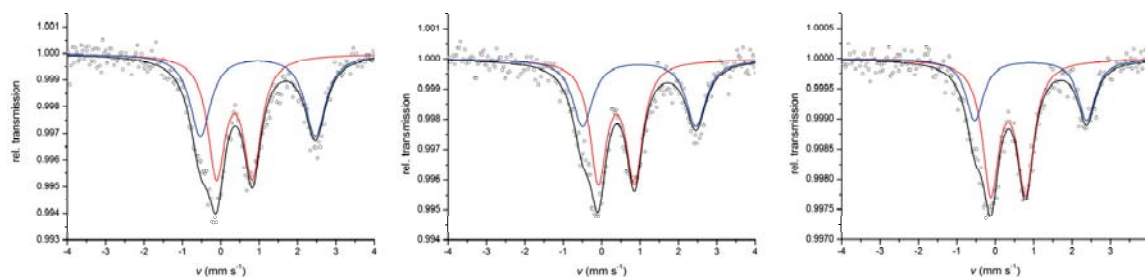


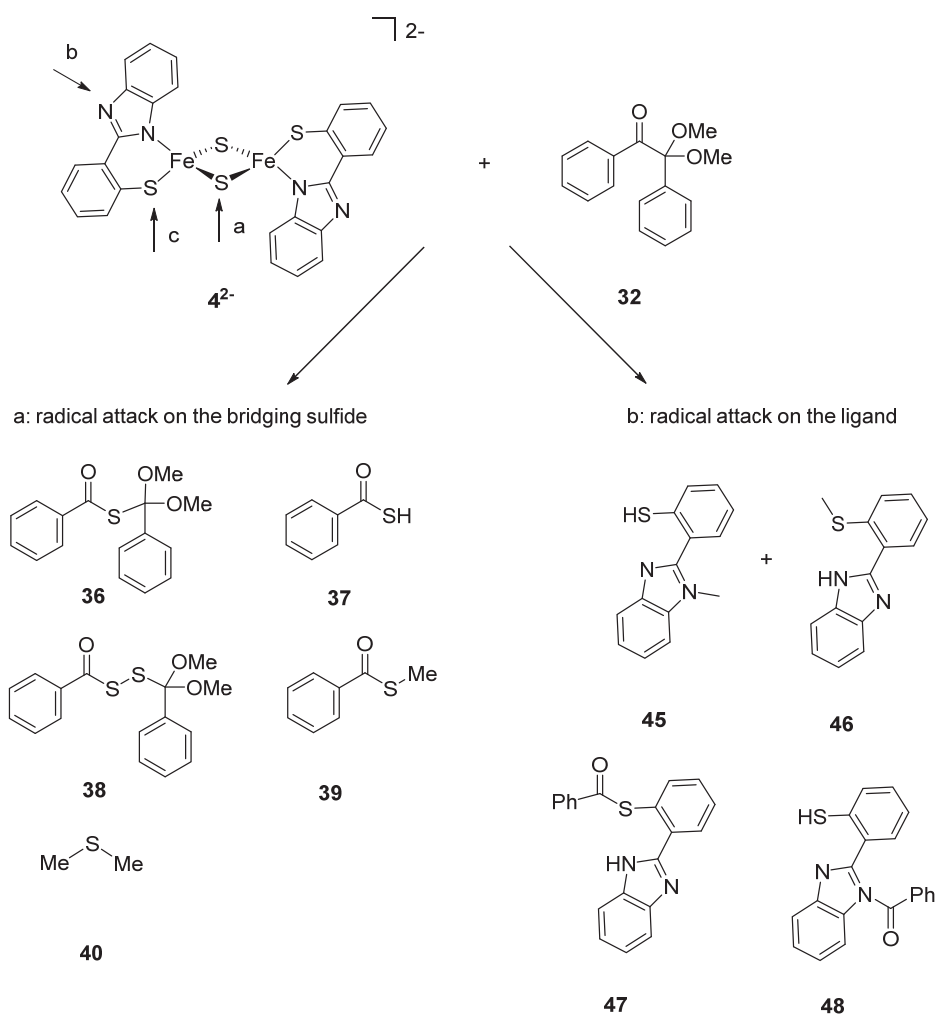
**Figure 9.14:** Zero field Mössbauer of solid product of the radical reaction of  $4^{2-}$  and DMPA at 12 K (left), 80 K (middle), and 200 K (right).

**Table 9.6:** Mößbauer parameters for the product of the reaction of  $4^{2-}$  and DMPA.

	12 K	80 K	200 K	$4(\text{NEt}_4)(\text{CoCp}^*_2)_2$ 12K
$\delta$ (mm s <sup>-1</sup> )	0.37	0.38	0.34	0.35
$\delta$ (mm s <sup>-1</sup> )	0.99	0.98	0.92	0.62
$\Delta E_Q$ (mm s <sup>-1</sup> )	0.90	0.94	0.91	1.20
$\Delta E_Q$ (mm s <sup>-1</sup> )	2.94	2.95	2.92	3.09
fwhm (mm s <sup>-1</sup> )	0.56	0.52	0.52	0.87
fwhm <sub>2</sub> (mm s <sup>-1</sup> )	0.66	0.64	0.56	0.56
Fe <sup>III</sup> :Fe <sup>II</sup>	46:54	59:41	66:34	51:49

### 9.4.3 Analysis of Final Reaction Products

A mass spectrometric analysis of the products of the radical reaction may provide hints on the nature of the active radical and the position of radical attack. Similar to the mass spectrometric analysis described for cluster **12a**<sup>2-</sup> (chapter 9.3.3), a 1:1 mixture of  $4(\text{NEt}_4)_2$  and DMPA in MeCN was irradiated with LEDs emitting at 365 nm for 4 min. Then water was added to hydrolyse the iron sulfur core and release the possible organic products of the reaction and an ESI mass spectrum of the reaction mixture was obtained. All species found therein are summarized in table 9.7 along with a preliminary assignment to possible species. For comparison, a sample containing  $\text{L}^{\text{SN}}\text{H}_2$  and 1.0 eq DMPA in MeCN and DMF was prepared and irradiated for 1 min with LEDs emitting at 365 nm. Subsequently, water (0.1 mL) was added and an ESI mass spectrum of the reaction mixture was obtained. The fragments observed therein are summarized in table 9.8.



**Scheme 9.4:** Possible decomposition products after attack of different radicals on the bridging sulfides or the on the thiolate or backbone N-atom of the terminal ligand in  $4^{2-}$ .

## 9 Biomimetic [2Fe–2S] Clusters in Radical Reactions

**Table 9.7:** Fragments  $m/z$  observed *via* ESI MS in reaction mixtures after irradiation of 1.0 eq DMPA and  $4(\text{NET}_4)_2$  in MeCN.

$m/z$	possible species
+ MS	
197.1	
225.1	$[\mathbf{32} - \text{OMe}]^+$
281.1	$[\mathbf{L}^{\text{SN}} + \text{Fe}]^+$
331.1	
363.1	
– MS	
137.0	$[\mathbf{37} - \text{H}]^-$
193.1	
225.1	$[\mathbf{L}^{\text{SN}}\text{H}]^-$
257.0	
289.0	
305.0	
337.0	

**Table 9.8:** Fragments  $m/z$  observed *via* ESI MS in reaction mixtures after irradiation of DMPA only and of DMPA +  $\mathbf{L}^{\text{NN}}\text{H}_2$  in MeCN.

$m/z$ (DMPA)	$m/z$ (DMPA + $\mathbf{L}^{\text{SN}}\text{H}_2$ )	possible species
105 (–MS)	105 (–MS)	rad1
151 (–MS)	151 (–MS)	rad2
165 (+MS)		
197 (+MS)	197 (+MS)	
225 (+MS)	225 (+MS)	$[\mathbf{32} - \text{OMe}]^+$
	225 (–MS)	$[\mathbf{L}^{\text{SN}} - \text{H}]^-$
	241.0 (+MS)	$[\mathbf{L}^{\text{SN}} + \text{Me} + \text{H}]^+$ ( <b>45</b> or <b>46</b> )
279.1 (+MS)	279.0 (+MS)	$[\mathbf{32} + \text{Na}]^+$
	331.1 (+MS)	$[\mathbf{L}^{\text{SN}} + \text{rad1} + \text{H}]^+$ ( <b>47</b> or <b>48</b> )

A comparison of the species found in these different reaction mixtures shows that the ESI mass spectrum obtained after the reaction of cluster  $\mathbf{4}^{2-}$  contains peaks, which have not been observed after reaction of the free ligand  $\mathbf{L}^{\text{SN}}\text{H}_2$  with DMPA. Most notably, the species corresponding to the observed signal at  $m/z = 137.0$  might be a combination of rad1 and sulfur (**37**) that may have formed upon radical attack on the bridging sulfide. On the other hand, the methylated ligand (**45** or **46**) was not observed after reaction of the cluster with DMPA. These findings may point toward a reaction in which the organic radical attacks the cluster on the bridging sulfide. However, all of the observed species may have formed upon

aqueous work up under aerobic conditions or in the ESI machine during ionization. They are thus not sufficient for drawing final conclusions on the position of radical attack in this reaction.

After irradiation ( $\lambda_{\max} = 365 \text{ nm}$ ) of a mixture of  $\mathbf{4}(\text{NEt}_4)_2$  and 1.0 eq DMPA in MeCN for 5 min at  $-20 \text{ }^\circ\text{C}$ , crystalline material of an all-ferric tetra-iron-tetra-oxo species  $\mathbf{49}(\text{NEt}_4)_4$  was obtained (Figure 9.15). Crystalline material of this decomposition product was obtained twice from two independent experiments, indicating that  $\mathbf{49}^{4-}$  may indeed be the final decomposition product of the reaction of  $\mathbf{4}^{2-}$  with organic radicals generated from DMPA. It is remarkable that neither the bridging sulfides of  $\mathbf{4}^{2-}$  nor any of the anticipated radicals rad1 or rad2 are present in  $\mathbf{49}^{4-}$ . Decomposition may also have occurred due to the intrusion of traces of water or oxygen during crystallization. However, the ligand seems to be intact even after radical reaction, indicating that no radical attack takes place on the terminal S/N-capping ligand neither at the N-atoms of the benzimidazole moiety nor at the thiolate. This may point toward a scenario in which radical attack occurs on the bridging sulfides and a radical-sulfur adduct is released in a subsequent decomposition reaction.

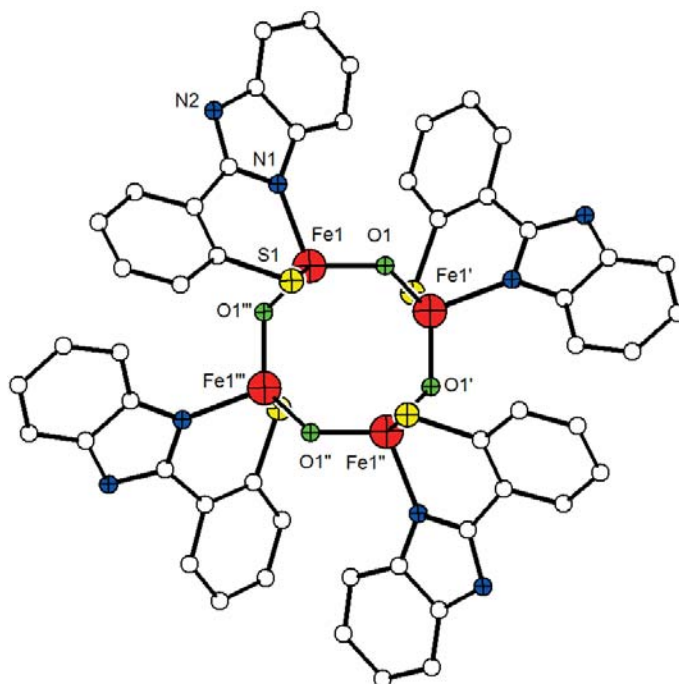


**Figure 9.15:** Molecular structure of the anion of  $\mathbf{49}(\text{NEt}_4)_4$  in the solid. Hydrogen atoms and counterions have been omitted for clarity.

## 9.5 Reactivity of a Neutral [2Fe–2S] Cluster Toward Organic Radicals Generated from DMPA

Cluster **50** was prepared and kindly provided by the group of Prof. Dr. Marc Walter at the Technical University of Braunschweig (Figure 9.16).<sup>[193]</sup> It was shown to be stable in solution in toluene up to 100 °C. In addition, [2Fe–2S] cluster **50** is a neutral compound since it features mono-anionic capping ligands, and thus it is soluble in a broad range of solvents such as hexane, toluene and dichloromethane, which cannot be used for doubly-anionic clusters such as **12a**<sup>2-</sup> and **4**<sup>2-</sup>. As expected both iron centers are antiferromagnetically coupled and the diferric form of the cluster is EPR silent. Consequently, cluster **50** appeared to be a promising candidate for reactions with organic radicals.

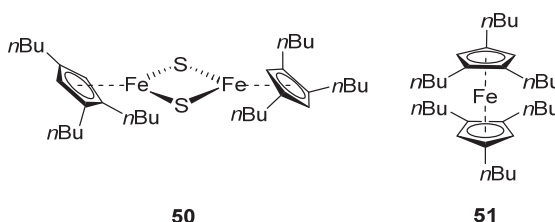


**Figure 9.16:** Neutral [2Fe–2S] cluster **50** prepared by Walter and coworkers and related ferrocene analogue **51**.

To compare the properties of the product of the radical reaction with the chemically one-electron reduced cluster, **50** was reduced by addition of CoCp<sub>2</sub> and an EPR spectrum of the mixed valent cluster was recorded in frozen toluene solution. As expected for a mixed valent [2Fe–2S] cluster, the spectrum shows a rhombic signal indicative of the presence of a species with an  $S = 1/2$  ground state. A simulation yielded the following parameters:  $g_1 = 2.16$ ,  $g_2 = 2.042$ ,  $g_3 = 2.000$ .  $g_{av} = 2.067$  at 162 K (Figure 9.17, left). These  $g$ -values are very unusual for a mixed valent [2Fe–2S] cluster, since they are all larger than 2. However, **50** does not show a tetrahedral coordination of the individual iron centers which might lead to deviations from the predicted behavior. Cluster **50** was then irradiated with LEDs ( $\lambda_{max} = 365$  nm) in toluene both in the presence and in the absence of DMPA and EPR spectra of the samples were recorded in frozen solution at 162 K. Upon irradiation in toluene in absence of DMPA an intense, sharp, isotropic signal with  $g = 2.0003$  was detected, clearly showing that **50** is not stable upon irradiation (Figure 9.17, right).

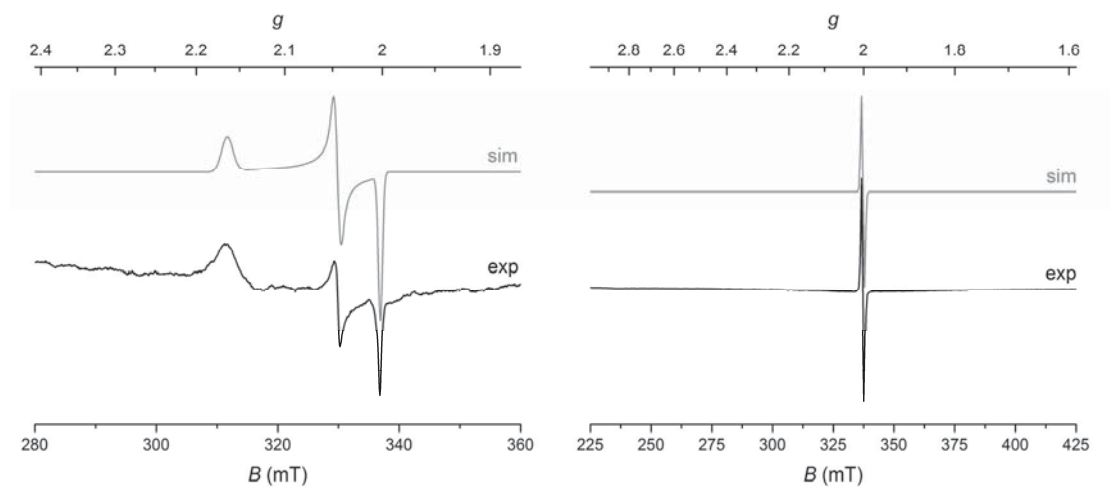


**Figure 9.17:** EPR spectra observed upon chemical reduction of cluster **50** (left) and signal observed upon irradiation of **50** in toluene with  $\lambda_{\max} = 365$  nm (right) spectra recorded in frozen toluene solution at 162 K.

After irradiation of **50** in presence of DMPA, the EPR spectrum showed the presence of two species (Figure 9.18). One of these species is characterized by an EPR signal similar to that observed upon irradiation of the cluster in the absence of DMPA ( $g = 2.0038$ , 6%). The second species is characterized by a signal, which closely resembles the signal obtained after chemical reduction of **50** ( $g = 2.154, 2.049, 2.013$ ).

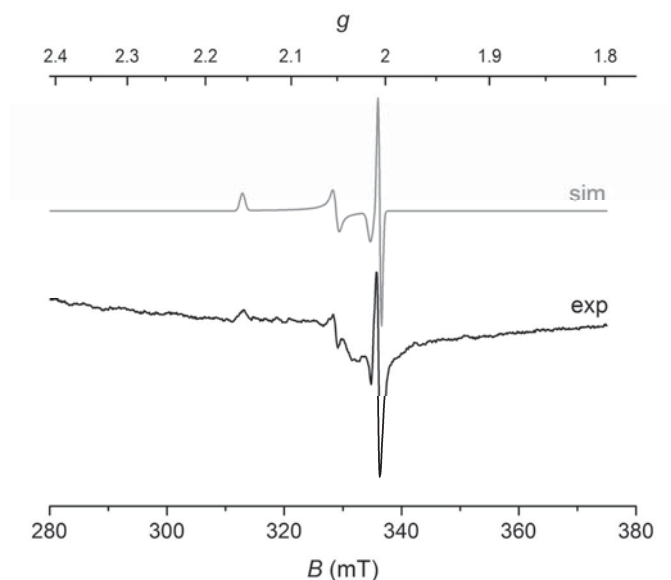


**Figure 9.18:** EPR spectrum observed after irradiation of **50** in the presence of DMPA in toluene measured in frozen solution at 162 K. The spectrum can be simulated as an overlay of two species with  $g_1 = 2.153$ ,  $g_2 = 2.049$ ,  $g_3 = 2.013$  and  $g_{\text{av}} = 2.072$  for the first species and  $g_1 = 2.0038$  for the second species (accounting for 6% of the total intensity).

This shows, that two processes take place simultaneously: part of the cluster decomposes upon irradiation while another part of the cluster is attacked and thus reduced by organic radicals generated from DMPA. The low overall intensity of the spectrum makes an accurate determination of the ratio of both species difficult. ESI mass spectra indicated formation of the ferrocene analogue Cp'<sub>2</sub>Fe (**51**) after irradiation. Attempts to crystallize the product of the radical reaction also led to crystallization of **51**. The same results were obtained when using hexane or THF as solvents. The results show that **50** reacts with organic radicals generated from DMPA and radical attack leads to formation of the reduced cluster. However, since the cluster itself is not stable against irradiation and formation of the respective ferrocene analogue seems to be thermodynamically favored, a detailed analysis of the radical reaction was not possible and no further experiments were performed.

## 9.6 Conclusion

In conclusion first insights into reactions of biomimetic [2Fe–2S] clusters with organic radicals have been presented in this chapter. Two different approaches for generating a suitable organic radical were explored in combination with three different synthetic [2Fe–2S] clusters. Radical generation using bis(catechol)silicates **30a** and **30b** and [Ru(bpy)<sub>3</sub>](PF<sub>6</sub>)<sub>2</sub> as a photocatalyst resulted in the formation of a mixed valent [2Fe–2S] species, similar to what has been reported for radical SAM enzymes such as BioB. However, the use of [Ru(bpy)<sub>3</sub>](PF<sub>6</sub>)<sub>2</sub> in combination with [2Fe–2S] clusters resulted in several problems including side reactions, solubility issues and difficulties in assigning bands in visible absorption spectra. Mass spectrometric analysis of these reactions was not successful in identifying any products of the reaction, which might have provided indications about the position of the potential radical attack.

Reactions utilizing photolytical radical generation from DMPA **32** as a radical starter were performed and some of the initial problems could be overcome. Reaction of **12a**<sup>2-</sup> and **4**<sup>2-</sup> with organic radicals generated from DMPA *via* irradiation appear to proceed under full and clean conversion to a mixed valent [2Fe–2S] clusters with characteristic rhombic EPR spectra. It was also possible to isolate the product of this reaction as solid material and obtain Mößbauer spectra which clearly prove the presence of Fe<sup>II</sup> and Fe<sup>III</sup> centers in the product. Both Mößbauer and EPR spectroscopy have established that the product of the proposed radical reaction is similar to but not identical with chemically reduced clusters **12a**<sup>3-</sup> or **4**<sup>3-</sup>. Indeed a novel mixed valent species, with strong localization of the unpaired electron is formed. A mass spectrometric analysis of the observed mixed valent intermediate as well as of the resulting decomposition products did not yield fully conclusive results. Since crystallization attempts were unsuccessful so far, it cannot be established unambiguously whether the attack of the radical occurs on the bridging sulfide or the ligand backbone.



Future studies will have to focus both on optimizing reaction conditions for radical generation and crystallization as well as on careful design of [2Fe–2S] clusters, which show an increased stability and eliminate the possibility of radical attack on the ligand backbone. Bearing in mind the reactivity of the auxiliary [4Fe–4S] cluster in lipoyl synthase, future studies will also have to focus on the development of functional model systems for the reactivity of synthetic [4Fe–4S] clusters toward organic radicals. Nevertheless, the systems presented in this chapter provide the first models for studying radical reactions in biomimetic iron-sulfur chemistry and thus present a crucial step toward the description of a high fidelity model for this unique reactivity.



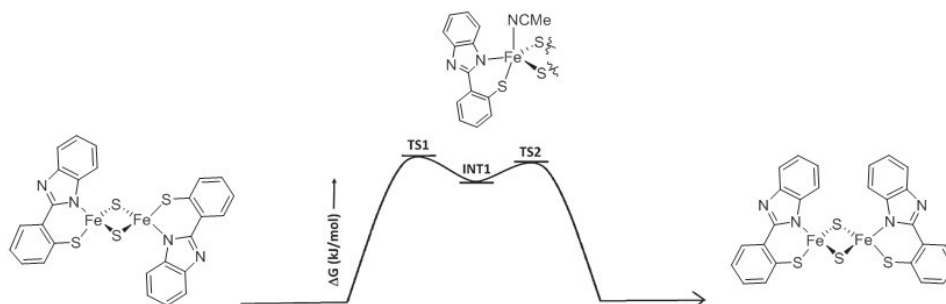
---

## 10 Conclusion and Perspectives

This thesis has presented new insights into the role of alternative ligands in [2Fe–2S] clusters by using various synthetic analogues. Four different homo- and heteroleptic clusters featuring a varying number of N- or S- donors were studied to mimic various reactivities relevant to the multitude of functions observed for biological iron sulfur cofactors.

Previously reported homoleptic cluster  $4(\text{NEt}_4)_2$  features two benzimidazole moieties which emulate the presence of two histidine ligands. The cluster has now been fully characterized in its diferric and mixed valent form, including characterization by X-ray crystallography. It was further shown that the benzimidazole moieties serve as proton responsive ligands and a  $pK_a$  of 23.0(1) was determined for  $4\text{H}^-$ .  $^1\text{H}$  NMR studies have revealed fast exchange of protons between clusters. Since protonation on the backbone of the ligand turns the dianionic into a monoanionic ligand, the mixed valent species is better stabilized in the cluster's protonated form. This becomes evident by a shift of 65 mV observed for the first reduction wave in the cyclic voltammogram. However, this shift is much smaller than expected for protonation of a benzimidazole unit in [2Fe–2S] clusters, and the reason for this small shift could not be elucidated in this work.<sup>[192,194]</sup>

Since two different isomers of  $4^{2-}$  are present in solution, which differ by the relative arrangement of the two capping ligands, this cluster provided the first example of a [2Fe–2S] cluster in which the kinetics of slow isomerization *via* ligand rearrangement could be studied (Scheme 11.1). Based on  $^1\text{H}$  NMR spectroscopy, activation parameters of  $\Delta S^\ddagger = -253 \text{ J mol}^{-1} \text{ K}^{-1}$ ,  $\Delta H^\ddagger = 14.0 \text{ kJ mol}^{-1}$ , and  $\Delta G_{293\text{K}}^\ddagger = 88.1 \text{ kJ mol}^{-1}$  were determined for the isomerization in MeCN- $d_3$ . The relatively large value of the activation entropy points toward an associative mechanism. Indeed, theoretical studies support a mechanistic scenario in which a solvent molecule coordinates to one of the ferric iron centers to form a five-coordinate intermediate (Scheme 10.1). The second isomer is then formed *via* dissociation of the solvent molecule from this intermediate. Protonation of the cluster or reduction is shown to accelerate the isomerization process by at least one order of magnitude. This indicates a possible mechanism for iron sulfur cofactors in sensing cellular conditions such as pH and oxidative stress since these factors seem to affect the possibility for changes in the cluster's coordination environment.<sup>[194]</sup>



**Scheme 10.1:** Isomerization of a biomimetic [2Fe–2S] cluster *via* a five coordinate intermediate involving solvent coordination.<sup>[194]</sup>

As no synthetic [2Fe–2S] cluster emulating the special Cys<sub>3</sub>His coordination found in mitoNEET proteins was known prior to this work, heteroleptic cluster **26**(NEt<sub>4</sub>)<sub>2</sub> was synthesized and characterized in its diferric, mixed valent and protonated form. It was shown to mimic both the structural as well as the spectroscopic properties of its biological blueprint very well. EPR and Mößbauer spectroscopy revealed that the asymmetric ligation in this model led to a higher localization of the unpaired electron in the cluster's mixed valent form compared to the mixed valent **4**<sup>3-</sup>. Furthermore, the benzimidazole ligand acts as a proton responsive ligand and a *pK<sub>a</sub>* of 23.7(1) for **26H**<sup>-</sup> was determined by titration experiments. Cyclic voltammetry measurements reveal a shift of 245 mV upon protonation for the first reduction wave, which is in good agreement with values typically found for protonation of benzimidazole units in [2Fe–2S] clusters.<sup>[192]</sup>

Temperature dependent electrochemical measurements provided further insight into the thermodynamic parameters of electron transfer in a series of synthetic [2Fe–2S] clusters and the effect of non-cysteine ligation. A larger absolute value for the reaction entropy  $\Delta S^\circ$  was observed for asymmetrically ligated clusters, proving that a higher localization in the mixed valent form is indeed translated into more pronounced structural changes, *i.e.* larger inner-sphere reorganization upon electron transfer (Figure 10.1). Additionally, the redox potential for one electron reduction of the diferric clusters is linearly dependent on the number of N-donors. This emphasizes the role non-cysteine ligation plays in tuning the cluster's redox properties.

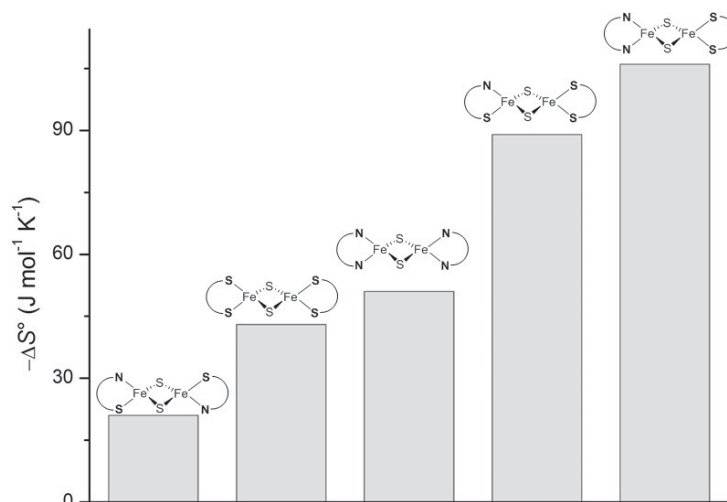
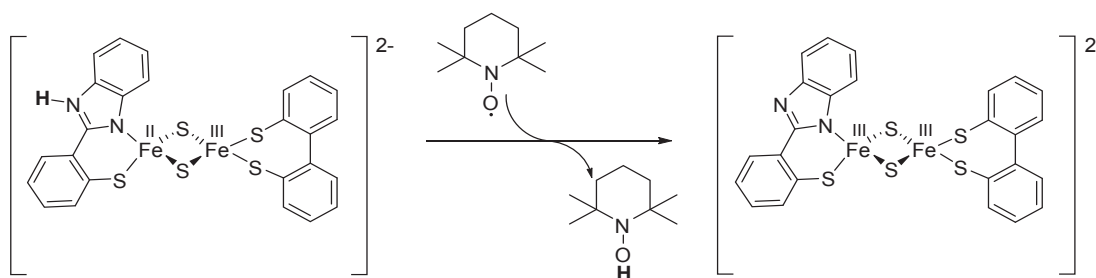


**Figure 10.1:** Increasing negative value for the entropy  $\Delta S^\circ$  for one-electron reduction with increasing degree of localization in synthetic [2Fe–2S] clusters.

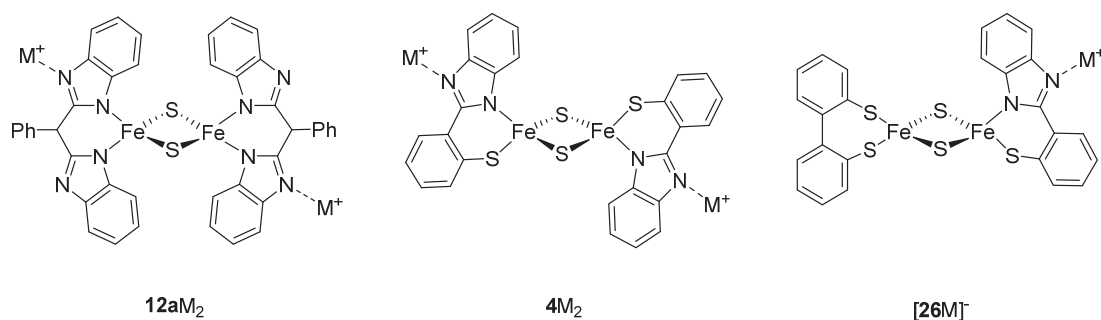
Both homoleptic cluster  $4\text{H}^{2-}$  and heteroleptic cluster  $26\text{H}^{2-}$  have successfully been tested as possible PCET reagents, suggesting a potential role in PCET for the [2Fe–2S] cluster in mitoNEET and related proteins (Scheme 10.2). Double-mixing stopped flow experiments revealed that even though the driving force for the reactions of  $4\text{H}^{2-}$  and  $26\text{H}^{2-}$  with TEMPO are essentially the same, heteroleptic cluster  $26\text{H}^{2-}$  reacts about one order of magnitude slower. According to Marcus theory the rate of a PCET reaction depends on the driving force and the reorganization energy. The experiments presented in this chapter highlight the importance of localization in [2Fe–2S] clusters, as a result of asymmetric ligation. This higher localization is associated with more pronounced structural rearrangements upon electron transfer and is thus directly translated into a higher reorganization energy, which in turn leads to a decreased rate in PCET reactions.



**Scheme 10.2:** PCET reactivity of synthetic mitoNEET model  $26\text{H}^{2-}$ .

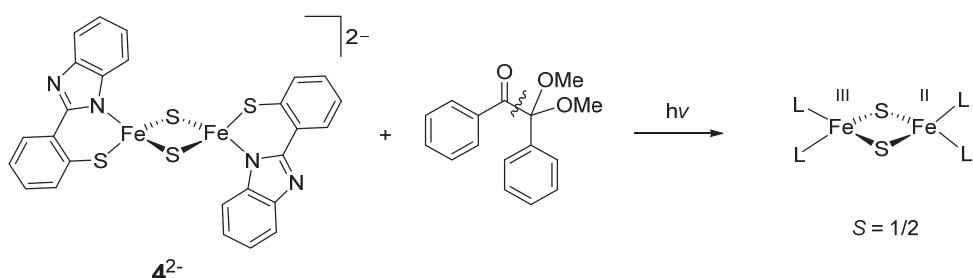
Benzimidazole units can act as proton responsive ligands and may also act as sensors for small monovalent metal cations such as  $\text{Li}^+$  and  $\text{Na}^+$  (Scheme 10.3). Indeed, addition of these metal cations led to spectroscopic changes very similar to those observed upon protonation.

For homoleptic model  $4^{2-}$  a 1:2 interaction with these metal cations was proposed based on titrations experiments using the method of continuous variation. The binding constants for the interaction of clusters  $4^{2-}$  and  $26^{2-}$  are, however, very small ( $K = 279, 131 \text{ M}^{-1}$  for  $4^{2-}$ ,  $K = 4.24 \text{ M}^{-1}$  for  $26^{2-}$ )



**Scheme 10.3:** Proposed interaction of monovalent metal cations with synthetic  $[2Fe-2S]$  clusters.

Finally, first steps toward a functional model system mimicking the unique reactivity of the auxiliary  $[2Fe-2S]$  cluster in biotin synthase were taken (Scheme 10.4). Therefore, two different approaches for photolytic generation of organic radicals were pursued. Using silicates in combination with  $[Ru(bpy)_3](PF_6)_2$  as photocatalyst in reactions with clusters  $4^{2-}$  and  $12a^{2-}$  led to characteristic EPR signals for mixed valent  $[2Fe-2S]$  clusters. However, no solid material of the product of this reaction could be obtained. Using DMPA as a radical initiator, EPR signals for mixed valent  $[2Fe-2S]$  clusters could be detected and solid material suitable for Mössbauer spectroscopy could also be obtained. Mössbauer spectroscopy proved that both a ferric and a ferrous iron center are present in the product of the radical reaction. However, these findings did not succeed in unambiguously establishing whether the radical attack takes place on the bridging sulfides or at the backbone of the ligand. Due to their high sensitivity, the intermediate products eluded isolation in crystalline form. Nevertheless, these experiments provide the first examples of radical attack on synthetic iron sulfur clusters leading to the formation of the mixed valent species, as observed in natural systems such as BioB.



**Scheme 10.4:** Formation of a mixed valent iron sulfur species upon reaction with photolytically generated organic radicals.



In conclusion, this thesis has presented several model systems that provide insight into the reactivity of [2Fe–2S] clusters with alternative ligands as possible PCET reagents, as well as in radical reactions, and in sensing conditions such as pH and the presence of metal cations. It has also yielded unprecedented insight into ligand rearrangement processes relevant to iron sulfur cluster biogenesis and into the effects of asymmetric and non-cysteine ligation on the thermodynamic signatures of electron transfer in these systems. Further studies will have to focus on expanding the series of synthetically available [2Fe–2S] clusters to include {N<sub>3</sub>S} coordination and coordination by other donors such as O-based ligands. These models may serve to gain further understanding of the intrinsic trend determining their properties as electron transfer reagents and the PCET reactivity of [2Fe–2S] clusters. Furthermore, tuning the properties of ligands in [2Fe–2S] clusters may provide systems which allow for a more thorough determination of the steric and electronic factors that control the rate of ligand rearrangement or allow to study ligand exchange between clusters. Experiments concerning radical reactions may be extended by designing ligands which prevent radical attack on the ligand and by including reactivity studies on [4Fe–4S] clusters. Even though this thesis has shed light on a number of roles alternative ligands play in the chemistry of [2Fe–2S] clusters, a multitude of intriguing questions remains to be answered by future generations.



---

## 11 Experimental Section

### 11.1 General Considerations

Parts of these experimental considerations have been adapted from recent publications.<sup>[192]</sup> KH was purchased as dispersion in mineral oil, washed repetitively with hexane and dried in vacuum. Decamethylcobaltocene was dissolved in pentane, filtered and recrystallized by addition of MeCN prior to use. The ligands 1,1'-biphenyl-2,2'-dithiol ( $H_2L^{SS}$ ) and  $H_2L^{SN}$  as well as precursor complex bis-(tetraethylammonium)-bis-[(dichloro)-( $\mu$ -sulfido)-ferrate(III)], and complexes **12a**(NEt<sub>4</sub>)<sub>2</sub>, **13**(NEt<sub>4</sub>)<sub>2</sub>, **27**(NEt<sub>4</sub>)<sub>2</sub> and **4**(NEt<sub>4</sub>)<sub>2</sub> and silicates **30a** and **30b** have been synthesized according to literature known procedures.<sup>[136,139,148,195,245]</sup> THF was dried with potassium and sodium in the presence of benzophenone, Et<sub>2</sub>O was dried with sodium in the presence of benzophenone, DMF and MeCN were dried with CaH<sub>2</sub>; all solvents were distilled prior to use. Deuterated solvents were dried and distilled in the same way as the undeuterated analogues. All manipulations were carried out under an anaerobic and anhydrous atmosphere of dry dinitrogen by standard Schlenk techniques, or in an MBraun glovebox. All glassware was dried at 120 °C before using.

<sup>1</sup>H NMR spectra of all clusters were recorded on a Bruker Avance 500 MHz and an Agilent DD2 500 MHz spectrometer. All chemical shifts are reported in ppm relative to residual proton signals of MeCN-d<sub>3</sub> (1.94 ppm).<sup>[249]</sup> Line shapes were analyzed using the “fit region” function in MestreNova. <sup>7</sup>Li NMR and <sup>19</sup>F NMR spectra as well as <sup>1</sup>H NMR spectra of ligands and precursors were recorded on a Bruker Avance 300 MHz spectrometer.

UV-vis absorption spectra were recorded with a Cary5000 Bio Spectrophotometer, using Schlenk quartz cuvettes, and with an Agilent A453 spectrometer with a Unisoku USP 203 cryostat. Spectra were analyzed by Cary Win UV software.

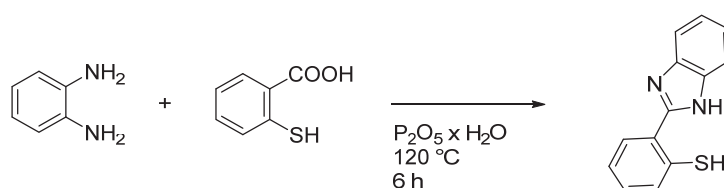
ESI mass spectra were measured on a Thermo Finnigan Trace LCQ spectrometer.

Irradiation experiments were carried out in Schlenk cuvettes, EPR tubes, or other reaction tubes made from quartz. The following light sources were used: Mercury arc lamp: 200 V, 20 Hz, 15 W, 200–600 nm or Light Emitting Diodes (LEDs) by Sahlmann Photochemical Solutions with 3 x 365 nm, 3400 mW, LED type Nichia NC4U133A.

## 11.2 Syntheses of Ligands and Clusters

Synthesis of the ligand  $L^{SN}H_2$  and of diferric, protonated, and mixed valent clusters  $4(NEt_4)_2$  and  $26(NEt_4)_2$  were carried out as reported previously.<sup>[192]</sup> Synthesis of  $L^{SN}H_2$  and of diferric  $4(NEt_4)_2$  was partially adapted from literature.

### Ligand Synthesis of $L^{SN}H_2$



Ligand synthesis was partially adapted from literature.<sup>[139]</sup>

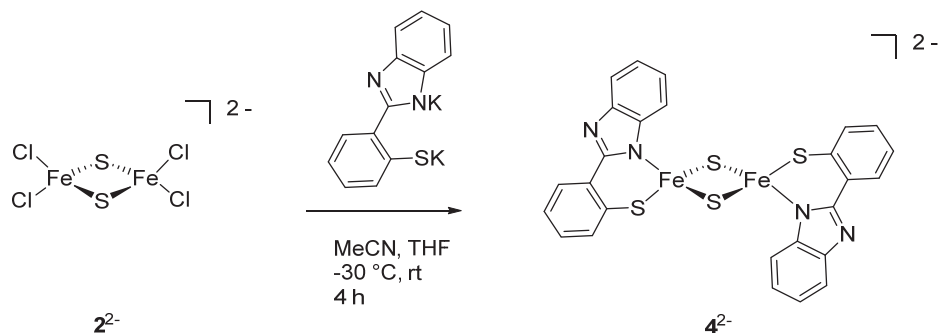
Polyphosphoric acid (3.0 g) and MeOH (3.0 g) were heated to  $80\text{ }^\circ\text{C}$ . Thiosalicylic acid (3.0 g, 19.5 mmol, 1.0 eq) and o-phenyldiamine (2.4 g, 19.5 mmol, 1.0 eq) were added and the mixture was stirred at  $120\text{ }^\circ\text{C}$  for 6 h. The resulting mixture was poured onto ice and neutralized by adding NaOH (2.4 g). The resulting precipitate was filtered off and suspended in MeOH and stirred at  $68\text{ }^\circ\text{C}$  for 12 h. The resulting precipitate was filtered off, washed repeatedly with hot MeOH and  $H_2O$  and dried under reduced pressure to afford the product  $L^{SN}H_2$  (2.0 g, 8.85 mmol, 45.4 %).

$^1H$  NMR (300MHz, DMSO- $d_6$ ):  $\delta$  (ppm) = 7.28 (q,  $J = 8.6, 7.8$  Hz, 2 H, Ar-H), 7.52 – 7.39 (m, 3 H, Ar-H), 7.60 (d,  $J = 7.7$  Hz, 1 H, Ar-H), 7.84 – 7.70 (m, 2 H, Ar-H), 7.96 (d,  $J = 7.9$  Hz, 1 H, Ar-H), 13.0 (1 H, NH).

MS (ESI (+), MeCN):  $m/z = 226.0$   $[M + H]^+$

## Complex Synthesis

### Synthesis of $4(\text{NEt}_4)_2$



Complex synthesis was partially adapted from literature.<sup>[139]</sup>

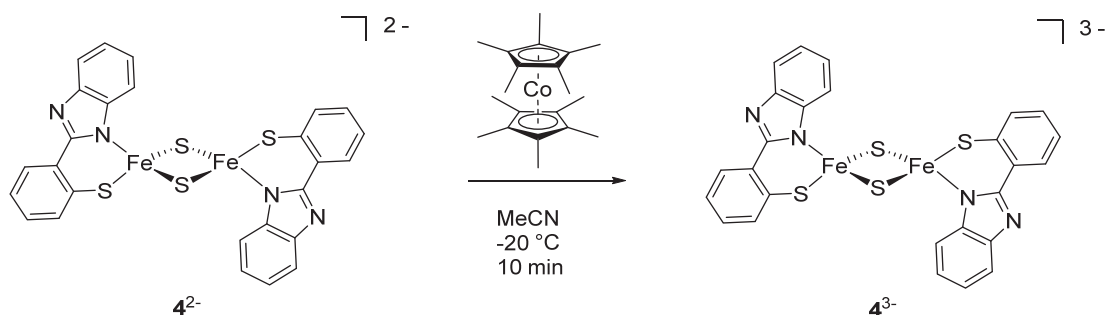
To a solution of the proligand (1.00 g, 4.44 mmol, 2.56 eq) in THF (100 mL), KH (352 mg, 8.8 mmol, 5.10 eq) was added and the resulting solution was stirred overnight and added to a solution of  $(\text{NEt}_4)_2[\text{Fe}_2\text{S}_2\text{Cl}_4]$  (1.00 g, 1.73 mmol, 1.0 eq) in MeCN (100 mL) at  $-30^\circ\text{C}$ . The mixture was stirred for 4 h while slowly warming up to room temperature. After storage at  $-20^\circ\text{C}$  for 2 days, the precipitate was filtered off and diethyl ether (40 mL) was added to the remaining solution. Black crystals were filtered off after storage at  $-20^\circ\text{C}$  for 10 d and washed with diethyl ether (2 x 15 mL). Drying under reduced pressure afforded the product  $4(\text{NEt}_4)_2$  (360 mg, 0.45 mmol, 26 %). Single crystals suitable for X-ray diffraction were obtained by slow diffusion of diethyl ether into a solution of  $4(\text{NEt}_4)_2$  in MeCN at  $8^\circ\text{C}$ .

**$^1\text{H}$  NMR** (500 MHz, MeCN- $d_3$ , 243 K):  $\delta$  (ppm) = 1.07 (s, 24H, 8  $\text{CH}_3$ ), 3.08 (s, 16H, 8  $\text{CH}_2$ ), 3.51 (s, 1 H, H-3), 4.71 (s, 1 H, H-1), 5.54 (s, 1 H, H-6), 7.29 (s, 1 H, H-7), 9.54 (s, 1 H, H-2), 10.73 (s, 1 H, H-5), 10.91 (s, 1 H, H-4).

**MS** (ESI  $-$ ), MeCN):  $m/z$  = 624.9  $[\text{M} - \text{H}]^-$ , 754.9  $[\text{M} + \text{NEt}_4]^+$ .

**UV-vis** (MeCN, 243 K):  $\lambda$  [nm]( $\epsilon_{\text{rel}}$ ) = 438 (6711), 510 (7000), 584 (6200).

### Mixed Valent Cluster $4(\text{NEt}_4)(\text{CoCp}^*_2)$

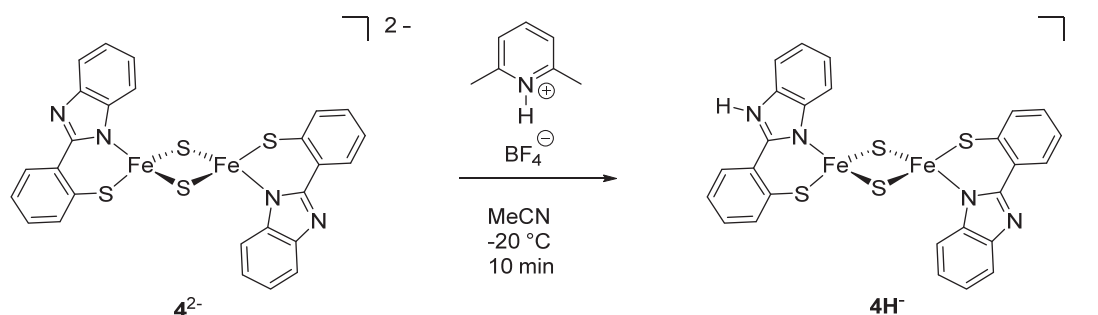


$4^{3-}$  was generated by addition of decamethylcobaltocene (3.5 mg, 0.0106 mmol, 1.03 eq) to a solution of  $4(\text{NEt}_4)_2$  (9.2 mg, 0.0103 mmol) in MeCN (5 mL)  $-20^\circ\text{C}$ . Solid material can be obtained by addition of diethyl ether (15 mL) and filtration of the resulting solid. Single crystals suitable for X-ray diffraction were obtained by slow diffusion of diethyl ether into a solution of  $4(\text{NEt}_4)(\text{CoCp}^*_2)$  in MeCN at  $8^\circ\text{C}$ .

$^1\text{H NMR}$  (500 MHz, MeCN- $\text{d}_3$ , 243 K):  $\delta$  (ppm) = 1.07 (s, 24 H, 8  $\text{CH}_3$ ), 2.62 (s, 2 H), 3.08 (s, 16 H, 8  $\text{CH}_2$ ), 4.57 (s, 2 H), 5.11 (s, 1H), 5.17 (s, 1 H), 7.35 (s, 1 H), 7.52 (s, 1 H), 10.79 (s, 1 H), 10.97 (s, 1 H), 11.70 (s, 1 H), 11.91 (s, 1 H), 12.43 (s, 1 H), 12.57 (s, 1 H).

UV-vis (MeCN, 243 K):  $\lambda$  [nm]( $\epsilon_{\text{rel}}$  [ $\text{M}^{-1} \text{cm}^{-1}$ ]) = 556 (4100), 670 (980).

### Protonated Cluster $4\text{H}^-$



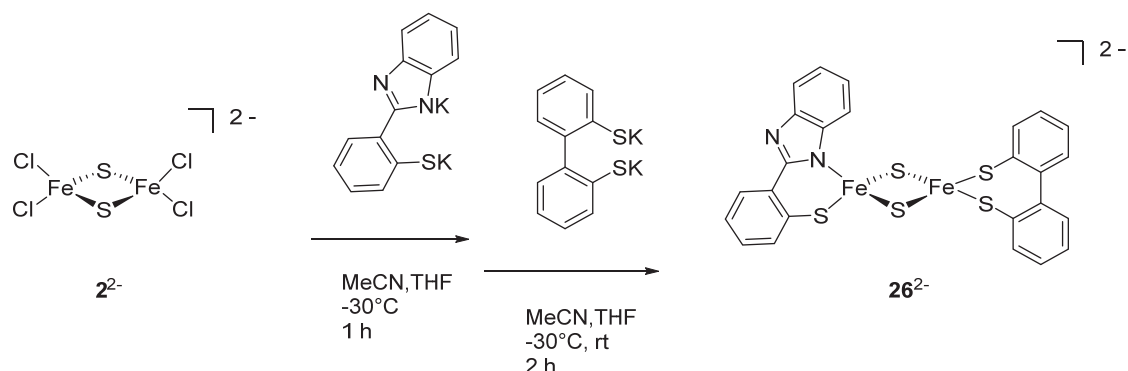
$4\text{H}^-$  was generated *in situ* by addition of 2,6-dimethylpyridinium tetrafluoroborate [DMPH]( $\text{BF}_4$ ) (3.5 mg, 0.0106 mmol, 1.03 eq) to a solution of  $4(\text{NEt}_4)_2$  (9.2 mg, 0.0103 mmol) in MeCN (5 mL) at  $-30^\circ\text{C}$ .

$^1\text{H NMR}$  (500 MHz, MeCN- $\text{d}_3$ , 243 K):  $\delta$  (ppm) = 1.07 (s, 24 H, 8  $\text{CH}_3$ ), 3.08 (s, 16 H, 8  $\text{CH}_2$ ), 3.55 (s, 1 H), 3.61 (s, 1 H), 4.47 (s, 1 H), 4.68 (s, 1 H), 5.94 (s, 1 H), 6.11 (s, 1 H), 6.91

(s, 1 H), 7.39 (s, 1 H), 9.52 (s, 1 H), 9.55 (s, 1 H), 10.36 (s, 1 H), 10.40 (s, 1 H), 10.58 (s, 1 H), 10.65 (s, 1 H), 15.66 (s, 1 H, NH).

UV-vis (MeCN, 243 K):  $\lambda$  [nm] ( $\epsilon_{\text{rel}}[\text{M}^{-1} \text{cm}^{-1}]$ ) = 518 (6800), 575 (6100).

### Diferriic Cluster **26**(NEt<sub>4</sub>)<sub>2</sub>

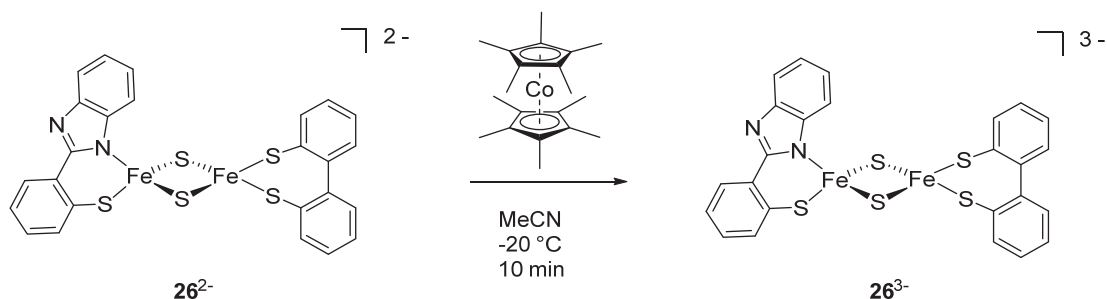


To a solution of H<sub>2</sub>L<sup>SN</sup> (335 mg, 1.49 mmol, 1.07 eq) in THF (100 mL), KH (120 mg, 3.00 mmol, 2.14 eq.) was added and the solution was stirred overnight (solution A). To a suspension of H<sub>2</sub>L<sup>SS</sup> (305 mg, 1.40 mmol, 1.0 eq) in THF (100 mL) was added KH (115 mg, 2.87 mmol, 2.07 eq) and the solution was stirred overnight. (NEt<sub>4</sub>)<sub>2</sub>[Fe<sub>2</sub>S<sub>2</sub>Cl<sub>4</sub>] (0.80 g, 1.39 mmol) was dissolved in MeCN and solution A was added at –30 °C. After stirring for 1 h solution B was added and stirring was continued at –30 °C for 2 h, slowly warming up to 20° C. After storage at –20° C for 2 d the precipitate was filtered off and Et<sub>2</sub>O (40 ml) was added to the remaining solution. After storage at –20°C for 10 d black crystals were filtered off, washed with Et<sub>2</sub>O (2 x 20 mL) and dried under reduced pressure. Several recrystallization steps were found necessary to obtain the pure product (135 mg, 0.15 mmol, 11%).

<sup>1</sup>H NMR (500 MHz, MeCN-d<sub>3</sub>):  $\delta$  [ppm] = 1.02 (s, 24 H, CH<sub>3</sub>), 2.81 (s, 16 H, CH<sub>2</sub>), 3.15 (s, 1 H, L<sup>1</sup>), 3.35 (s, 1 H, L<sup>1</sup>), 3.55 (s, 1 H, L<sup>2</sup>), 4.26 (s, 1 H, L<sup>1</sup>), 4.45 (s, 1 H, L<sup>1</sup>), 4.75 (s, 1 H, L<sup>2</sup>), 5.82 (s, 1 H, L<sup>2</sup>), 7.24 (s, 1 H, L<sup>2</sup>), 8.71 (s, 1 H, L<sup>1</sup>), 8.76 (s, 1 H, L<sup>1</sup>), 8.90 (s, 1 H, L<sup>1</sup>), 9.00 (s, 1 H, L<sup>1</sup>), 9.43 (s, 1 H, L<sup>2</sup>), 10.58 (s, 1 H, L<sup>2</sup>), 10.67 (s, 1 H, L<sup>2</sup>).

MS (ESI(–), MeCN):  $m/z$  = 616.9 [M – H]<sup>–</sup>, 746.9 [M + NEt<sub>4</sub>]<sup>–</sup>.

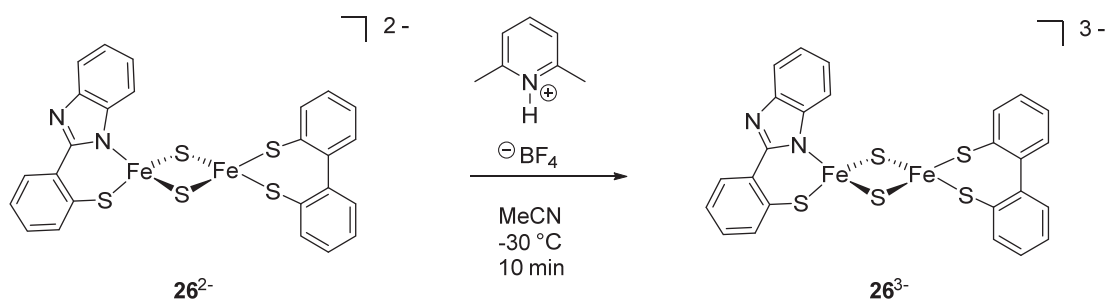
UV-vis (MeCN, 243 K):  $\lambda$  [nm] ( $\epsilon$  [M<sup>–1</sup> cm<sup>–1</sup>]) = 326 (17000), 375 (9500), 422 (7100), 453 (6500), 550 (4600).

**Mixed Valent Cluster  $26(\text{NEt}_4)_2(\text{CoCp}^*_2)$** 


To a solution of  $26(\text{Et}_4\text{N})_2$  (9.2 mg, 0.0105 mmol) in MeCN (5 mL) was added a solution of decamethylcobaltocene (3.5 mg, 0.0106 mmol, 1.01 eq) in THF (1 mL) at  $-20^\circ\text{C}$ . Addition of  $\text{Et}_2\text{O}$  (10 mL) led to precipitation of the crude product. Rinsing with  $\text{Et}_2\text{O}$  and drying under reduced pressure afforded the reduced cluster  $26(\text{NEt}_4)_2(\text{CoCp}^*_2)$ .

$^1\text{H NMR}$  (500 MHz,  $\text{MeCN-d}_3$ , 293 K):  $\delta$  [ppm] =  $-6.00$ ,  $-5.85$ ,  $1.02$  (s, 24 H,  $\text{CH}_3$ ),  $2.81$  (s, 16 H,  $\text{CH}_2$ ),  $3.65$  (s, 1 H),  $6.09$  (s, 1 H),  $6.31$  (s, 1 H),  $7.42$  (s, 1 H),  $7.77$  (s, 2 H),  $8.71$  (s, 1 H),  $9.71$  (s, 1 H),  $10.75$  (s, 2 H),  $11.97$  (s, 2 H).

**UV-vis** (MeCN, 243 K):  $\lambda$  [nm]( $\epsilon$  [ $\text{M}^{-1} \text{cm}^{-1}$ ]) = 562 (3300).

**Protonated Cluster  $26\text{H}^+$** 


$26\text{H}^+$  was generated *in situ* by addition of 2,6-dimethylpyridinium tetrafluoroborate [DMPH]( $\text{BF}_4$ ) (3.5 mg, 0.0106 mmol, 1.03 eq) to a solution of  $(\text{Et}_4\text{N})_226$  (9.2 mg, 0.0103 mmol) in MeCN (5 mL) at  $-30^\circ\text{C}$ .

$^1\text{H NMR}$  (500 MHz,  $\text{MeCN-d}_3$ , 293 K):  $\delta$  (ppm) =  $1.23$  (s, 24 H, 8  $\text{CH}_3$ ),  $3.16$  (s, 16 H, 8  $\text{CH}_2$ ),  $4.27$  (s, 1 H),  $4.46$  (s, 1 H),  $6.65$  (s, 1 H),  $8.98$  (s, 1 H),  $9.11$  (s, 1 H),  $9.18$  (s, 1 H),  $9.31$  (s, 1 H),  $9.89$  (s, 1 H),  $10.46$  (s, 1 H),  $10.77$  (s, 1 H).

**UV-vis** (MeCN, 243 K):  $\lambda$  [nm]( $\epsilon$  [ $\text{M}^{-1} \text{cm}^{-1}$ ]) = 372 (9950), 452 (5650), 551 (4200).

## Crystallization of $12a[Na(15\text{-crown-5})]_2$

To a solution of  $12a(NEt_4)_2$  (5.00 mg, 4.62 mmol) in DMF (10 mL) was added benzyl-bis(catechole)silicate-sodium(15-crown-5) (8.01 mg, 13.81 mmol, 2.98 eq). Slow diffusion of diethyl ether into this solution at 8 °C afforded dark red crystals suitable for X-ray diffraction.

### 11.3 Details of Cation Binding Titrations and Job Plot Experiments

For determination of bonding stoichiometry between  $4^{2-}$  and  $Li^+$  the method of continuous variation (Job Plot) was employed. Therefore, stock solutions of  $4(NEt_4)_2$  and LiOTf with identical molar concentrations (0.36 mM each) were prepared in MeCN. Samples containing these stock solutions in varying ratios were prepared while keeping the total sample volume constant (2 mL). UV-vis absorption spectra of these samples were recorded on a Cary 5000 spectrophotometer at 23 °C. The extinction coefficient of the band at 438 nm was determined from each spectrum. The difference in extinction coefficient ( $\Delta\varepsilon(438\text{ nm}) - \Delta\varepsilon(438\text{ nm})_0$ ) as a measure of the presence of the binding product was multiplied by  $(1 - r_{Li})$ ,  $r_{Li}$  being the molar ratio of  $Li^+$  in the respective sample and plotted vs.  $r_{Li}$ . Three independent runs were performed using three independently prepared stock solutions of  $4(NEt_4)_2$  and LiOTf. The resulting Job Plots showed maxima at  $r_{Li} = 0.59, 0.63, \text{ and } 0.64$ , resulting in an average maximum of 0.62. Thus a 1:2 interaction between  $4(NEt_4)_2$  and LiOTf is assumed.

Binding constants were determined from titrations of  $4(NEt_4)_2$  and LiOTf or NaOTf as well as from titrations of  $26(NEt_4)_2$  and LiOTf or NaOTf. For the determination of binding constants between  $4(NEt_4)_2$  and LiOTf stock solutions of  $4(NEt_4)_2$  (0.16 mM) and LiOTf (27 mM) were prepared in MeCN. A UV-vis spectrum of pure  $4(NEt_4)_2$  was recorded and LiOTf was then added in steps of 5 eq and monitored by UV-vis spectroscopy. The extinction coefficient at 438 nm was determined for each spectrum by correcting for dilution effects caused by addition of LiOTf solution. The resulting data was then fitted using bindfit v0.5 assuming a 1:2 interaction. Three independent runs were performed and the individual values  $K_1 = 314\text{ M}^{-1}$ ,  $K_1 = 209\text{ M}^{-1}$ ;  $K_1 = 271\text{ M}^{-1}$ ,  $K_2 = 30\text{ M}^{-1}$  and  $K_1 = 252\text{ M}^{-1}$ ,  $K_1 = 155\text{ M}^{-1}$  were averaged. The same approach was followed for the determination of the binding constants between  $4(NEt_4)_2$  and NaOTf (NaOTf stock solution: 289 mM). NaOTf was added in steps of eq. Three independent runs yielded binding constant of  $K_1 = 1.446\text{ M}^{-1}$ ,  $K_2 = 0.231\text{ M}^{-1}$ ;  $K_1 = 4.58\text{ M}^{-1}$ ,  $K_2 = 4.60\text{ M}^{-1}$ , and  $K_1 = 7.23\text{ M}^{-1}$ ,  $K_1 = 9.48\text{ M}^{-1}$

For the determination of binding constants between **26**(NEt<sub>4</sub>)<sub>2</sub> and LiOTf stock solutions of **26**(NEt<sub>4</sub>)<sub>2</sub> (0.16 mM) and LiOTf (11 mM) were prepared in MeCN. A UV-vis spectrum of pure **26**(NEt<sub>4</sub>)<sub>2</sub> was recorded and LiOTf was then added in steps of 14 eq and monitored by UV-vis spectroscopy. The extinction coefficient at 424 nm was determined for each spectrum by correcting for dilution effects caused by addition of LiOTf solution. The resulting data was then fitted using bindfit v0.5 assuming a 1:1 interaction and binding constants of  $K_a = 1.232, 0.140, 0.292 \text{ M}^{-1}$  were obtained.

## 11.4 Electrochemical Measurements

Cyclic voltammograms for **4**(NEt<sub>4</sub>)<sub>2</sub> and **26**(NEt<sub>4</sub>)<sub>2</sub> and their protonated forms were measured using a CH Instruments 600D potentiostat in a glove box, with a glassy carbon working electrode (0.3 cm diameter), Ag reference electrode, and Pt auxiliary electrode. All CVs were referenced internally to  $Fc/Fc^+$  (0 V) by addition of Fc to the solution of analyte.<sup>[192]</sup>

Temperature dependent electrochemical measurements were carried out with an AUTOLAB PGSTAT12 potentiostat/galvanostat using a platinum disc electrode with a reaction surface of 2 mm as working electrode. A platinum rod electrode (along with internal referencing versus  $Fc/Fc^+$ ) was used as a reference electrode and a Metrohm glassy carbon electrode was used as auxiliary electrode. All measurements were carried out inside an MBraun Unilab AV glove box under argon atmosphere. Tetrabutylammonium hexafluorophosphate (0.1 M in MeCN; electrochemical grade from Fluka) was used as electrolyte. The concentration of each sample was about 0.12 mM in 5.5 ml anhydrous MeCN, which was purified on an MB-SPS 800 system. Before recording the voltammograms, the sample was stirred for 5 min. The temperature was varied using a Julabo thermostat and measured directly inside the CV cell. No significant variations of the temperature were observed during the single CV measurements. For each compound three independent measurements were performed *i.e.* three independent sample solutions were prepared. The temperature was varied in a cyclic fashion to exclude effects from solvent evaporation over the course of the experiment. No significant differences between warming up and cooling down were observed. For each sample three cyclic CV scans were performed, the first of which was discarded. As a final step, ferrocene was added to each sample for internal referencing at 23 °C. Data were recorded and analyzed using the Metrohm NOVA2.1 software. Linear fits of  $E_{1/2}$  (V vs. SHE) vs.  $T$  (K) were calculated in Origin Pro 8.5.

## 11.5 Double Mixing Stopped Flow Experiments

Kinetic measurements on PCET reactions were performed using a HI-TECH SCIENTIFIC CryoStopped-Flow System (SF- 61DX2) capable of double-mixing, and equipped with a TC-61 temperature controller and a diode array detector. The stopped-flow system was controlled by the Kinetic Studio 2.20 software. The system was thermally equilibrated for 30 min before data acquisition at each temperature, and prior to kinetic runs, the stopped-flow was thoroughly flushed with dry MeCN. All volumetric glassware and glass syringes employed were rinsed with dry MeCN in the glove-box prior to use. In the glove-box, MeCN solutions of  $\mathbf{4}^{3-}$  (0.738 mM) or  $\mathbf{26}^{3-}$  (0.738 mM), [DMPH](BF<sub>4</sub>) (0.738 mM), and TEMPO (3.3, 6.4, 9.6, 12.8 and 16.0 mM) were prepared. Reagents and MeCN were loaded into gas-tight syringes (SGE), which were attached to gas-tight 2-way valves (SGE). Protonation of the mixed valent clusters was carried out in the first mixing and after a reaction time/ delay of 1 ns, TEMPO solution was added in the second mixing step and the subsequent spectral changes in the range of 300 nm to 700 nm was monitored for 2 s (in case of  $\mathbf{4H}^{2-}$ ) or 8 s (in case of  $\mathbf{26H}^{2-}$ ). First-order fitting of the experimental data was performed with SPECFIT/32 (Version 3.0). Linear fits of  $k$  vs.  $c$  were calculated in OriginPro 8.5.<sup>[192]</sup>

## 11.6 EPR Measurements

EPR spectra were measured with a Bruker E500 ELEXSYS X-band spectrometer equipped with a standard cavity (ER4102ST, 9.45 GHz). The sample temperature was maintained constant with an Oxford instrument Helium flow cryostat (ESP910) and an Oxford temperature controller (ITC-4). The microwave frequency was measured with the built-in frequency counter and the magnetic field was calibrated by using a NMR field probe (Bruker ER035M).

**Table 11.1:** EPR parameters of mixed valent [2Fe-2S] species described in this thesis.

	$g_1$	$g_2$	$g_3$	$g_{av}$	conditions
$\mathbf{12a}^{3-}$ <sup>[149]</sup>	2.0	1.935	1.885	1.945	MeCN, 0.1 M [NBu <sub>4</sub> ](PF <sub>6</sub> ), 20 K
$\mathbf{4}^{3-}$ <sup>[192]</sup>	2.01	1.932	1.882	1.941	MeCN, 160 K
$\mathbf{26}^{3-}$ <sup>[192]</sup>	2.005	1.932	1.875	1.937	MeCN, 160 K
$\mathbf{12a}^{2-}$ + silicate	2.015	1.936	1.891	1.947	DMF, 144 K
$\mathbf{4}^{2-}$ + silicate	2.012	1.936	1.890	1.946	DMF, 144 K
$\mathbf{12a}^{2-}$ + DMPA	2.01	1.915	1.850	1.925	MeCN, 169 K
$\mathbf{4}^{2-}$ + DMPA	2.011	1.933	1.885	1.942	DMF, 144 K

## 11.7 Mößbauer Measurements

Mößbauer spectra were recorded with a  $^{57}\text{Co}$  source in a Rh matrix using an alternating constant acceleration *Wissel* Mößbauer spectrometer operated in the transmission mode and equipped with a *Janis* closed-cycle helium cryostat. Isomer shifts are given relative to iron metal at ambient temperature. Simulation of the experimental data was performed with the *Mfit* program using *Lorentzian* line doublets.<sup>[250]</sup>

**Table 11.2:** Mößbauer parameters of diferric and mixed valent [2Fe–2S] species described in this thesis.

compound	$T$ (K)	$\delta_1$ (mm/s)	$\delta_2$ (mm/s)	$\Delta E_{Q1}$ (mm/s)	$\Delta E_{Q2}$ (mm/s)	Fe <sup>III</sup> : Fe <sup>II</sup>
<b>4</b> (NEt <sub>4</sub> ) <sub>2</sub>	80	0.27	–	0.81	–	–
<b>4</b> (CoCp <sup>*</sup> ) <sub>2</sub> (NEt <sub>4</sub> )	12	0.35	0.62	1.20	3.09	51:49
	200	0.41	–	1.39	–	–
<b>26</b> (NEt <sub>4</sub> ) <sub>2</sub>	80	0.27	0.29	0.77	1.01	–
<b>26</b> (CoCp <sup>*</sup> ) <sub>2</sub> (NEt <sub>4</sub> ) <sub>2</sub>	12	0.39	0.66	1.29	3.13	44:56
	80	0.41	0.66	1.06	3.01	53:47
	200	0.33	0.63	1.06	2.71	48:52
<b>12a</b> (NEt <sub>4</sub> ) <sub>2</sub> + DMPA	12	0.35	0.85	1.18	3.10	34:66
	80	0.35	0.86	1.15	3.06	39:61
	200	0.31	0.80	1.11	2.91	46:54
<b>4</b> (NEt <sub>4</sub> ) <sub>2</sub> + DMPA	13	0.37	0.99	0.90	2.94	46:54
	80	0.38	0.98	0.94	2.95	59:41
	200	0.34	0.92	0.91	2.92	66:34

## 11.8 X-Ray Crystallography

Crystal data and details of the data collections are given in Tables S1-S3. X-ray data were collected on a STOE IPDS II diffractometer (graphite monochromated Mo-K $\alpha$  radiation,  $\lambda = 0.71073$  Å) by use of  $\omega$  scans at  $-140$  °C. The structures were solved with SHELXT<sup>[251]</sup> and refined on  $F^2$  using all reflections with SHELXL-2014.<sup>[252]</sup> Non-hydrogen atoms were refined anisotropically. Hydrogen atoms were placed in calculated positions and assigned to an isotropic displacement parameter of 1.2/1.5  $U_{\text{eq}}(\text{C})$ . Face-indexed absorption corrections were performed numerically with the program X-RED.<sup>[253]</sup> CCDC-1524048 and - 1524049 contain the supplementary crystallographic data for **4**(NEt<sub>4</sub>)<sub>2</sub> and **4**(NEt<sub>4</sub>)(CoCp<sup>\*</sup>)<sub>2</sub>. These data can be obtained from The Cambridge Crystallographic Data Centre *via* [http://www.ccdc.cam.ac.uk/data\\_request/cif](http://www.ccdc.cam.ac.uk/data_request/cif).

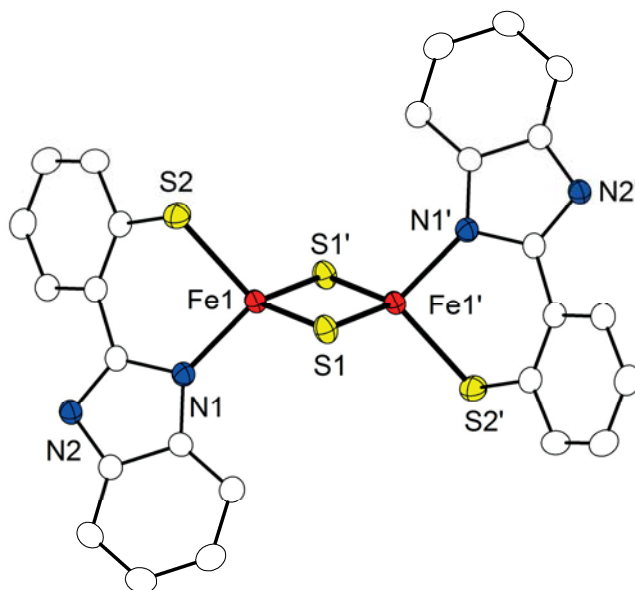


**Figure 11.1:** Plot (50% probability thermal ellipsoids) of  $4(\text{NEt}_4)_2$  (hydrogen atoms and counter ions omitted for clarity). Selected bond lengths [ $\text{\AA}$ ] and angles [ $^\circ$ ]: Fe1–N1 1.9905(13), Fe1–S1 2.1898(5), Fe1–S1' 2.2026(5), Fe1–S2 2.2770(5), Fe1 $\cdots$ Fe1' 2.6479(5); N1–Fe1–S1 114.21(4), N1–Fe1–S1' 113.92(4), S1–Fe1–S1' 105.854(16), N1–Fe1–S2 95.79(4), S1–Fe1–S2 112.515(19), S1'–Fe1–S2 114.707(18), Fe1–S1–Fe1' 74.144(16), C1–S2–Fe1 97.71(6). Symmetry transformation used to generate equivalent atoms: (')  $1-x, 1-y, 1-z$ .

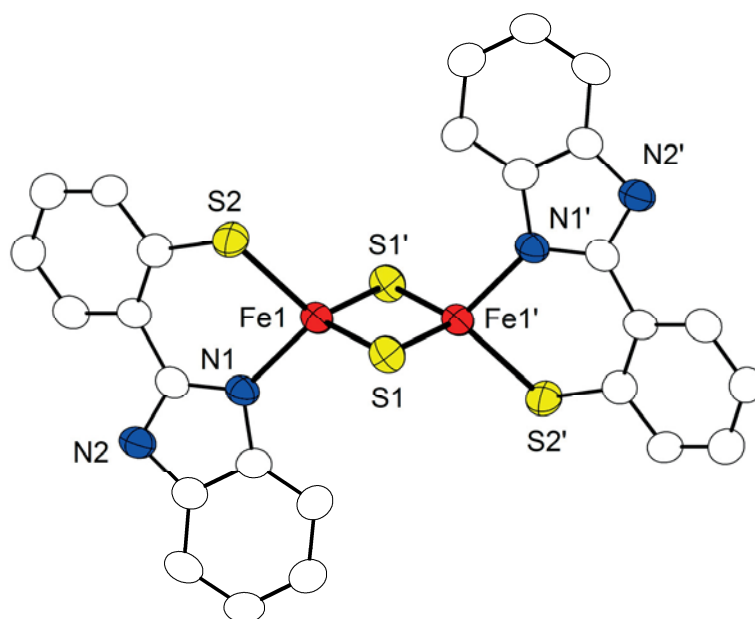


**Figure 11.2:** Plot (50% probability thermal ellipsoids) of  $4(\text{Cp}^*_2\text{Co})(\text{NEt}_4)$  (hydrogen atoms and counter ions omitted for clarity). Selected bond lengths [ $\text{\AA}$ ] and angles [ $^\circ$ ]: Fe1–N1 2.029(3), Fe1–S1 2.2224(12), Fe1–S1' 2.2225(12), Fe1–S2 2.3238(11), Fe1 $\cdots$ Fe1' 2.6500(11); N1–Fe1–S1 113.83(11), N1–Fe1–S1' 113.84(10), S1–Fe1–S1' 106.81(4), N1–Fe1–S2 92.16(9), S1–Fe1–S2 110.97(5), S1'–Fe1–S2 119.00(5), Fe1–S1–Fe1' 73.20(4), C1–S2–Fe1 107.33(13). Symmetry transformation used to generate equivalent atoms: (')  $1-x, 2-y, -z$ .

**Table 11.3:** Crystal data and refinement details for  $4(\text{NEt}_4)_2$  and  $4(\text{Cp}^*_2\text{Co})_2(\text{NEt}_4)$ 

	$4(\text{NEt}_4)_2$	$4(\text{Cp}^*_2\text{Co})_2(\text{NEt}_4)$
empirical formula	$\text{C}_{42}\text{H}_{56}\text{Fe}_2\text{N}_6\text{S}_4$	$\text{C}_{74}\text{H}_{96}\text{Co}_2\text{Fe}_2\text{N}_5\text{S}_4$
formula weight	884.86	1413.35
crystal size [ $\text{mm}^3$ ]	$0.29 \times 0.19 \times 0.07$	$0.35 \times 0.19 \times 0.15$
crystal system		triclinic
space group		$P\bar{1}$
$a$ [ $\text{\AA}$ ]	8.9097(5)	11.9682(15)
$b$ [ $\text{\AA}$ ]	10.0041(5)	12.0886(15)
$c$ [ $\text{\AA}$ ]	13.5958(8)	13.1959(18)
$\alpha$ [ $^\circ$ ]	108.442(4)	73.383(10)
$\beta$ [ $^\circ$ ]	105.863(4)	66.648(10)
$\gamma$ [ $^\circ$ ]	98.503(4)	86.700(10)
$V$ [ $\text{\AA}^3$ ]	1068.74(11)	1676.2(4)
$Z$	1	1
$\rho$ [ $\text{g/cm}^3$ ]	1.375	1.400
$F(000)$	466	745
$\mu$ [ $\text{mm}^{-1}$ ]	0.912	1.082
$T_{\min} / T_{\max}$	0.6991 / 0.8994	0.6659 / 0.8944
$\theta$ -range [ $^\circ$ ]	1.680 - 26.764	1.755 - 27.060
$hkl$ -range	-11 - 9, $\pm 12$ , $\pm 17$	$\pm 15$ , -15 - 14, $\pm 16$
measured refl.	12238	21216
unique refl. [ $R_{\text{int}}$ ]	4518 [0.0232]	7133 [0.1221]
observed refl. ( $I > 2\sigma(I)$ )	3871	4827
data / restraints / param.	4518 / 0 / 248	7133 / 237 / 535
goodness-of-fit ( $F^2$ )	1.026	0.975
$R1, wR2$ ( $I > 2\sigma(I)$ )	0.0270, 0.0608	0.0575, 0.1284
$R1, wR2$ (all data)	0.0359, 0.0631	0.0933, 0.1465
resid. el. dens. [ $\text{e}/\text{\AA}^3$ ]	-0.271 / 0.358	-0.852 / 0.770

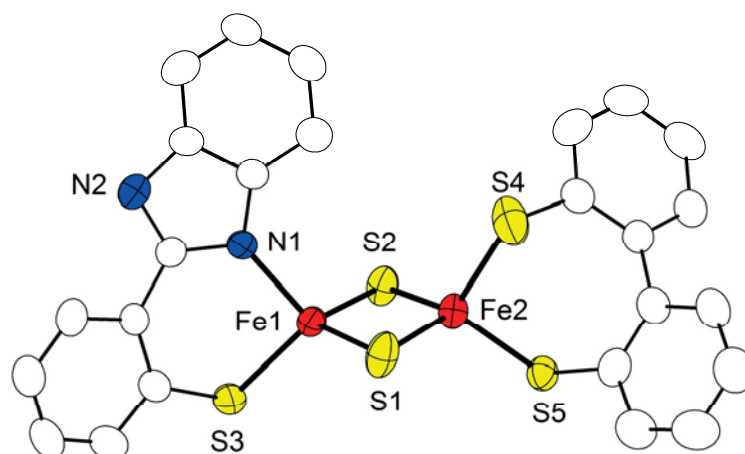


**Figure 11.3:** Plot (50% probability thermal ellipsoids) of **26(NEt<sub>4</sub>)<sub>2</sub>**. (hydrogen atoms, counter ions and solvent molecules omitted for clarity). Selected bond lengths [Å] and angles [°]: Fe1–N1 2.009(4), Fe1–S1 2.2001(15), Fe1–S2 2.2047(16), Fe1–S3 2.2891(16), Fe2–S1 2.2068(15), Fe2–S2 2.2132(17), Fe2–S4 2.278(2), Fe2–S5 2.2965(15), Fe1···Fe2 2.6920(10); N1–Fe1–S1 109.08(12), N1–Fe1–S2 116.80(12), S1–Fe1–S2 104.92(6), N1–Fe1–S3 95.65(12), S1–Fe1–S3 110.43(6), S2–Fe1–S3 119.69(7), S1–Fe2–S2 104.40(6), S1–Fe2–S4 118.21(8), S2–Fe2–S4 104.42(8), S1–Fe2–S5 102.67(6), S2–Fe2–S5 124.51(7), S4–Fe2–S5 103.81(6), Fe1–S1–Fe2 75.30(5), Fe1–S2–Fe2 75.08(5).

**Table 11.4:** Crystal data and refinement details for **26(NEt<sub>4</sub>)<sub>2</sub>**.

compound	<b>26(NEt<sub>4</sub>)<sub>2</sub></b>
empirical formula	C <sub>42</sub> H <sub>57.50</sub> Fe <sub>2</sub> N <sub>4.50</sub> S <sub>5</sub>
formula weight	897.42
crystal size [mm <sup>3</sup> ]	0.41 × 0.11 × 0.06
crystal system	triclinic
space group	<i>P</i> $\bar{1}$
<i>a</i> [Å]	10.6068(7)
<i>b</i> [Å]	13.4660(9)
<i>c</i> [Å]	16.6462(11)
$\alpha$ [°]	89.972(5)
$\beta$ [°]	85.800(5)
$\gamma$ [°]	67.854(5)
<i>V</i> [Å <sup>3</sup> ]	2195.3(3)
<i>Z</i>	2
$\rho$ [g/cm <sup>3</sup> ]	1.358
<i>F</i> (000)	946
$\mu$ [mm <sup>-1</sup> ]	0.934
<i>T</i> <sub>min</sub> / <i>T</i> <sub>max</sub>	0.6308 / 0.9072
$\theta$ -range [°]	1.227 - 25.666
<i>hkl</i> -range	-11 - 12, $\pm 16$ , $\pm 20$
measured refl.	25223
unique refl. [ <i>R</i> <sub>int</sub> ]	8261 [0.0939]
observed refl. ( <i>I</i> > 2 $\sigma$ ( <i>I</i> ))	5025
data / restraints / param.	8261 / 54 / 582
goodness-of-fit ( <i>F</i> <sup>2</sup> )	1.035
<i>R</i> 1, <i>wR</i> 2 ( <i>I</i> > 2 $\sigma$ ( <i>I</i> ))	0.0682, 0.1169
<i>R</i> 1, <i>wR</i> 2 (all data)	0.1273, 0.1340
resid. el. dens. [e/Å <sup>3</sup> ]	-0.314 / 0.607

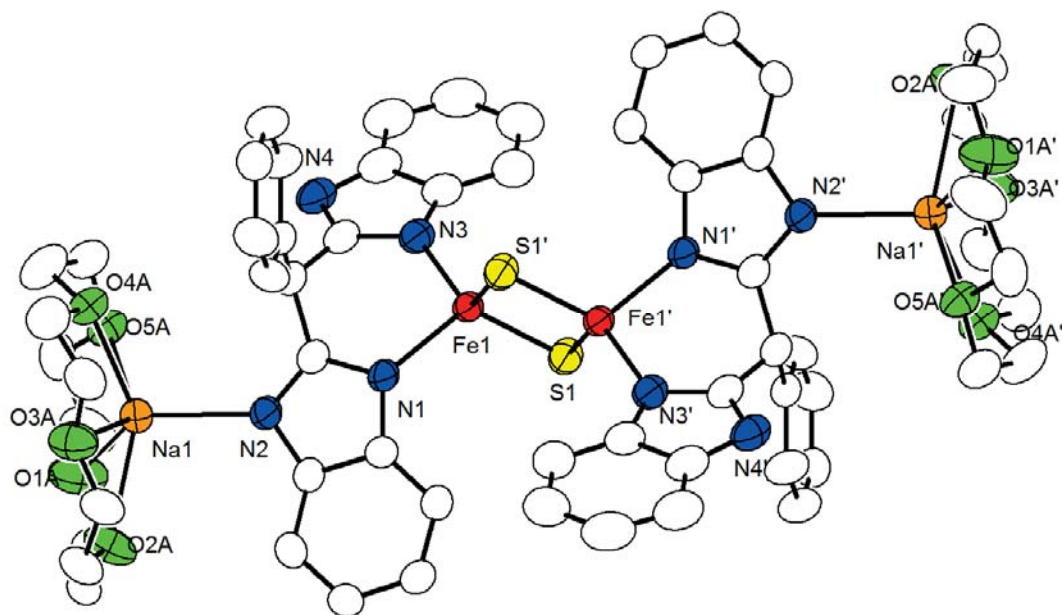


**Figure 11.4:** Plot (50% probability thermal ellipsoids) of **12a**[Na(15-crown-5)]<sub>2</sub>. (hydrogen atoms and solvent molecules omitted for clarity). Selected bond lengths [Å] and angles [°]: Fe1–N1 1.980(2), Fe1–N3 1.9921(2), Fe1–S1 2.1831(8), Fe1–S1' 2.191(8), Fe2–Fe1' 2.6474(7), Fe1'–S1 2.1922(8), N2–Na1 2.400(2); N1–Fe1–N3 94.31(9), S1–Fe1–S1' 105.53(3), Fe1–S1–Fe1' 74.47(3).

**Table 11.5:** Crystal data and refinement details for **12a**[Na(15-crown-5)]<sub>2</sub>

compound	<b>12a</b> [Na(15crown-5)] <sub>2</sub>
empirical formula	C <sub>62</sub> H <sub>68</sub> Fe <sub>2</sub> N <sub>8</sub> Na <sub>2</sub> O <sub>10</sub> S <sub>2</sub>
formula weight	1307.04
<i>T</i> [K]	133(2)
crystal size [mm <sup>3</sup> ]	0.500 x 0.490 x 0.390
crystal system	monoclinic
space group	<i>P</i> 2 <sub>1</sub> / <i>n</i> (No. 14)
<i>a</i> [Å]	11.1265(3)
<i>b</i> [Å]	23.2880(6)
<i>c</i> [Å]	11.9861(4)
α [°]	90
β [°]	98.143(3)
γ [°]	90
<i>V</i> [Å <sup>3</sup> ]	3074.45(16)
<i>Z</i>	2
ρ [g·cm <sup>-3</sup> ]	1.412
<i>F</i> (000)	1364
μ [mm <sup>-1</sup> ]	0.619
<i>T</i> <sub>min</sub> / <i>T</i> <sub>max</sub>	0.6895 / 0.8268
θ-range [°]	1.749 - 25.669
<i>hkl</i> -range	±13, ±28, ±14
measured refl.	36477
unique refl. [ <i>R</i> <sub>int</sub> ]	5804 [0.0376]
observed refl. ( <i>I</i> > 2σ( <i>I</i> ))	5024
data / restr. / param.	5804 / 450 / 518
goodness-of-fit ( <i>F</i> <sup>2</sup> )	1.024
<i>R</i> 1, <i>wR</i> 2 ( <i>I</i> > 2σ( <i>I</i> ))	0.0462 / 0.1179
<i>R</i> 1, <i>wR</i> 2 (all data)	0.0540 / 0.1225
res. el. dens. [e·Å <sup>-3</sup> ]	-0.449 / 0.910

---

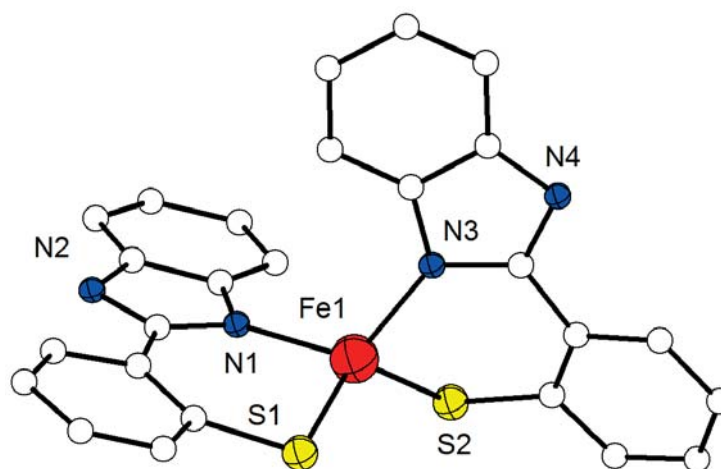


**Figure 11.5:** Plot (50% probability thermal ellipsoids) of **27**(CoCp\*<sub>2</sub>)<sub>2</sub>. (hydrogen atoms, counter ions and solvent molecules omitted for clarity). Selected bond lengths [Å] and angles [°]: Fe1–N1 2.028(4), Fe1–N3 2.016(4), Fe1–S1 2.3150(12), Fe1–S2 2.3329(16); N3–Fe1–S1 115.53(12), N1–Fe1–S1 94.72(11), N3–Fe1–S2 94.48(12), N1–Fe1–S2 113.40(12), S1–Fe1–S2 122.75(6).

11 Experimental Section
 

---

**Table 11.6:** Crystal data and refinement details for  $27(\text{CoCp}^*_2)_2$ .

compound	$27(\text{CoCp}^*_2)_2$ .
empirical formula	$\text{C}_{66}\text{H}_{76}\text{Co}_2\text{FeN}_4\text{S}_2$
formula weight	1163.13
$T$ [K]	133(2)
crystal size [ $\text{mm}^3$ ]	0.500 x 0.500 x 0.490
crystal system	monoclinic
space group	$P2_1$ (No. 4)
$a$ [Å]	11.6625(3)
$b$ [Å]	20.1780(6)
$c$ [Å]	11.9747(3)
$\alpha$ [°]	90
$\beta$ [°]	92.322(2)
$\gamma$ [°]	90
$V$ [Å <sup>3</sup> ]	2815.64(13)
$Z$	2
$\rho$ [ $\text{g}\cdot\text{cm}^{-3}$ ]	1.372
$F(000)$	1224
$\mu$ [ $\text{mm}^{-1}$ ]	0.956
$T_{\text{min}} / T_{\text{max}}$	0.6300 / 0.7228
$\theta$ -range [°]	1.702 - 26.738
$hkl$ -range	$\pm 14, \pm 25, \pm 15$
measured refl.	37002
unique refl. [ $R_{\text{int}}$ ]	11918 [0.0342]
observed refl. ( $I > 2\sigma(I)$ )	11562
data / restr. / param.	11918 / 718 / 977
goodness-of-fit ( $F^2$ )	1.110
$R1, wR2$ ( $I > 2\sigma(I)$ )	0.0291 / 0.0711
$R1, wR2$ (all data)	0.0305 / 0.0716
res. el. dens. [ $\text{e}\cdot\text{Å}^{-3}$ ]	-0.301 / 0.400

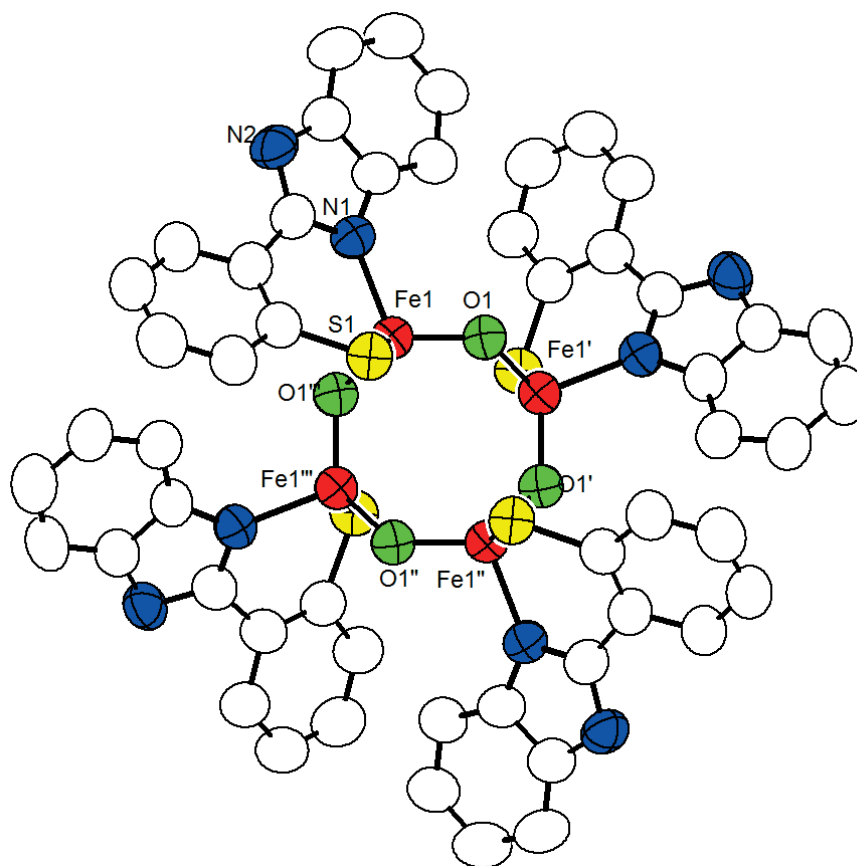
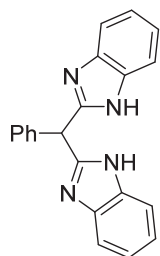


**Figure 11.5:** Plot (50% probability thermal ellipsoids) of  $49(\text{NEt}_4)_4$ . (hydrogen atoms, counter ions and solvent molecules omitted for clarity). Selected bond lengths [ $\text{\AA}$ ] and angles [ $^\circ$ ]: Fe1–O1 1.785(3), Fe1–O1' 1.809(3), Fe1–S1 2.3236(12), Fe1–N1 1.995(3); O1–Fe1–O1' 114.64(14), N1–Fe1–S1 92.34(11), N1–Fe1–O1 110.51(14).

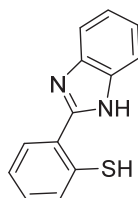
**Table 11.6.** Crystal data and refinement details for **49(NEt<sub>4</sub>)<sub>4</sub>**.

compound	<b>49(NEt<sub>4</sub>)<sub>4</sub></b>
empirical formula	C <sub>84</sub> H <sub>112</sub> Fe <sub>4</sub> N <sub>12</sub> O <sub>4</sub> S <sub>4</sub>
formula weight	1705.49
<i>T</i> [K]	133(2)
crystal system	tetragonal
space group	<i>I</i> 4 <sub>1</sub> / <i>a</i> (No. 88)
<i>a</i> [Å]	19.2763(5)
<i>b</i> [Å]	19.2763(5)
<i>c</i> [Å]	35.2930(10)
α [°]	90
β [°]	90
γ [°]	90
<i>V</i> [Å <sup>3</sup> ]	13114.0(8)
<i>Z</i>	4
ρ [g·cm <sup>-3</sup> ]	0.864
<i>F</i> (000)	3600
μ [mm <sup>-1</sup> ]	0.533
<i>T</i> <sub>min</sub> / <i>T</i> <sub>max</sub>	0.7087 / 0.9636
θ-range [°]	1.204 - 25.933
<i>hkl</i> -range	±23, ±23, -42 to 43
measured refl.	80124
unique refl. [ <i>R</i> <sub>int</sub> ]	6266 [0.1016]
observed refl. ( <i>I</i> > 2σ( <i>I</i> ))	4440
data / restr. / param.	6266 / 0 / 249
goodness-of-fit ( <i>F</i> <sup>2</sup> )	1.099
<i>R</i> 1, <i>wR</i> 2 ( <i>I</i> > 2σ( <i>I</i> ))	0.0739 / 0.2199
<i>R</i> 1, <i>wR</i> 2 (all data)	0.0977 / 0.2405
res. el. dens. [e·Å <sup>-3</sup> ]	-0.338 / 0.484

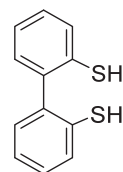
## Structures of Ligands and Clusters



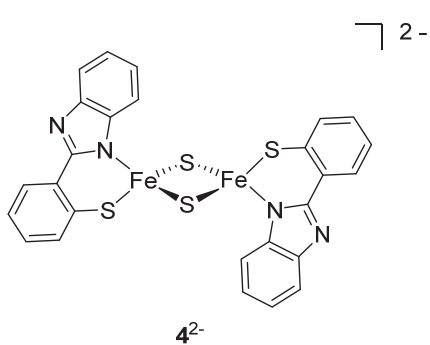
$L^{N NH_2}$



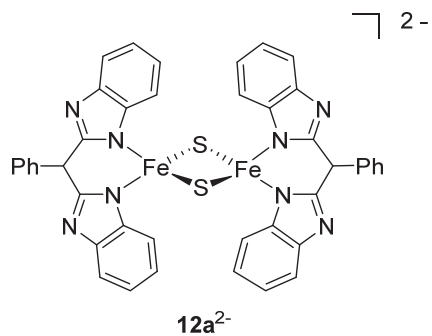
$L^{S NH_2}$



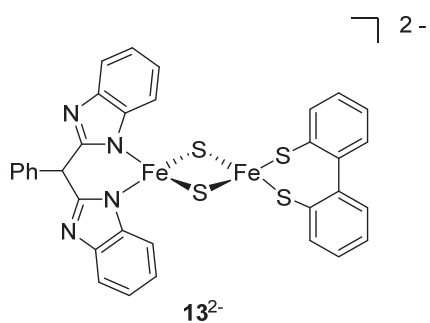
$L^{S SH_2}$



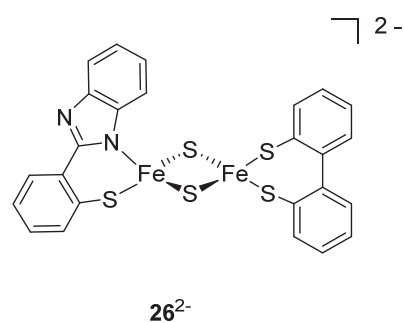
$4^{2-}$



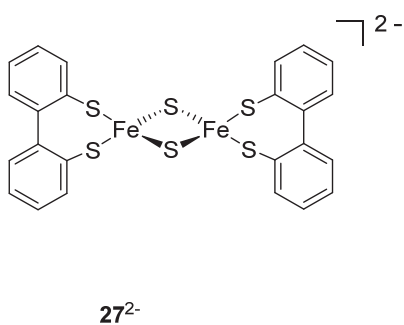
$12a^{2-}$



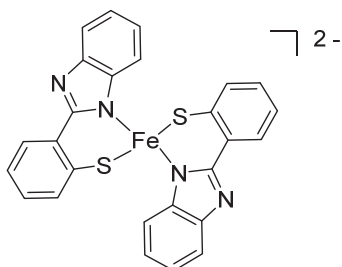
$13^{2-}$



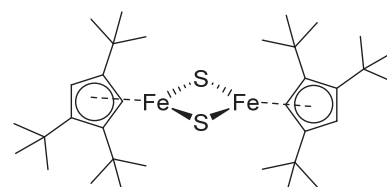
$26^{2-}$



$27^{2-}$



$28^{2-}$



50





---

## List of Abbreviations

15-crown-5	crown ether 15-crown-5 (C <sub>10</sub> H <sub>20</sub> O <sub>5</sub> )
5'-doA	5'-Desoxyadenosyl
Ala	alanine
Arg	arginine
Asp	aspartate
ATF1	cyclic AMP dependent transcription factor
ATP	adenosine triphosphate
av	average
BDFE	bond dissociation free energy
BioB	biotin synthase
bpy	bipyridine
br	broad
Bu	butyl-
COSY	correlation spectroscopy
Cp	cyclopentadienyl
Cp*	pentamethylcyclopentadienyl
CPET	concerted proton and electron transfer
CV	cyclic voltammetry
Cys	cysteine
d	doublet
DBU	diazabicycloundecene
DCM	dichloromethane
DFT	density functional theory
DMF	dimethylformamid
DMP	2,6-dimethylpyridin
DMPA	2,2-dimethoxy-2'-phenylacetophenon
DMSO	dimethylsulfoxide
DNA	deoxyribonucleic acid
DNIC	dinitrosyl iron complex
DTB	dethiobiotin
EI	electron impact ionization
EPR	electron paramagnetic resonance
eq	equivalent
ESI	electro spray ionization
Et	ethyl
ET	electron transfer
<i>f</i>	Lamb-Mößbauer factor
Fc	ferrocene



## List of Abbreviations

---

FD <sub>Pf</sub>	ferredoxine from <i>Pyrococcus furiosus</i>
FeMoco	iron-molybdenum cofactor
FNR	transcriptional activator of fumarate and nitrate reductase
fwhm	full width half maximum
<i>g</i>	Landé factor
GC-MS	coupled gas chromatography and mass spectrometry
HAT	hydrogen atom transfer
HDvV	Heisenberg-Diac-van-Vleck
HiPIP	high potential iron sulfur protein
His	histidine
hs	high spin
INT	intermediate
ISC	iron sulfur cluster formation system
IscR	iron sulfur cluster regulator
IscU	scaffold protein in ISC system
IUPAC	International Union of Pure and Applied Chemistry
$J_{\text{eff}}$	effective coupling constant
LCP	lipoyl carrier protein
LED	light emitting diode
LipA	lipoyl synthase
LMCT	ligand to metal charge transfer
Lys	lysine
<i>m</i>	multiplett
Me	methyl
MNIC	mononitrosyl iron complex
MS	mass spectrometry
NHE	normal hydrogen electrode
NIF	nitrogen fixation system
NMR	nuclear magnetic resonance
obs	observed
OTf	triflate (CF <sub>3</sub> SO <sub>3</sub> )
PDB	protein database
PCET	proton coupled electron transfer
Ph	phenyl
ppm	parts per million
PT	proton transfer
<i>q</i>	quartett
Q	quinole
RimO	ribosomal protein S12
RNA	ribonucleic acid



RS	radical SAM
RT	room temperature
SAM	<i>S</i> -adenosyl-L-methionine
SOC	spin orbit coupling
Ser	serine
sh	shoulder
SHE	standard hydrogen electrode
SQUID	superconducting quantum interference device
SUF	sulfur formation system
TEMPO	2,2,6,6-tetramethylpiperidinyloxy
THF	tetrahydrofuran
TIP	temperature-independent paramagnetism
tRNA	transfer ribonucleic acid
TS	transition state
UV-vis	ultraviolet and visible
<i>X</i>	arbitrary amino acid





---

## References

- [1] H. Beinert, *Science* **1997**, *277*, 653.
- [2] M. Fontecave, *Nat. Chem. Biol.* **2006**, *2*, 171.
- [3] D. C. Johnson, D. R. Dean, A. D. Smith, M. K. Johnson, *Annu. Rev. Biochem.* **2005**, *74*, 247.
- [4] J. Meyer, *J. Biol. Inorg. Chem.* **2008**, *13*, 157.
- [5] M. K. Johnson, *Curr. Opin. Chem. Biol.* **1998**, *2*, 173.
- [6] G. Wächtershauser, *Proc. Natl. Acad. Sci. USA* **1990**, *87*, 200.
- [7] H. Beinert, *Biochem. Biophys. Res. Commun.* **1960**, *3*, 41.
- [8] B. K. Burgess, D. J. Lowe, *Chem. Rev.* **1996**, *96*, 2983.
- [9] O. Einsle, *J. Biol. Inorg. Chem.* **2014**, *19*, 737.
- [10] B. M. Hoffman, D. Lukoyanov, Z.-Y. Yang, D. R. Dean, L. C. Seefeldt, *Chem. Rev.* **2014**, *114*, 4041.
- [11] J. A. Rees, R. Bjornsson, J. Schlesier, D. Sippel, O. Einsle, S. DeBeer, *Angew. Chem. Int. Ed. Engl.* **2015**, *54*, 13249.
- [12] L. Noodleman, C. Y. Peng, D. A. Case, J.-M. Mouesca, *Coord. Chem. Rev.* **1995**, *144*, 199.
- [13] L. Noodleman, D. A. Case, J.-M. Mouesca, B. Lamotte, *J. Biol. Inorg. Chem.* **1996**, *1*, 177.
- [14] A. Messerschmidt, *Handbook of Metalloproteins*, Wiley, Chichester, **2004**.
- [15] L. Noodleman, T. Lovell, T. Liu, F. Himo, R. A. Torres, *Curr. Opin. Chem. Biol.* **2002**, *6*, 259.
- [16] G. Hanson, L. Berliner (Eds.) *Biological Magnetic Resonance*, Springer New York, New York, NY, **2010**.
- [17] C. W. Carter, J. Kraut, S. T. Freer, R. A. Alden, L. C. Sieker, E. Adman, L. H. Jensen, *Proc. Natl. Acad. Sci. USA* **1972**, *69*, 3526.
- [18] R. Kümmerle, P. Kyritsis, J. Gaillard, J.-M. Moulis, *J. Inorg. Biochem.* **2000**, *79*, 83.
- [19] A. Soriano, D. Li, S. Bian, A. Agarwal, J. A. Cowan, *Biochem.* **1996**, *35*, 12479.
- [20] H. Beinert, M. C. Kennedy, C. D. Stout, *Chem. Rev.* **1996**, *96*, 2335.
- [21] J. C. Crack, J. Green, A. J. Thomson, N. E. Le Brun, *Acc. Chem. Res.* **2014**, *47*, 3196.
- [22] P. J. Kiley, H. Beinert, *FEMS Microbiol. Rev.* **1998**, *22*, 341.
- [23] T. A. Rouault, R. D. Klausner, *Trends Biochem. Sci.* **1996**, *21*, 174.
- [24] P. J. Kiley, H. Beinert, *Curr. Opin. Microbiol.* **2003**, *6*, 181.
- [25] J. O. Fuss, C.-L. Tsai, J. P. Ishida, J. A. Tainer, *Biochim. Biophys. Acta* **2015**, *1853*, 1253.
- [26] G. D. Shimberg, J. L. Michalek, A. A. Oluyadi, A. V. Rodrigues, B. E. Zucconi, H. M. Neu, S. Ghosh, K. Sureschandra, G. M. Wilson, T. L. Stemmler *Proc. Natl. Acad. Sci. USA* **2016**, *113*, 4700.



## References

---

- [27] Y. Liu, D. J. Vinyard, M. E. Reesbeck, T. Suzuki, K. Manakongtreecheep, P. L. Holland, G. W. Brudvig, D. Soll, *Proc. Natl. Acad. Sci. USA* **2016**.
- [28] O. A. Lukianova, S. S. David, *Curr. Opin. Chem. Biol.* **2005**, *9*, 145.
- [29] A. R. Crofts, *Biochim. Biophys. Acta* **2004**, *1655*, 77.
- [30] S. J. Booker, R. M. Cicchillo, T. L. Grove, *Analytical Techniques / Mechanisms* **2007**, *11*, 543.
- [31] R. Lill, *Nature* **2009**, *460*, 831.
- [32] T. A. Rouault, *Dis. Model. Mech.* **2012**, *5*, 155.
- [33] T. A. Rouault, W. H. Tong, *Trends Genet.* **2008**, *24*, 398.
- [34] R. Lill, U. Muhlenhoff, *Annu. Rev. Biochem.* **2008**, *77*, 669.
- [35] R. Malkin, J. C. Rabinowitz, *Biochem. Biophys. Res. Commun.* **1966**, *23*, 822.
- [36] E. L. Mettert, P. J. Kiley, *Annu. Rev. Microbiol.* **2015**, *69*, 505.
- [37] R. Lill, R. Dutkiewicz, H.-P. Elsässer, A. Hausmann, D. J. Netz, A. J. Pierik, O. Stehling, E. Urzica, U. Mühlenhoff, *Cell Biol. Met.* **2006**, *1763*, 652.
- [38] D. C. Johnson, M.-C. Unciuleac, D. R. Dean, *J. Bacteriol.* **2006**, *188*, 7551.
- [39] B. Blanc, M. Clemancey, J.-M. Latour, M. Fontecave, S. Ollagnier de Choudens, *Biochemistry* **2014**, *53*, 7867.
- [40] W. Yeo, J. Lee, K. Lee, J. Roe, *Mol. Microbio.* **2006**, *61*, 206.
- [41] L. Zheng, R. H. White, V. L. Cash, R. F. Jack, D. R. Dean, *Proc. Natl. Acad. Sci. USA* **1993**, *90*, 2754.
- [42] U. Muhlenhoff, J. Gerber, N. Richhardt, R. Lill, *EMBO J.* **2003**, *22*, 4815.
- [43] J. Gerber, U. Muhlenhoff, R. Lill, *EMBO Rep.* **2003**, *4*, 906.
- [44] K. Z. Bencze, K. C. Kondapalli, J. D. Cook, S. McMahon, C. Millan-Pacheco, N. Pastor, T. L. Stemmler, *Crit. Rev. Biochem. Mol. Biol.* **2006**, *41*, 269.
- [45] N. G. Fox, D. Das, M. Chakrabarti, P. A. Lindahl, D. P. Barondeau, *Biochemistry* **2015**, *54*, 3880.
- [46] E. C. Raulfs, I. P. O'Carroll, P. C. Dos Santos, M.-C. Unciuleac, D. R. Dean, *Proc. Natl. Acad. Sci. USA* **2008**, *105*, 8591.
- [47] P. Yuvaniyama, J. N. Agar, V. L. Cash, M. K. Johnson, D. R. Dean, *Proc. Natl. Acad. Sci. USA* **2000**, *97*, 599.
- [48] D. J. Sommer, A. Roy, A. Astashkin, G. Ghirlanda, *Biopolymers* **2015**, *104*, 412.
- [49] C. Wachnowsky, I. Fidai, J. A. Cowan, *J. Biol. Inorg. Chem.* **2016**, *21*, 825.
- [50] J. L. Markley, J. H. Kim, Z. Dai, J. R. Bothe, K. Cai, R. O. Frederick, M. Tonelli, *FEBS Letters* **2013**, *587*, 1172.
- [51] D. Brancaccio, A. Gallo, M. Piccioli, E. Novellino, S. Ciofi-Baffoni, L. Banci, *J. Am. Chem. Soc.* **2017**, *139*, 719.
- [52] K. Chandramouli, M.-C. Unciuleac, S. Naik, D. R. Dean, B. H. Huynh, M. K. Johnson, *Biochemistry* **2007**, *46*, 6804.
- [53] B. Blanc, C. Gerez, S. Ollagnier de Choudens, *Biochim. Biophys. Acta* **2015**, *1853*, 1436.



- [54] N. G. Fox, M. Chakrabarti, S. P. McCormick, P. A. Lindahl, D. P. Barondeau, *Biochemistry* **2015**, *54*, 3871.
- [55] H. Ye, T. A. Rouault, *Biochemistry* **2010**, *49*, 4945.
- [56] B. Roche, L. Aussel, B. Ezraty, P. Mandin, B. Py, F. Barras, *Biochim. Biophys. Acta Bioenergetics* **2013**, *1827*, 455.
- [57] C. Ayala-Castro, A. Saini, F. W. Outten, *Microbiol. Mol. Biol. Rev.* **2008**, *72*, 110.
- [58] S.-p. Wu, G. Wu, K. K. Surerus, J. A. Cowan, *Biochemistry* **2002**, *41*, 8876.
- [59] L. E. Vickery, J. R. Cupp-Vickery, *Crit. Rev. Biochem. Mol. Biol.* **2007**, *42*, 95.
- [60] S. Iametti, A. Barbiroli, F. Bonomi, *J. Biol. Inorg. Chem.* **2015**, *20*, 1039.
- [61] K. Chandramouli, M. K. Johnson, *Biochemistry* **2006**, *45*, 11087.
- [62] R. A. Marcus, N. Sutin, *Inorg. Chem.* **1975**, *14*, 213.
- [63] R. A. Marcus, *Biochim. Biophys. Acta Bioenergetics* **1985**, *811*, 265.
- [64] J. J. Warren, T. A. Tronic, J. M. Mayer, *Chem. Rev.* **2010**, *110*, 6961.
- [65] J. M. Mayer, *J. Phys. Chem. Lett.* **2011**, *2*, 1481.
- [66] J. M. Mayer, *Acc. Chem. Res.* **2011**, *44*, 36.
- [67] J. P. Roth, J. C. Yoder, T.-J. Won, J. M. Mayer, *Science* **2001**, *294*, 2524.
- [68] S. Hammes-Schiffer, *J. Am. Chem. Soc.* **2015**, *137*, 8860.
- [69] E. I. Stiefel, *Proc. Natl. Acad. Sci. USA* **1973**, *70*, 988.
- [70] J. J. Warren, J. M. Mayer, *Biochemistry* **2015**, *54*, 1863.
- [71] A. Wu, E. A. Mader, A. Datta, D. A. Hrovat, W. T. Borden, J. M. Mayer, *J. Am. Chem. Soc.* **2009**, *131*, 11985.
- [72] E. A. Mader, A. S. Larsen, J. M. Mayer, *J. Am. Chem. Soc.* **2004**, *126*, 8066.
- [73] D. W. Bak, S. J. Elliott, *Curr. Opin. Chem. Biol.* **2014**, *19*, 50.
- [74] D. J. Ferraro, L. Gakhar, S. Ramaswamy, *Biochem. Biophys. Res. Commun.* **2005**, *338*, 175.
- [75] J. R. Colca, W. G. McDonald, D. J. Waldon, J. W. Leone, J. M. Lull, C. A. Bannow, E. T. Lund, W. R. Mathews, *Am. J. Physiol. Endocrinol. Metab.* **2004**, *286*, E252.
- [76] J. T. Jarrett, *Arch. Biochem. Biophys.* **2005**, *433*, 312.
- [77] J. S. Rieske, D. H. MacLennan, R. Coleman, *Biochem. Biophys. Res. Commun.* **1964**, *15*, 338.
- [78] D. Kuila, J. A. Fee, *J. Biol. Chem.* **1986**, *261*, 2768.
- [79] T. A. Link in *Advances in Inorganic Chemistry*, Elsevier, **1999**, 83.
- [80] M. E. Ali, V. Staemmler, D. Marx, *Phys. Chem. Chem. Phys.* **2015**, *17*, 6289.
- [81] S. Boxhammer, S. Glaser, A. Kuhl, A. K. Wagner, C. L. Schmidt, *Biomaterials* **2008**, *21*, 459.
- [82] I.-J. Lin, Y. Chen, J. A. Fee, J. Song, W. M. Westler, J. L. Markley, *J. Am. Chem. Soc.* **2006**, *128*, 10672.
- [83] Y. Zu, M. M.-J. Couture, D. R. J. Kolling, A. R. Crofts, L. D. Eltis, J. A. Fee, J. Hirst, *Biochemistry* **2003**, *42*, 12400.
- [84] Y. Zu, J. A. Fee, J. Hirst, *J. Am. Chem. Soc.* **2001**, *123*, 9906.



## References

---

- [85] B. R. Jagger, A. M. Koval, R. A. Wheeler, *ChemPhysChem* **2016**, *17*, 216.
- [86] K.-L. Hsueh, W. M. Westler, J. L. Markley, *J. Am. Chem. Soc.* **2010**, *132*, 7908.
- [87] C. M. Kusminski, W. L. Holland, K. Sun, J. Park, S. B. Spurgin, Y. Lin, G. R. Askew, J. A. Simcox, D. A. McClain, C. Li, *Nat. Med.* **2012**, *18*, 1539.
- [88] Y.-S. Sohn, S. Tamir, L. Song, D. Michaeli, I. Matouk, A. R. Conlan, Y. Harir, S. H. Holt, V. Shulaev, M. L. Paddock, *Archives of Biochemistry and Biophysics* **2013**, *110*, 14676.
- [89] C. H. Lipper, M. L. Paddock, J. N. Onuchic, R. Mittler, R. Nechushtai, P. A. Jennings, *PLoS One* **2015**, *10*, e0139699.
- [90] S. E. Wiley, M. L. Paddock, E. C. Abresch, L. Gross, P. van der Geer, R. Nechushtai, A. N. Murphy, P. A. Jennings, J. E. Dixon, *J. Biol. Chem.* **2007**, *282*, 23745.
- [91] M. L. Paddock, S. E. Wiley, H. L. Axelrod, A. E. Cohen, M. Roy, E. C. Abresch, D. Capraro, A. N. Murphy, R. Nechushtai, J. E. Dixon, *Arch. Biochem. Biophys.* **2007**, *104*, 14342.
- [92] D. W. Bak, J. A. Zuris, M. L. Paddock, P. A. Jennings, S. J. Elliott, *Biochemistry* **2009**, *48*, 10193.
- [93] S. Tamir, M. L. Paddock, M. Darash-Yahana-Baram, S. H. Holt, Y. S. Sohn, L. Agranat, D. Michaeli, J. T. Stofleth, C. H. Lipper, F. Morcos, *Biochim. Biophys. Acta* **2015**, *1853*, 1294.
- [94] J. Lin, T. Zhou, K. Ye, J. Wang, *Proc. Natl. Acad. Sci. USA* **2007**, *104*, 14640.
- [95] A. R. Conlan, H. L. Axelrod, A. E. Cohen, E. C. Abresch, J. Zuris, D. Yee, R. Nechushtai, P. A. Jennings, M. L. Paddock, *J. Mol. Biol.* **2009**, *392*, 143.
- [96] D. W. Bak, S. J. Elliott, *Biochemistry* **2013**, *52*, 4687.
- [97] J. A. Zuris, Y. Harir, A. R. Conlan, M. Shvartsman, D. Michaeli, S. Tamir, M. L. Paddock, J. N. Onuchic, R. Mittler, Z. I. Cabantchik, *Proc. Natl. Acad. Sci. USA* **2011**, *108*, 13047.
- [98] M. M. Dicus, A. Conlan, R. Nechushtai, P. A. Jennings, M. L. Paddock, R. D. Britt, S. Stoll, *J. Am. Chem. Soc.* **2010**, *132*, 2037.
- [99] T. Iwasaki, R. I. Samoilova, A. Kounosu, D. Ohmori, S. A. Dikanov, *J. Am. Chem. Soc.* **2009**, *131*, 13659.
- [100] J. A. Zuris, D. A. Halim, A. R. Conlan, E. C. Abresch, R. Nechushtai, M. L. Paddock, P. A. Jennings, *J. Am. Chem. Soc.* **2010**, *132*, 13120.
- [101] M.-P. Golinelli-Cohen, E. Lescop, C. Mons, S. Goncalves, M. Clemancey, J. Santolini, E. Guittet, G. Blondin, J.-M. Latour, C. Bouton, *J. Biol. Chem.* **2016**, *291*, 7583.
- [102] G. Tan, D. Liu, F. Pan, J. Zhao, T. Li, Y. Ma, B. Shen, J. Lyu, *Biochem. Biophys. Res. Commun.* **2016**, *470*, 226.
- [103] P. A. Frey, *FASEB J.* **1993**, *7*, 662.
- [104] D. P. Dowling, J. L. Vey, A. K. Croft, C. L. Drennan, *Biochim. Biophys. Acta* **2012**, *1824*, 1178.



- [105] N. D. Lanz, S. J. Booker, *Biochim. Biophys. Acta* **2012**, 1824, 1196.
- [106] H. J. Sofia, *Nucleic Acids Res.* **2001**, 29, 1097.
- [107] N. D. Lanz, S. J. Booker, *Biochim. Biophys. Acta* **2015**, 1853, 1316.
- [108] G. Layer, D. W. Heinz, D. Jahn, W.-D. Schubert, *Curr. Opin. Chem. Biol.* **2004**, 8, 468.
- [109] T. A. Stich, W. K. Myers, R. D. Britt, *Acc. Chem. Res.* **2014**, 47, 2235.
- [110] C. J. Fugate, J. T. Jarrett, *Biochim. Biophys. Acta Proteins Proteomics* **2012**, 1824, 1213.
- [111] G. N. L. Jameson, M. M. Cosper, H. L. Hernandez, M. K. Johnson, B. H. Huynh, *Biochemistry* **2004**, 43, 2022.
- [112] N. B. Ugulava, B. R. Gibney, J. T. Jarrett, *Biochemistry* **2001**, 40, 8343.
- [113] B. Tse Sum Bui, D. Florentin, F. Fournier, O. Ploux, A. Méjean, A. Marquet, *FEBS Letters* **1998**, 440, 226.
- [114] S. B. B. Tse, M. Lotierzo, F. Escalettes, D. Florentin, A. Marquet, *Biochemistry* **2004**, 43, 16432.
- [115] F. Berkovitch, Y. Nicolet, J. T. Wan, J. T. Jarrett, C. L. Drennan, *Science* **2004**, 303, 76.
- [116] A. M. Taylor, S. Stoll, R. D. Britt, J. T. Jarrett, *Biochemistry* **2011**, 50, 7953.
- [117] B. Tse Sum Bui, T. A. Mattioli, D. Florentin, G. Bolbach, A. Marquet, *Biochemistry* **2006**, 45, 3824.
- [118] M. Lotierzo, B. Tse Sum Bui, D. Florentin, F. Escalettes, A. Marquet, *Biochem. Soc. Trans.* **2005**, 33, 820.
- [119] P. Douglas, M. Kriek, P. Bryant, P. L. Roach, *Angew. Chem. Int. Ed.* **2006**, 45, 5197.
- [120] J. E. Cronan, *Biochem. J.* **2014**, 464, e1.
- [121] J. E. Harmer, M. J. Hiscox, P. C. Dinis, S. J. Fox, A. Iliopoulos, J. E. Hussey, J. Sandy, F. T. van Beek, J. W. Essex, P. L. Roach, *Biochem. J.* **2014**, 464, 123.
- [122] M. I. McLaughlin, N. D. Lanz, P. J. Goldman, K.-H. Lee, S. J. Booker, C. L. Drennan, *Proc. Natl. Acad. Sci. USA* **2016**, 113, 9446.
- [123] N. D. Lanz, M.-E. Pandelia, E. S. Kakar, K.-H. Lee, C. Krebs, S. J. Booker, *Biochemistry* **2014**, 53, 4557.
- [124] M. McLaughlin, N. Lanz, P. Goldman, K. H. Lee, S. Booker, C. Drennan, *FASEB J.* **2015**, 29, 895.4.
- [125] N. Lanz, M.-E. Pandelia, M. McLaughlin, J. Rectenwald, A. Silakov, C. Drennan, C. Krebs, S. Booker, *FASEB J.* **2015**, 29, 572.4.
- [126] B. P. Anton, L. Saleh, J. S. Benner, E. A. Raleigh, S. Kasif, R. J. Roberts, *Proc. Natl. Acad. Sci. USA* **2008**, 105, 1826.
- [127] H. L. Hernandez, F. Pierrel, E. Elleingand, R. Garcia-Serres, B. H. Huynh, M. K. Johnson, M. Fontecave, M. Atta, *Biochemistry* **2007**, 46, 5140.
- [128] B. P. Anton, S. P. Russell, J. Vertrees, S. Kasif, E. A. Raleigh, P. A. Limbach, R. J. Roberts, *Nucleic Acids Res.* **2010**, 38, 6195.



## References

---

- [129] S. Arragain, R. Garcia-Serres, G. Blondin, T. Douki, M. Clemancey, J.-M. Latour, F. Forouhar, H. Neely, G. T. Montelione, J. F. Hunt, *J. Biol. Chem.* **2010**, *285*, 5792.
- [130] S. Arragain, S. K. Handelman, F. Forouhar, F.-Y. Wei, K. Tomizawa, J. F. Hunt, T. Douki, M. Fontecave, E. Mulliez, M. Atta, *J. Biol. Chem.* **2010**, *285*, 28425.
- [131] B. J. Landgraf, A. J. Arcinas, K.-H. Lee, S. J. Booker, *J. Am. Chem. Soc.* **2013**, *135*, 15404.
- [132] P. V. Rao, R. H. Holm, *ChemInform* **2004**, 35.
- [133] S. Ohta, Y. Ohki, *Coord. Chem. Rev.* **2017**, *338*, 207.
- [134] R. H. Holm, E. I. Solomon, *Chem. Rev.* **2004**, *104*, 347.
- [135] J. J. Mayerle, R. B. Frankel, R. H. Holm, J. A. Ibers, W. D. Phillips, J. F. Weiher, *Proc. Natl. Acad. Sci. USA* **1973**, *70*, 2429.
- [136] R. H. Holm, *Inorg. Chem.* **1983**, 3809.
- [137] R. H. Holm, *Inorg. Chem.* **1978**, 17.
- [138] J. Ballmann, S. Dechert, E. Bill, U. Ryde, F. Meyer, *Inorg. Chem.* **2008**, *47*, 1586.
- [139] P. Beardwood, J. F. Gibson, *J. Chem. Soc., Dalton Trans.* **1992**, 2457.
- [140] Y. Ohki, Y. Sunada, K. Tatsumi, *Chem. Lett.* **2005**, *34*, 172.
- [141] M. E. Reesbeck, M. M. Rodriguez, W. W. Brennessel, B. Q. Mercado, D. Vinyard, P. L. Holland, *J. Biol. Inorg. Chem.* **2015**, *20*, 875.
- [142] S. Yao, F. Meier, N. Lindenmaier, R. Rudolph, B. Blom, M. Adelhardt, J. Sutter, S. Mebs, M. Haumann, K. Meyer, *Angew. Chem. Int. Ed. Engl.* **2015**, *54*, 12506.
- [143] L. Fohlmeister, K. R. Vignesh, F. Winter, B. Moubaraki, G. Rajaraman, R. Pottgen, K. S. Murray, C. Jones, *Dalton Trans.* **2015**, *44*, 1700.
- [144] J. Ballmann, A. Albers, S. Demeshko, S. Dechert, E. Bill, E. Bothe, U. Ryde, F. Meyer, *Angew. Chem. Int. Ed. Engl.* **2008**, *47*, 9537.
- [145] J. A. Fee, K. L. Findling, T. Yoshida, R. Hille, G. E. Tarr, D. O. Hearshen, W. R. Dunham, E. P. Day, T. A. Kent, E. Munck, *J. Biol. Chem.* **1984**, *259*, 124.
- [146] R. Cammack, F. MacMillan in *Biological Magnetic Resonance* (Eds.: G. Hanson, L. Berliner), Springer New York, New York, NY, **2010**, 11.
- [147] A. Albers, T. Bayer, S. Demeshko, S. Dechert, F. Meyer, *Chem. Eur. J.* **2013**, *19*, 10101.
- [148] A. Albers, S. Demeshko, S. Dechert, C. T. Saouma, J. M. Mayer, F. Meyer, *J. Am. Chem. Soc.* **2014**, *136*, 3946.
- [149] A. Albers, S. Demeshko, S. Dechert, E. Bill, E. Bothe, F. Meyer, *Angew. Chem. Int. Ed. Engl.* **2011**, *50*, 9191.
- [150] C. T. Saouma, W. Kaminsky, J. M. Mayer, *J. Am. Chem. Soc.* **2012**, *134*, 7293.
- [151] C. T. Saouma, M. M. Pinney, J. M. Mayer, *Inorg. Chem.* **2014**, *53*, 3153.
- [152] A. Albers, S. Demeshko, K. Propper, S. Dechert, E. Bill, F. Meyer, *J. Am. Chem. Soc.* **2013**, *135*, 1704.
- [153] C. T. Saouma, W. Kaminsky, J. M. Mayer, *Polyhedron* **2013**, *58*, 60.
- [154] K. Tanifuji, S. Tajima, Y. Ohki, K. Tatsumi, *Inorg. Chem.* **2016**, *55*, 4512.



- [155] A. J. Jervis, J. C. Crack, G. White, P. J. Artymiuk, M. R. Cheesman, A. J. Thomson, N. E. Le Brun, J. Green, *Proc. Natl. Acad. Sci. USA* **2009**, *106*, 4659.
- [156] J. Fitzpatrick, E. Kim, *Acc. Chem. Res.* **2015**, *48*, 2453.
- [157] H. Ding, B. Demple, *Proc. Natl. Acad. Sci. USA* **2000**, *97*, 5146.
- [158] T. C. Harrop, Z. J. Tonzetich, E. Reisner, S. J. Lippard, *J. Am. Chem. Soc.* **2008**, *130*, 15602.
- [159] Z. J. Tonzetich, L. H. Do, S. J. Lippard, *J. Am. Chem. Soc.* **2009**, *131*, 7964.
- [160] C. T. Tran, E. Kim, *Inorg. Chem.* **2012**, *51*, 10086.
- [161] C. T. Tran, P. G. Williard, E. Kim, *J. Am. Chem. Soc.* **2014**, *136*, 11874.
- [162] J. Fitzpatrick, H. Kalyvas, M. R. Filipovic, I. Ivanovic-Burmazovic, J. C. MacDonald, J. Shearer, E. Kim, *J. Am. Chem. Soc.* **2014**, *136*, 7229.
- [163] J. Fitzpatrick, E. Kim, *Inorg. Chem.* **2015**, *54*, 10559.
- [164] S. C. Lee, W. Lo, R. H. Holm, *Chem. Rev.* **2014**, *114*, 3579.
- [165] Thomas C. Bruick, *Proc. Natl. Acad. Sci. USA* **1975**, *77*, 2478.
- [166] G. R. Dukes, R. H. Holm, *J. Am. Chem. Soc.* **1975**, *97*, 528.
- [167] Kay E. Oglieve, *J. Chem. Soc. Chem. Commun.* **194**, 377.
- [168] L. Deng, R. H. Holm, *J. Am. Chem. Soc.* **2008**, *130*, 9878.
- [169] G. D. Watt, K. Reddy, *J. Inorg. Biochem.* **1994**, *53*, 281.
- [170] Y. Ohki, K. Tanifuji, N. Yamada, M. Imada, T. Tajima, K. Tatsumi, *Proc. Natl. Acad. Sci. USA* **2011**, *108*, 12635.
- [171] T. Terada, K. Hirabayashi, D. Liu, T. Nakamura, T. Wakimoto, T. Matsumoto, K. Tatsumi, *Inorg. Chem.* **2013**, *52*, 11997.
- [172] T. O'Sullivan, M. M. Millar, *J. Am. Chem. Soc.* **1985**, *107*, 4096.
- [173] K. Tanifuji, N. Yamada, T. Tajima, T. Sasamori, N. Tokitoh, T. Matsuo, K. Tamao, Y. Ohki, K. Tatsumi, *Inorg. Chem.* **2014**, *53*, 4000.
- [174] Y. Ohki, K. Tatsumi, *Z. Anorg. Allg. Chem.* **2013**, *639*, 1340.
- [175] Y. Ohki, Y. Sunada, M. Honda, M. Katada, K. Tatsumi, *J. Am. Chem. Soc.* **2003**, *125*, 4052.
- [176] Y. Ohki, M. Imada, A. Murata, Y. Sunada, S. Ohta, M. Honda, T. Sasamori, N. Tokitoh, M. Katada, K. Tatsumi, *J. Am. Chem. Soc.* **2009**, *131*, 13168.
- [177] T. Hashimoto, Y. Ohki, K. Tatsumi, *Inorg. Chem.* **2010**, *49*, 6102.
- [178] Y. Ohki, K. Tanifuji, N. Yamada, R. E. Cramer, K. Tatsumi, *Chem. Asian. J.* **2012**, *7*, 2222.
- [179] B. Guigliarelli, P. Bertrand in *Advances in Inorganic Chemistry*, Elsevier, **1999**, pp. 421–497.
- [180] M. Brustolon, G. Giamello, *Electron Paramagnetic Resonance. A Practitioner's Toolkit*, Wiley, Hoboken, N.J., **2009**.
- [181] P. Day, N. S. Hush, R. J. H. Clark, *Philos. Trans. A Math. Phys. Eng. Sci.* **2008**, *366*, 5.
- [182] F. R. Whatley, *Proc. Natl. Acad. Sci. USA* **1966**, *56*, 987.



## References

---

- [183] M. Orio, J.-M. Mouesca, *Inorg. Chem.* **2008**, *47*, 5394.
- [184] P. Bertrand, B. Guigliarelli, J.-P. Gayda, B. Peter, J. F. Gibson, *Biochim. Biophys. Acta - Protein Structure and Molecular Enzymology* **1985**, *831*, 261.
- [185] P. Gütllich, *Chem. Ing. Tech.* **1971**, *43*, 1049.
- [186] H. Winkler, *Rep. Prog. Phys* **2000**, *63*, 263.
- [187] M.-E. Pandelia, N. D. Lanz, S. J. Booker, C. Krebs, *Biochim. Biophys. Acta* **2015**, *1853*, 1395.
- [188] R. L. Mössbauer, *Hyperfine Interactions* **2000**, *126*, 1.
- [189] E. Münck, P. G. Debrunner, J. C. M. Tsibris, I. C. Gunsalus, *Biochemistry* **1972**, *11*, 855.
- [190] E. Münck, *Proc. Natl. Acad. Sci. USA* **1980**, *77*, 6574.
- [191] E. Münck, *J. Biol. Chem.* **1984**, *259*, 14463.
- [192] M. Bergner, S. Dechert, S. Demeshko, C. Kupper, J. M. Mayer, F. Meyer, *J. Am. Chem. Soc.* **2017**, *139*, 701.
- [193] M. Reiners, M. Maekawa, C. G. Daniliuc, M. Freytag, P. G. Jones, P. S. White, J. Hohenberger, J. Sutter, K. Meyer, L. Maron, *Chem. Sci.* **2017**, *8*, 4108.
- [194] M. Bergner, L. Roy, S. Dechert, F. Neese, S. Ye, F. Meyer, *Angew. Chem. Int. Ed.* **2017**, *277*, 653.
- [195] Joachim Ballmann, *Dissertation*, **2008**, Göttingen.
- [196] K. E. Schwarzthans, *Angew. Chem. Int. Ed. Engl.* **1970**, *9*, 946.
- [197] N. G. Connelly, W. E. Geiger, *Chem. Rev.* **1996**, *96*, 877.
- [198] J. T. Hoggins, H. Steinfink, *Inorg. Chem.* **1976**, *15*, 1682.
- [199] S. Stoll, *Methods. Enzymol.* **2015**, *563*, 121.
- [200] S. Stoll, A. Schweiger, *J. Magn. Reson.* **2006**, *178*, 42.
- [201] I. Kaljurand, A. Kutt, L. Soovali, T. Rodima, V. Maemets, I. Leito, I. A. Koppel, *J. Org. Chem.* **2005**, *70*, 1019.
- [202] S. B. Harkins, J. C. Peters, *J. Am. Chem. Soc.* **2004**, *126*, 2885.
- [203] F. E. Sowrey, C. J. MacDonald, R. D. Cannon, *Faraday Trans.* **1998**, *94*, 1571.
- [204] R. Poli, *Comm. Inorg. Chem.* **2009**, *30*, 177.
- [205] S. J. Meek, C. L. Pitman, A. J. M. Miller, *J. Chem. Educ.* **2016**, *93*, 275.
- [206] F. Neese, *WIREs Comput. Mol. Sci.* **2012**, *2*, 73.
- [207] A. D. Becke, *J. Chem. Phys.* **1993**, *98*, 5648.
- [208] A. Schäfer, C. Huber, R. Ahlrichs, *J. Chem. Phys.* **1994**, *100*, 5829.
- [209] C. Schulzke, *Dalton Trans.* **2009**, 6683.
- [210] E. D. Eastman, *J. Am. Chem. Soc.* **1928**, *50*, 292.
- [211] J. Heinze, *Angew. Chem.* **1984**, *98*, 823.
- [212] W. A. Donald, R. D. Leib, J. T. O'Brien, M. F. Bush, E. R. Williams, *J. Am. Chem. Soc.* **2008**, *130*, 3371.
- [213] W. A. Donald, R. D. Leib, M. Demireva, J. T. O'Brien, J. S. Prell, E. R. Williams, *J. Am. Chem. Soc.* **2009**, *131*, 13328.



- [214] S. Trasatti, *Pure Appl. Chem.* **1986**, *58*, 956.
- [215] V. T. Taniguchi, N. Sailasuta-Scott, F. C. Anson, H. B. Gray, *Pure Appl. Chem.* **1980**, *52*.
- [216] S. Benini, M. Borsari, S. Ciurli, A. Dikiy, M. Lamborghini, *J. Biol. Inorg. Chem.* **1998**, *3*, 371.
- [217] G. Battistuzzi, M. Borsari, L. Loschi, A. Martinelli, M. Sola, *Biochemistry* **1999**, *38*, 7900.
- [218] T. A. Link, O. M. Hatzfeld, P. Unalkat, J. K. Shergill, R. Cammack, J. R. Mason, *Biochemistry* **1996**, *35*, 7546.
- [219] P. L. Hagedoorn, M. C. Driessen, M. van den Bosch, I. Landa, W. R. Hagen, *FEBS Letters* **1998**, *440*, 311.
- [220] P. D. Swartz, T. Ichiye, *Biochemistry* **1996**, *35*, 13772.
- [221] R. R. Gagne, C. A. Koval, G. C. Lisensky, *Inorg. Chem.* **1980**, *19*, 2854.
- [222] L. Ebersson, *Electron Transfer Reactions in Organic Chemistry*, Springer-Verlag Berlin, **2012**.
- [223] G. Grampp, K. Rasmussen, *Phys. Chem. Chem. Phys.* **2002**, *4*, 5546.
- [224] K. Usuda, K. Kono, T. Dote, M. Watanabe, H. Shimizu, Y. Tanimoto, E. Yamadori, *Environ. Health Prev. Med.* **2007**, *12*, 231.
- [225] R. Williams, W. J. Ryves, E. C. Dalton, B. Eickholt, G. Shaltiel, G. Agam, A. J. Harwood, *Biochem. Soc. Trans.* **2004**, *32*, 799.
- [226] Y. Su, J. Ryder, B. Li, X. Wu, N. Fox, P. Solenberg, K. Brune, S. Paul, Y. Zhou, F. Liu et al., *Biochemistry* **2004**, *43*, 6899.
- [227] M. S. Muller, *Nat. Chem.* **2011**, *3*, 974.
- [228] F. H. Yu, W. A. Catterall, *Genome Biol.* **2003**, *4*, 207.
- [229] B. Valeur, *Coord. Chem. Rev.* **2000**, *205*, 3.
- [230] J. M. Dubach, E. Lim, N. Zhang, K. P. Francis, H. Clark, *Integr. Biol.* **2011**, *3*, 142.
- [231] H. He, M. A. Mortellaro, M. J. P. Leiner, R. J. Fraatz, J. K. Tusa, *J. Am. Chem. Soc.* **2003**, *125*, 1468.
- [232] A. J. Smetana, A. I. Popov, *J. Solution Chem.* **1980**, *9*, 183.
- [233] Y. Takeda, *Bull. Chem. Soc. Jpn.* **1988**, *61*, 627.
- [234] M. Formica, V. Fusi, M. Micheloni, R. Pontellini, P. Romani, *Coord. Chem. Rev.* **1999**, *184*, 347.
- [235] S. Fukuzumi, K. Ohkubo, *Coord. Chem. Rev.* **2010**, *254*, 372.
- [236] K. E. Dalle, T. Gruene, S. Dechert, S. Demeshko, F. Meyer, *J. Am. Chem. Soc.* **2014**, *136*, 7428.
- [237] F. Meyer, A. Brinkmeier, *unpublished results*.
- [238] S. Bang, Y.-M. Lee, S. Hong, K.-B. Cho, Y. Nishida, M. S. Seo, R. Sarangi, S. Fukuzumi, W. Nam, *Nat. Chem.* **2014**, *6*, 934.
- [239] E. Y. Tsui, R. Tran, J. Yano, T. Agapie, *Nat. Chem.* **2013**, *5*, 293.



## References

---

- [240] R. J. M. K. Gebbink, S. I. Klink, M. C. Feiters, R. J. M. Nolte, *Eur. J. Inorg. Chem.* **2000**, 2000, 253.
- [241] J. S. Renny, L. L. Tomasevich, E. H. Tallmadge, D. B. Collum, *Angew. Chem. Int. Ed. Engl.* **2013**, 52, 11998.
- [242] F. Ulatowski, K. Dabrowa, T. Balakier, J. Jurczak, *J. Org. Chem.* **2016**, 81, 1746.
- [243] A. E. Hargrove, Z. Zhong, J. L. Sessler, E. V. Anslyn, *New. J. Chem.* **2010**, 34, 348.
- [244] P. Thordarson, *Chem. Soc. Rev.* **2011**, 40, 1305.
- [245] V. Corce, L.-M. Chamoreau, E. Derat, J.-P. Goddard, C. Ollivier, L. Fensterbank, *Angew. Chem. Int. Ed. Engl.* **2015**, 54, 11414.
- [246] C. K. Prier, D. A. Rankic, D. W. C. MacMillan, *Chem. Rev.* **2013**, 113, 5322.
- [247] C. Barner-Kowollik, P. Vana, T. P. Davis, *J. Polym. Sci. A Polym. Chem.* **2002**, 40, 675.
- [248] Manfred Walbiner, *J. Chem. Soc. Perkin Trans. 2* **1990**, 787.
- [249] H. E. Gottlieb, V. Kotlyar, A. Nudelman, *J. Org. Chem.* **1997**, 62, 7512.
- [250] E. Bill, *Max Planck Institute for Chemical Energy Conversion, Mülheim/Ruhr, Germany*
- [251] G. M. Sheldrick, *Acta Crystallogr. A Found. Adv.* **2015**, 71, 3.
- [252] G. M. Sheldrick, *Acta Crystallogr. C Struct. Chem.* **2015**, 71, 3.
- [253] X-RED, STOE & CIE GmbH, Darmstadt, Germany, **2002**.



---

## Curriculum Vitae

### PERSONAL DATA

---

Marie Bergner  
\* 08/22/1989 in Gera, Germany

### EDUCATION

---

PhD Thesis	PhD student in the group of Prof. Dr. F. Meyer, Department of Inorganic Chemistry, Georg August University Göttingen, Germany. Thesis: “ <i>Biomimetic Function of Fe/S Clusters with Alternative Ligands: Model Studies Using Synthetic Analogues</i> ”	01/2014 – 08/2017
Research Stays Abroad	Visiting Assistant in Research in the group of Prof. James M. Mayer, Yale University, New Haven, USA.	04/2015 – 06/2015
	Research student in the group of Prof. Roberta Sessoli, University of Florence, Italy	10/2012 – 03/2013
M.Sc. Studies	<i>Studies of Chemistry</i> Degree: <i>M.Sc.</i> ; cumulative grade: 1.6 Master thesis in the group of Prof. F. Meyer, Department of Inorganic Chemistry, Georg-August University Göttingen, Germany. Thesis: “ <i>Radical Reactions of Biomimetic [2Fe-2S] Clusters</i> ” (grade 1.0)	10/2011 – 10/2013
B.Sc. Studies	<i>Studies of Chemistry</i> Degree: <i>B.Sc.</i> ; cumulative grade: 1.4 (with distinction) Bachelor thesis in the group of Prof. F. Meyer, Department of Inorganic Chemistry, Georg-August University Göttingen, Germany. Thesis: “ <i>Heterobimetallic Complexes of the Siamese Twin-Porphyrin</i> ” (grade 1.0)	10/2008 – 06/2011
Secondary School	<i>Abitur</i> (university-entrance diploma): 1.0 (cumulative grade), Pestalozzi Gymnasium Stadtroda, Germany	09/2000 – 06/2008

### SCIENTIFIC CONTRIBUTIONS

---

#### *Publications*

M. Bergner, L. Roy, S. Dechert, S. Ye, F. Neese, F. Meyer, “*Ligand Rearrangement at Fe/S Cofactors: Slow Isomerization of a Biomimetic [2Fe-2S] Cluster*“, *Angew. Chem. Int. Ed.* **2017**, *56*, 4882–4886.



M. Bergner, S. Dechert, S. Demeshko, C. Kupper, J. M. Mayer, F. Meyer, “*Model of the MitoNEET [2Fe-2S] Cluster Shows Proton Coupled Electron Transfer*”, *J. Am. Chem. Soc.* **2017**, *139*, 701-707.

C. Kupper, A. Schober, S. Demeshko, M. Bergner, F. Meyer, “*An Exclusively Organometallic {FeNO}<sub>3</sub><sup>7</sup> Complex with Tetracarbene Ligation and a Linear FeNO Unit*”, *Inorg. Chem.* **2015**, *54*, 3096–3098.

*Presentations at International Conferences and Workshops*

M. Bergner, S. Demeshko, S. Dechert, J. Mayer, F. Meyer, “*Structural and Functional Model Systems for the [2Fe-2S] Cluster in mitoNEET Proteins*”, 42<sup>nd</sup> ICCS, Brest, France, July 2016 (Talk).

M. Bergner, S. Demeshko, S. Dechert, F. Meyer, “*Structural and Functional Model Systems for the [2Fe-2S] Cluster in mitoNEET Proteins*”, 6<sup>th</sup> IMBG Meeting, Grenoble, France, September 2015 (Poster).

M. Bergner, S. Demeshko, S. Dechert, F. Meyer, “*Structural and Functional Model Systems for the [2Fe-2S] Cluster in mitoNEET Proteins*”, Final Symposium of the International Research Training Group 1422 “*Metal Sites in Biomolecules: Structures, Regulation and Mechanisms*”, Göttingen, Germany, August 2015 (Poster).

M. Bergner, F. Meyer, “*Synthesis and Properties of New Biomimetic [2Fe-2S] Clusters*”, Trends in Inorganic Chemistry (TINC), Lund, Sweden, May 2014 (Poster).

---

## Acknowledgment

First of all I would like to thank Prof. Franc Meyer, for the opportunity to work on this challenging project, for his continuous support, for providing an excellent working atmosphere, and for the scientific freedom he has granted me during the past years. I would also like to thank Prof. Kai Tittmann for co-supervising this thesis and for useful discussion about all my questions concerning kinetics. I want to thank Prof. Sven Schneider for co-supervising the final stage of this thesis.

I am very thankful to Prof. Jim Mayer for the opportunity to spend three months in his group during which I learned a lot, and for his continuous support and encouragement. I would also like to thank everybody in the Mayer lab for welcoming me to the group and to New Haven.

I am thankful to Dr. Sebastian Dechert for measuring crystal structures and for patiently looking through what feels like hundreds of test tubes which did not contain single crystals. I would also like to thank him for his support with all computer related questions. I would like to thank Dr. Claudia Stückl for teaching me how to use the EPR spectrometer, measuring samples for me, for many useful discussions, and her continuous enthusiasm for this project.

I would like to thank Dr. Michael John, the whole NMR service department, and especially Ralf Schöne for measuring countless  $^1\text{H}$  NMR spectra. I would like to thank Dr. Lisa Roy, Prof. Dr. Shengfa Ye and Prof. Frank Neese for performing DFT calculations on the isomerization project. I am thankful to Claudia Kupper, Christine Schiewer, and Dr. Serhiy Demeshko for Mößbauer and SQUID measurements. I want to thank Claudia Kupper and Claudia Schremmer as well as Dr. Fraundorf and the mass spectrometry department for ESI measurements and I also want to thank the glass service, chemical storage service, and all care takers.

I would also like to thank my labmates Christine Schiewer and Mattia Veronelli for the great atmosphere in the lab, and for drying solvents and sharing chemicals. Furthermore, I want to thank Andreas Schwarz for providing me with ligand  $\text{L}^{\text{SS}}\text{H}_2$  and his support during the practical work. I would also like to thank Alexander Brinkmeier for useful tips and tricks in the alkali metal project. I would like to thank the group of Dr. Alexander Breder for providing  $[\text{Ru}(\text{bpy})_3](\text{PF}_6)_2$  and Prof. Marc Walter at TU Braunschweig for providing their iron sulfur cluster. I would like to thank Maximilian Dürr and Prof. Ivana Ivanovic-Brumzavoic at the University of Erlangen for Cryo-ESI measurements.

I am also thankful to Prof. Carola Schulzke and her group for hosting me in their lab in Greifswald for one week, for allowing me to use their set up for temperature-dependent electrochemistry, and for performing additional measurements.



## Acknowledgment

---

I would like to thank Dr. Claudia Stückl, Britta Müller, and Petra Unger for taking care of all administrative issues.

I would like to thank Oliver Mitevski, Christian Schmidt, Barbara Hubrich, Claudia Kupper, Joanne Wong, Serhiy Demeshko, and Eleonora Feretti for thoroughly proof-reading my thesis.

I want to thank everybody in AK Meyer, especially Claudia Kupper, for a wonderful time in and out of the lab, and for being colleagues and friends. I would like to thank my friends in and out of Göttingen, Christian, Annika, Basti, Barbara, Christoph, Tine, Anna-Lena, Frederik and Magdalena for a wonderful time during the last 9 years. Finally, I want to thank my family for their love and support.



